LBL-26449
c.2

Center for Advanced Materials

CAM

RECEIVED
LAWRENCE
BERKELEY LABORATORY

MAR 27 1989

LIBRARY AND
DOCUMENTS SECTION

Mechanisms of Fatigue Crack Propagation and Fracture Toughness Behavior in Advanced Aluminum-Lithium Alloys

K.T. Venkateswara Rao
(Ph.D. Thesis)

June 1988

TWO-WEEK LOAN COPY

This is a Library Circulating Copy which may be borrowed for two weeks.

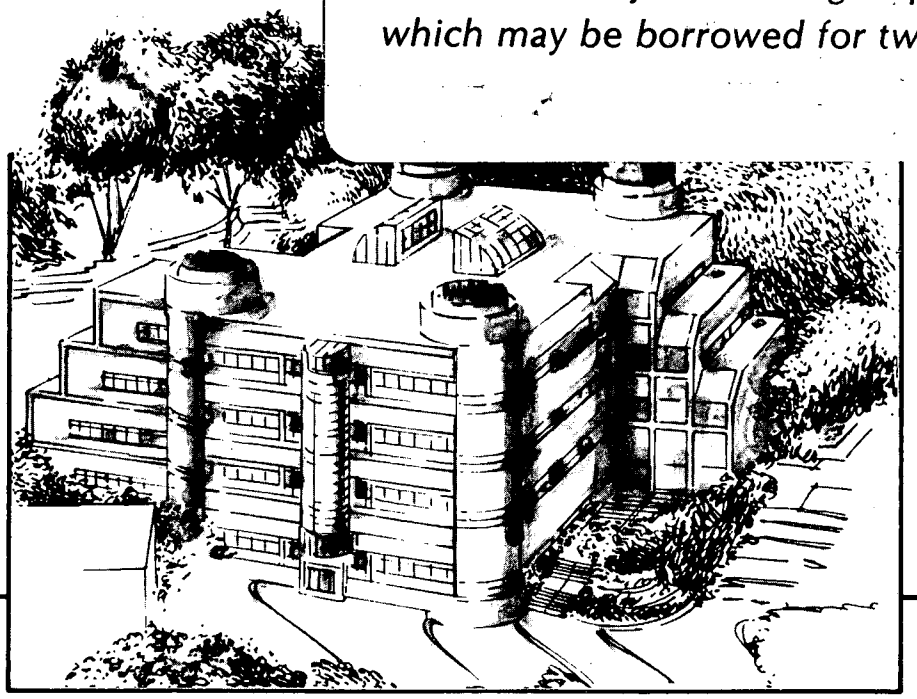

Materials and Chemical Sciences Division

Lawrence Berkeley Laboratory • University of California

ONE CYCLOTRON ROAD, BERKELEY, CA 94720 • (415) 486-4755

Prepared for the U.S. Department of Energy under Contract DE-AC03-76SF00098

LBL-26449
c.2

DISCLAIMER

This document was prepared as an account of work sponsored by the United States Government. While this document is believed to contain correct information, neither the United States Government nor any agency thereof, nor the Regents of the University of California, nor any of their employees, makes any warranty, express or implied, or assumes any legal responsibility for the accuracy, completeness, or usefulness of any information, apparatus, product, or process disclosed, or represents that its use would not infringe privately owned rights. Reference herein to any specific commercial product, process, or service by its trade name, trademark, manufacturer, or otherwise, does not necessarily constitute or imply its endorsement, recommendation, or favoring by the United States Government or any agency thereof, or the Regents of the University of California. The views and opinions of authors expressed herein do not necessarily state or reflect those of the United States Government or any agency thereof or the Regents of the University of California.

LBL-26449

MECHANISMS OF FATIGUE CRACK PROPAGATION AND FRACTURE TOUGHNESS BEHAVIOR IN ADVANCED ALUMINUM-LITHIUM ALLOYS

Kondapavuluru Tirumala Venkateswara Rao

Department of Materials Science and Mineral Engineering
University of California at Berkeley, and
Center for Advanced Materials
Materials and Chemical Sciences Division
1 Cyclotron Road
Lawrence Berkeley Laboratory
Berkeley, CA 94720

Ph.D. Dissertation

June 1988

This work was supported by the Director, Office of Energy Research, Office of Basic Energy Sciences, Materials Sciences Division, of the U. S. Department of Energy under Contract No. DE-AC03-76SF00098.

MECHANISMS OF FATIGUE CRACK PROPAGATION AND FRACTURE-TOUGHNESS BEHAVIOR IN ADVANCED ALUMINUM-LITHIUM ALLOYS

Kondapavuluru T. Venkateswara Rao

ABSTRACT

Mechanisms and mechanics influencing the fatigue crack propagation and plane-strain fracture toughness behavior of commercial aluminum-lithium alloys are investigated as a function of the microstructure and plate orientation, both at ambient and liquid nitrogen temperatures. With ultra-low density, improved elastic modulus and high strength, in comparison to existing 7XXX and 2XXX alloys, the alloys additionally exhibit superior long ($\gtrsim$ 10 mm) fatigue crack properties, even after prolonged exposures at high temperatures, excel under tension-dominated spectrum loading and in some instances show superior fracture toughness values at ambient and liquid nitrogen temperatures. However, the properties are strongly dependent on plate orientation; moreover the benefits of lithium additions are not realized for small (2-1000 μm) fatigue cracks.

These observations are rationalized as consequences of the dominant role of extrinsic toughening (or crack tip shielding) mechanisms on the mechanical behavior of aluminum-lithium alloys. For example, enhanced crack deflection and crack path tortuousity promote high levels of shielding and reduce long fatigue crack growth rates, whereas, small flaws of limited wake devoid of similar benefits of crack deflection and meandering, accordingly propagate at faster rates.

As the grain structures are largely unrecrystallized, anisotropic and textured, analogous to laminated composites, the weak planes of faster crack growth by delamination are responsible for the anisotropy in mechanical properties. Conversely, such delaminations along weak planes are also accountable for the remarkable properties in the other orientations, through crack-arrester and crack-divider delamination toughening; the latter being a prime reason for the excellent fracture toughness and ductility properties of aluminum-lithium alloys at cryogenic temperatures.

Professor Robert O. Ritchie,

Chairman,

Ph.D Thesis Committee.

ACKNOWLEDGEMENTS

Words can hardly express my deep sense of appreciation and gratitude to Professor R. O. Ritchie, for his motivation, inspiration and guidance throughout this entire investigation. I sincerely thank him for his encouragement, stimulating ideas and friendship.

Thanks are due to Profs. J. W. Morris, Jr., R. L. Taylor and T. M. Devine, Jr., for their participation in this research work and careful review of the manuscript.

My thanks to other members of the Ritchie Group, particularly, Dr. W. Yu, who has been a part of the Aluminum-Lithium Alloy Research at Berkeley. Experimental assistance of H. Hayashigatani, J. E. Miles, L. Rumaner, L. Gill and J. Cullinan, and many helpful discussions with J. Glazer are also gratefully acknowledged.

Thanks are also due to Drs. P. E. Bretz, R. J. Bucci, R. R. Sawtell of Alcoa, Dr. W. E. Quist of Boeing, Drs. G. R. Chanani, G. V. Scarich and K. M. Bresnahan of Northrop, G. J. Petrak of AFWAL and P. E. Wakeling of Alcan for their advice and help in procuring materials. And finally I am thankful to Ms. M. Penton for her help in preparing this thesis.

This work was supported by the Director, Office of Energy Research, Office of Basic Energy Sciences, Materials Sciences Division of the United States Department of Energy under Contract No. DE-AC03-76SF00098, under the auspices of the Center for Advanced Materials, Lawrence Berkeley Laboratory. Partial support was also received through an International Business Machines Fellowship, during 1987-88.

TABLE OF CONTENTS

ABSTRACT 1

ACKNOWLEDGEMENTS i

TABLE OF CONTENTS ii

1. ALUMINUM-LITHIUM ALLOYS: AN OVERVIEW 1

   1.1 Historical Background 1
   1.2 Impetus for Al-Li Alloy Development 2
   1.3 Early Problems- Solutions 6
   1.4 Commercial Alloys: Current Status 7
   1.5 Other Competing Technologies 9
   1.6 Scope of the Present Work 10
   1.7 References 11

2. MATERIALS AND EXPERIMENTAL PROCEDURES 16

   2.1 Materials 16
   2.2 Microstructures 16
   2.3 Mechanical Testing 19
   2.4 Fractography and Crack Path Profiles 26
   2.5 References 27

3. MICROSTRUCTURES AND FRACTURE TOUGHNESS 28

   3.1 Introduction 28
   3.2 Experimental Details 28
   3.3 Results 29
   3.4 Discussion 44
   3.5 Conclusions 58
   3.6 References 61

4. FATIGUE CRACK GROWTH: LONG CRACKS 64

   4.1 Introduction 64
   4.2 Experimental Details 64
   4.3 Results 65
   4.4 Discussion 76
   4.5 Conclusions 89
   4.6 References 90

5. FATIGUE CRACK GROWTH: SMALL CRACKS 93

   5.1 Introduction 93
   5.2 Experimental Details 94
   5.3 Results 94
   5.4 Discussion 99

5.5 Conclusions 107
5.6 References 108

6. FATIGUE CRACK GROWTH: EFFECT OF SINGLE TENSILE OVERLOADS 110

6.1 Introduction 110
6.2 Background 110
6.3 Experimental Details 113
6.4 Results 115
6.5 Discussion 129
6.6 Conclusions 134
6.7 References 137

7. INFLUENCE OF HIGH-TEMPERATURE EXPOSURES 140

7.1 Introduction 140
7.2 Experimental Details 140
7.3 Results 142
7.4 Discussion 148
7.5 Conclusions 151
7.6 References 154

8. FRACTURE TOUGHNESS AT CRYOGENIC TEMPERATURES 156

8.1 Introduction 156
8.2 Experimental Details 157
8.3 Results 159
8.4 Discussion 165
8.5 Conclusions 174
8.6 References 178

9. CONCLUDING REMARKS 181

9.1 Synopsis of the Present Work 181
9.2 The Alloy Design Perspective 182
9.3 Areas for Further Research 185
9.4 References 188

CHAPTER I

ALUMINUM-LITHIUM ALLOYS: AN OVERVIEW

1.1 HISTORICAL BACKGROUND

Goals for future subsonic, supersonic and hypersonic flight and space exploration require advanced materials with low density, high strength and stability at elevated temperatures (1). Efforts to design materials conforming to these requirements by adding lithium to aluminum alloys, date back as early as 1924 in Germany, when the first lithium-containing alloy, Scleron (Al-12Zn-3Cu-0.6Mn-0.1Li) was introduced (2). Research and patents on alloys using higher lithium contents and other trace elements (Cd, Mn etc.,) soon followed in U.S and Germany. Such developments were however, greatly overshadowed by the introduction of Duralumin-type and Al-Cu-Zn-Mg aluminum alloys, which were the dominant advanced high strength materials of that time. Also, the influence of cold work on the precipitation kinetics and thermomechanical treatments, so critical for achieving optimal combinations of strength and toughness, were relatively unexplored (3).

Nevertheless, continued efforts at Alcoa (4), Pechiney (5) and in Great Britain (6,7), culminated in the first commercial alloy registered as 2020 with nominal composition (wt. %) of Al-4.5Cu-1.1Li-0.5Mn-0.2Cd, by Alcoa in 1957 (8,9). In the T6 temper, the alloy exhibits yield and ultimate strengths of 531 and 579 MPa, respectively, with an elongation of 3 %. Aircraft producers quickly recognized the potential for weight savings and built the A-5A and RA-5C, Vigilante aircraft for the U.S Navy. Just simply substituting 2020 for 7075-T651

in the upper and lower wing skins, weight savings of 73 kg or nearly 6 % were realised (3). However, following general concerns over the fracture behavior of 2020, production was halted and the aircraft recalled, in spite of their successful performance for over two decades without any serious corrosion or fatigue problems. Thus the Vigilantes remain the only production application for aluminum-lithium alloys to date. Since then, substantial research effort at several universities, funding agencies and research laboratories, have brought forefront the low density aluminum-lithium alloy technology as summarized chronologically in Fig. 1.1 (10-14).

1.2 IMPETUS FOR AL-LI ALLOY DEVELOPMENT

The rapid escalation in fuel costs in the aerospace industry in 1973 has rekindled research on aluminum-lithium alloy development (10-13), with the objective of developing more fuel efficient aircraft. Of the various engineering properties of materials that can lead to potential weight savings, reducing the density as shown in Fig. 1.2, is the most effective (15,16). Apart from beryllium, which is very hazardous to health, lithium is the only other metal known to reduce the density and increase the stiffness of aluminum. Each weight percent of lithium added to aluminum lowers the density approximately 3 % and improves the elastic modulus by nearly 6 % (Fig. 1.3), for lithium additions upto 4 wt. % (17,18). As a result, direct substitutions by aluminum-lithium for conventional alloys can yield nearly 11 % weight savings; and upto 17 % by redesigning aircraft, taking full advantage of the new materials, thus offering substantial fuel cost savings (14).

Today, using improved alloy design and thermo-mechanical

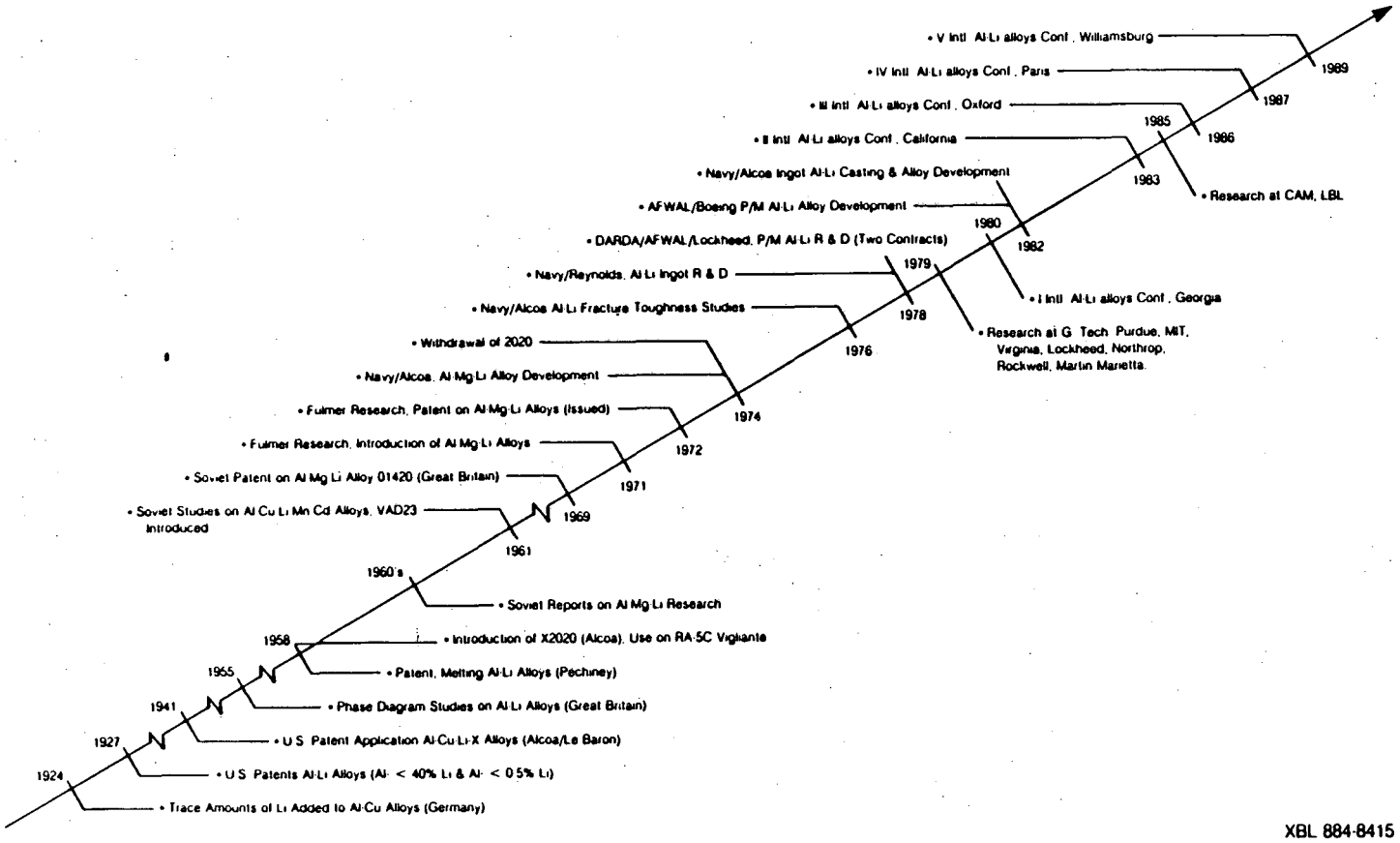

Fig. 1.1: Chronological order of events during the development of aluminum-lithium alloys spanning over a period of over 60 years (adapted from Ref. 14).

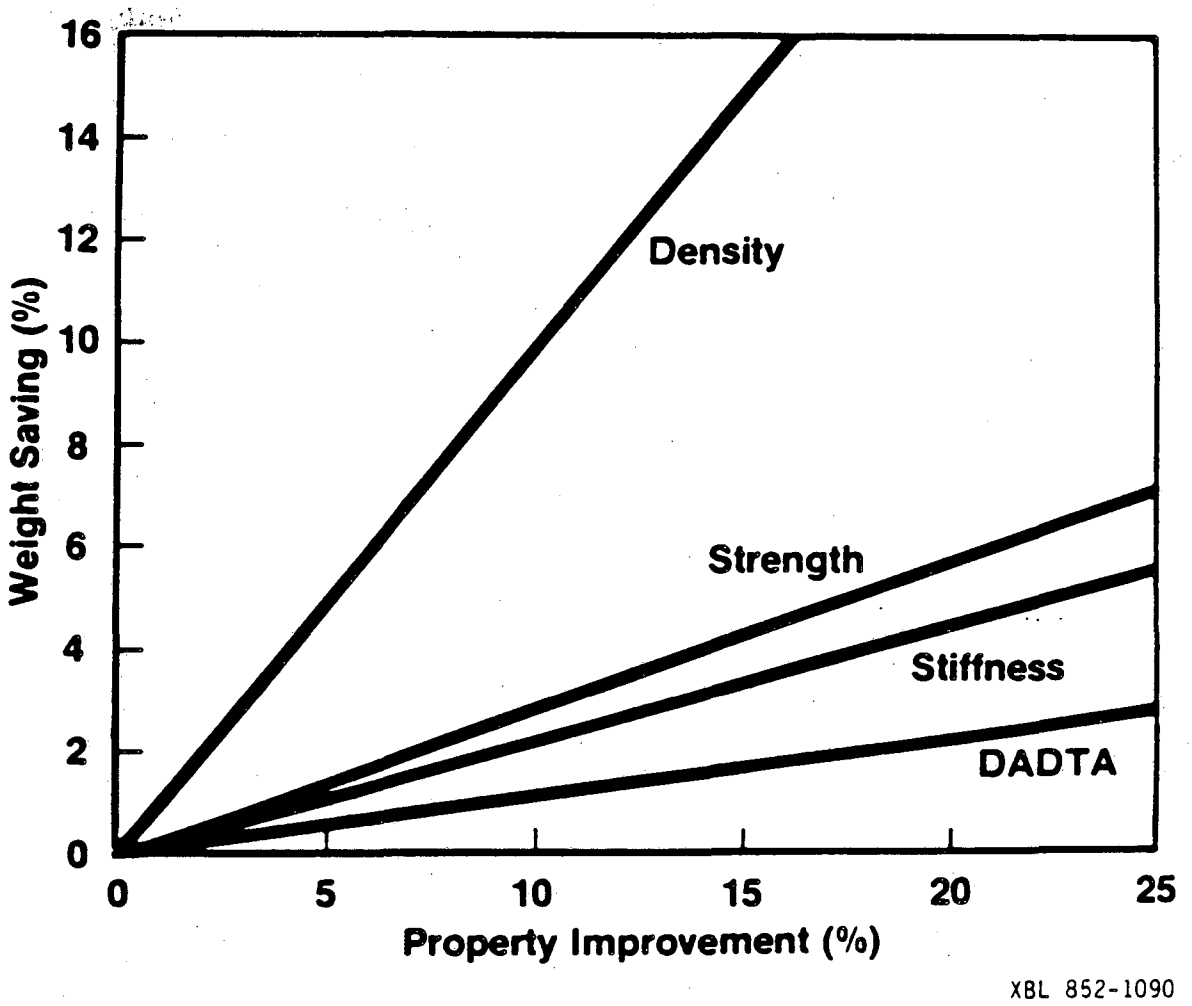

Fig. 1.2: Structural weight savings for the S-3A aircraft due to improvements of the individual engineering properties of aerospace materials (23). Note that reducing the density has the most significant influence.

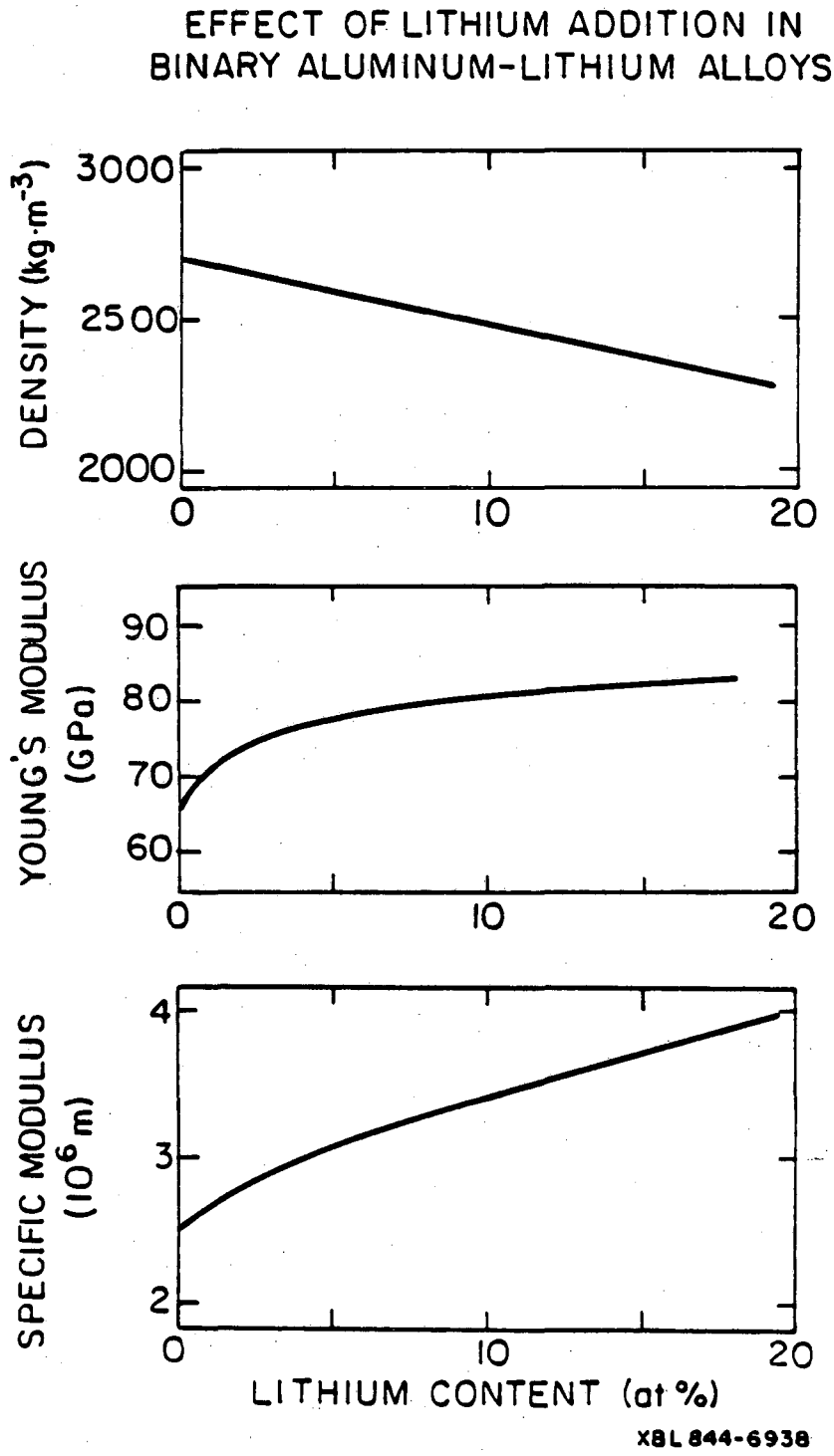

Fig. 1.3: Influence of lithium additions on the density and elastic modulus of aluminum (50).

treatment procedures, aluminum-lithium alloys currently offer attractive combinations of strength, ductility, fracture toughness and fatigue crack propagation resistance, comparable and in many cases superior to traditional high strength Al-Cu and Al-Zn-Mg alloys (10-13), particularly at cryogenic temperatures (19-21). In addition, the alloys are superplastic (10-13,22,23), and the components can be produced to near-net shape in a single operation. Typical structural applications include, skins and spars for the fuselage and wings, doors, and body stringers and frames of commercial transport, military and fighter aircraft, in various product forms. In view of the remarkable cryogenic properties of these materials, they are additionally strong candidates for liquid-hydrogen, -oxygen and natural gas fuel tanks, in particular, for existing and future transatmospheric and hypersonic aircraft applications.

1.3 EARLY PROBLEMS- SOLUTIONS

Early development of binary aluminum-lithium alloys was plagued by concerns over poor ductility and fracture properties. Such deficiencies in ductility and toughness of aluminum-lithium alloys can be traced, at least in part, to the inhomogenous nature of their deformation characteristics or slip (24), resulting from coherent particle hardening of spherical $\delta'(Al_3Li)$ precipitates. In addition, the presence of equilibrium δ (AlLi) precipitates at the grain boundaries can cause δ'-precipitate free zones (PFZs), which can induce further strain localization and promote intergranular failure (25). Moreover, alkali impurities (Na, K, and Ca), sulphur and hydrogen can also segregate to the grain boundaries (26-29), lower the grain

boundary strength and additionally contribute to the poor toughness of these planar slip materials.

Consequently, for the development of commercial alloys, slip has been homogenized by introducing dispersoids (Zr, Mn additions) and semi-coherent or incoherent plate precipitates such as $T_1(Al_2CuLi)$, $\theta'(Al_2Cu)$ and $S'(Al_2CuMg)$, through copper and magnesium additions (10-13,17,30-32. Also refer Figs. 3.2-3.5, Sections 3.3 & 3.4 of this thesis). Concurrent developments in the thermo-mechanical processing have optimized aluminum-lithium alloy microstructures for the best combinations of strength and toughness, although the resulting material tends to be highly anisotropic and textured, particularly where small Zr additions are used to inhibit recrystallization. The thermo-mechanical treatments typically involve, solution treating (or homogenizing) just above the solvus temperature, water quenching and a 2-3 % permanent stretch, before aging naturally (at room temperature), or artificially at a higher temperature, to obtain the desired combination of strength, ductility and fracture toughness (32). Simultaneously, improved casting procedures minimized the embrittlement effects due to Na, K and H at the grain boundaries.

1.4 COMMERCIAL ALLOYS: CURRENT STATUS

Extensive research and development efforts over the past seven years, in academic and industrial laboratories have identified Al-Li-Cu-Zr and Al-Li-Cu-Mg-Zr systems to meet alloy design target specifications concerning density, strength, ductility and fracture toughness properties. Most alloys investigated have compositions in the range of 2-3 wt. % Li, 1-3 wt. % Cu, 1-2 wt. % Mg and 0.1-0.2 wt. % Zr,

and are mainly processed by ingot metallurgy (I/M) techniques. All of the major aluminum producers including Alcoa, Alcan, Pechiney, Kaiser and Reynolds have converged on such compositions registered as 2090, 2091, 8090 and 8091, and already established large-scale production facilities (33,34).

The variations in composition of the commercial Al-Li-Cu-Zr and Al-Li-Cu-Mg-Zr systems reflect alloys developed specifically for the five primary categories, namely for low density, high strength, damage tolerance, stress corrosion cracking resistance and superplasticity. Prominent among these materials are 2090 and 8091, projected as high strength replacements for 7XXX alloys, whereas 8090 and 2091 are aimed for medium strength and damage tolerant applications replacing 2XXX alloys. Materials are currently available in various product forms, i.e., sheets, plates, extrusions and forgings, in different tempers (or microstructures), invariably controlled by thermomechanical treatments discussed earlier. In the present study, the mechanical properties of alloys 2090, 2091, 8090 and 8091 were all examined in the plate form.

Although, production by I/M techniques appears to be the most popular route, the powder metallurgy (P/M) approach has also received considerable attention. Notable among the methods are rapid solidification, rotary atomization and mechanical alloying (35). The potential payoffs using these techniques, result from additional reductions in density by incorporating lithium in excess of 3 wt. %, high strengths by unique compositions of alloying elements (Zr, Cr, Mn, Ge, Cu, Mg), not possible through conventional I/M techniques. Besides, the strengthening oxides and carbides also contribute to their

superior corrosion resistance and high temperature properties. In this regard, Al-4Li-1Cu-0.5Mg-0.5Zr and AL-905-XL (Al-4Mg-2Li) alloys of Allied-Signal Inc. and Inco-Alloys International (or Novamet) appear promising (36,37). Presently, they are limited by adversities concerning segregation of alloying elements, large amounts of second phases, intermetallic particles and low fracture toughness (35). Economics of manufacturing will be a critical aspect for the success of the Al-Li P/M technology.

1.5 OTHER COMPETING TECHNOLOGIES

With the advent of aluminum-lithium alloys, the aluminum alloy technology appears rejuvenated and now strongly competes with emerging advanced composite technologies, for structural aircraft and aerospace applications. Based on organic (graphite-epoxy, graphite-polyimide, carbon-carbon) and metal (aluminum, titanium and their alloys) matrices, and alumina (Al_2O_3), boron (B), boron carbide (B_4C), silicon carbide (SiC), Kevlar (an organic fiber) and carbon, in the form of fibers, whiskers or particulates, these composites offer impressive combinations of strength, stiffness and high temperature resistance (1,38). In addition, aramid polymer reinforced aluminum laminates (ARALL) being developed at Delft University and Alcoa, by bonding aramid fibers sandwiched between thin sheets of aluminum, using resins show exceptional fatigue resistance (39,40).

Despite meager limitations regarding specific stiffness and high temperature stability, aluminum-lithium alloys enjoy several advantages over composite materials. Economically, Al-Li alloys are only three times as expensive as conventional aluminum alloys, whereas competing

composites are at least ten times, and upto thirty times as expensive; either as raw materials or manufactured items (41). Secondly, lithium alloy development technology is compatible with existing manufacturing methods such as sheet forming, forging etc., to obtain the finished product; composites may require new forming processes and investments. Finally, in spite of the isotropy in mechanical properties of metal matrix composites, their ductility and fracture toughness levels are unacceptably low (42,43), similar to early experiences in Al-Li alloy development. Moreover, similar to behavior reported in aluminum-lithium alloys (44), there are questions concerning the performance of fatigue-resistant ARALL laminates, under compression loading (41).

1.6 SCOPE OF THE PRESENT WORK

In the present study, the mechanical properties of the principal commercial Al-Li-Cu-Zr and Al-Li-Cu-Mg-Zr systems are experimentally investigated in detail, and the underlying mechanisms, mechanics and the mechanistic implications carefully documented. The fatigue crack growth properties of commercial aluminum-lithium alloys, with respect to long and small fatigue cracks (Chs. IV and V), under the influence of single peak tensile overloads (Ch. VI) and after prolonged high temperature exposures (Ch. VII), are examined and the results compared to traditional high strength aluminum alloys. In addition, the fracture toughness and uniaxial tensile properties are evaluated, as a function of microstructure and plate orientation, at ambient and liquid nitrogen temperatures, in chapters III and VIII, respectively.

In general, the materials exhibit excellent (long) fatigue crack growth resistance, enhanced retardations following tensile overloads

under spectrum fatigue loading and superior strength-toughness combinations at cryogenic temperatures (with a few exceptions), when compared to 2XXX and 7XXX series high-strength aluminum alloys. Concurrently however, the observed discrepancies between long and small fatigue crack growth rates are the highest, and the strength, toughness and fatigue properties strongly sensitive to plate orientation.

Such contrasting effects are reasoned to be consequences of the principal role of "crack-tip shielding" (45,46), in the mechanical behavior of aluminum-lithium alloys. The term "crack tip shielding", common in ceramic literature, refers to the general phenomenon, where the crack advance is impeded by reducing the "local crack driving force" (extrinsic toughening), as opposed to increasing the microstructural resistance of the material (intrinsic toughening). Stress-induced martensitic phase transformations (47), microcracking (48) and crack bridging (49) are a few examples of shielding mechanisms, which are responsible for the improved toughness of brittle solids (Fig. 1.4). In the case of aluminum-lithium alloys, extensive crack deflection, crack-path tortuosity, crack-wake plasticity and premature wedging of fracture surface asperities (crack closure) in fatigue, and the incidence of short transverse delaminations during monotonic fracture are responsible for crack tip shielding.

1.7 REFERENCES

1. M. A. Steinberg: Sci. Amer., 255:4 (1986), p. 66.
2. E. Scheuer: Z. Metall., 19 (1927), p. 16.
3. S. Balmuth and R. Schmidt: in Ref. 10, p. 69.

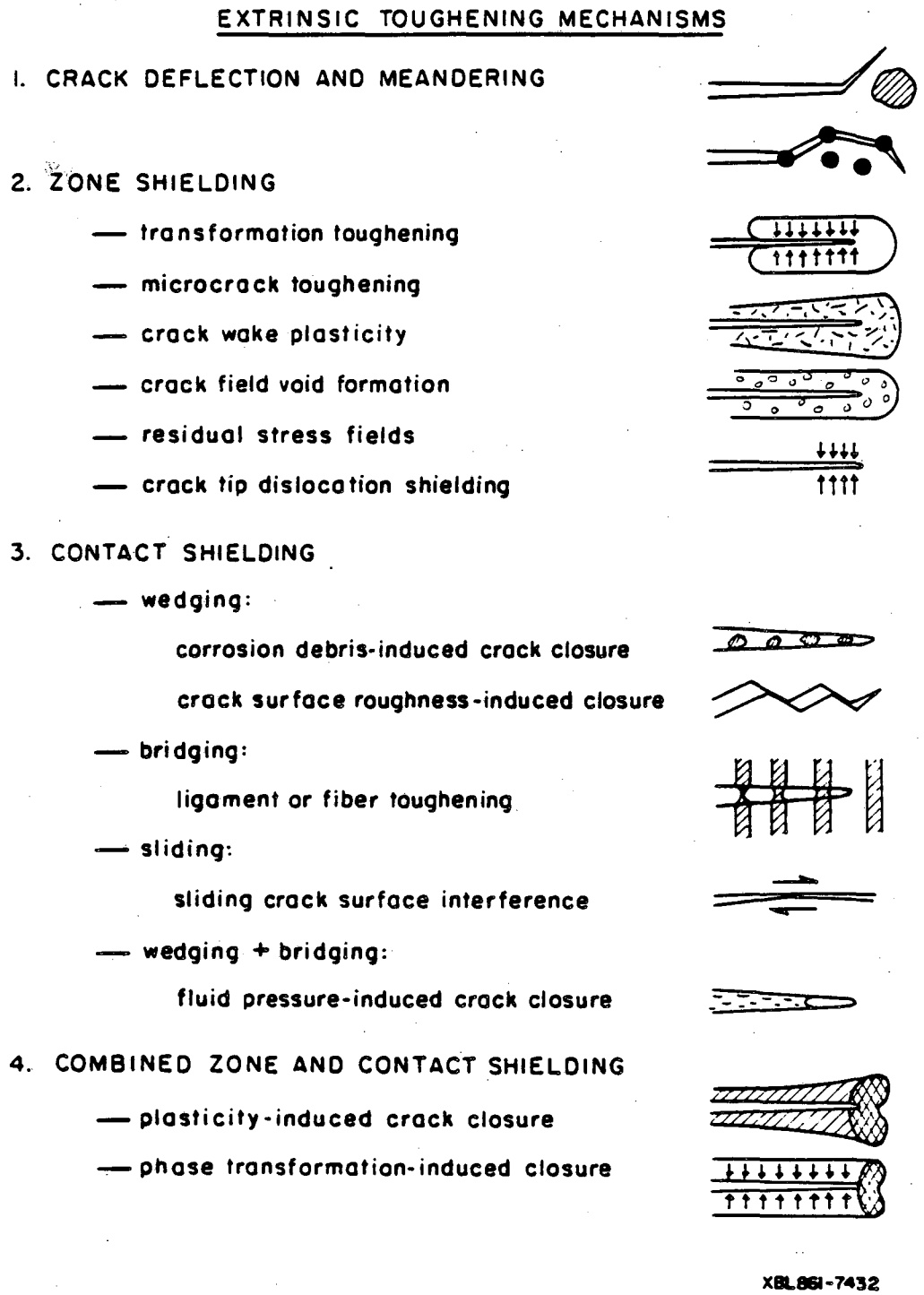

Fig. 1.4: General schematic of the various crack tip shielding mechanisms, by which materials (ceramics, metals) may be extrinsically toughened to improve their fracture and fatigue resistance (46).

4. I. M. LeBaron: U.S. Patent No. 2,381,219, Application date 1942, Granted 1945.

5. P. Vachet: French Patent No. 1,161,306, Application date 1956, Granted 1958.

6. H. K. Hardy and J. M. Silcock: J. Inst. Metals, 84 (1955-56), p. 423.

7. H. K. Hardy: J. Inst. Metals, 84 (1955-56), p. 429.

8. E. H. Spuhler: 'Alcoa Alloy X-2020', Green Letter 156-9-58 (1958), p. 27.

9. E. H. Spuhler, A. H. Knoll and J. G. Kaufman: Met. Prog., 79 (1960), p. 80.

10. T. H. Sanders and E. A. Starke (eds.): 'Aluminum-Lithium Alloys', TMS-AIME, Warrendale, PA (1981).

11. T. H. Sanders and E. A. Starke (eds.): ' Aluminum-Lithium Alloys II', TMS-AIME, Warrendale, PA (1983).

12. C. Baker, P. J. Gregson, S. J. Harris and C. J. Peel (eds.): 'Aluminum-Lithium Alloys III', Institute of Metals, London (1986).

13. G. Champier et al. (eds.): 'Aluminum-Lithium Alloys IV', J. Phys. Coll., C3 (1988).

14. W. E. Quist, G. H. Narayanan and A. L. Wingert: in Ref. 11, p. 313.

15. J. C. Ekvall, J. E. Rhodes and G. G. Wald: in 'Design of Fatigue and Fracture Resistant Structures', ASTM STP 761 (1982), p. 328.

16. R. E. Lewis, D. Webster and I. G. Palmer: Lockheed Palo Alto Research Laboratory Final Report, Contract F33615-77-C-5186, Technical Report No. AFML-TR-78-102.

17. E. A. Starke, T. H. Sanders and I. G. Palmer: J. Metals, 33 (1981), p. 24.

18. B. Noble, S. J. Harris and K. Dinsdale: J. Mat. Sci., 17 (1982), p. 461.

19. J. Glazer, S. L. Verzasconi, E. N. Dalder, W. Yu, R. A. Emigh, R. O. Ritchie and J. W. Morris: Adv. Cryog. Eng., 32 (1986), p. 397.

20. D. Webster: Met. Prog., 125 (1984), p. 31.

21. R. C. Dorward: Scripta Metall., 20 (1986), p. 1379.

22. J. Wadsworth, I. G. Palmer, D. D. Crooks and R. E. Lewis: in Ref. 11, p. 111.

23. R. J. Lederich and S. M. L. Sastry: in Ref. 11, p. 137.

24. T. H. Sanders and E. A. Starke: Acta Metall., 30 (1982), p. 527.

25. A. K. Vasudevan and R. D. Doherty: Acta Metall., 35 (1987), p. 1193.

26. T. H. Sanders: Naval Air Development Center, Contract No. N62269-76-C-0271, Final Report (1979).

27. R. J. M. Payne and J. D. L. Eynon: J. Inst. Metals, 86 (1957-58), p. 351.

28. P. D. Frost, J. H. Jackson, A. C. Loonam and C. H. Lorig: Trans. AIME, 188 (1950), p. 1171.

29. A. K. Vasudevan, A. C. Miller and M. M. Kersker: in Ref. 11, p. 181.

30. T. H. Sanders and E. A. Starke: in Ref. 11, p. 1.

31. P. J. Gregson and H. M. Flower: Acta Metall., 33 (1985), p. 529.

32. R. J. Rioja, P. E. Bretz, R. R. Sawtell, W. H. Hunt and E. A. Ludwiczak: in 'Aluminum Alloys: Their Physical and Mechanical Properties', E. A. Starke and T. H. Sanders (eds.), EMAS Ltd., Warley, U.K. (1986).

33. S. P. Agrawal, R. J. Kar and W. E. Quist (eds.): 'Aluminum-Lithium Alloys: Development Application and Superplastic Forming', ASM International, Metals Park, Ohio (1986).

34. S. P. Agrawal, R. J. Kar and W. E. Quist (eds.): 'Aluminum-Lithium Alloys: Design, Development and Application Update', ASM International, Metals Park, Ohio (1987).

35. W. E. Quist, G. H. Narayanan, A. L. Wingert and T. M. F. Ronald: in Ref. 12, p. 625.

36. N. J. Kim, D. J. Skinner, K. Okazaki and C. M. Adam: in Ref. 12, p. 78.

37. P. S. Gilman, J. W. Brooks and P. J. Bridges: in Ref. 12, p. 112.

38. T. W. Chou, R. L. McCullough and R. B. Pipes: Sci. Amer., 255:4 (1986), p. 192.

39. J. Schijve and L. B. Vogelsang: 'Development of ARALL: A New Material for Aircraft Structures', Memorandum M-434, Delft Univ. of Technol., Dept. of Aerospace Eng. (1982).

40. R. O. Ritchie, W. Yu and R. J. Bucci: Eng. Fract. Mech., 23 (1988), in press.

41. C. J. Peel: Mat. Sci. Technol., 4 (1987), p. 1169.

42. J. K. Shang, W. Yu and R. O. Ritchie: Mat. Sci. Eng., 100 (1988), in press.

43. J. J. Lewandowski, C. Liu and W. H. Hunt: in 'Powder Metallurgy Composites', P. Kumar, A. Ritter and K. Vedula (eds.), TMS-AIME, Warrendale, PA (1987).

44. W. Yu and R. O. Ritchie: J. Eng. Mat. Technol., Trans. ASME Series H, 109 (1987), p. 81.

45. R. O. Ritchie: in 'Mechanical Behavior of Materials - V', M. G. Yan, S. H. Zhang and Z. M. Zheng (eds.), Pergamon Press, Oxford, U.K., 3 (1987).

46. R. O. Ritchie, R. H. Dauskardt and R. M. Cannon: Lawrence Berkeley Laboratory Report No. LBL-20656, University of California, Berkeley, 1986.

47. A. G. Evans and R. M. Cannon: Acta Metall., 34 (1986), p. 761.

48. A. G. Evans and K. T. Faber: J. Amer. Ceram. Soc., 67 (1984), p. 250.

49. D. B. Marshall, B. N. Cox and A. G. Evans: Acta Metall., 33 (1985), p. 2013.

50. J. Glazer: unpublished work, University of California, Berkeley.

CHAPTER II

MATERIALS AND EXPERIMENTAL PROCEDURES

2.1 MATERIALS

Commercial 12-15 mm thick plates of aluminum-lithium alloys ALCAN-8090, 8091 and PECHINEY-2091 were tested in their recommended peak and naturally aged tempers, whereas, ALCOA-2090 was investigated in the experimental T8E41 condition. In addition, traditional high strength aluminum alloys 2124, 7150 were also examined in the various tempers to draw parallels between the fatigue and fracture resistance of various commercial aluminum and aluminum-lithium alloys. Nominal composition limits for the alloys tested and the heat treatment procedures used to obtain the different microstructures are listed in Tables 2.1 and 2.2, respectively.

2.2 MICROSTRUCTURES

All alloys tend to show a pancake-shaped grain structure elongated along the rolling direction, with a greater degree of anisotropy and general lack of recrystallization in the lithium-containing alloys. Respective grain size measurements along the longitudinal (L), transverse (T) and short-transverse (S) directions are summarized in Table 2.3, together with the primary hardening precipitates.

Microstructures in commercial aluminum-lithium alloys are primarily unrecrystallized and hardened by coherent δ' (Al_3Li), θ'-like (Al_2Cu), T_1 (Al_2CuLi), S' (Al_2CuMg) precipitates and β'(Al_3Zr)

Table 2.1: Nominal Chemical Compositions of Commercial Aluminum and Aluminum-Lithium alloys investigated (wt. %)

		Li	Cu	Mg	Zn	Fe	Si	Ti	Zr	Al	
Alcoa	2090	2.05	2.86	0.01	0.01	0.02	0.01	0.02	0.12	bal	
Alcan	8090	2.50	1.30	0.70	--	0.20	0.10	--	0.12	bal	
Alcan	8091	2.60	1.90	0.90	--	0.10	0.10	--	0.12	bal	
Pechiney	2091	1.7-2.3	1.8-2.5	1.1-1.9	0.25	0.30	0.20	0.10	0.04-0.16	bal	
Alcoa	2124	--	4.50	1.50	0.25	0.30	0.20	0.15	--	bal	
Alcoa	7150	--	2.10	2.16	6.16	0.11	0.07	0.02	0.13	bal	

Table 2.2: Heat Treatments Utilized on Commercial Alloys Investigated

Alloy	Condition	Heat Treatment
2090	T8E41(peak aged)	solution treat, 6% stretch, aged 24 hr at 163°C
8090	T351 (underaged)	solution treat, 3% stretch, naturally aged
8090	T8X (peak aged)	T351 + aged 16 hr at 190°C
8091	T351 (underaged)	solution treat, 3% stretch, naturally aged
8091	T8X (peak aged)	T351 + aged 16 hr at 190°C
2091	T351 (underaged)	solution treat, 3% stretch, naturally aged
2091	T8X (peak aged)	T351 + aged 10 hr at 135°C
2124	T351 (underaged)	solution treat, 2% stretch, naturally aged
2124	T751 (over aged)	solution treat, 2% stretch, aged 48 hr at 190°C
7150	T351 (underaged)	solution treat, 2% stretch, aged 1.5 hr at 121°C
7150	T651 (peak aged)	solution treat, 2% stretch, aged 100 hr at 121°C
7150	T751 (over aged)	solution treat, 2% stretch, aged 24 hr at 121°C + 40 hr at 163°C

Table 2.3: Summary of the Grain-Size Dimensions and Strengthening Precipitates in the Various Commercial Aluminum Alloys

Alloy	Grain Size L mm	T µm	S µm	Primary Hardening Precipitates
2090-T8E41	2-3	500	50	$\delta'(Al_3Li)$, $T_1(Al_2CuLi)$, $\theta'(Al_2Cu)$, $\beta'(Al_3Zr)$
8090-T351	1-2	350	40	$\delta'(Al_3Li)$, $\beta'(Al_3Zr)$
8090-T8X				$\delta'(Al_3Li)$, $T_1(Al_2CuLi)$, $S'(Al_2CuMg)$, $\beta'(Al_3Zr)$
8091-T351	0.3	65	25	$\delta'(Al_3Li)$, $\beta'(Al_3Zr)$
8091-T8X				$\delta'(Al_3Li)$, $S'(Al_2CuMg)$, $\beta'(Al_3Zr)$
2091-T351	1-2	600	50	$\delta'(Al_3Li)$, $\beta'(Al_3Zr)$
2091-T8X				$\delta'(Al_3Li)$, $\beta'(Al_3Zr)$
2124-T351	0.7	350	50	GP zones
2124-T751				$\Theta(Al_2Cu)$, Al_7Cu_2Fe, $Al_{12}(Fe,Mn)_3Si$, Mg_2Si
7150-T351	2-3	750	30	GP zones
7150-T651				$\eta'(MgZn_2\text{-}Mg(CuAl)_2)$
7150-T751				matrix $\eta'(MgZn_2\text{-}Mg(CuAl)_2)$, $\eta(MgZn_2$ compounds)

Table 2.4: Room Temperature Mechanical Properties of Existing High-Strength Aluminum Alloys Investigated

Alloy	Yield Strength (MPa)	U.T.S (MPa)	% Elongation (on 25 mm)	Fracture Toughness $K_{Ic}(MPa\sqrt{m})$
2124-T351	360	488	17.8	24
2124-T751	370	440	10.2	42
7150-T351	371	485	6.8	37
7150-T651	404	480	6.0	21
7150-T751	372	478	7.1	29

dispersoids in the matrix. Evolution of these microstructures in the various Al-Li alloys is discussed in Chapter III. Among the various lithium-containing alloys, 8091 alloy is relatively fine grained, hence less anisotropic and 2091 shows evidence of a small degree of recrystallization.

On the other hand, structures in 2124 are recrystallized and show evidence of GP zones and several constituent phases, including Al_7Cu_2Fe, $Al_{12}(Fe,Mn)_3Si$, Mg_2Si and Al_2CuMg; overaging leads to grain boundary precipitation (1). In 7150, 4 to 8 nm diameter GP zones are present in the underaged structures, which are replaced by semi-coherent η' ($MgZn_2$-$Mg(CuAl)_2$) precipitates on peak aging, and coarsened matrix η' and incoherent η ($MgZn_2$ compounds) in both matrix and grain boundaries on overaging (2). Room temperature mechanical properties of high-strength aluminum alloys 2124, 7150 are listed in Table 2.4 (1,2).

2.3 MECHANICAL TESTING

2.3.1 Fatigue Crack Growth: Long Cracks

Crack growth tests on long ($\gtrsim$ 10 mm) through thickness cracks were performed with 6 to 7 mm thick test pieces, using compact C(T) specimens in the L-T, T-L, and L+45 (LT-TL) orientations, double cantilever beam DC(B) specimens in the S-L and S-T orientations, and four-point single-edge-notched bend SEN(B) specimens in the T-S orientation (Fig. 2.1). The two letters used in the nomenclature as per ASTM specifications, refer to the loading and crack growth directions, respectively, in that order. Details of the various specimen geometries are shown in Fig. 2.2. Since the through thickness strength variations in the commercial plates are quite significant all specimens were

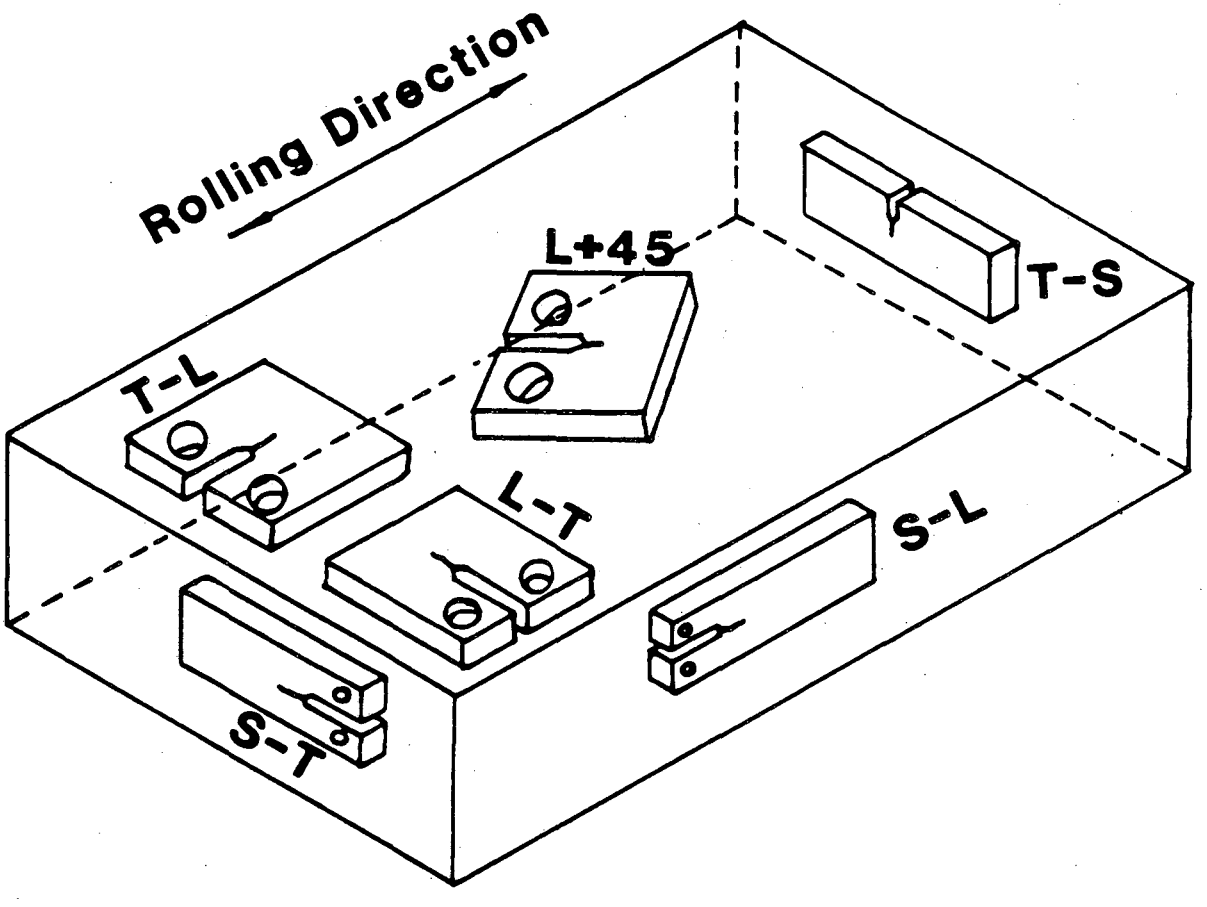

XBL 8610-3731

Fig. 2.1: Nomenclature relating to test specimen orientation and geometry relevant to long fatigue crack growth tests. Note that the first and second letters refer to the loading and crack growth direction respectively.

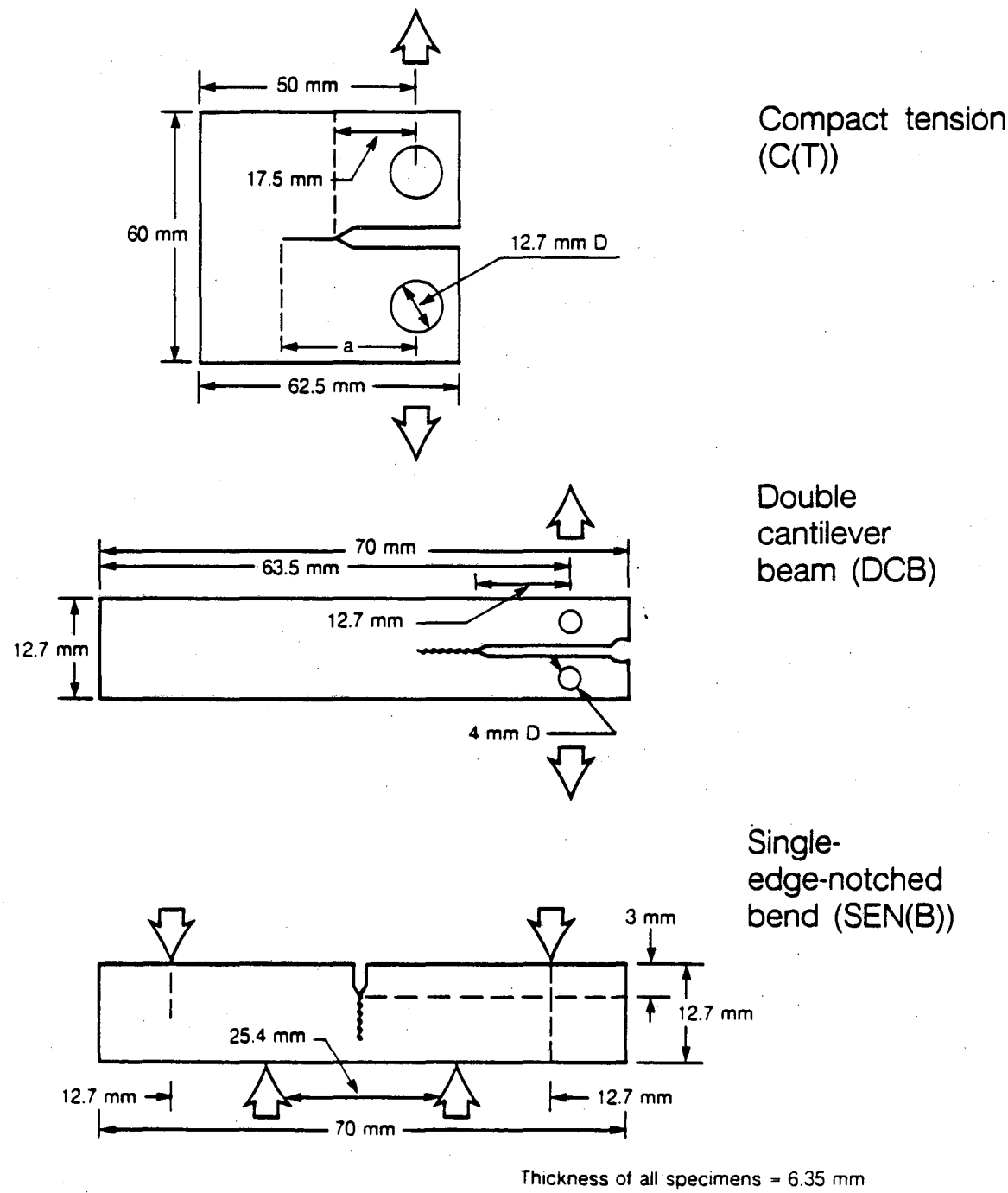

Fig. 2.2: Dimensions of the compact C(T), single-edged-notched bend SEN(B)and double-cantilever-beam DC(B) samples used to study the fatigue and fracture toughness behavior in the various plate orientations.

machined from the mid-section thicknesses.

Tests were conducted in controlled room temperature air (22°C, 45 % relative humidity), using automated electro-servo-hydraulic testing machines operating under stress intensity (K) control at a sinusoidal frequency of 50 Hz, over a range of load ratios ($R = K_{min}/K_{max}$) from 0.1 to 0.75. Fatigue threshold stress intensity ranges (ΔK_{TH}), defined at a maximum growth rate of 10^{-11} m/cycle, were approached using both manual and computer-controlled load-shedding procedures (normalized K-gradient set between 0.1-0.15 mm^{-1}), with crack lengths continuously monitored using d.c. electrical potential methods. Simultaneous measurement of crack closure was achieved using back-face strain gages on C(T) and SEN(B) samples, and crack mouth opening displacement gages on DC(B) samples. Using these techniques, the closure stress intensity (K_{cl}) was defined during unloading, at first contact of the fracture surfaces, from the load corresponding to the initial deviation from linearity of the elastic compliance curve (Fig. 2.3). Crack growth rate data are presented in terms of the nominal stress intensity range ($\Delta K = K_{max} - K_{min}$), and the effective stress intensity range, defined as $\Delta K_{eff} = K_{max} - K_{cl}$.

2.3.2 Fatigue Crack Growth: Small Cracks

To examine the early growth of naturally-occurring, microstructurally-small (2-1000 μm) surface cracks, fatigue tests were performed by acetate replication techniques on smooth, unnotched, rectangular specimens, cycled in four-point bending (Fig. 2.4a) in room temperature air using electro-servo-hydraulic testing machines. Tests were conducted at a cyclic frequency of 50 Hz (sine wave) with a load

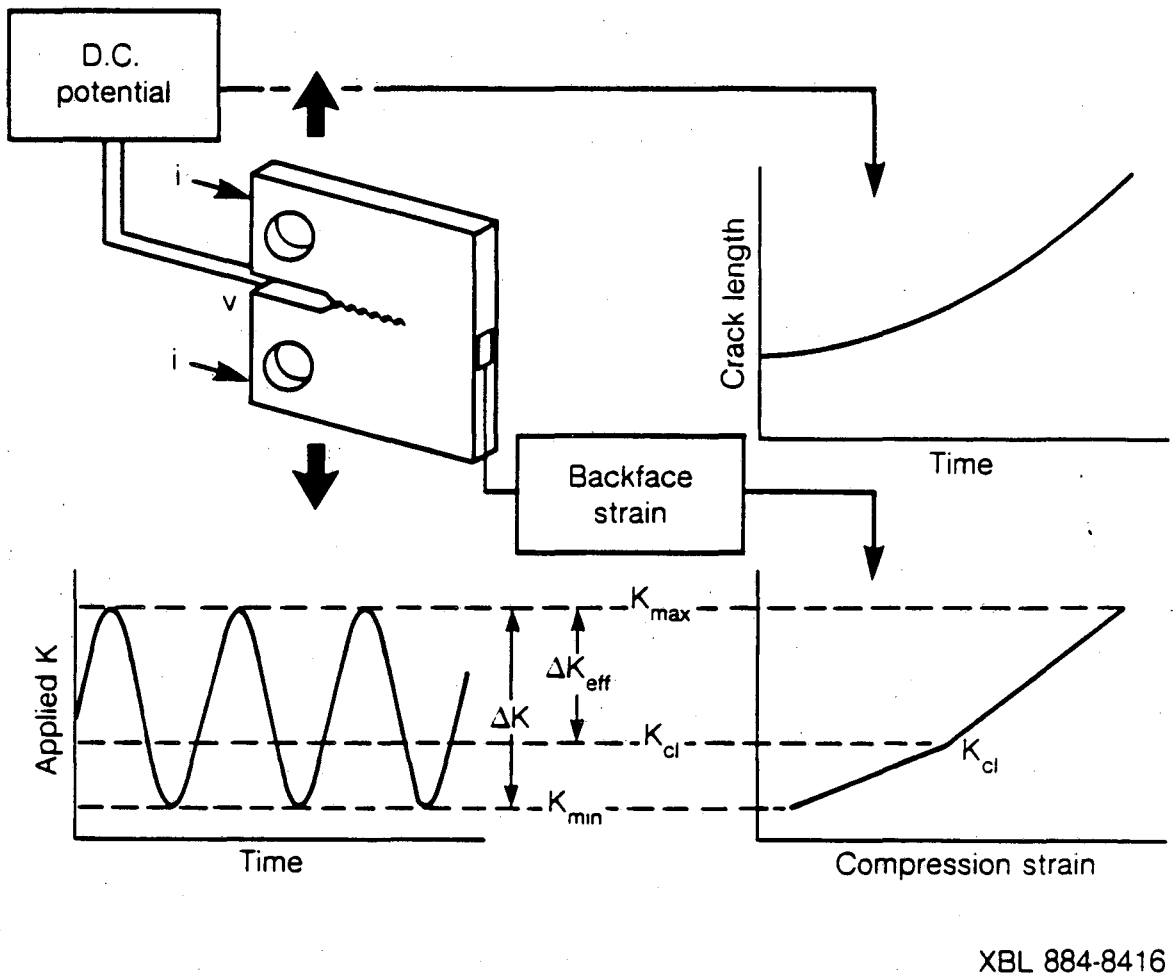

Fig. 2.3: Schematic illustration of the principal experimental methods used to continuously monitor crack length and crack closure. Crack closure was measured as the closure stress intensity (K_{cl}), at first deviation from linearity on the compliance curve, obtained using back-face strain compliance techniques.

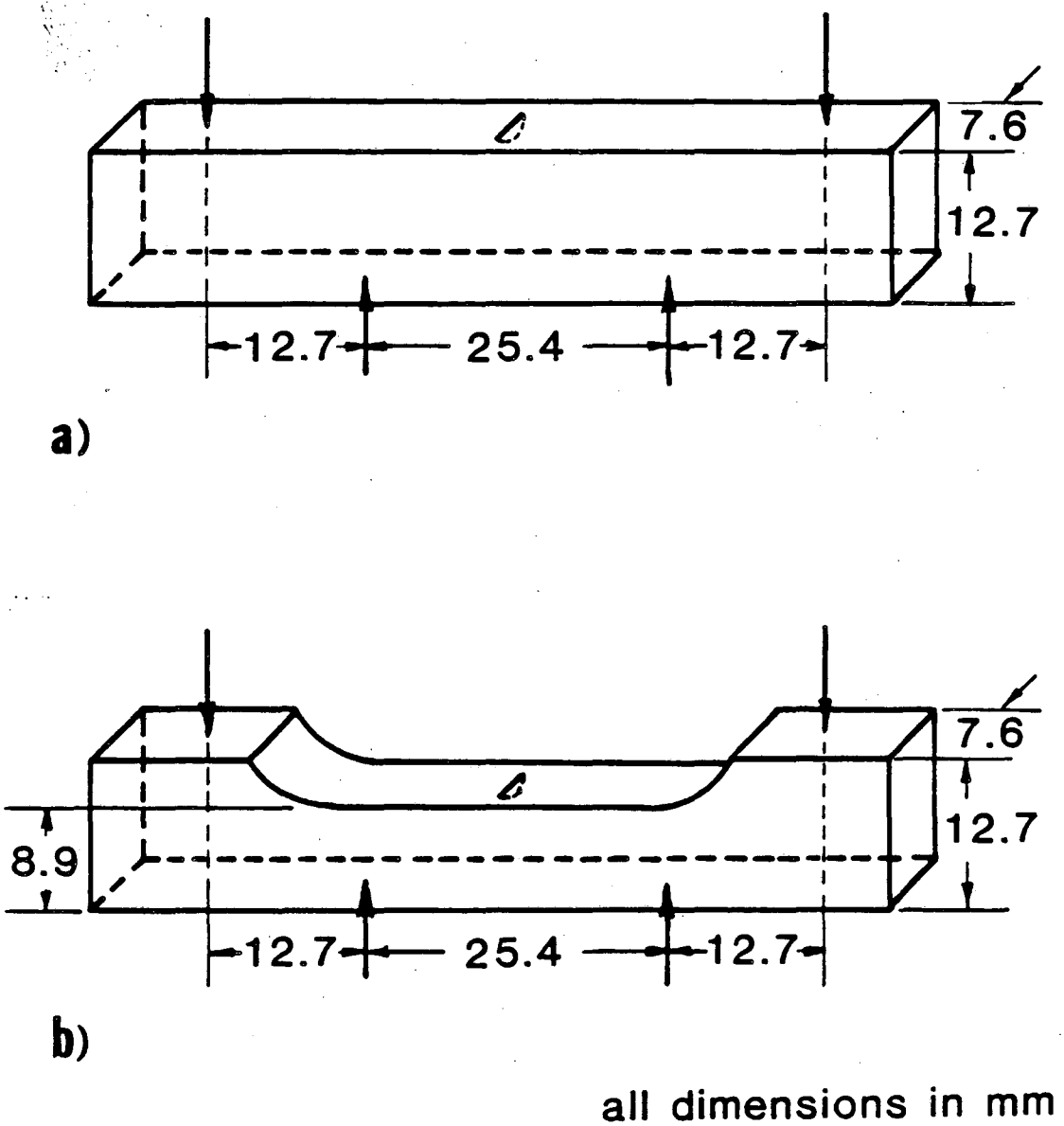

Fig. 2.4: a) Smooth and b) waisted geometries of four-point bend specimens used to measure small crack growth rates.

ratio of 0.1, where the maximium bending stresses on the surface did not exceed 0.9 times the yield stress of the material. Due to the high strength and poor short-transverse properties of 2090-T8E41, tests in this alloy were carried out on waisted specimens (Fig. 2.4b) to minimize the occurrence of mid-section delamination cracks in the plane of loading, where the shear stresses are a maximum.

Tests were interrupted approximately every 5,000 to 10,000 cycles and held at the mean load to permit replication of the electropolished and lightly etched specimen surface. Replicas were subsequently gold coated by sputtering, to permit better resolution of the surface crack length (2c), and examined using the optical microscope. With such procedures, small cracks of lengths between 2-1000 μm could be readily monitored, with a resolution of better than 0.5 μm. Growth rates ($\Delta a/\Delta N$) were then computed in terms of the mean crack extension within such time increments. Typical initiation lives, i.e, to detect a 0.5 mm visible crack, varied between 1-4 X 10^5 cycles. Using these procedures, detection of crack increments between 1-5 μm was possible such that crack growth rates as low as 5 X 10^{-10} m/cycle could be readily monitored.

As the computed plastic zone sizes remained small (typically 4 %) compared to the crack size, characterization of small-crack growth rates in terms of K was deemed to be appropriate. Stress intensity factors were computed using the Newman and Raju equation (3) for semi-elliptical surface flaws assuming an a/c (crack depth to half the surface crack length) ratio of 0.8, based on serial sectioning experiments. Owing to the high degree of crack deflection and

meandering, crack lengths were measured as the projected lengths normal to the bending tensile stresses.

2.3.3 Fracture Toughness and Tensile Properties

Fracture-toughness testing was performed with 6-8 mm thick compact C(T) and single-edge-notched bend SEN(B) samples loaded in four-point bending for the L-T, T-L, L+45 and T-S orientations, and double-cantilever-beam DC(B) specimens for the S-L and S-T orientations. All specimens were initially fatigue precracked, at R = 0.1, to a crack length-to-specimen width ratio (a/W) of 0.45-0.55. All results represent plane strain values, except where noted. Corresponding uniaxial tensile properties in the longitudinal direction were assessed using 6.4 mm round tensile specimens with a 25 mm gage length.

2.4 FRACTOGRAPHY AND CRACK PATH PROFILES

Fracture surfaces of the test specimens separated due to crack growth under fatigue and monotonic fracture, and the associated crack path morphologies in the various alloys, were examined in the scanning electron microscope. Crack path profiles were additionally observed, using the optical microscope, by metallographically polishing sections of the unbroken test pieces, taken at the center thickness, perpendicular to the fracture surface, in the plane of loading. Some sections were also taken normal to the crack growth direction and the fracture surface. Cracks were impregnated with epoxy prior to polishing, for better edge retention and the specimens etched using Kellers reagent. The extent of (excess) crack surface corrosion deposits was estimated by scanning Auger spectroscopy (4), using a

tantalum oxide standard and an Ar^+ sputtering rate of 25 nm/min.

2.5 REFERENCES

1. R. O. Ritchie and W. Yu: in 'Small Fatigue Cracks', R. O. Ritchie and J. Lankford (eds.), TMS-AIME, Warrendale, PA (1986), p. 167.

2. E. Zaiken and R. O. Ritchie: Mater. Sci. Eng., 70 (1985), p. 151.

3. J. C. Newman and I. S. Raju: Eng. Fract. Mech., 15 (1981), p. 185.

4. S. Suresh: Ph.D Thesis, Massachusetts Institute of Technology, 1981.

CHAPTER III

MICROSTRUCTURES AND FRACTURE TOUGHNESS

3.1 INTRODUCTION

The influence of microstructure on the strength, toughness and fatigue-crack growth resistance of experimental aluminum-lithium alloys is widely reported in literature (1-12), however, there is a paucity of data on the performance of commercial alloys. Moreover, the properties are expected to be strongly sensitive to plate orientation, since the commercial alloys show highly elongated and primarily unrecrystallized grain structures, due in part to zirconium additions and extensive thermo-mechanical processing treatments. It is therefore the primary objective of this chapter to characterize and compare the strength and fracture toughness properties of the principal commercial aluminum-lithium alloys, 2090-T8E41, 8090, 8091 and 2091, as a function of microstructure and plate orientation at ambient temperatures, and identify the related mechanisms of monotonic fracture. In the following chapters, the cyclic crack growth properties of these materials are examined in detail.

3.2 EXPERIMENTAL DETAILS

Commercial Al-Li alloys, 8090, 8091 and 2091 were examined in the as received, underaged (T351) and recommended peak (T8X) tempers, and 2090 in the experimental T8E41 temper. Microstructural characterization was performed by optical and transmission electron (TEM) microscopy. Thin foils were prepared by mechanical grinding and electropolishing,

using twin-jet polishing in a 30 % HNO_3-methanol electrolyte solution at -25°C with a potential difference of 15-20 V; samples were subsequently examined in a Philips-400 microscope equipped with energy-dispersive X-ray analysis facilities.

Uniaxial tensile tests were performed on round tensile samples machined in the longitudinal direction, whereas the fracture toughness, K_{Ic}, measurements were obtained for the L-T, T-L, T-S, L+45, S-L and S-T orientations, using different specimen geometries (see Ch. II for details). Crack path morphologies and fracture surfaces were inspected using optical and scanning electron microscopy, respectively.

3.3 RESULTS

3.3.1 Microstructures

Three-dimensional optical micrographs of the as-received microstructures in the 2090, 8090, 8091 and 2091 alloys are illustrated in Fig. 3.1; in general they reveal unrecrystallized, anisotropic grain structures typical of thermomechanical processing, with pancake-shaped grains grossly elongated in the rolling direction. Certain alloys, however, show small differences, notably 8091 is much finer grained and hence the least anisotropic, and some degree of recrystallization is evident in 2091 along with a high density of inclusions or constituent phases. Quantitative estimates of the grain-size dimensions are listed in Table 2.3; no apparent changes were noticed after artificial aging.

Further microstructural examination using TEM revealed fine equiaxed subgrain structures, approximately 2-3 μm in diameter, within the larger unrecrystallized grains (Fig. 3.2a). In the naturally-aged

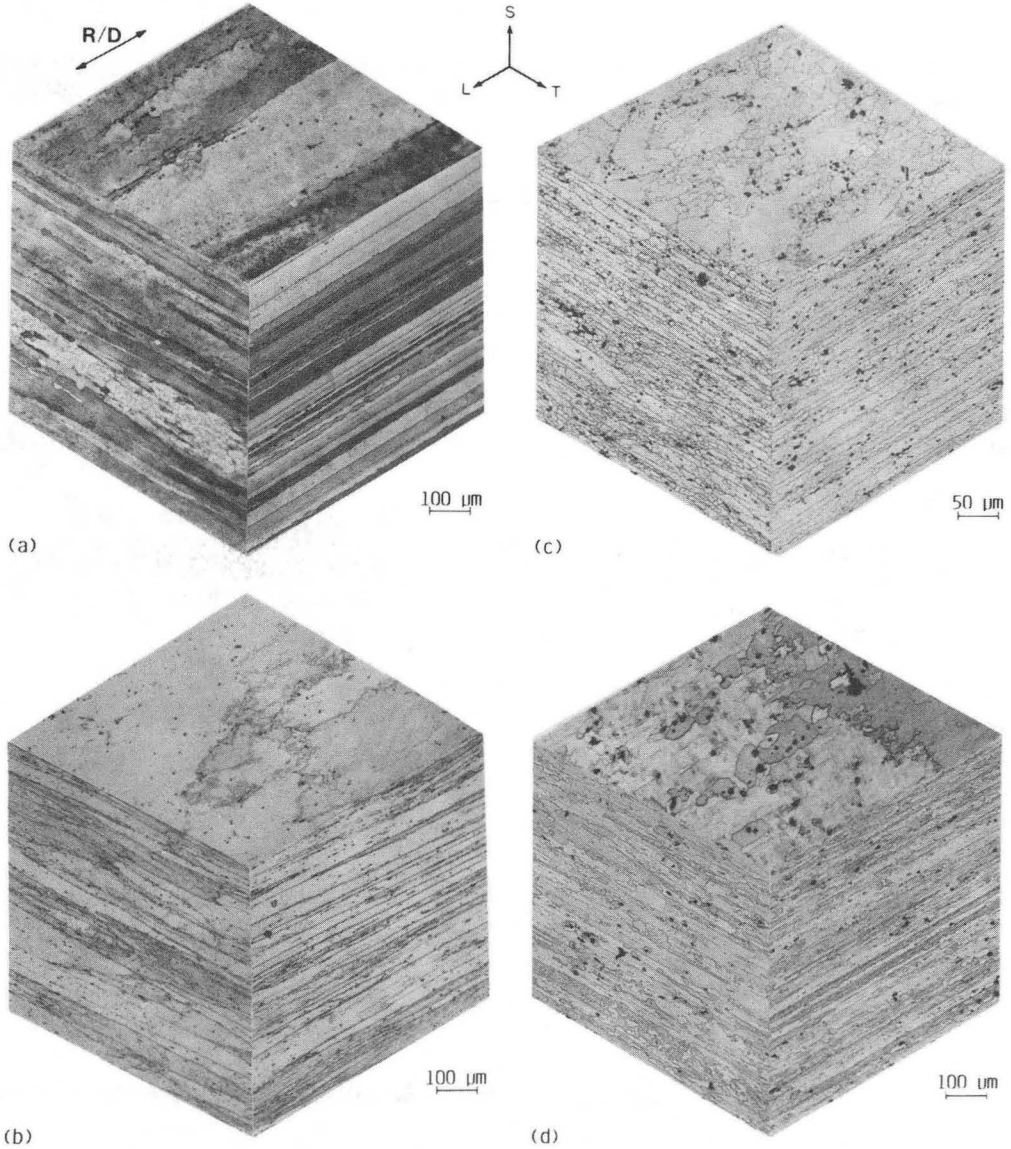

XBB 864-3075D

Fig. 3.1: Three-dimensional optical micrographs of commercial aluminum-lithium alloys, showing the unrecrystallized and pancake-shaped grain structures in a) 2090, b) 8090, c) 8091, and d) 2091. Note the smaller degree of recrystallization in the 2091 alloy and the finer grain size of the 8091 alloy. (etched in Keller's reagent).

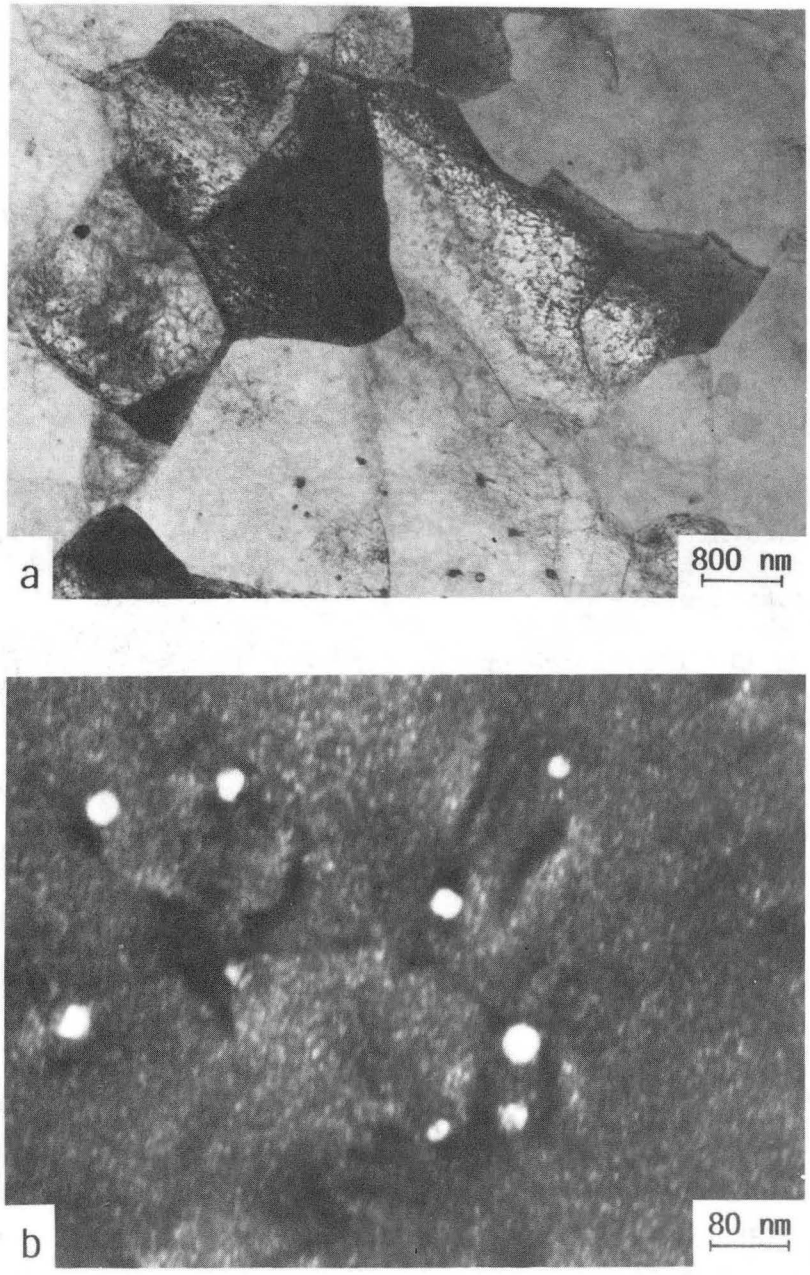

XBB 884-4114A

Fig. 3.2: Transmission electron micrographs of microstructures in 8090-T351 which are typical of all alloys in the naturally-aged condition, showing a) bright-field and b) dark-field images of the fine distribution of δ' (Al_3Li) precipitates and β' (Al_3Zr) dispersoids. The centered dark-field micrograph in b) was obtained using the $\delta'(100)$ superlattice reflection.

T351 condition, all alloys were strengthened by an extremely fine homogenous distribution of coherent, ordered, spherical $\delta'(Al_3Li)$ precipitates and β' (Al_3Zr) dispersoids; no evidence of other precipitate phases was seen in this condition. Precipitation of δ' and β' was generally uniform within the matrix, without preference for grain or subgrain boundaries (Fig. 3.2b).

With artificial aging to commercial peak-aged (T8) tempers, all alloys showed δ'-precipitate coarsening, coupled with the formation of other plate or lathe-like precipitates. In the Al-Li-Cu-Zr alloy 2090, precipitation of T_1 (Al_2CuLi) and Θ'-like (Al_2Cu/Al_2CuLi) plates, with (111) and (100) habits respectively, was evenly distributed throughout the matrix, as shown in Fig. 3.3. In addition, δ' precipitates formed on Θ'-like platelets and around β' dispersoids (17-20). Grain-boundary precipitation in this alloy appears to be largely suppressed by the pre-aging deformation which accelerates the heterogenous nucleation of T_1 precipitates.

In the Mg-containing 8090 and 8091 alloys, precipitation of Θ'-like plates is replaced by heterogenously nucleated S (Al_2CuMg) or S' (precursor to S) laths, which are orthorhombic with a (021) habit (20). In Fig. 3.4, TEM micrographs show the various phases present in 8090, namely spherical δ', composite β'-δ', T_1-plate and S-lathe precipitates. Small degrees of grain- boundary precipitation result in 0.5 μm-wide δ'-PFZs in this alloy after aging 16 hr at 190°C. In comparison, the copper-rich Al-Li-Cu-Mg-Zr alloy 8091 is strengthened by δ' and S phases (Fig. 3.5), with T_1 precipitation largely suppressed; however, widespread grain-boundary precipitation is

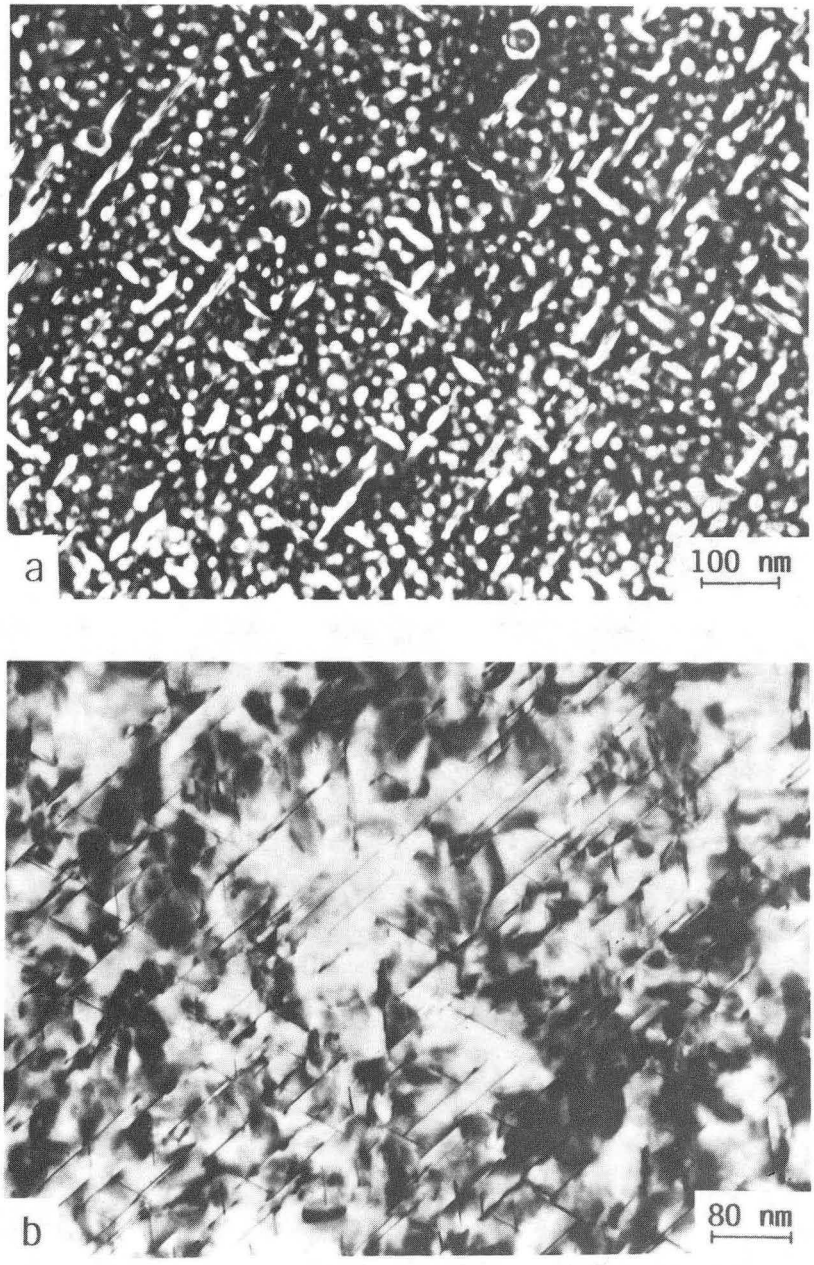

XBB 884-4115A

Fig. 3.3: Predominant strengthening precipitates in alloy 2090-T8E41, showing a) centered dark-field micrograph of δ' (Al_3Li), with δ' precipitates wetting β' (Al_3Zr) and θ'-like (Al_2Cu) precipitates (zone axis close to [001]), and b) bright-field micrograph of T_1 (Al_2CuLi) plates. Note, θ' precipitates show a (100) habit whereas T_1 precipitates show a (111) habit.

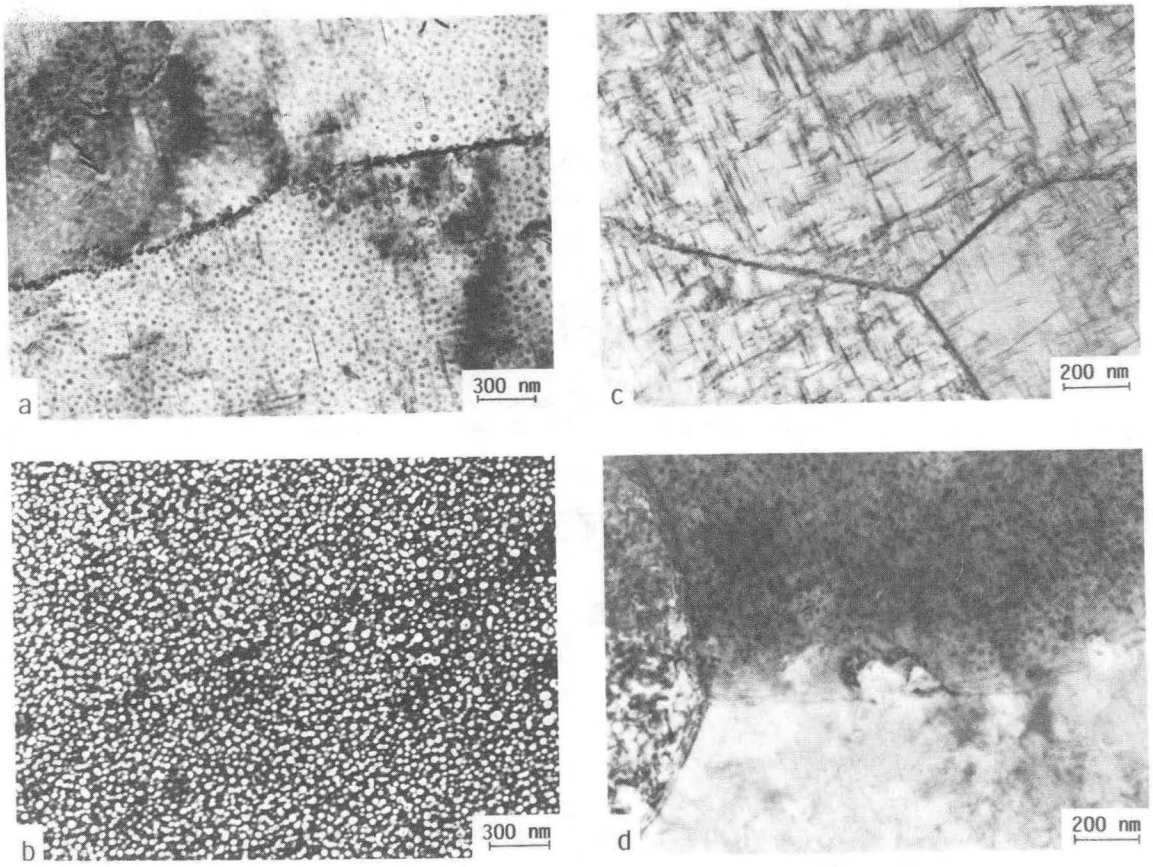

XBB 883-2385A

Fig. 3.4: Transmission electron micrographs of microstructures of peak-aged 8090-T8X alloy, showing a) bright-field image of the spherical δ′ (Al_3Li), composite β′-δ′ and plate-like T_1 (Al_2CuLi) precipitates, b) corresponding centered dark-field micrograph of δ′ precipitates, c) heterogeneously nucleated S′ or S (Al_2CuMg) lathes, and d) grain-boundary precipitates and associated δ′-precipitate-free zone (PFZ).

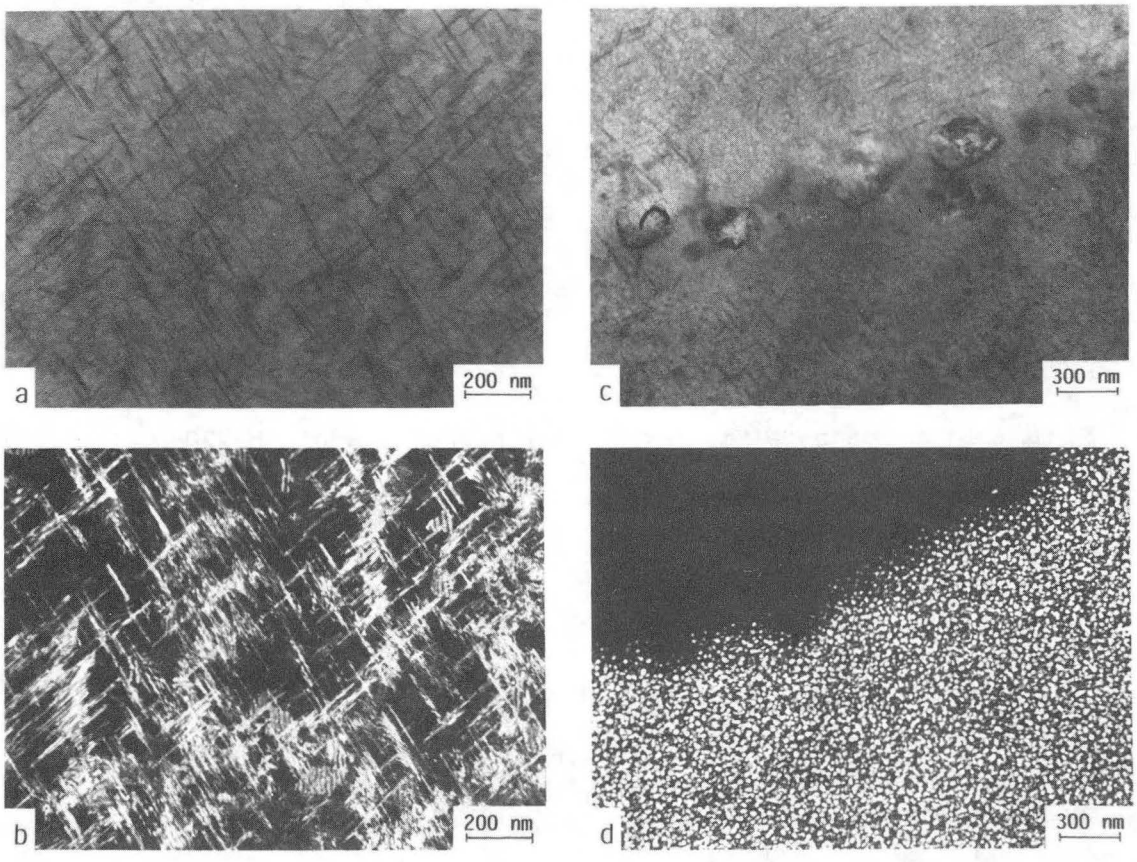

XBB 883-2386A

Fig. 3.5: Transmission electron micrographs of microstructures of peak-aged 8091-T8X alloy, showing a) bright-field and b) dark-field images of heterogeneous dispersion of lathes of the S′ or S (Al_2CuMg) phase, and c) bright-field and d) dark-field images of δ′ and grain-boundary precipitates and corresponding δ′-PFZ. Dark-field micrographs were imaged using the S and δ′ precipitate reflections, respectively.

evident, with the consequent formation of lithium-depleted PFZs.

Microstructures in 2091 following aging for 10 hr at 135°C appear to be hardened predominantly by intense dislocation tangles, δ′ precipitation and β′ dispersoids (Fig. 3.6). The size of δ′ precipitates on artificial aging remained extremely fine (∿7 nm in diameter), with no evidence of S or T_1 precipitation (21,22). A listing of the primary hardening precipitates in each alloy is given in Table 2.3.

3.3.2 Tensile Properties

Ambient-temperature mechanical properties of the 2090, 8090, 8091 and 2091 alloys as a function of aging condition are compared in Table 3.1 (Refer Table 1.4 for the properties of traditional alloys 2124 and 7150). Typical of precipitation-hardened systems, aging to peak temper results in an increase in yield and tensile strengths with a concurrent reduction in ductility and strain-hardening exponents. Alloy 2090-T8E41 showed the highest strength, approximately 20 to 30 % stronger than the highest toughness 2091-T8X alloy; moreover, this alloy was between 20 to 53 % stronger than 2124-T351 and 23 to 37 % stronger than 7150-T651 (Table 2.4).

3.3.3 Plane-Strain Fracture Toughness

Fracture toughnesses in the L-T orientation were generally improved with artificial aging, except in 8091 where a ∿47 % loss was evident (resulting from extensive grain-boundary precipitation). Conversely, toughnesses in the S-L orientation, which were 40 to 50 % lower than in the L-T orientation, were degraded with aging, except in 2091 where a ∿32 % increase was apparent. In general, strength,

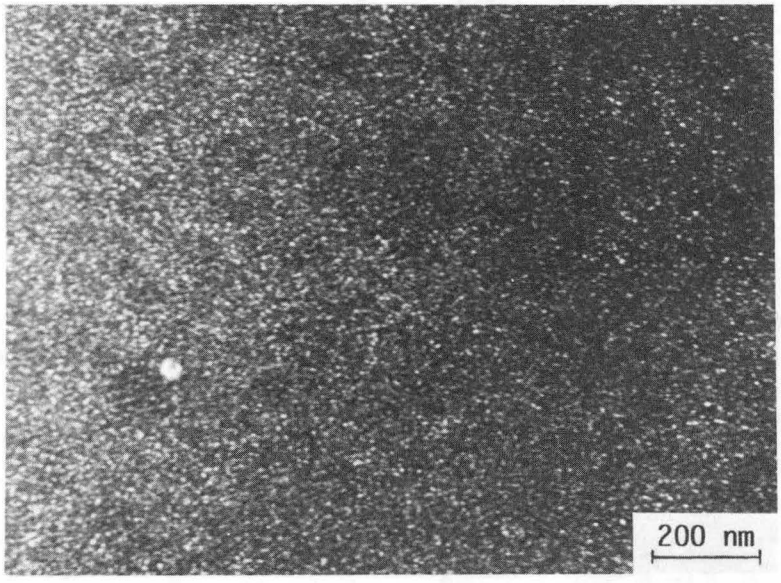

XBB 884-4116A

Fig. 3.6: Transmission electron micrographs of microstructures of peak-aged 2091-T8X alloy, showing fine uniform distribution of δ′ (Al_3Li) precipitates and β′ (Al_3Zr) dispersoids. Centered dark-field image obtained δ′ superlattice reflection.

Table 3.1: Ambient-Temperature Mechanical Properties of Commercial Aluminum-Lithium Alloys

Alloy	Yield Strength* (MPa)	U.T.S.* (MPa)	% Elongation* (on 25 mm)	Strain-Hardening Exponent* n	Fracture Toughness (MPa$\sqrt{m}$)
2090-T8E41	552	589	9.3	0.06	36 (L-T) 17 (S-L)
2091-T351	369	442	10.3	0.12	33+ (L-T) 19 (S-L)
2091-T8X	425	483	8.0	0.10	46+ (L-T) 25 (S-L)
8090-T351	226	352	16.7	0.19	27+ (L-T) 16 (S-L)
8090-T8X	482	534	6.1	0.08	36 (L-T) 13 (S-L)
8091-T351	309	417	10.7	0.16	38+ (L-T) 17 (S-L)
8091-T8X	537	581	6.3	0.07	20 (L-T) 9 (S-L)

*L direction

Table 3.2: Orientation Dependence of Mechanical Properties in 2090-T8E41 Alloy

Orientation	Yield Strength (MPa)	U.T.S (MPa)	% Elongation (on 25 mm)	Fracture Toughness K_{Ic} (MPa$\sqrt{m}$)
Longitudinal	552	589	9.3	36 (L-T)
Transverse	548	579	5.4	24 (T-L) 65+ (T-S)
Short-Transverse	372	448	1.0	17 (S-L) 16 (S-T)
Longitudinal + 45°	460	514	10.9	28 (L+45)

+K_q values not meeting the ASTM E 399 plane-strain thickness requirement.

ductility and toughness properties were all strongly dependent upon orientation. For example, in the 2090-T8E41 alloy (Table 3.2), yield strengths varied by almost 50 %, from 372 MPa (S-L) to 552 MPa (L-T); ductility values by almost an order of magnitude, from 1 % (S-T) to 10.9 % (L+45); and fracture toughness values by a factor of over 4, from 16 MPa$\sqrt{m}$ (S-T) to 65 MPa$\sqrt{m}$ (T-S).

3.3.4 Fractography and Crack Path Morphology

Scanning electron microscopy of fracture surfaces revealed that all uniaxial tensile specimens failed predominantly in shear at roughly 35 to 45 deg to the tensile axis, without significant necking prior to failure. Corresponding fracture morphologies and crack-path profiles in the toughness samples are shown in Figs. 3.7-3.10. For the underaged T351 conditions (L-T orientation), whereas fracture surfaces in the 2091 alloy were characterized by a predominantly transgranular shear mechanism, in 8091 and 8090 fractures consisted of (ductile) void coalescence around cracked and uncracked Cu-rich and Mg-rich intermetallics, second-phase particles and constituent phases (Fig. 3.7). In addition, all underaged alloys showed evidence of <u>isolated</u> secondary cracks (short-transverse delaminations) surrounded by small shear regions (Fig. 3.7). With artificial aging, failure mechanisms in (peak-aged) 2091-T8X changed to ductile void coalescence (Fig. 3.8d), with <u>no</u> evidence of secondary cracking (Fig. 3.9), consistent with the higher short-transverse toughness of this microstructure. In contrast, fracture mechanisms in (peak-aged) 8091-T8X became fully intergranular, whereas in (peak-aged) 8090-T8X they changed to predominantly transgranular shear with a small fraction of

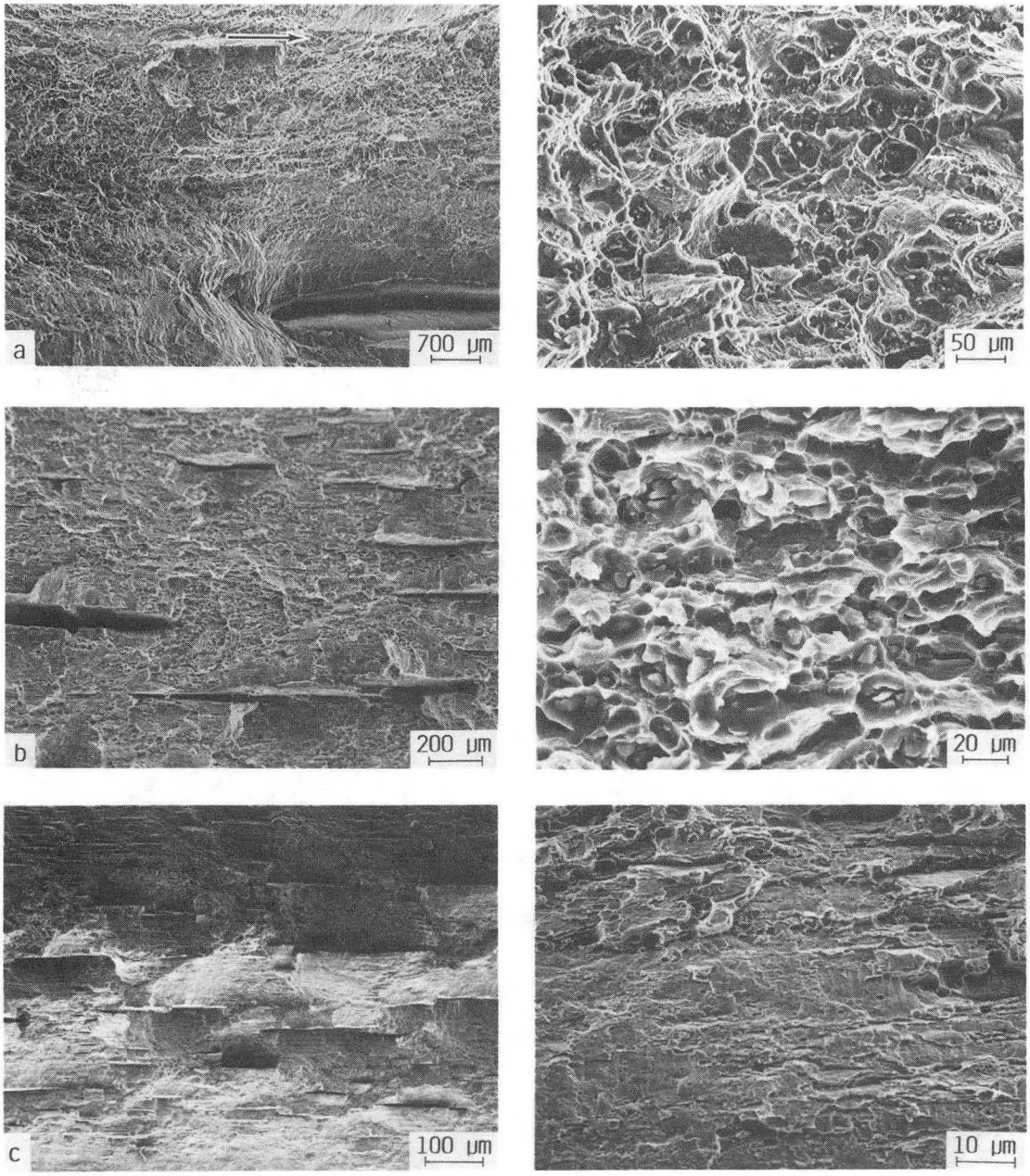

XBB 884-4117A

Fig. 3.7: Scanning electron micrographs of fracture surfaces of naturally-aged (T351) microstructures in a) 8090, b) 8091 and c) 2091 in the longitudinal (L-T) orientation. Fracture occurs by microvoid coalescence in 8090 and 8091 and by a transgranular shear mechanism in 2091. Note the incidence of short-transverse delaminations (splitting), particularly in 2091. Arrow indicates the general direction of crack growth.

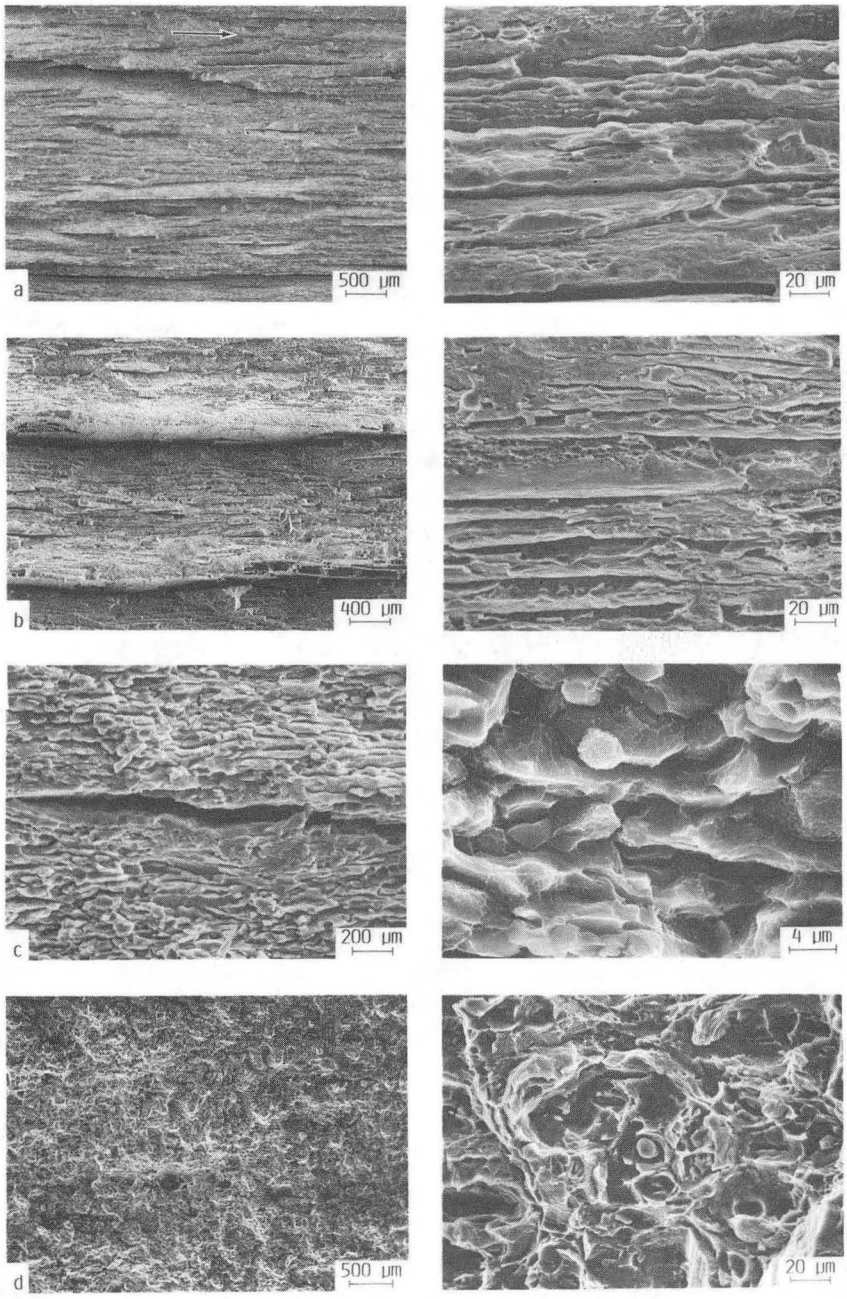

XBB 884-4118A

Fig. 3.8: Scanning electron micrographs of fracture surfaces of peak-aged (T8) microstructures in a) 2090, b) 8090, c) 8091 and d) 2091 in the longitudinal (L-T) orientation. Fracture occurs by transgranular microvoid coalescence in 2091, by intergranular ductile fracture in 8091, and by a transgranular shear mechanism with short-transverse delaminations (through-thickness splitting) in 8090 and 2090. Arrow indicates the general direction of crack growth.

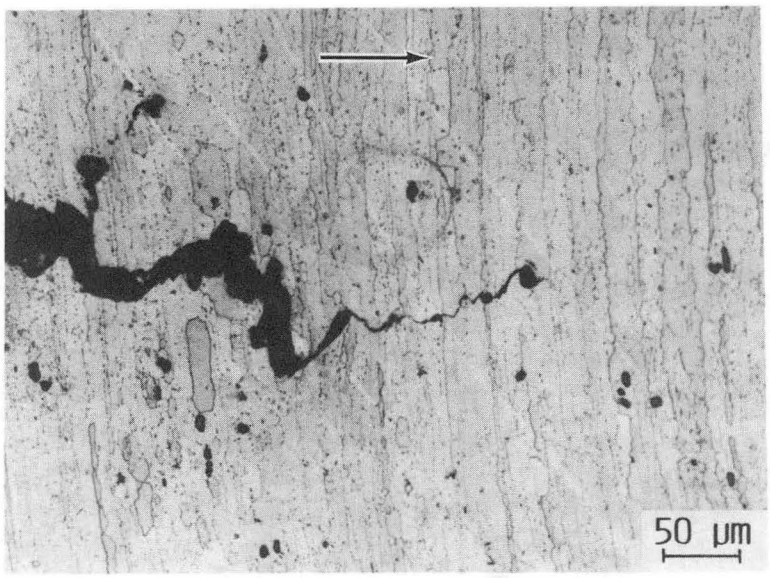

XBB 884-4119A

Fig. 3.9: Optical micrograph showing ductile fracture by void initiation and growth around intermetallic particles in the 2091-T8X alloy (L-T orientation). Arrow indicates the general direction of crack growth.

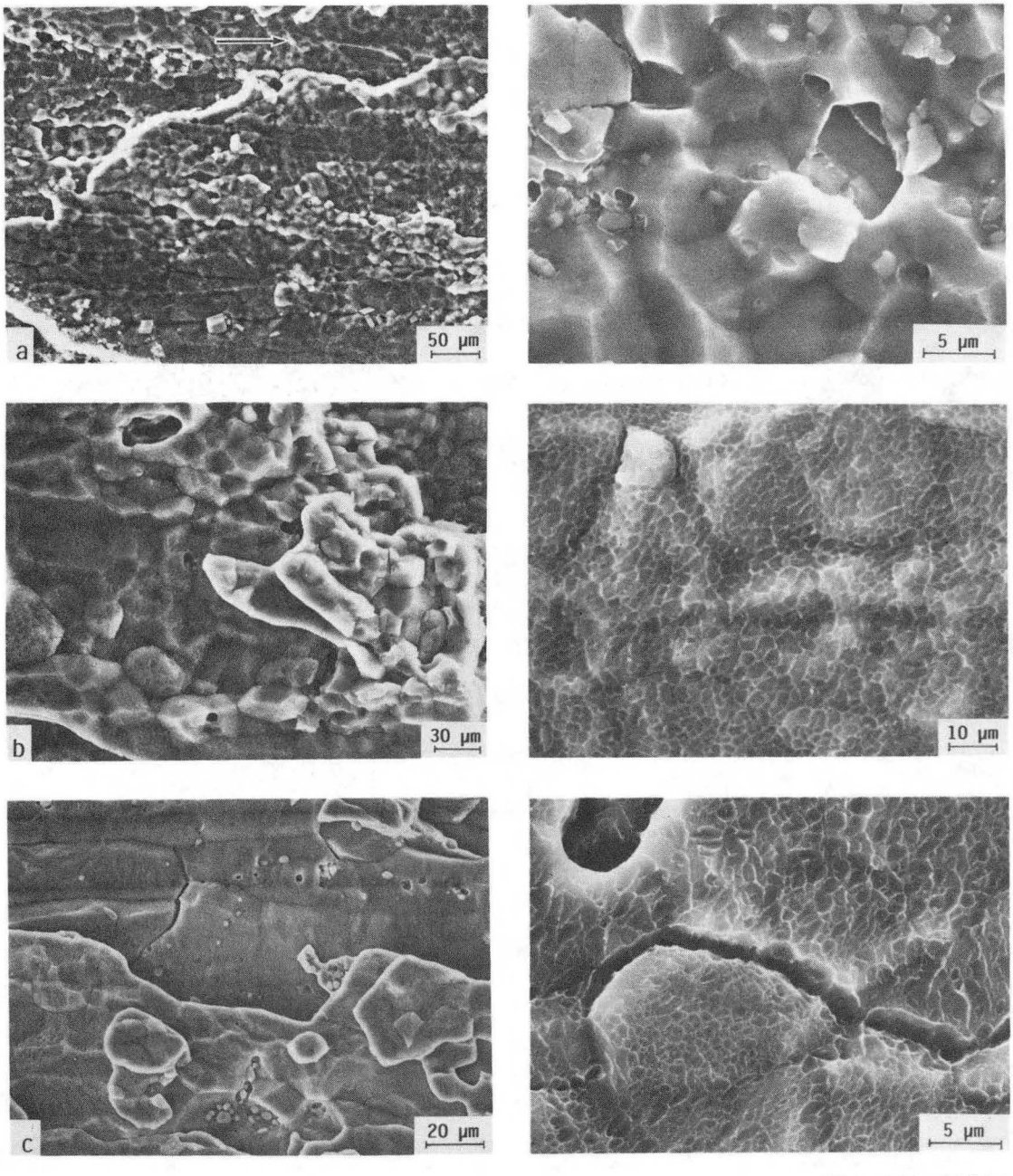

XBB 884-4120A

Fig. 3.10: Scanning electron micrographs of fracture surfaces of a) 8091-T351, b) 8091-T8X and c) 2090-T8E41 in the short-transverse (S-L) orientation, showing intergranular delamination-type fractures. Note the fine dimpled substructure on grain-boundary facets in peak-aged (T8) alloys, characteristic of microstructures with significant grain-boundary precipitation and soft PFZs. Arrow indicates the general direction of crack growth.

void growth around small uncracked particles; secondary cracking was also evident in 8090 as continuous short-transverse delaminations, similar to behavior in 2090-T8E41 (Fig. 3.8).

Fractures in the short-transverse orientations occurred by a predominantly intergranular delamination mechanism in all materials (Fig. 3.10), except 2091 and 8090-T351 which failed by ductile void coalescence. Spectroscopy on the intergranular surfaces revealed pockets of Cu- and Fe-rich intermetallics; in addition, the presence of fine dimples on the intergranular facets in 8090, 2090-T8E41, 8090-T8X suggest preferential failure in the soft PFZs. Both these factors contribute to poor short-transverse toughness in these alloys.

3.4 DISCUSSION

3.4.1 Microstructure and Strengthening Precipitates

Current observations regarding the strengthening precipitates in commercial aluminum-lithium alloys are consistent with studies on solid-state phase transformations in the Al-Li-Cu-Zr and Al-Li-Cu-Mg-Zr systems reported elsewhere (5-10,17-20). Naturally-aged microstructures are seen to be strengthened primarily by a fine homogeneous dispersion of δ' precipitates and β' dispersoids. Further aging promotes the growth of δ' and the formation of S and T_1 plates. Precipitation of T_1 occurs in competition with S for copper atoms and available nucleation sites, although it is absent in the copper-rich 8091 alloy. The widespread precipitation of S or S′ is heterogeneous around regions of high dislocation density in the matrix and along grain and subgrain boundaries. It is not clear, however, whether the dislocations result from pre-aging deformation or from vacancies

released by lithium atoms during the progressive growth of δ', although the fine-scale nature of δ' precipitation and the absence of S and T_1 phases in the 2091 alloy, even after peak aging, would appear to support the latter explanation.

3.4.2 Tensile Properties

Variations in strength and ductility observed during aging of the commercial alloys are typical of many precipitation-hardened systems. In the naturally-aged condition, hardening results from Li, Cu and Mg in solid solution, the precipitation of δ' and β', and the presence of dislocation substructures from pre-aging deformation. With further aging, the coarsening of δ', coupled with the formation of T_1, θ' and/or S plates, leads to further improvements in strength. In the T351 and T8X conditions, these precipitates remain coherent with the matrix and thus deformation proceeds by dislocation shearing; the highest strength levels are thus attained in alloys with the highest copper content, e.g., 2090, which has the largest volume fraction of strengthening T_1, θ'-like, plate precipitates.

3.4.3 Fracture Toughness Behavior

3.4.3.1 Longitudinal (L-T) Fracture Toughness

In precipitation-hardened aluminum alloys, aging to peak hardness generally results in a decrease in the ambient-temperature fracture toughness, concurrent with a change in fracture mode from transgranular to intergranular ductile fracture (24). Specifically, the lower toughness is associated with the formation of grain-boundary precipitates which act as preferential sites for void nucleation; in addition, strain localization in the softer PFZs further weakens the

boundaries, an effect accentuated by the lower strain-hardening capacity of peak-aged microstructures (23-26). In certain alloys, overaging results in a partial recovery in toughness, despite further reductions in strength.

Similar behavior has been reported for several experimental aluminum-lithium alloys (27-29), although the superior toughness of underaged microstructures has been additionally related to crack deflection and bifurcation (27,28). For the commercial Al-Li alloys studied in the present work, however, superior strength/toughness properties are achieved generally with peak-aging tempers (8091 is the exception); possible reasons for this are discussed below.

<u>8091:</u> Underaged microstructures in 8091 fail by transgranular ductile fracture associated with void coalescence around second-phase in the matrix; with further aging, the formation of grain-boundary precipitates leads to intergranular ductile fracture (29) and a corresponding reduction in fracture toughness. Evidence for the latter is shown by the fine dimples on intergranular and intersubgranular facets on fracture surfaces for the T8X condition (Fig. 3.8c).

<u>8090 and 2091:</u> In contrast, aging to peak strength in the 8090 and 2091 alloys causes an increase in fracture toughness, despite reductions in ductility and strain-hardening exponent. However, the low volume fraction of grain-boundary precipitates, which are completely absent in 2091 and seen only at high-angle grain boundaries in 8090, suggests that other mechanisms are active.

First, in peak-aged 8090, the copious matrix precipitation of T_1-

plates and S-lathes tends to disperse slip by promoting cross slip within individual slip bands. Concurrently, the very low short-transverse toughness leads to extensive intergranular (through-thickness) delaminations (Fig. 3.8b); such splitting tends to relax through-thickness constraint by causing the plane-strain fracture process to be divided into several parallel plane-stress fractures. As modelled and experimentally verified in Ch. VIII, the plane-stress fracture toughness in Al-Li alloys is typically some 25 % higher than for plane strain, such that the occurrence of through-thickness splitting can result in a significant increase in toughness. This mechanism is termed crack-divider delamination toughening, and is commonly observed in laminated materials (30-32); in Al-Li alloys, it is also enhanced by low temperatures and is a major factor contributing to the large <u>increases</u> in toughness shown by certain Al-Li alloys at cryogenic temperatures (14,16).

Second, in 2091, extensive short-transverse splitting is seen in underaged microstructures; moreover, since aging to peak strength improves the S-L toughness by over 25 %, splitting is not seen on fracture surfaces of the T8X microstructure. The higher peak-aged toughness in this alloy instead appears to be associated with a ductile transgranular void-coalescence mechanism (Fig. 3.8d). Such differences in the extent of short-transverse splitting in peak-aged microstructures of 2091 and 8090 can be seen in Fig. 3.11. Although precise reasons for this anomaly are unclear, the effect may be related to the small degree of recrystallization and lower aging times and temperatures in the 2091 alloy.

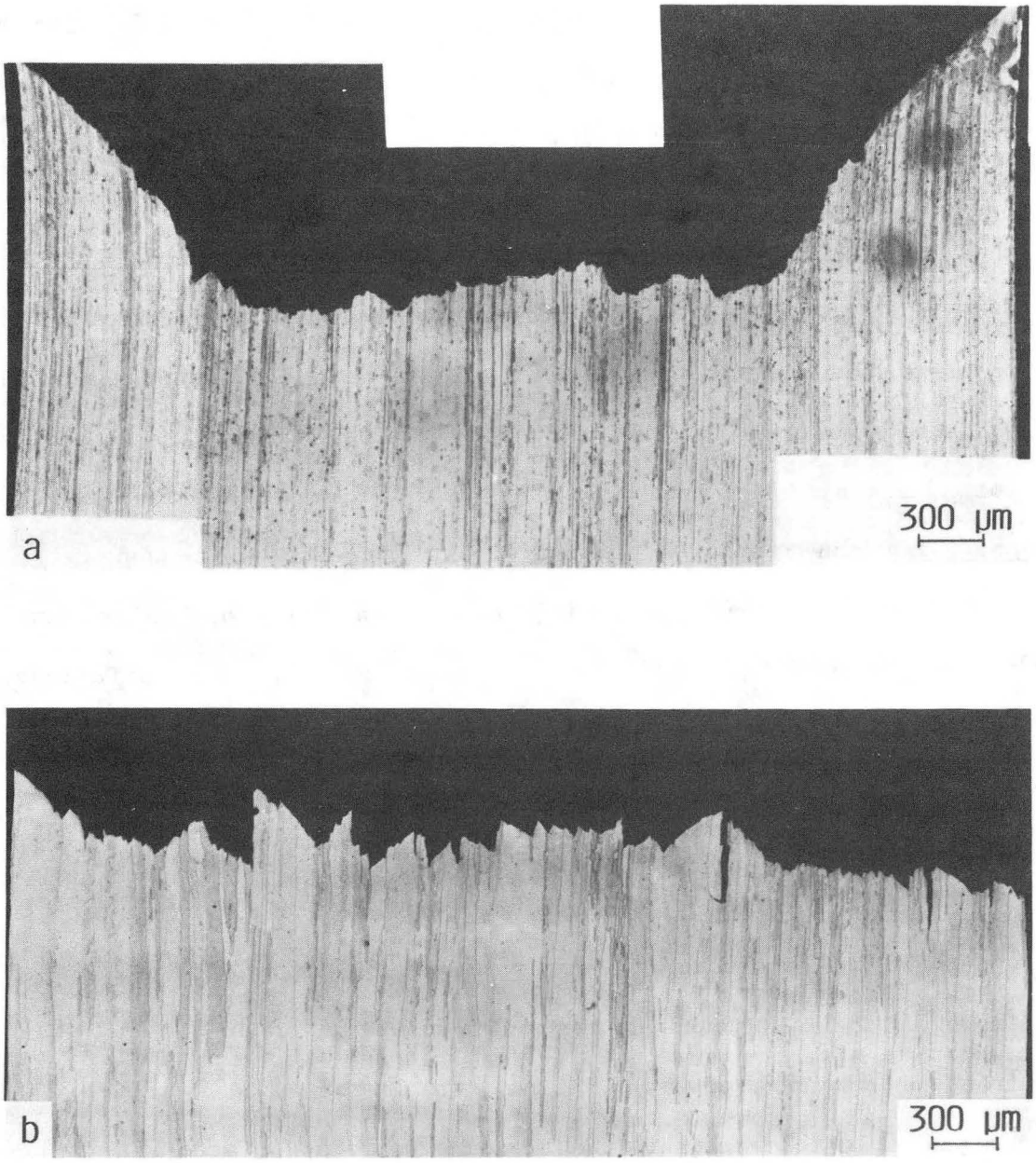

XBB 884-4121A

Fig. 3.11: Metallographic sections, perpendicular to the crack-growth direction, in peak-aged microstructures of a) 2091-T8X and b) 2090-T8E41, showing high-toughness ductile fracture with substantial shear lips in 2091-T8X, in contrast to failure by a local transgranular shear mechanism with extensive short-transverse delaminations in 2090.

Underaged microstructures of 2091 and 8090 are also seen to exhibit some degree of crack bifurcation at the onset of fracture. Such bifurcation, however, is predominantly a surface effect (Fig. 3.12), and was never seen in the other alloys. It is therefore concluded that toughening from crack deflection and bifurcation, although deemed to be important in experimental Al-Li alloys (27), is a relatively insignificant mechanism in commercial alloys for L-T orientations.

2090: The behavior of 2090-T8E41 is similar to that of peak-aged 8090; the excellent toughness appears to result from uniform precipitation of T_1 and θ'-plates, negligible grain-boundary precipitation, and significant crack-divider delamination toughening. This commercial temper offers an optimal strength/toughness combination; further aging degrades both properties due to grain-boundary precipitation and related phenomena as shown in Ch. VII.

3.4.3.2 Short-Transverse (S-L) Fracture Toughness

For all commercial alloys, the short-transverse fracture toughness is roughly 50 % lower than in the L-T orientation. With the exception of 2091 and 8090-T351, such low toughnesses are associated with an intergranular delamination-type fracture (Fig. 3.10). Plausible reasons for the poor grain-boundary strength, even in underaged structures, are the presence of coarse Fe/Cu- or Mg/Cu-rich constituent particles (1-2 μm in diameter), and the segregation of Na and K impurities to grain boundaries (15,34). In addition, in situ Auger spectroscopy studies (33) have shown that lithium segregation to grain boundaries can occur readily during aging, prior to the formation of grain-boundary particles and PFZs. Since a large fraction

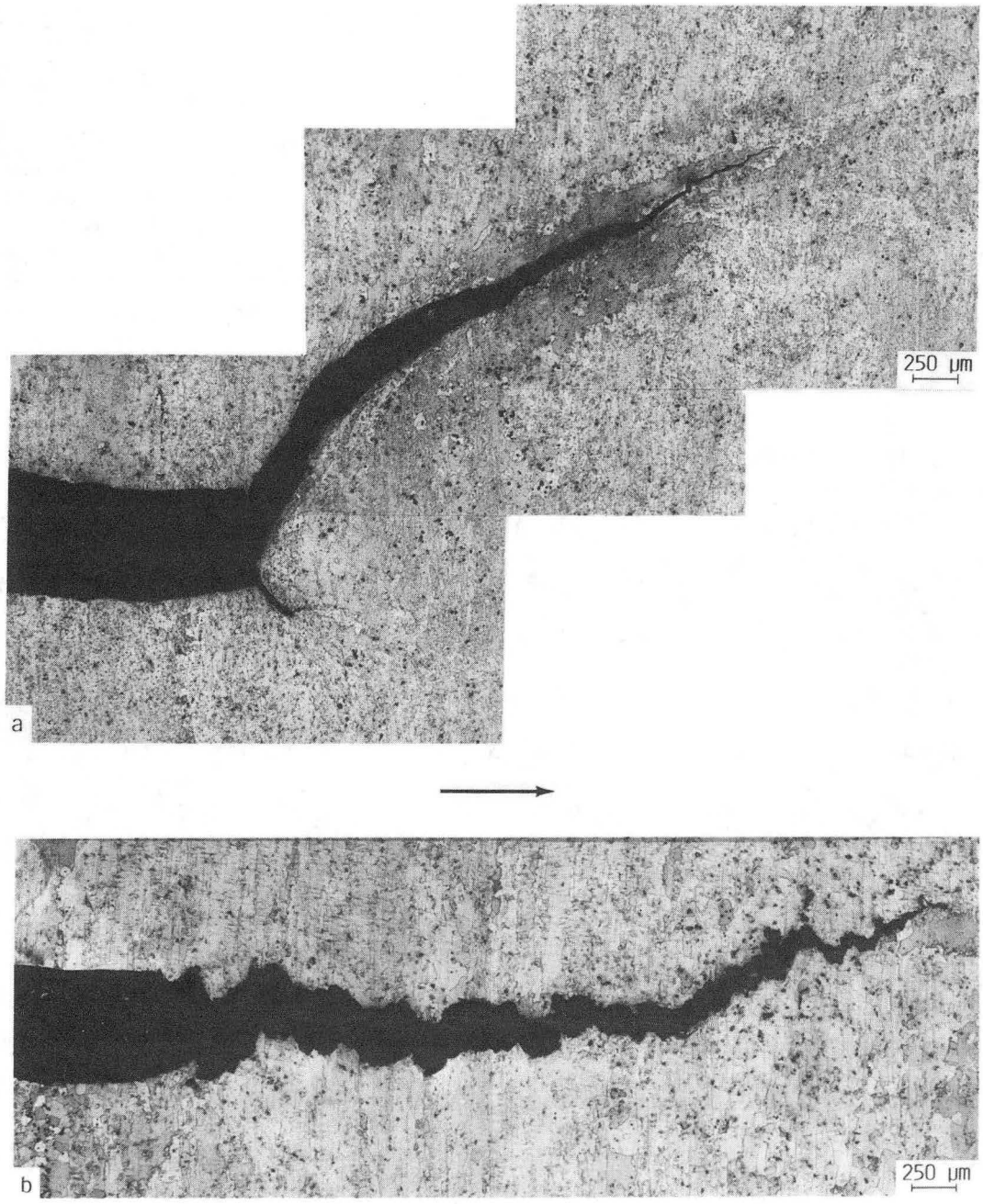

XBB 884-4122A

Fig. 3.12: Metallographic sections taken perpendicular to the crack-growth direction at a) the surface and b) the interior of a sample of 2091-T351 alloy (L-T orientation), showing that crack bifurcation at the onset of fracture is predominantly a surface effect. Arrow indicates the general direction of crack growth.

of the weak grain boundaries are aligned normal to the short-transverse direction, owing to the unrecrystallized, anisotropic nature of the grain structure, low short-transverse toughness is to be expected. With continued aging, general grain-boundary precipitation further weakens the boundaries and accentuates this effect, leading to ductile intergranular failures (Fig. 3.10b,c), and even lower short-transverse toughness values.

3.4.4 Influence of Plate Orientation

As alluded to above, akin to behavior in laminated composites (30-32), the poor short-transverse strength and toughness of commercial aluminum-lithium alloys can provide a source of weak interfaces which act to improve toughness in perpendicular orientations, particularly at lower temperatures (14,16). As illustrated schematically in Fig. 3.13 (also see Section 8.4), in the L-T and T-L orientations short-transverse delaminations give rise to crack-divider delamination toughening, which promotes local plane-stress fracture. Even greater toughening, however, is achieved in the T-S and L-S (crack-arrester) orientations through crack deflection and bifurcation at $\sim$90 deg (i.e., the Cook-Gordon mechanism (36) for crack stopping at weak interfaces), as shown for the 2090 alloy in Fig. 3.14. Experimental results showing the influence of orientation on the mechanical properties of the 2090 alloy are listed in Table 3.2; toughness values for the T-S orientation can be seen to be over 80 % higher than in the L-T orientation and over a factor of 4 times higher than in the S-T and S-L orientations.

Estimates for the toughness improvements in the T-S (crack arrester) orientation due to delamination normal to the crack growth

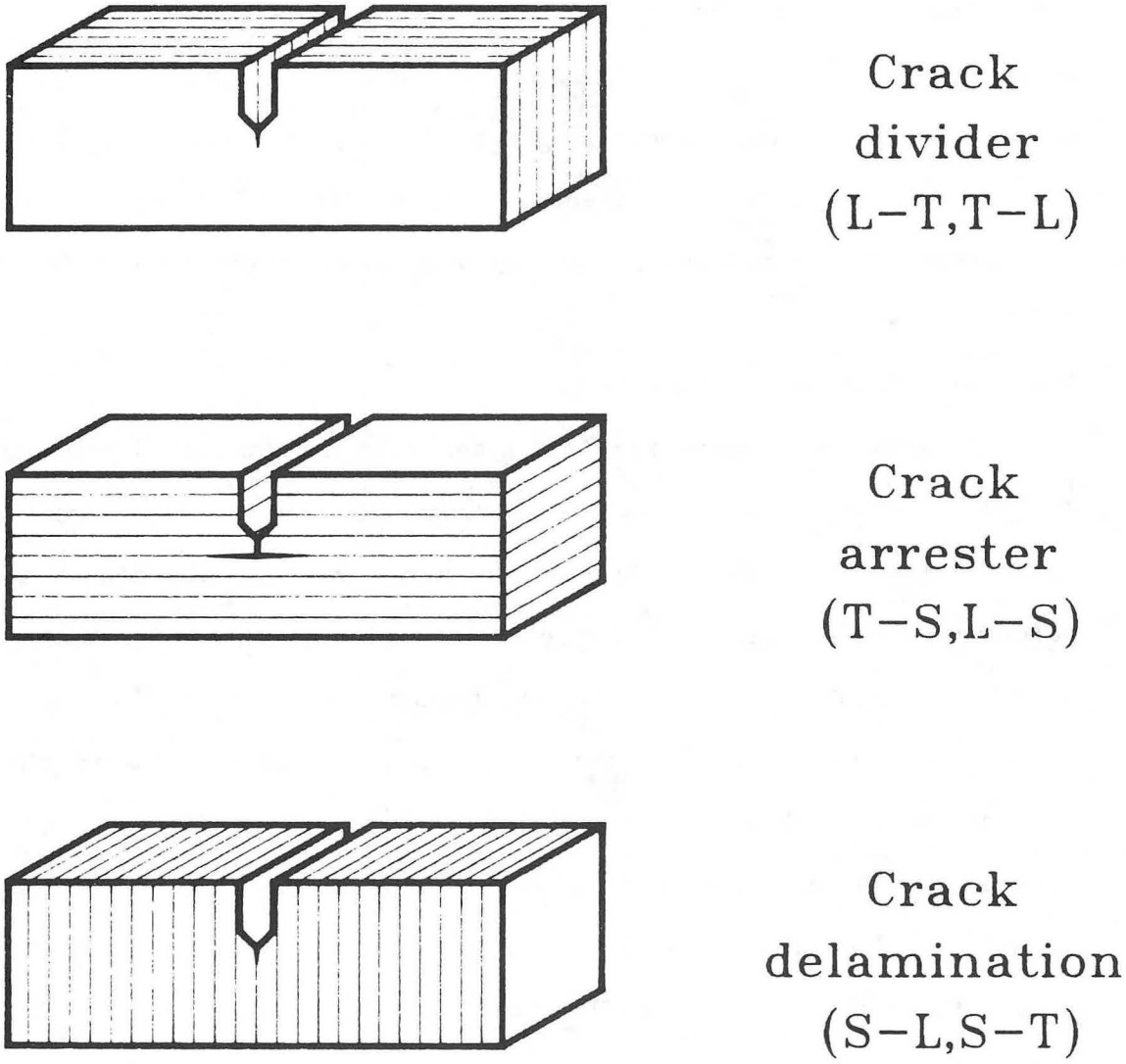

XBL 883-844

Fig. 3.13: Schematic illustration of orientations for crack extension in an anisotropic material containing specific planes of weakness in one direction. L-T and T-L orientations correspond to crack divider, T-S and L-S to crack arrester, and S-L ans S-T to crack delamination (or short-transverse).

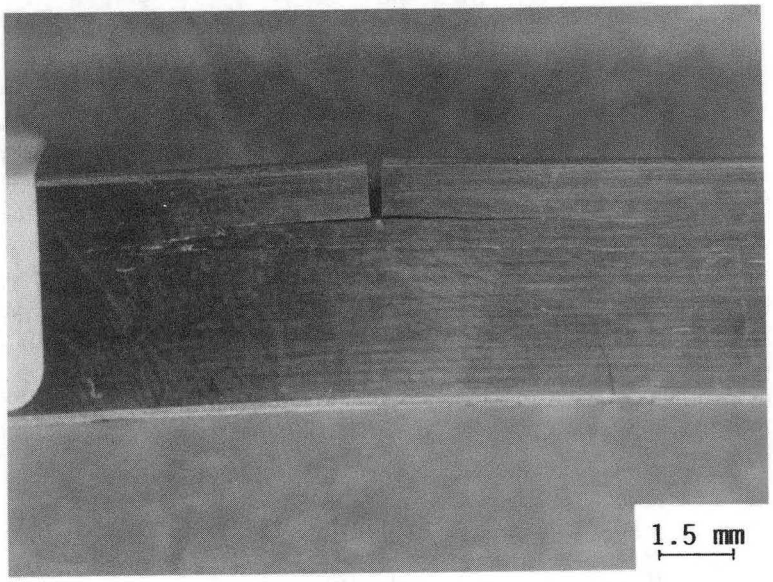

XBB 883-2355A

Fig. 3.14: Delamination toughening in the crack-arrester orientation due to crack deflection along weak short-transverse planes for 2090-T8E41 alloy tested in the T-S orientation

direction, compared to the L-T value can be made using the linear-elastic solutions of Cotterell and Rice (37). For the in-plane deflection of a crack through an angle θ (deflected segment small compared to crack length), the <u>local</u> Mode I and Mode II stress-intensity factors, k_1 and k_2, are given in terms of their <u>global</u> values, K_I and K_{II}, and angular functions $a_{ij}(\theta)$ as:

$$k_1 = a_{11}(\theta)\ K_I + a_{12}(\theta)\ K_{II} \quad \text{and}$$
$$k_2 = a_{21}(\theta)\ K_I + a_{22}(\theta)\ K_{II} \qquad \ldots\ldots (1)$$

Since K_{II} is zero and first-order solutions for $a_{ij}(\theta)$ give:

$$a_{11}(\theta) = \cos^3(\theta/2) \quad \text{and}$$
$$a_{21}(\theta) = \sin(\theta/2)\ \cos^2(\theta/2) \qquad \ldots\ldots\ldots (2)$$

such that the effective stress intensity ahead of the crack tip deflected through 90 deg is approximately:

$$K_{eff} \approx (k_1{}^2 + k_2{}^2)^{1/2} = 0.49\ K_I \qquad \ldots\ldots\ldots (3)$$

Nonlinear-elastic solutions would suggest a slightly larger effect (38). Such simple modelling predicts that the toughness in the crack arrester orientation should be nearly two (1/0.49) times higher. In 2090-T8E41 the room temperature L-T toughness is 36 MPa$\sqrt{m}$; the calculated K_{IC} value for the T-S orientation is thus of the order of 70 MPa$\sqrt{m}$, which is close to the measured value of 65 MPa$\sqrt{m}$.

Anisotropy in mechanical properties is also evident for orientations in the rolling plane due to the pronounced texture imparted during prior deformation, which persists due to inhibition of

recrystallization. For example, compared to the L-T orientation, the L+45 (LT-TL) orientation shows approximately 20 % lower strength and toughness (Table 3.2). Texture is also promoted by the preferred habit planes of the plate-like precipitates in the matrix. In addition, strength variations through the thickness of commercial plates of Al-Li alloys are presently quite significant; this has been attributed to variations in texture, quench rate and subsequent microstructure (39).

3.4.5 Models for Fracture Toughness Behavior

Modelling of fracture-toughness behavior in ductile alloys, where the crack extends by a microvoid coalescence mechanism, is often based on criteria of the critical crack-tip opening displacement (δ_c) exceeding the mean spacing of the void initiating particles (d_p) (23,40), or a critical fracture strain (ε_f^*) being exceeded over a characteristic microstructural dimension (r_o^*) (41,42). Proposed models in literature for high strength aluminum alloys, and the expressions suggested are summarized below:

Hahn and Rosenfield (23): Critical crack-tip displacement model,

$$K_{IC} \sim [\sigma_y E' D_p (\pi/6)]^{1/2} v_f^{-1/6} \qquad \text{..... (4)}$$

Garrett and Knott (24): Critical strain criterion applied over the characteristic width of the plastic zone size,

$$K_{IC} \propto n [\sigma_y \varepsilon_f^* E']^{1/2} \qquad \text{..... (5)}$$

Chen and Knott (43): Critical stress model, where exceeding the cohesion strength of the dispersoid/matrix interface triggers void coalescence within the shear bands,

$$K_{IC} \propto n\,[\sigma_y\, E'\, d_p \sigma_c^{*}/D_p]^{1/2} \qquad \text{..... (6)}$$

where, E′ is the Young's modulus E in plane stress and $E/(1 - \nu^2)$ in plane strain, ν is Poisson's ratio, σ_y is the flow stress, D_p and v_f are respectively the diameter and volume fraction of the void initiating particles, σ_c^{*}, is the cohesion strength of the particle/matrix interface and the value of ε_f^{*} is the fracture strain appropriate to the crack-tip stress state. As noted by the authors themselves, the Hahn and Rosenfield model predicts unusual trends of increasing toughness with increasing strength and particle size. On the other hand, in the models proposed by Knott and co-workers (24,43), the constant of proportionality has the dimensions of $(\text{length})^{1/2}$, and appear to be dimensionally unsound.

In essence, these models imply that the fracture toughness, $J_{IC} = K_{IC}^2/E'$, for the extension of a ductile crack is simply the product of the flow stress, a local ductility and a characteristic microstructural dimension (44), except where the length dimension has been empirically related to the strain hardening coefficient (23,43). Applying these concepts to the present results on the (L-T) fracture-toughness behavior of commercial aluminum-lithium alloys (Fig. 3.15), indicates that a critical-strain approach works reasonably well for microstructures which fail predominantly by ductile microvoid coalescence (e.g., most underaged structures and 8091). However, for more complex failure mechanisms which often additionally involve short-transverse splitting (e.g., in peak-aged microstructures and at 77 K, see Ch. VIII for further discussion), observed trends in K_{Ic} are almost exactly the reverse of that predicted by these models, implying that a

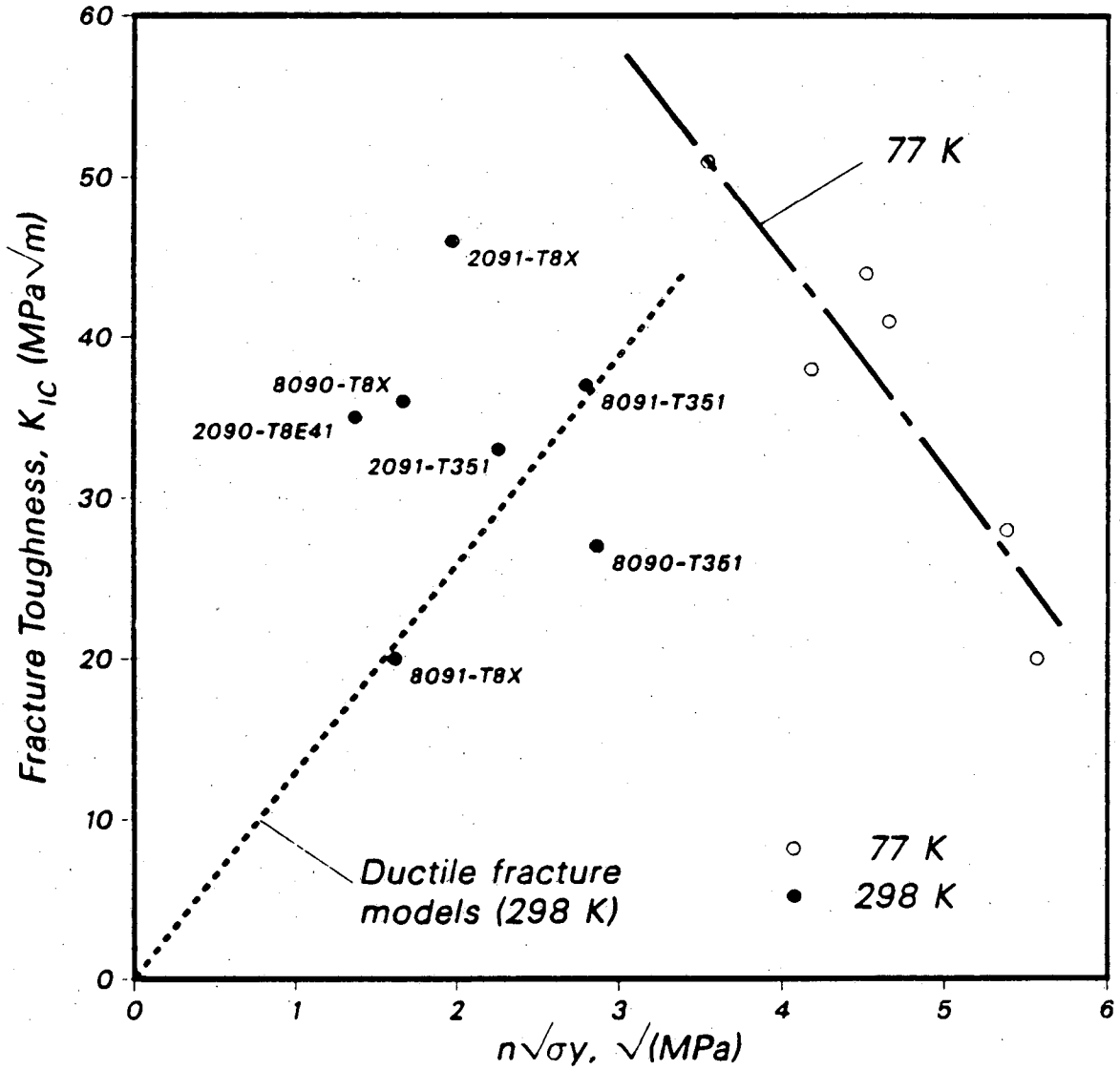

XBL 885-1574

Fig. 3.15: Comparison of experimental fracture-toughness results for commercial Al-Li alloys with Hahn and Rosenfield's (23) and Garrett and Knott's (24) models for ductile fracture in aluminum alloys, showing K_{Ic} values at ambient temperature and at 77 K plotted as a function of $n\sqrt{\sigma_y}$ (n is strain-hardening coefficient, σ_y is yield strength). Note that, apart from 8091 alloy at 298 K, the toughness properties of 2090, 2091 and 8090 with respect to aging condition and at 77 K show opposite behavior to model predictions.

precise understanding of the fracture mechanisms in these instances is far from complete.

3.4.6 Comparison with Traditional Aluminum Alloys

As illustrated in Fig. 3.16a for peak-aged microstructures in the L-T orientation, the ambient-temperature strength-toughness combinations shown by commercial aluminum-lithium alloys are comparable with, and in many cases exceed, that shown by traditional high-strength 2000 and 7000 series aluminum alloys currently used for structural aerospace applications. Similar results have been reported for behavior at cryogenic temperatures (14,16). It is considered that the superior strength and toughness properties shown by these alloys, specifically 2090, 2091 and 8090, are related to such factors as limited grain-boundary precipitation, homogeneous deformation promoted by uniform and widespread precipitation of S and T_1 phases, and the occurrence of delamination toughening from short-transverse (through-thickness) splitting. However, it must be remembered that, unlike traditional alloys, these properties are highly anisotropic, and the superior strength and crack-growth resistance shown by Al-Li alloys in the longitudinal and transverse directions must be balanced by generally far inferior short-transverse properties (Fig. 3.16b). In this regard, commercial aluminum-lithium alloys behave more like aligned composites and laminates than monolithic materials.

3.5 CONCLUSIONS

Based on above study of the role of microstructure in influencing the ambient-temperature strength and fracture-toughness properties of commercial aluminum-lithium alloys 2090, 2091, 8090 and 8091 as a

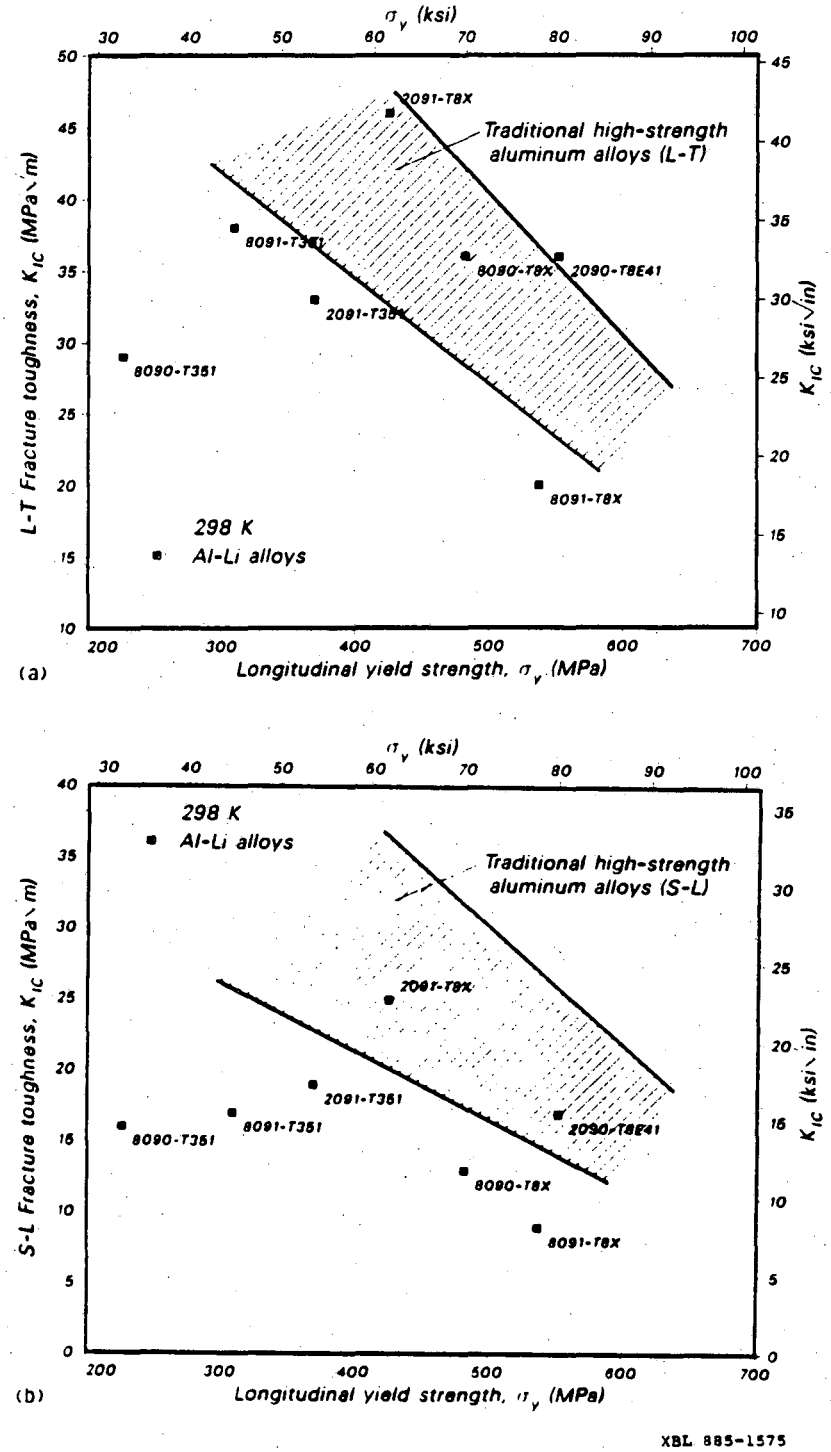

Fig. 3.16: Ambient-temperature strength-toughness properties of commercial aluminum-lithium alloys, compared to traditional high-strength aluminum alloys, for a) L-T and b) S-L orientations. Note the excellent strength-toughness combinations shown by 2090-T8E41, 8090-T8X and 2091-T8X in the L-T orientation.

function of plate orientation, the following conclusions can be made:

1. With the exception of 8091, commercial aluminum-lithium alloys show superior combinations of strength and toughness in the peak-aged condition (L and L-T orientations). Such behavior is contrary to that observed in several experimental Al-Li alloys and in traditional high-strength aluminum alloys.

2. Such superior strength/toughness properties shown by peak-aged (T8X) 2090, 2091 and 8090 alloys in the L and L-T orientations are primarily attributed to an increased volume fraction of coherent, strengthening precipitates in the matrix, minimal grain-boundary precipitation and thus negligible PFZs, and delamination toughening from the occurrence of extensive short-transverse (through-thickness) splitting.

3. In the 8091 alloy, conversely, grain-boundary precipitation is not suppressed during artificial aging, with the result that the fracture toughness of the peak-aged (T8X) microstructure in this alloy is much reduced. Such behavior is similar to that shown by traditional aluminum alloys and is associated with fracture via a ductile intergranular mechanism.

4. The anisotropic, unrecrystallized grain structure and marked deformation texture shown by commercial Al-Li alloys lead to mechanical properties that are highly dependent on plate orientation. For example, compared to the L and L-T orientations, strength and toughness properties in the 2090-T8E41 alloy are approximately 20 % lower in the L+45 orientation, and 30 to 50 % lower in the S-L and S-T orientations. On the other hand, the poor short- transverse properties provide a

contribution to "toughening" in perpendicular orientations, i.e., from crack-divider and crack-arrester delamination toughening in the L-T and T-S orientations, respectively.

5. Despite such strongly directional properties, the strength-toughness combinations exhibited by peak-aged microstructures of commercial 2090, 2091 and 8090 alloys (L and L-T orientations) are superior to that shown by traditional high-strength aluminum alloys currently used for structural aerospace applications.

3.6 REFERENCES

1. T. H. Sanders and E. A. Starke (eds.): 'Aluminum-Lithium Alloys', TMS-AIME, Warrendale, PA (1981).

2. T. H. Sanders and E. A. Starke (eds.): 'Aluminum-Lithium Alloys II', TMS-AIME, Warrendale, PA (1983).

3. C. Baker, P. J. Gregson, S. J. Harris and C. J. Peel (eds.): 'Aluminum-Lithium Alloys III', Institute of Metals, London (1986).

4. G. Champier, B. Dubost, D. Miannay and L. Sabetay (eds.): 'Aluminum-Lithium Alloys IV', J. de Physique, Coll. C3, 48, Les Editions de Physique, France (1987).

5. E. A. Starke, T. H. Sanders and I. G. Palmer: J. Metals, 32 (1981), p. 24.

6. K. V. Jata and E. A. Starke: Metall. Trans. A, 17A (1986), p. 1011.

7. P. J. Gregson and H. M. Flower: Acta Metall., 33 (1985), p. 527.

8. S. J. Harris, B. Noble and K. Dinsdale: in Ref. 2, p. 219.

9. W. X. Feng, F. S. Lin and E. A. Starke: Metall. Trans. A, 15A (1984), p. 1209.

10. S. Suresh, A. K. Vasudévan, M. Tosten and P. R. Howell: Acta Metall., 35 (1987), p. 25.

11. A. K. Vasudévan, P. E. Bretz, A. C. Miller and S. Suresh: Mat. Sci. Eng., 64 (1986), 113.

12. J. Petit, S. Suresh, A. K. Vasudévan and R. C. Malcolm: in Ref. 3, p. 239.

13. J. Glazer, S. L. Verzasconi, E. N. C. Dalder, W. Yu, R. A. Emigh, R. O. Ritchie and J. W. Morris: Adv. Cryog. Eng., 32 (1986), p. 397.

14. R. C. Dorward: Scripta Metall., 20 (1986), p. 1379.

15. D. Webster: Metall. Trans. A, 18A (1987), p. 2181.

16. K. T. Venkateswara Rao, H. F. Hayashigatani, W. Yu and R. O. Ritchie: Scripta Metall., 22 (1988), p. 93.

17. M. H. Tosten, A. K. Vasudévan and P. R. Howell: Metall. Trans. A, 19A (1988), p. 51.

18. J. C. Huang and A. J. Ardell: Mat. Sci. Tech., 3 (1987), p. 176.

19. R. J. Rioja, P. E. Bretz, R. R. Sawtell, W. H. Hunt and E. A. Ludwiczak: in 'Aluminum Alloys: Their Physical and Mechanical Properties', T. H. Sanders and E. A. Starke (eds.), EMAS, Warley, U.K. (1986).

20. H. M. Flower and P. J. Gregson: Mat. Sci. Technol., 3 (1987), p. 81.

21. P. Meyer and B. Dubost: in Ref. 3, p. 37.

22. R. De Jesus and A. J. Ardell: in 'Aluminum-Lithium Alloys', R. Kar, S. Agrawal and W. E. Quist (eds.), American Society for Metals International, Metals Park, Ohio (1988).

23. G. T. Hahn and A. R. Rosenfield: Metall. Trans. A, 6A (1975), p. 653.

24. G. G. Garrett and J. F. Knott: Metall. Trans. A, 9A (1978), p. 1187.

25. I. Kirman: Metall. Trans. A, 2A (1971), p. 1761.

26. G. M. Ludtka and D. E. Laughlin: Metall. Trans. A, 13A (1982), p. 411.

27. S. Suresh and A. K. Vasudévan: Mat. Sci. Eng., 72 (1985), p. 37.

28. S. Suresh and A. K. Vasudévan: Mat. Sci. Eng., 79 (1986), p. 183.

29. A. K. Vasudévan and R. D. Doherty: Acta Metall., 35 (1987), p. 1193.

30. H. L. Leichter: J. Spacecraft, 3 (1966), p. 1113.

31. J. D. Embury, N. J. Petch, A. E. Wraith and E. S. Wright: Trans. Met. Soc. AIME, 239 (1967), p. 114.

32. K. Markstrom: Eng. Fract. Mech., 1 (1968), p. 55.

33. K. T. Venkateswara Rao and R. O. Ritchie: Mat. Sci. Eng., 100 (1988), p. 23.

34. A. K. Vasudévan, A. C. Miller and M. M. Kersker: in Ref. 2, p. 181.

35. W. S. Miller, M. P. Thomas, D. J. Lloyd and D. Creber: in Ref. 3, p. 584.

36. J. Cook and J. E. Gordon: Proc. Roy. Soc., A282 (1962), p. 509.

37. B. Cotterell and J. R. Rice: Int. J. Fract., 16 (1980), p. 155.

38. S. Suresh and C. F. Shih: Int. J. Fract., 30 (1986), p. 237.

39. A. K. Vasudévan, W. G. Fricke, R. C. Malcolm, R. J. Bucci, M. A. Przystupa and F. Barlat: Metall. Trans. A, 19A (1988), p. 731.

40. J. R. Rice and M. A. Johnson: in 'Inelastic Behavior of Solids', M. F. Kanninen, W. G. Adler, A. R. Rosenfield and R. I. Jaffee (eds.), McGraw Hill, New York (1970), p. 641.

41. R. O. Ritchie, W. L. Server and R. A. Wullaert: Metall. Trans. A, 10A (1978), p. 1557.

42. A. C. Mackenzie, J. W. Hancock and D. K. Brown: Eng. Fract. Mech., 9 (1977), p. 167.

43. C. Q. Chen and J. F. Knott: Met. Sci., 15 (1981), p. 357.

44. R. O. Ritchie and A. W. Thompson: Metall. Trans. A, 16A (1985), p. 233.

CHAPTER IV

FATIGUE CRACK GROWTH: LONG CRACKS

4.1 INTRODUCTION

Although several studies to date on the fatigue crack propagation behavior of lithium-containing aluminum alloys, have reported generally improved fatigue resistance compared to traditional 2000- and 7000-series alloys (1-9), several aspects regarding such inferences remain unexplored. First, the mechanisms responsible for their superiority are not clearly understood. Second, there are concerns over variations in the fatigue crack growth properties with plate orientation, specifically with regards to short-transverse (S-L, S-T) orientations. And finally, conclusions regarding their excellent fatigue properties are exclusively based on long ($\gtrsim$ 10 mm) crack results; little is known about the anomalous nature of small ($\lesssim$ 1 mm) fatigue cracks in these materials.

Accordingly, the objective of the present chapter is to investigate the mechanisms influencing the growth rate behavior of long fatigue cracks in commercial aluminum-lithium alloys 2090, 8090, 8091 and 2091, as a function of microstructure, load ratio and plate orientation, and compare the properties with standard aerospace aluminum alloys; small fatigue crack growth resistance of these materials is evaluated in the following chapter.

4.2 EXPERIMENTAL DETAILS

Alloys 8090, 8091 and 2091 were tested under constant amplitude

loading conditions (R = 0.1, 50 Hz. refer Ch. II for details), in the underaged (T351) and peak aged (T8X) microstructures, in the L-T orientation. Influence of load ratio and plate orientation were studied in the near-peak aged alloy 2090-T8E41. The L-T, T-L, L+45 and T-S orientations were tested for R = 0.1, 0.5 and 0.75; S-L and S-T orientations for R = 0.1.

Fatigue fracture surfaces and crack path morphologies were carefully examined using scanning electron and optical microscopy. Changes in the degree of crack deflection and fracture surface roughness were characterized in terms of the lineal roughness. In addition, the extent of (excess) crack surface corrosion deposits was estimated by scanning Auger spectroscopy, using a tantalum oxide standard and an Ar^+ sputtering rate of 25 nm/min.

4.3 RESULTS

4.3.1 Behavior in alloys 8090, 8091 and 2091

Variation in the fatigue crack propagation rates of long fatigue cracks, plotted as a function of the nominal stress intensity range, ΔK is shown in Fig. 4.1a for the naturally aged and peak aged microstructures of the Pechiney alloy 2091. Associated crack closure levels expressed in terms of the closure stress intensity normalized with respect to the maximum stress intensity (K_{cl}/K_{max}) are compared in Fig. 4.1b. It is apparent that artificial aging to peak temper clearly improves the (long) fatigue crack growth resistance of 2091, for all stress intensity levels ranging from fatigue-thresholds to near-instability. Measured levels of crack closure are also higher, concurrent with an observed increase in the degree of crack deflection

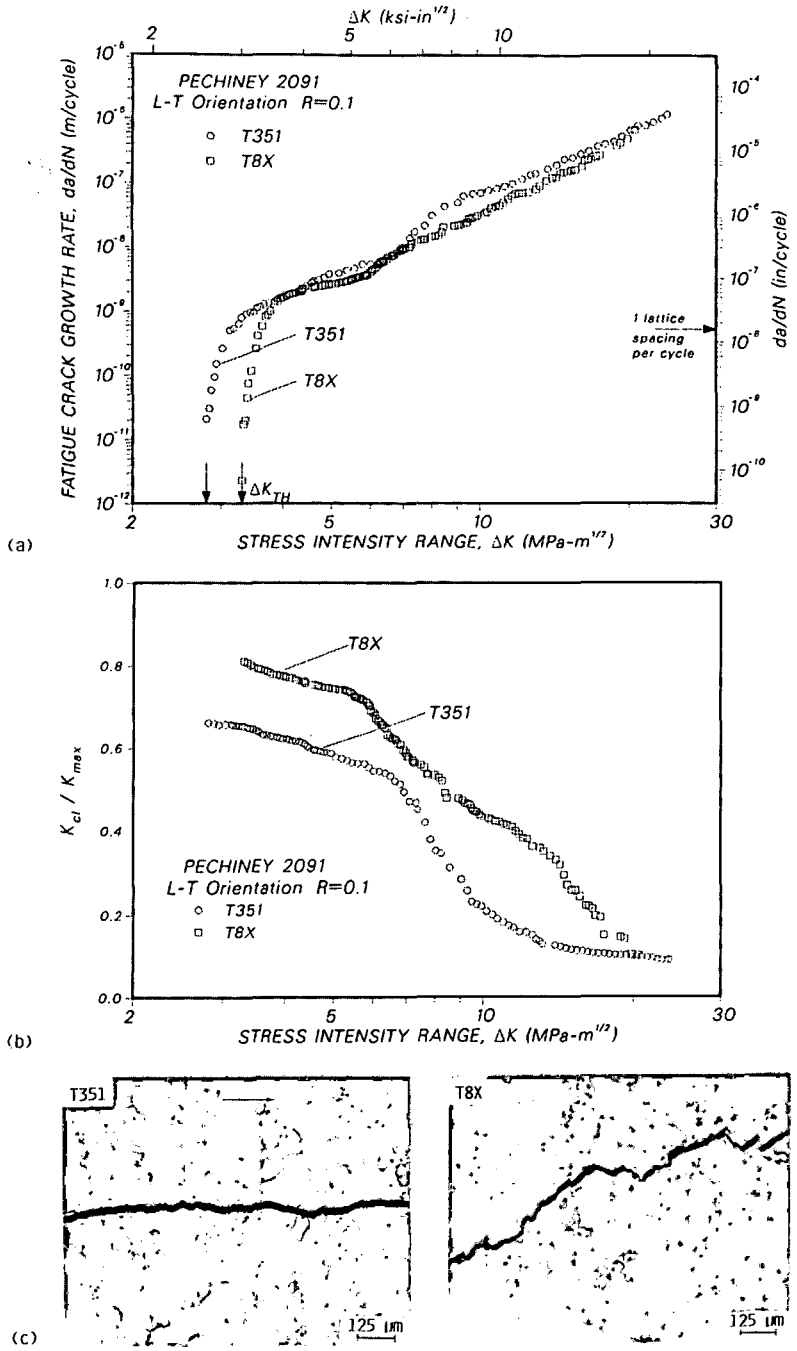

XBB 885-4511A

Fig. 4.1: a) Fatigue crack growth rates, b) normalized crack closure levels as a function of ΔK (R = 0.1) and c) fatigue crack path morphologies in 2091-T351 and 2091-T8X. Note the lower growth rates in the peak aged microstructure consistent with the higher levels of crack closure and increased degree of crack meandering. Arrow shows the general direction of crack growth .

and meandering in the fatigue crack path morphology (Fig. 4.1c).

Analogous growth rate behavior for long cracks in Alcan alloys 8090 and 8091 (R = 0.1) is compared Fig. 4.2. In both alloys nominal and effective threshold values are decreased by aging to peak strength (Table 4.1), although behavior at higher growth rates is less affected. Accordingly, growth rates are slower for the underaged condition in Al-Li-Cu-Mg-Zr alloy 8090, at near-threshold ΔK levels; behavior at high ΔK levels marked by crossovers. However, in case of 8091, artificially aging to peak strength clearly increases crack growth rates and impairs the fatigue resistance. Similar to observations on the fracture toughness, such behavior appears to be associated with the fine grain size and weakening of the grain boundaries, due to extensive grain boundary precipitation. Measured crack closure levels were correspondingly lower, as the fatigue crack path morphology becomes more linear (see Table 4.1).

4.3.2 Comparison with Traditional Alloys 2124 and 7150

A comparison of fatigue crack propagation rates of long cracks in the various commercial aluminum-lithium alloys (L-T orientation) in their recommended peak temper, with traditional high strength aluminum alloys, 2124-T351 and 7150-T651 (10,11), is shown in Fig. 4.3a as a function of ΔK. With the exception of near-threshold behavior of underaged 2124, growth rates in lithium-containing alloys are seen to be 1-2 orders of magnitude slower over the entire spectrum of growth rates. Such behavior can be related primarily to the high levels of crack closure, which unlike traditional high strength aluminum alloys are maintained at very high levels ($K_{cl}/K_{max} \sim 0.5$) even at ΔK's of upto

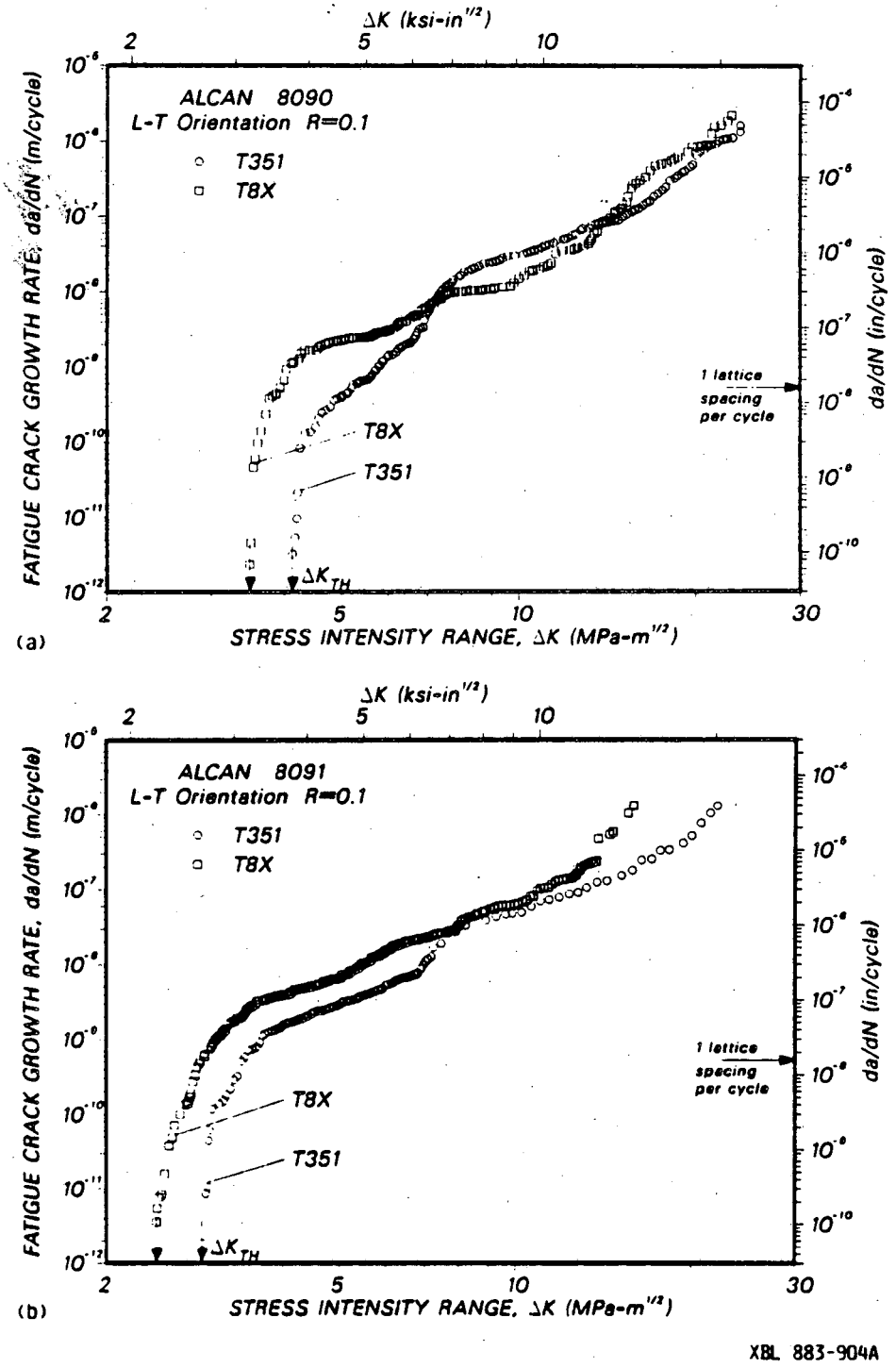

Fig. 4.2: Constant amplitude fatigue crack growth rate behavior of long cracks (R = 0.1) in the naturally aged (T351) and peak aged (T8X) microstructures of a) 8090 and b) 8091. Note that the properties of 8091 clearly deteriorate with artificial aging.

Table 4.1: Near-Threshold Fatigue Crack Propagation Data for Various Commercial Aluminum-Lithium Alloys

Alloy	Threshold (MPa$\sqrt{m}$) ΔK_{TH}	ΔK_{eff}	Closure K_{cl}/K_{max}	CTOD* (nm) Max	Cyclic	Lineal Roughness
2090-T8E41	3.86	0.84	0.86	255	103	1.23
8090-T351	4.13	0.87	0.85	356	144	1.22
8090-T8X	3.49	0.57	0.89	239	97	1.20
8091-T351	2.91	0.81	0.79	181	74	1.17
8091-T8X	2.43	0.78	0.67	105	43	1.07
2091-T351	2.81	1.04	0.66	169	68	1.20
2091-T8X	3.30	0.86	0.81	222	90	1.29

Table 4.2: Crack Path Morphology Measurements and Near-Threshold Crack Growth Data in 2090-T8E41 at R = 0.1

Orientation	Threshold ΔK_{TH}	ΔK_{eff}	CTOD* max	cyclic	Lineal Roughness	Mean Angular Deviation	Excess Oxide Thickness
	(MPa$\sqrt{m}$)		(nm)			(deg)	(nm)
L-T	3.86	0.84	255	103	1.23	20.4	-
T-L	3.21	0.97	177	72	1.26	17.3	2
T-S	3.06	0.97	162	65	1.83	39.2	-
S-L	2.60	1.36	117	47	1.11	3.6	-
S-T	2.75	1.09	130	53	1.11	4.5	-
L+45	2.46	0.71	124	50	1.09	5.8	-

*Maximum and cyclic CTOD computed from $0.6K_{max}^2/\sigma_y E$ and $0.6\ K^2/2\sigma_y E$, respectively, where E is Young's modulus and σ_y is the yield strength of the material (22).

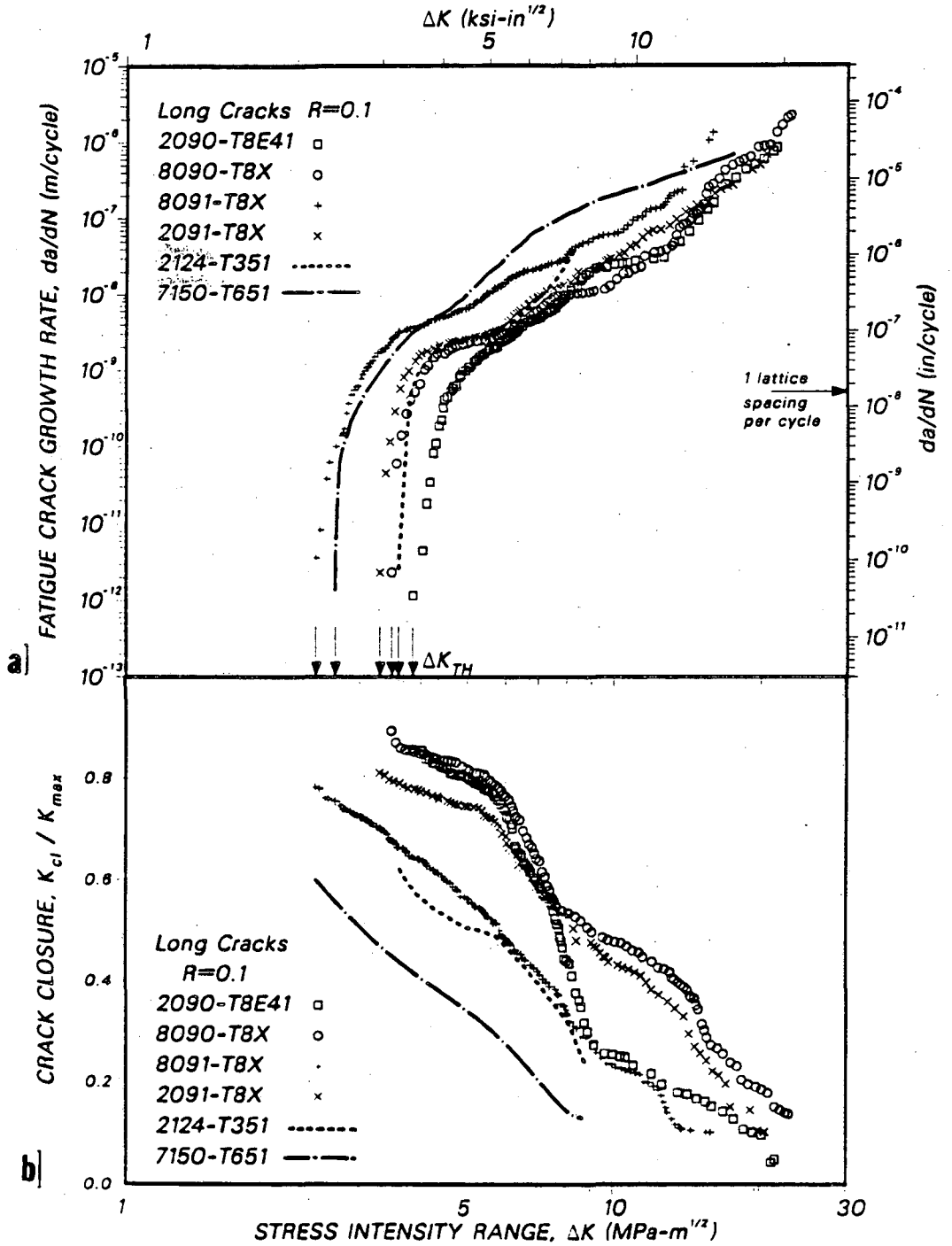

Fig. 4.3: Comparison of a) fatigue crack growth rates and b) crack closure levels for long cracks in the various commercial aluminum-lithium alloys and conventional high strength aluminum alloys (R = 0.1). Note the general superiority of the lithium-containing alloys, specifically, 2090-T8E41.

15 MPa$\sqrt{m}$. Among the Al-Li alloys, peak aged 2090 and 8091 display the best and worst (long crack) fatigue properties, respectively, concurrent with the highest and lowest levels of crack closure measured in these materials.

4.3.3 Alloy 2090-T8E41: Influence of Plate Orientation

Despite the slower crack growth rates in aluminum-lithium alloys in general, and 2090 in particular, the fatigue crack propagation behavior is strongly anisotropic, as shown in Fig. 4.4a for the L-T, T-L, T-S, S-L, S-T, and L+45 orientations in 2090-T8E41 (R = 0.1). Growth rates (at fixed ΔK) vary by up to 4 orders of magnitude between the various orientations, consistent with large changes in crack closure (Fig. 4.4b). The more commonly tested T-L and L-T orientations, and the T-S orientation, show the slowest growth rates, with threshold ΔK_{TH} values between 3 and 4 MPa$\sqrt{m}$. These orientations generally develop the highest closure levels, e.g., K_{cl} values approach 0.9 K_{max} close to ΔK_{TH} in the L-T orientation. Conversely, S-L and S-T orientations show the fastest growth rates, consistent with the lower measured levels of crack closure. The lowest threshold (ΔK_{TH} = 2.4 MPa$\sqrt{m}$) is found in the L+45 orientation, which has 16 % lower yield strength.

4.3.4 Alloy 2090-T8E41: Role of Load Ratio

Corresponding crack growth rate behavior at high load ratios, specifically for R = 0.1, 0.5 and 0.75, are shown for the L-T orientation in Fig. 4.5. Characteristic of most metallic materials (12), the role of load ratio is most prominent at near-threshold levels, resulting in faster crack growth rates and sharp reduction in ΔK_{TH} values, with increasing R. Similar trends were noted for the T-L,

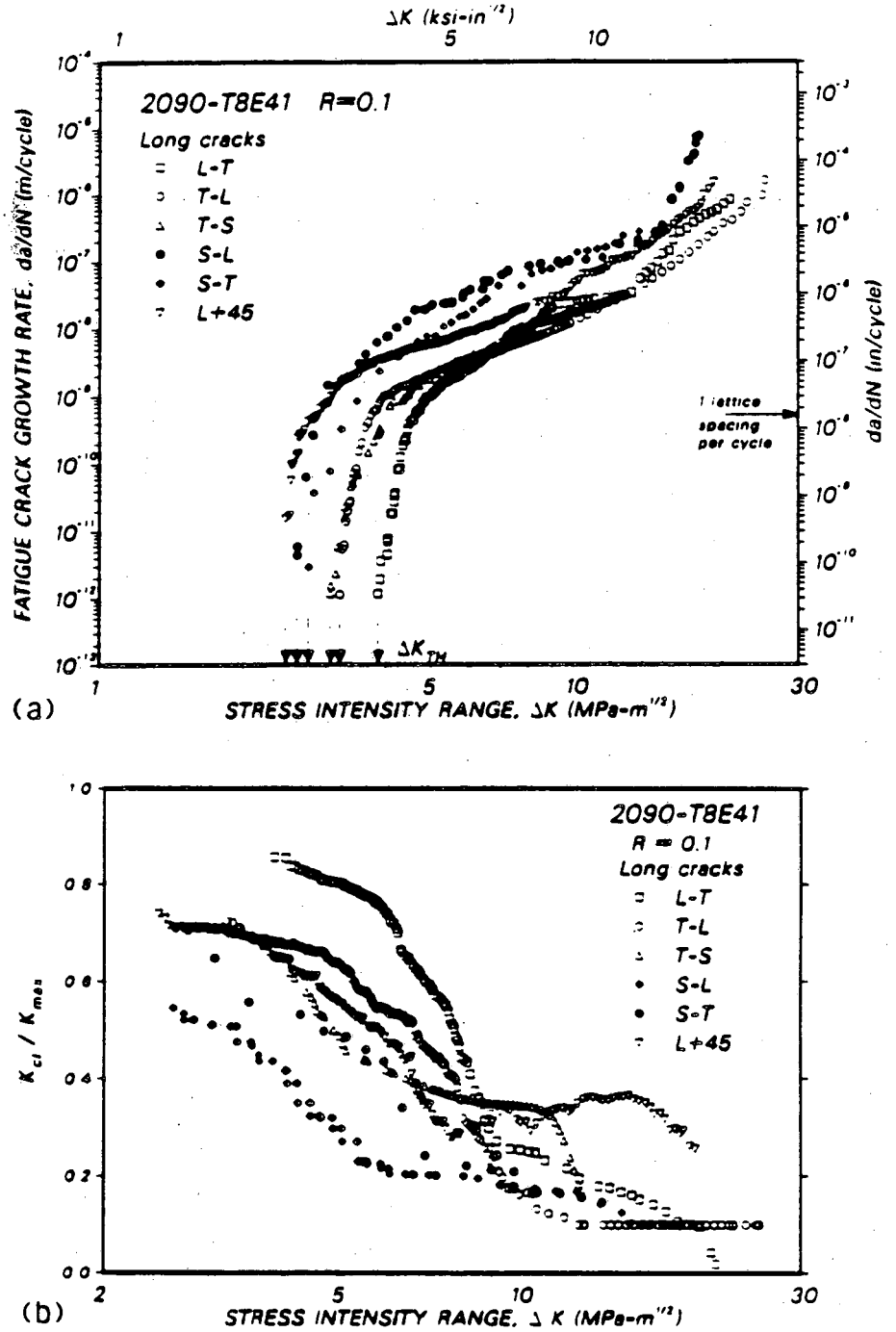

XBL 871-88 A

Fig. 4.4: Variation in a) fatigue crack growth rates and b) closure levels (long cracks) in 2090-T8E41 alloy at R = 0.1 as a function of orientation. Note how growth rates parallel to the rolling plane (S-L, S-T) are generally the fastest, whereas growth rates normal to the rolling plane (L-T, T-S) are the slowest consistent with the low and high measured levels of crack closure.

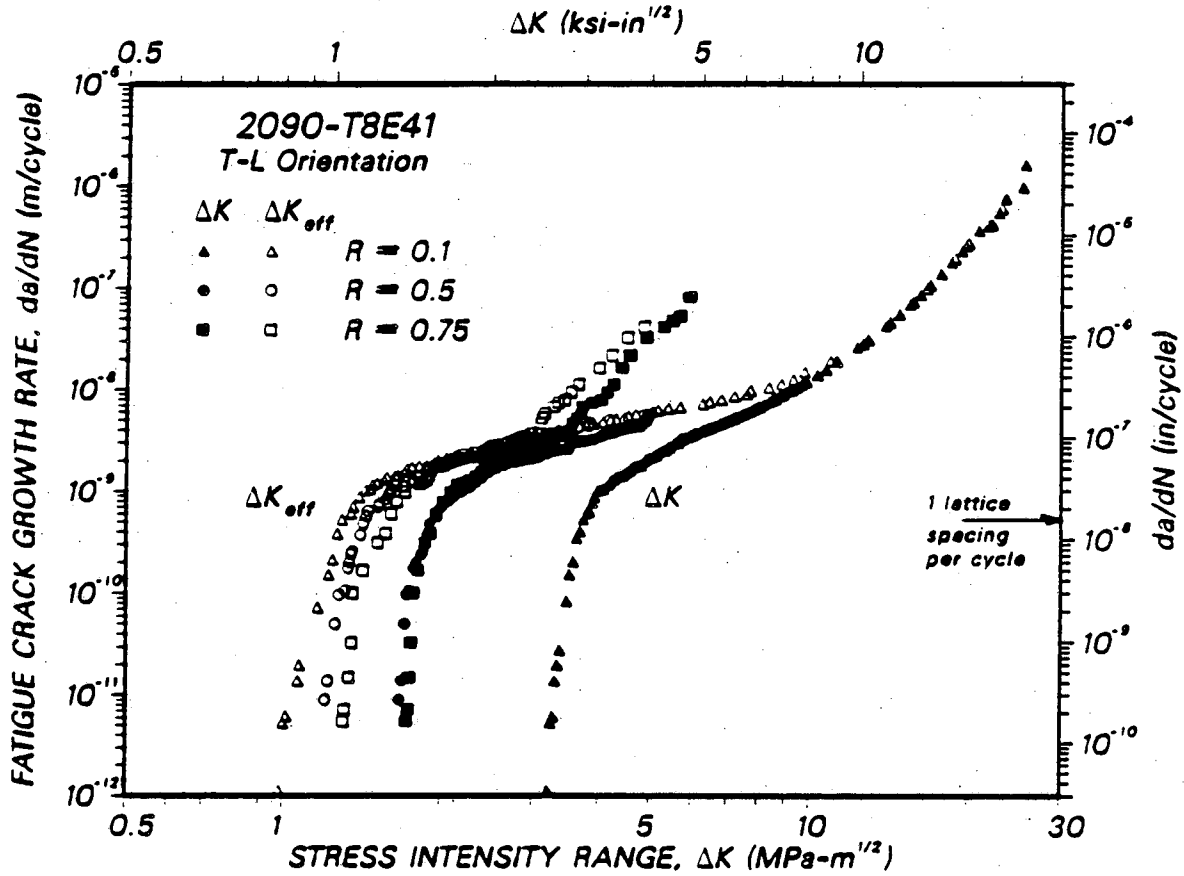

XBL 871-353 A

Fig. 4.5: Effect of load ratio R on the fatigue crack propagation behavior (long cracks) in 2090-T8E41 alloy, plotted as a function of both nominal and effective stress intensity ranges, ΔK and ΔK_{eff}, respectively for the L-T orientation.

T-S and L+45 orientations.

4.3.5 Fractography and Crack Path Morphology

Morphologies of the fatigue fracture surfaces and crack paths for the various alloys (peak aged T8X condition, L-T orientation, R = 0.1) are compared in Fig. 4.6. Qualitatively, surfaces in 2090, 8090 and 2091 are very rough with large transgranular shear facets or asperities, concurrent with highly deflected and zig-zag fatigue crack paths, characteristic of coherent-particle hardened (planar slip) microstructures (11,13,14). Conversely, crack paths are observed to be more or less linear in 8091 and the transgranular fatigue fracture surfaces relatively flat, consistent with lower closure levels and faster crack growth rates.

Although there is some evidence of slight abrasion and corrosion debris, resulting from asperity contact and fretting oxidation, excess oxide film thickness values measured using Auger spectroscopy (15) were of the order of 2-3 nm; a mere 2 % of the computed near-threshold crack opening displacements (Table 4.1), indicating that the contribution to closure from oxide deposits (15-18) is relatively minor in these alloys. Conversely, contributions from crack deflection (18) and the resultant roughness-induced crack closure (19-21) appear to be far more significant, evident from the high lineal roughnesses. Relevant (long) fatigue crack propagation data at near-threshold stress intensities, of all materials in the various conditions are summarized in Table 4.1.

Scanning electron micrographs of the fatigue fracture surfaces imaged at intermediate ΔK levels (5 - 10 MPa$\sqrt{m}$, R = 0.1), typical of the entire range of growth rates at all load ratios, are shown in

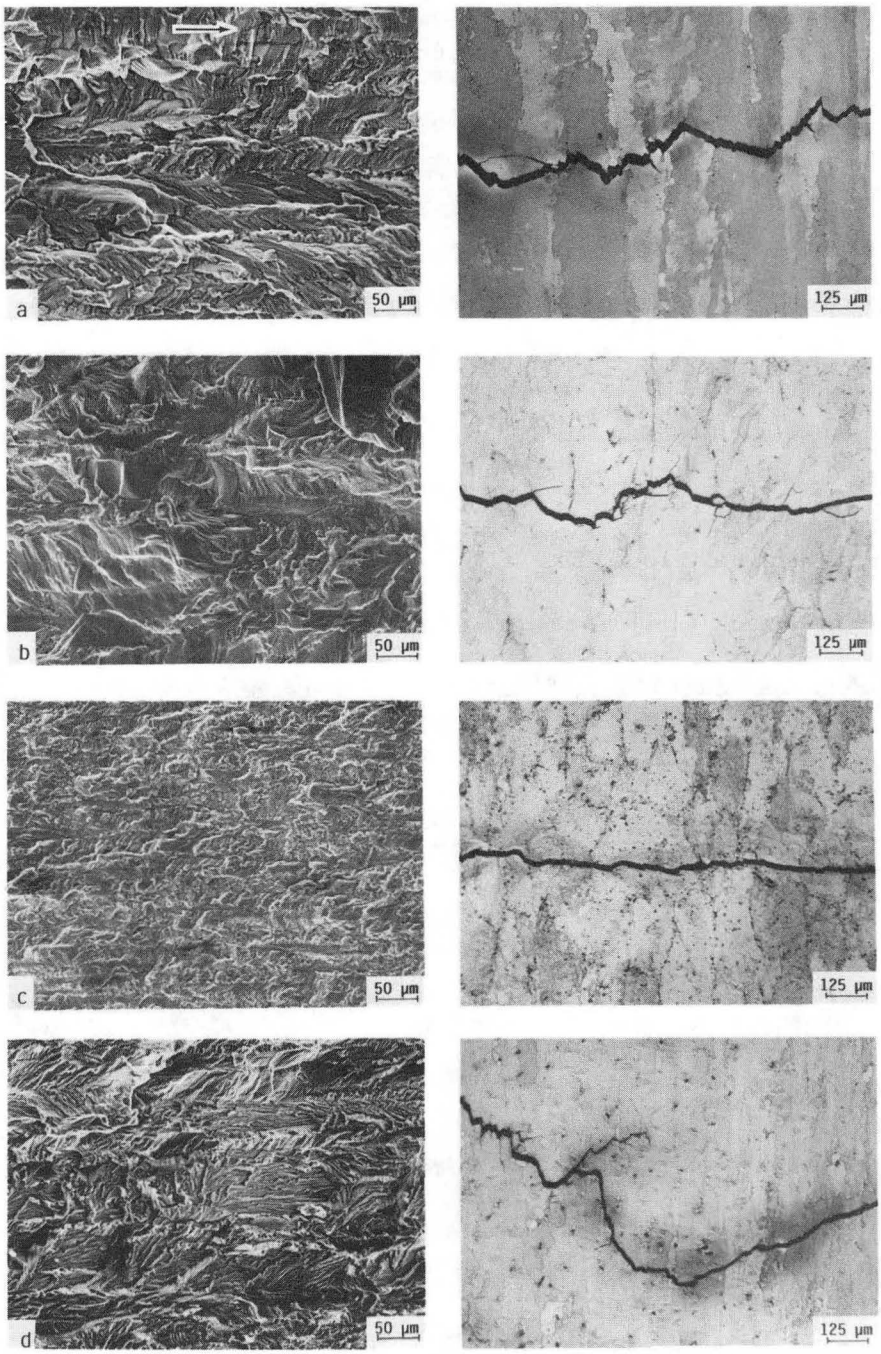

XBB 883-2387A

Fig. 4.6: Scanning electron and optical micrographs of the fatigue fracture surfaces and crack path morhologies, respectively, in the alloys a) 2090-T8E41, b) 8090-T8X, c)8091-T8X and d)2091-T8X. Note the rough surfaces and deflected crack paths in 2090, 2091 and 8090 and the relatively flat surface and linear crack path in 8091. Arrow indicates the general direction of crack growth.

Fig. 4.7 for the various orientations; corresponding crack path profiles are compared in Fig. 4.8. For the L-T and T-L orientations, where growth rates are slower, crack paths are relatively planar but show evidence of local slip-band cracking on the scale of the grain size (Fig. 4.7a,b). As a result, fracture surface morphology is faceted with alternating rough and smooth bands running parallel to the crack growth direction for the L-T and T-L (Fig. 4.8a,b), and normal to the crack growth direction for the T-S (Fig. 4.7d) orientations. However, in the T-S orientation, for all load ratios tested, at longer crack lengths the crack undergoes major ($\sim 90^{o}$) deflection (parallel to the tensile stress axis) to follow an intergranular, delamination-type failure along the rolling plane (Fig. 4.8d). Delamination-type separation parallel to the rolling plane is characteristic of the S-L and S-T orientations (Fig. 4.8e,f); fracture surfaces were smooth and intergranular (Fig. 4.7e,f), and the corresponding crack growth rates faster.

4.4 DISCUSSION

4.4.1 Mechanisms Influencing the Growth Rate Behavior

Present results confirm prior observations (1-9) on the superior fatigue crack growth behavior of commercial aluminum-lithium alloys, over conventional 7XXX and 2XXX aerospace aluminum alloys*. Various arguments such as lower crack opening displacements at a given stress intensity due to improvements in elastic modulus (2), shearable nature

---

* It is to be understood that this conclusion applies exclusively for long ($\gtrsim$ 10 mm) fatigue cracks, as small ($\lesssim$ 1 mm) cracks comparable to the scale of the microstructure or local plasticity can grow at faster rates and such excellence may not be apparent (See Ch. V).

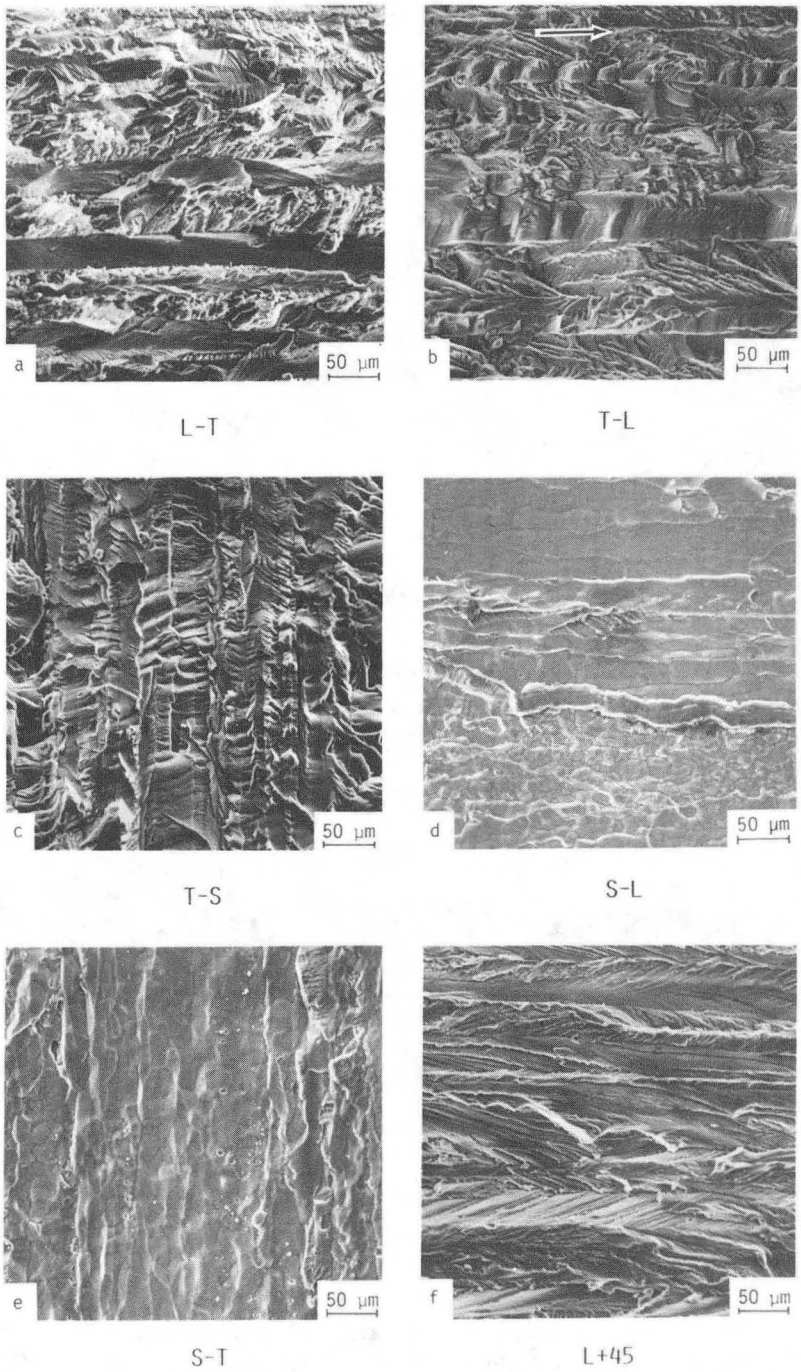

XBB 869-7355A

Fig. 4.7: Scanning electron micrographs of near-threshold fatigue fracture surfaces in 2090-T8E41 alloy, at ΔK levels between 3 and 8 $MPa\sqrt{m}$ ($R = 0.1$), for a) L-T, b) T-L, c) T-S, d) S-L, e) S-T, and f) L+45 orientations. Arrow indicates general direction of crack growth.

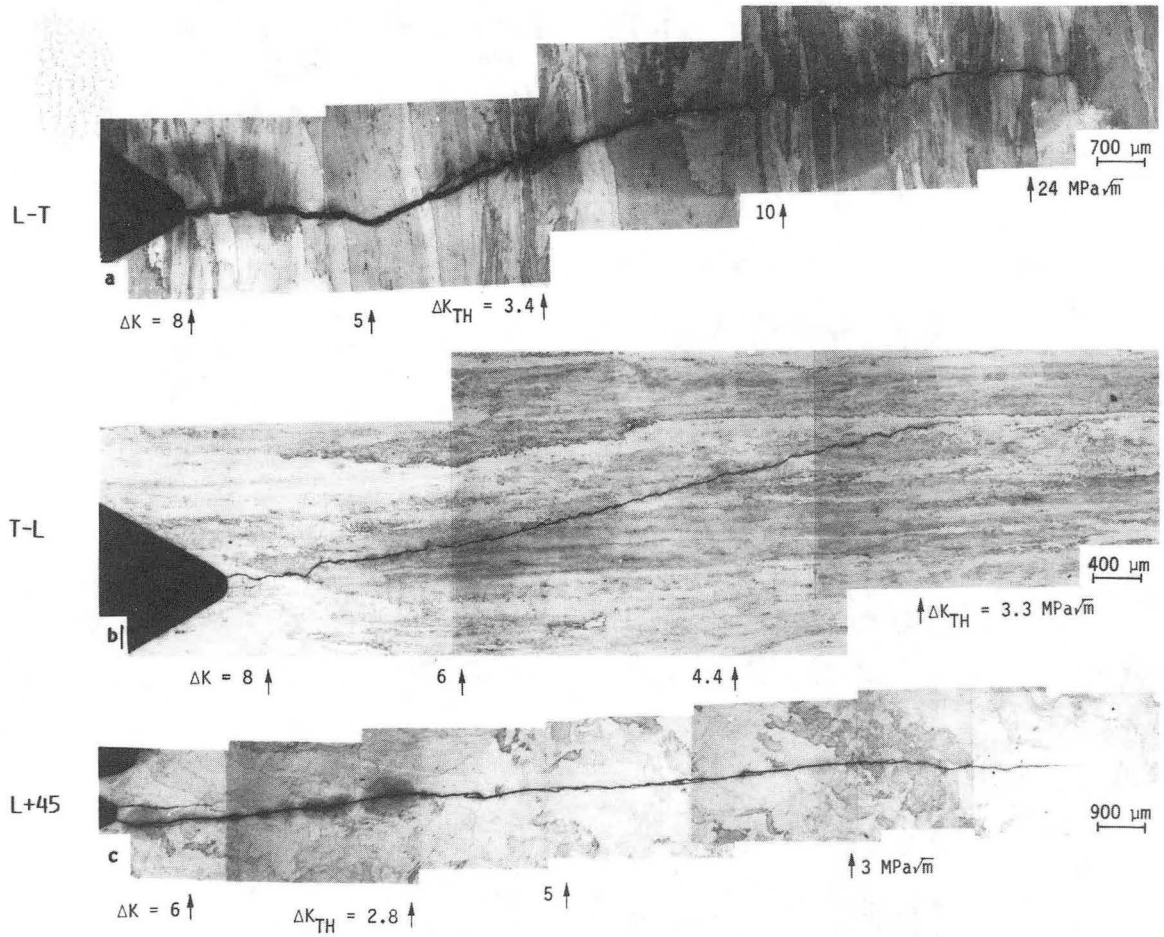

XBB 8610-7944A

Fig. 4.8: Crack path morphology for long crack growth at R = 0.1 in 2090-T8E41 alloy in a) T-L, b) L-T, c) L+45, d) T-S, e) S-L and f) S-T orientations. Profiles are derived from metallographic sections taken perpendicular to the crack surface at the center of the specimen, are typical for all load ratios tested.

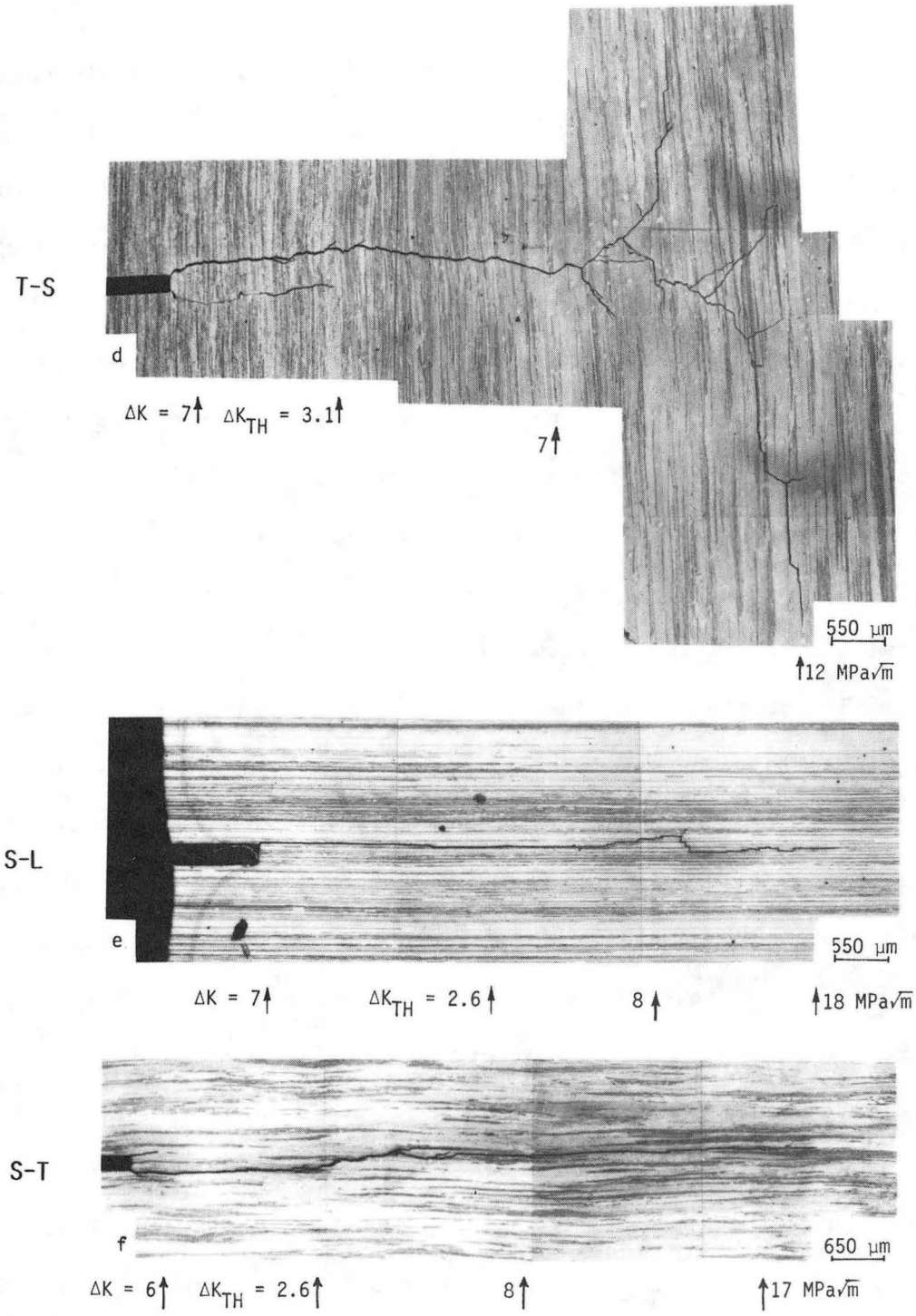

XBB 8610-7946A

of δ′ precipitates which assist reversible slip and reduce the damage ahead of the crack tip (2,3,6) and crack deflection, related closure mechanisms (4,6-9) induced by δ′ precipitates have been put forth to explain the observed excellent long fatigue crack properties of aluminum-lithium alloys. Considering, the high levels of crack closure measured in these materials, observed strong dependence of near-threshold growth rates on the load ratio and the anomalously high small crack growth rates (refer Ch. V), crack closure or what is now referred to as crack tip shielding in fatigue (see Refs. 10,23,24 and Section 1.7) in fatigue appears to be the prominent factor responsible for the excellent long fatigue crack properties.

The prominent mechanisms by which shielding develops in aluminum-lithium alloys, appear to be related to crack branching and deflection, which induce a multiplicative reduction in local stress intensity at the crack tip, and consequent roughness-induced crack closure (Fig. 4.9), where the wedging action of resulting enlarged fracture surface asperities acts to open the crack, thereby reducing the local stress intensity range by effectively raising K_{min} (Fig. 4.10). Such wedge or contact shielding mechanisms predominate, only at low load ratios and low ΔK levels, where the size of the wedge becomes comparable to the crack opening displacements. Shielding due to deflection is expected to be independent of R and ΔK (provided the crack path morphology remains similar) (10,23). In addition, contribution from cyclic plasticity (25) enhances the wedging effect; the role of corrosion debris being relatively minor in these alloys.

As shown in Fig. 4.11, the marked planar slip characteristics of

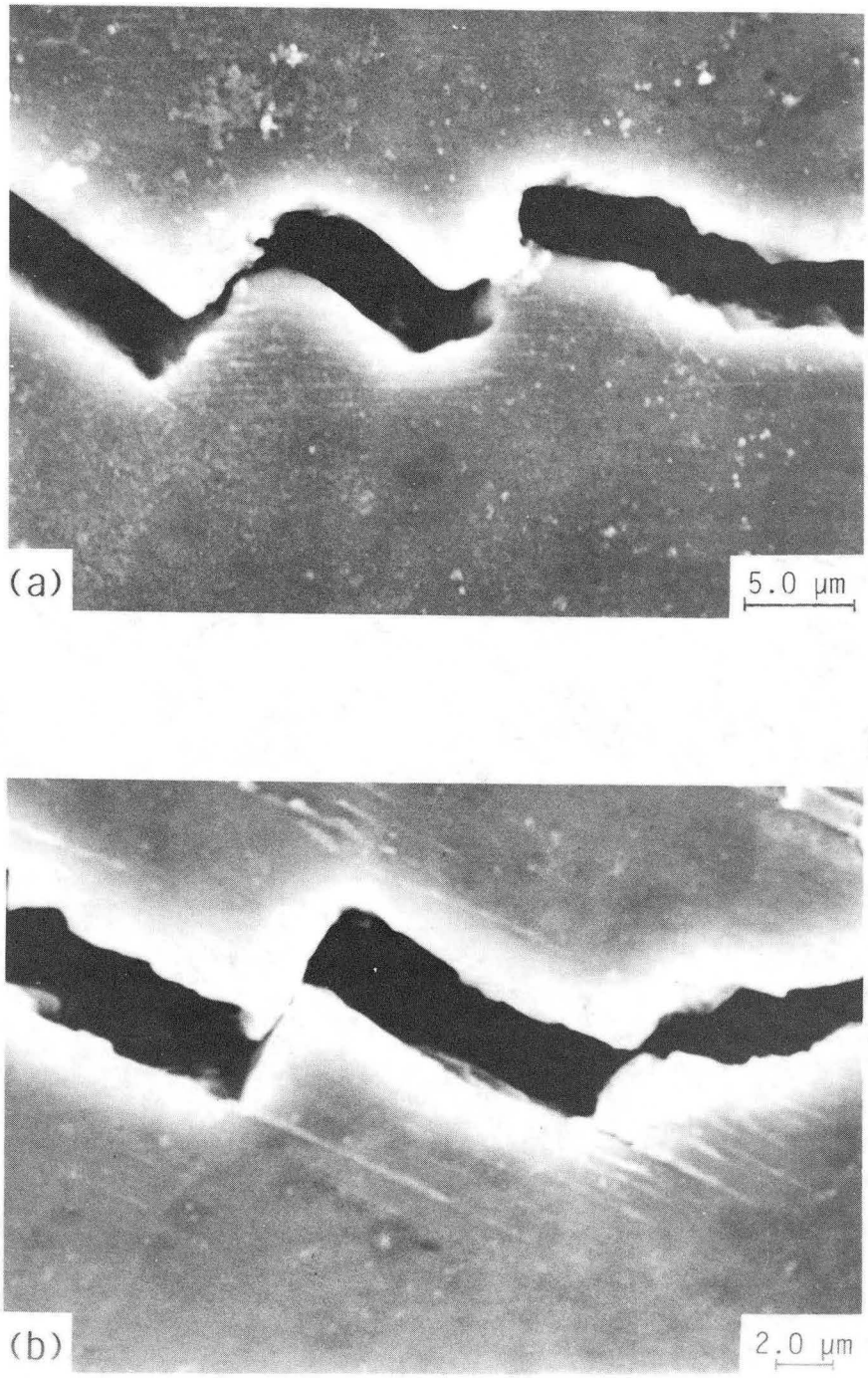

XBB 878-6961A

Fig. 4.9: Meandering fatigue crack paths and resultant wedging of fracture surface asperities combined with crack tip plasticity are the predominant mechanisms by which aluminum-lithium alloys develop superior (long) fatigue crack properties. Micrograph obtained on the specimen surface for 2090-T8E41. Arrow indicates the general direction of crack growth.

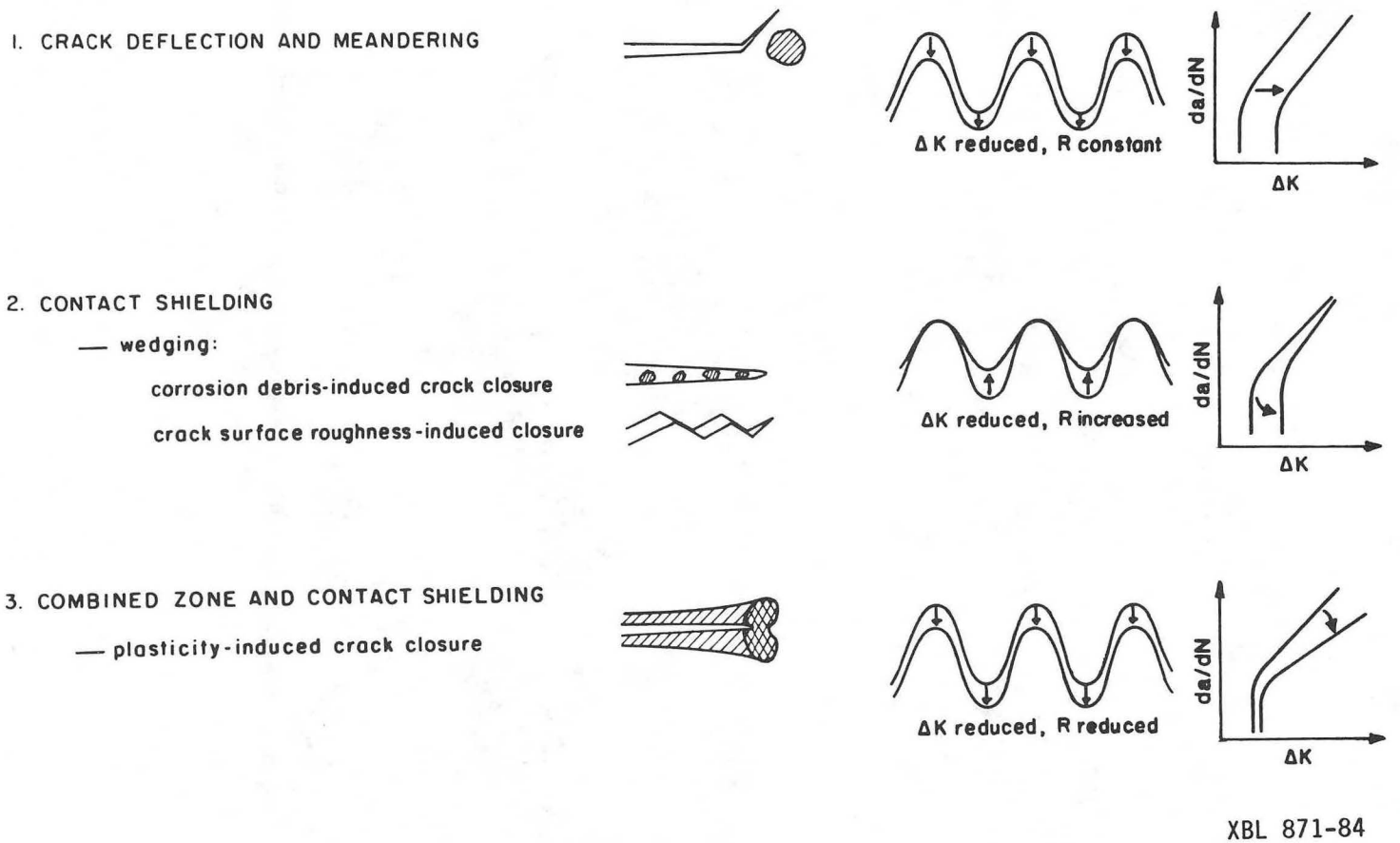

Fig. 4.10: Schematic illustration of crack tip shielding in aluminum-lithium alloy 2090-T8E41, showing primary mechanisms and their consequences to crack growth behavior.

aluminum-lithium alloys can induce crystallographic crack growth, with cracking along slip bands. This is clearly seen as either macroscopic crack branching, where the entire crack deviates at an angle ($\sim 45^{o}$) away from the plane of maximum tensile stresses (Fig. 4.11a, 2090-T8E41, L-T orientation), or faceted crack growth, where the crack "zig-zags" along the principal stress plane (Fig. 4.11b). In addition, deflection can also occur due to linkage between intergranular delaminations, all of which act to promote closure in aluminum-lithium alloys. Crystallographic texture and coarse, unrecrystallized grain structures further accentuate these effects and render the properties to be sensitive to plate orientation.

Although, such crystallographic crack growth and benefits of shielding are not uncommon during fatigue crack growth in age-hardened aluminum alloys (11,13,14), their role is limited to near-threshold growth rate regimes. In the case of Al-Li alloys, the attainable levels of crack closure are much higher and are maintained over higher ΔK levels, accounting for the much slower growth rates compared to traditional aluminum alloys. For example, K_{cl} values may approach as high as 90 % of the applied maximum stress intensity at near-thresholds, and are sustained to over 50 %, even at ΔK levels of 10 $MPa\sqrt{m}$, as seen for alloy 2090-T8E41 in the L-T orientation.

4.4.2 Influence of Plate Orientation

However, the degree to which cracks deflect in the various orientations, greatly dictates the anisotropy in crack growth rates. Thus, the fastest growth rates (and low levels of shielding) are expected in the short transverse, S-L and S-T orientations, where the

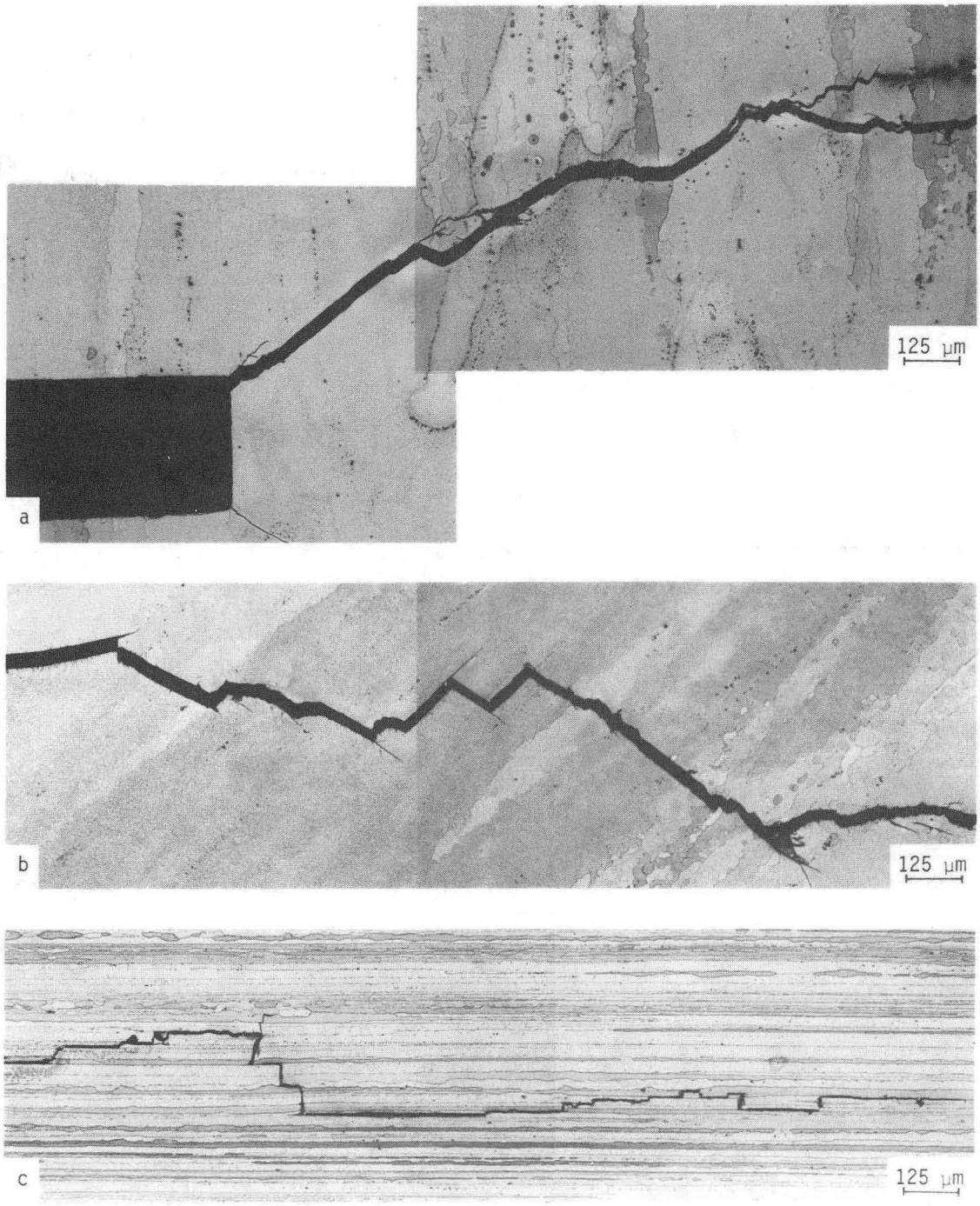

XBB 869-7356A

Fig. 4.11: Types of crack path meandering during fatigue crack propagation in 2090-T8E41 alloy, showing a) macroscopic crack branching in the L-T orientation, b) microscopic crack deflection (crystallographic slip-band cracking) in L+45 orientation, and c) intergranular delamination-type cracking in S-L orientation.

unrecrystallized elongated grain structure provides a weak path along the grain boundaries, with little deflection. Conversely, the slowest crack growth rates (high shielding levels) are seen in the L-T, T-L and T-S orientations, where cracks undergo significant crystallographic crack deflection and delamination normal to the crack plane. Behavior is thus analogous to an aligned composite (26,27), as the planes of weakness oriented perpendicular to the short-transverse direction benefits crack growth properties normal to these planes (by shielding), as observed for the fracture toughness alike.

4.4.3 Load Ratio Effects

The observed increase in the near-threshold fatigue crack growth rates with increase in R, is generally consistent with a diminished effect of closure at high load ratios, specifically from crack wedging mechanisms (10). In fact, by plotting the growth rate data in terms of ΔK_{eff} (after allowing for closure), the variation in da/dN with load ratio is much reduced (Fig. 4.5). Accordingly, the superior fatigue properties of Al-Li alloy 2090, so clearly apparent when compared at R = 0.1, appear to be partially compromised when evaluated at R = 0.75 (Fig. 4.12). Besides the observed ranking in materials, with respect to fatigue resistance, is expected to be quite different when evaluated under tension-compression (R = -1) loading, since the compression portion of the cycle acts to annul the benefits of wedge shielding mechanisms.

4.4.4 Microstructural Effects

Qualitatively, materials which show the highest levels of crack closure, concurrently show slower crack growth rates and vice versa.

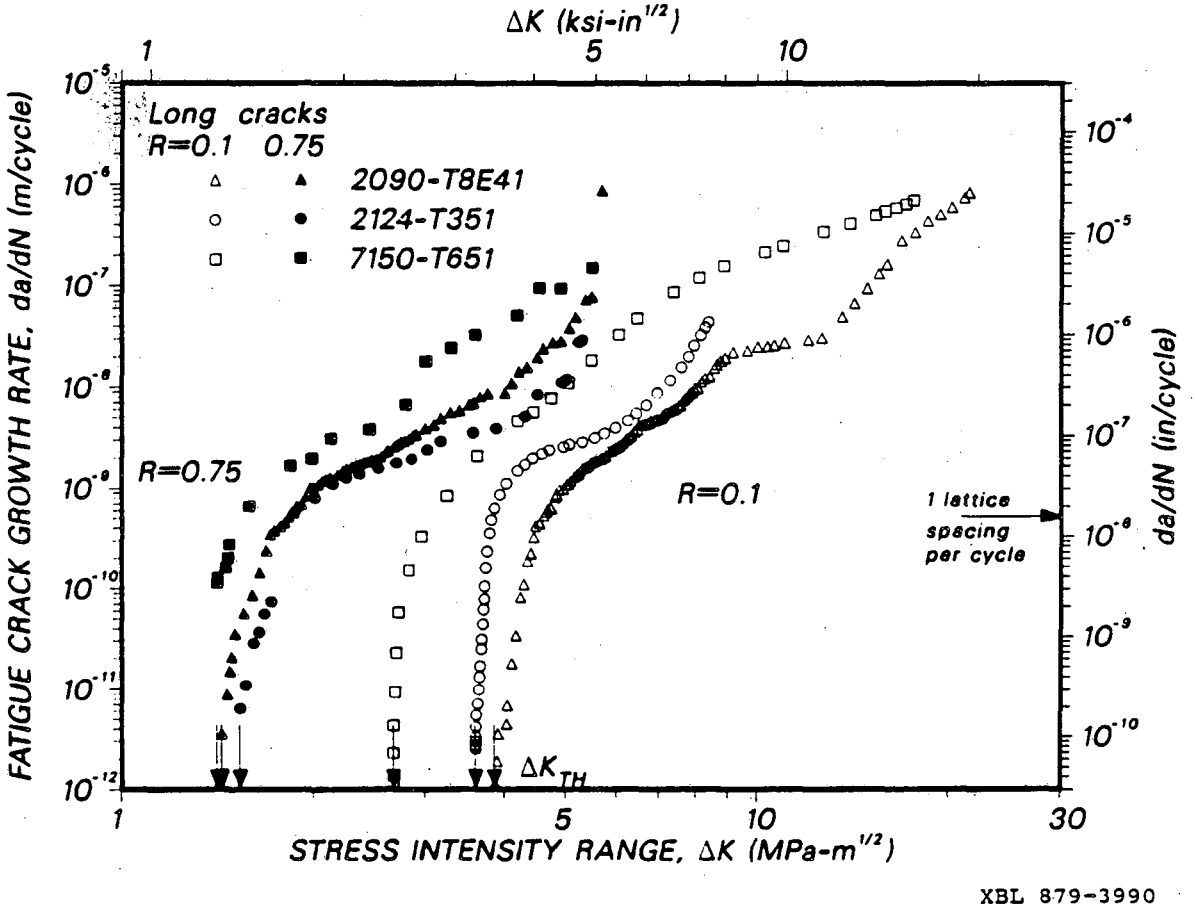

Fig. 4.12: Comparison of the fatigue crack growth rates of long cracks in Al-Li alloy 2090-T8E41 and traditional alloys 2124-T351 and 7150-T651 at R = 0.1 and 0.75. Note that the behavior of 2090 is no longer optimal. Data for 2124 and 7150 taken from ref.s 10,11.

Accordingly, recharacterizing the crack propagation data in terms of the closure corrected effective driving force, ΔK_{eff} (Fig. 4.13) rationalizes most of the observed differences with respect to microstructure and composition.

This should not to be seen to imply that alloy chemistry and microstructure are unimportant to fatigue in Al-Li alloys, since it is the microstructure which affects crack deflection, which in turn promotes crack closure. In fact, three microstructural sources of crack deflection can be identified in these alloys. First, the strong deformation texture in commercial alloys, which in unrecrystallized alloys persists from pre-aging stretch, often causes crack growth at odd angles to the plane of maximum tensile stress (macroscopic branching). Second, poor short-transverse properties, resulting from anisotropic grain structures and weakened grain boundaries due to grain boundary precipitates, segregation of Fe-, Cu-rich constituent particles and possible Na, K embrittlement can lead to intergranular crack deflection; depending upon orientation this leads to crack-arrester deflections or crack-divider delaminations. Third, and most importantly, the copius intragranular precipitation of δ', θ', T_1 and S' precipitates, which produces marked planarity of slip, induces crystallographic, zig-zag crack paths as shown in Figs. 4.9 and 4.10b. Accordingly, with extensive grain boundary precipitation and associated formation of PFZs, as for example in 8091-T8X, the degree of crack deflection and hence the extent of crack closure, is substantially reduced, with the result that crack growth rates are significantly faster. Overall, underaged microstructures of all

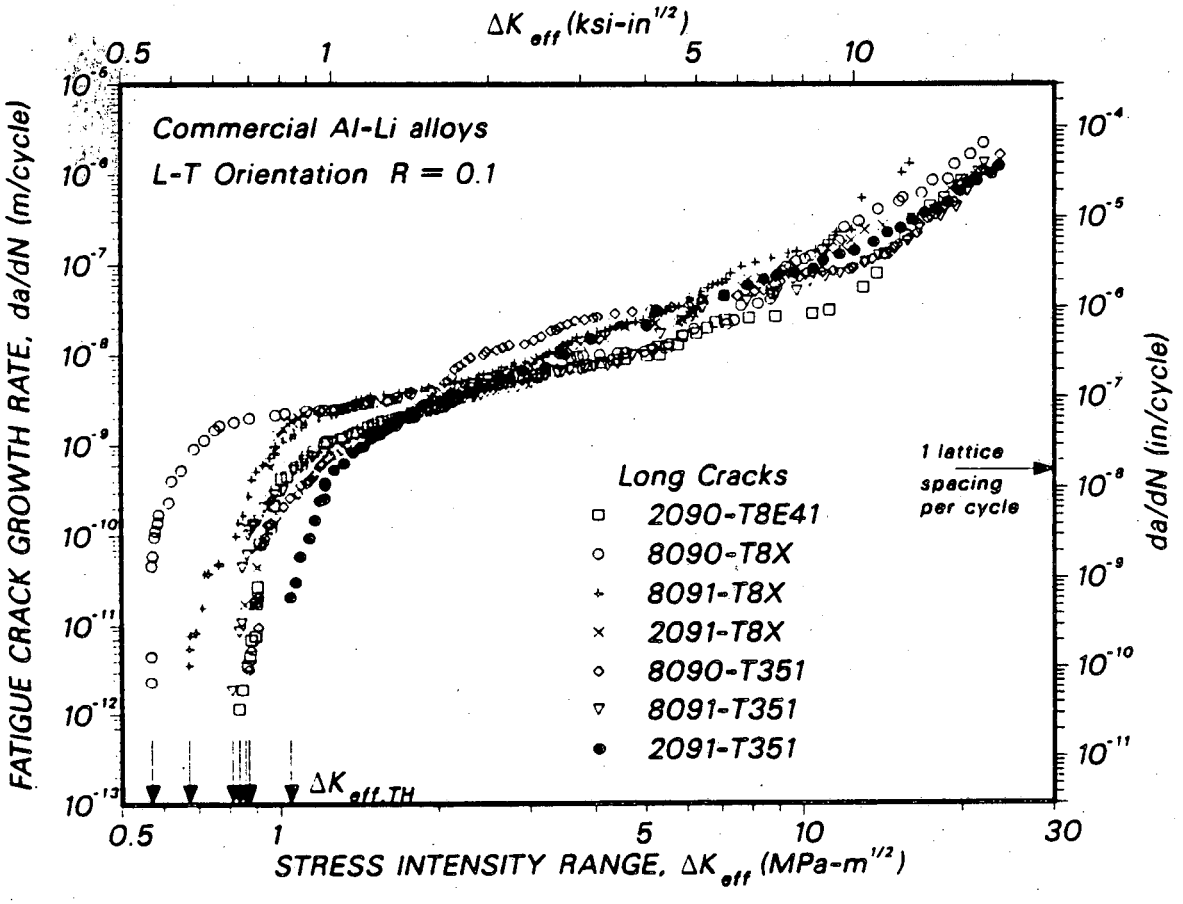

Fig. 4.13: Fatigue crack growth rates in the various commercial aluminum-lithium alloy microstructures characterized in terms of the effective stress intensity range, ΔK_{eff}, after correcting for crack closure. Note that the observed differences are greatly reduced (see Fig. 4.3a).

materials, including 2090 (28), show better fatigue resistance over the peak aged, concurrent with the enhanced crack deflection promoted by planar slip; 2091 is the only exception similar to observations on the fracture toughness behavior.

4.5 CONCLUSIONS

Based on the above study on the crack propagation and crack closure behavior of long ($\gtrsim$ 10 mm) fatigue cracks in commercial plates of aluminum-lithium alloys, the following conclusions can be made:

1. Rates of fatigue crack growth in commercial Al-Li alloys were found to be generally superior to those in 2124 and 7150 aluminum alloys (over the entire spectrum of da/dN from 10^{-12} to 10^{-6} m/cycle), despite having 30 % higher strength. The behavior was primarily associated with highly deflected and branched crack paths, which promote significant crack tip shielding from crack deflection and consequent closure due to premature contact of the mating fracture surfaces.

2. In general, naturally aged (T351) tempers of all lithium-containing aluminum alloys, excepting 2091, exhibit optimal (long crack) fatigue properties, consistent with improved levels of shielding. Although extensive grain boundary precipitation and resultant formation of δ'-precipitate free zones in peak aged 8091 was responsible for the faster growth rates and low shielding levels, other materials in peak temper still show optimal fatigue properties.

3. Fatigue crack growth rates in 2090, plotted as a function of the nominal stress intensity range ΔK, show large mean stress effects, consistent with the high closure levels at low R. By plotting as a

function of the effective stress intensity ΔK_{eff} (after correcting for closure), the load ratio dependence of growth rates is significantly diminished. Accordingly, the remarkable long fatigue properties of 2090 may not be apparent, when compared at R = 0.75.

4. Fatigue crack growth and closure behavior in commercial Al-Li alloys in general, and 2090-T8E41 in particular, was found to be highly anisotropic, with growth rates varying by up to 4 orders between various orientations. The fastest growth rates (and associated lowest levels of closure), are observed where crack extension occurs parallel to the rolling plane (S-L and S-T orientations); the slowest growth rates (with the highest levels of closure), conversely are observed where crack extension is perpendicular to the rolling plane (L-T, T-L and T-S orientations).

5. Marked differences observed in the growth rates with respect to plate orientation in 2090-T8E41, are also attributed to differences in crack tip shielding from crack deflection and closure, arising from differences in the crack path morphology. Unrecrystallized, elongated grain structures promote delamination failures in the S-L and S-T orientations, with little shielding. In contrast, significant shielding is developed for crack extension perpendicular to the rolling plane (L-T, T-L, T-S), which is primarily crystallographic with evidence of microscopic deflection and macroscopic branching.

4.6 REFERENCES

1. J. Glazer, S. L. Verzasconi, E. N. C. Dalder, W. Yu, R. A. Emigh, R. O. Ritchie, and J. W. Morris: Adv. Cryog. Eng., 32 (1986), p. 397.

2. E. J. Coyne, T. H. Sanders, and E. A. Starke: in 'Aluminum-Lithium Alloys', T. H. Sanders and E. A. Starke (eds.), TMS-AIME, Warrendale, PA (1981), p. 293.

3. S. J. Harris, B. Noble, and K. Dinsdale: in 'Aluminum-Lithium Alloys II', T. H. Sanders and E. A. Starke (eds.), TMS-AIME, Warrendale, PA, (1983), p. 219.

4. A. K. Vasudevan, P. E. Bretz, A. C. Miller, and S. Suresh: Mat. Sci. Eng., 64 (1984) p. 113.

5. G. R. Chanani, G. V. Scarich, and K. M. Bresnahan: in 'Mechanical Properties and Phase Transformations in Engineering Materials', S. D. Antolovich, R. O. Ritchie, and W. W. Gerberich (eds.), TMS-AIME, Warrendale, PA (1986), p. 271.

6. K. V. Jata and E. A. Starke: Metall. Trans. A, 17A (1986), p. 1011.

7. J. Petit, S. Suresh, A. K. Vasudévan, and R. C. Malcolm: in 'Aluminum-Lithium Alloys III', C. Baker, P. J. Gregson, S. J. Harris and C. J. Peel (eds.), Institute of Metals, London, U.K. (1986), p. 257.

8. M. Peters, K. Welpmann, W. Zink, and T. H. Sanders: in 'Aluminum-Lithium Alloys III', C. Baker, P. J. Gregson, S. J. Harris and C. J. Peel (eds.), Institute of Metals, London, U.K. (1986), p. 239.

9. W. Yu and R. O. Ritchie: J. Eng. Mat. Technol., Trans. ASME, Series H, 109 (1987), p. 81.

10. R. O. Ritchie and W. Yu: in 'Small Fatigue Cracks', R. O. Ritchie and J. Lankford, eds., TMS-AIME, Warrendale, PA (1986), p. 167.

11. E. Zaiken and R. O. Ritchie: Mat. Sci. Eng., 70 (1985), p. 151.

12. R. O. Ritchie: Intl. Metals Reviews, 20 (1979), p. 205.

13. S. Suresh, A. K. Vasudévan, and P. E. Bretz: Metall. Trans. A, 15A (1984), p. 369.

14. R. D. Carter, E. W. Lee, E. A. Starke, and C. J. Beevers: ibid., p. 555.

15. S. Suresh and R. O. Ritchie: Scripta Metall., 17 (1983), p. 575.

16. A. T. Stewart: Eng. Fract. Mech., 13 (1980), p. 463.

17. S. Suresh, G. F. Zamiski, and R. O. Ritchie: Metall. Trans. A, 12A (1981) p. 1435.

18. S. Suresh: ibid., 14A (1983) p. 2375.

19. N. Walker and C. J. Beevers: Fat. Eng. Mat. Struct., 1 (1979), p. 135.

20. K. Minakawa and A. J. McEvily: Scripta Metall., 6 (1981), p. 633.

21. S. Suresh and R. O. Ritchie: Metall. Trans. A, 13A (1982), p. 1627.

22. C. F. Shih: J. Mech. Phys. Solids, 29 (1981), p. 305.

23. R. O. Ritchie, R. H. Dauskardt and R. M. Cannon: Lawrence Berkeley Laboratory Report No. LBL-20656, University of California, Berkeley, 1986.

25. S. Suresh and R. O. Ritchie: in 'Fatigue Crack Growth Threshold Concepts', D. L. Davidson and S. Suresh (eds.), TMS-AIME, Warrendale, PA (1984), p. 227.

26. R. O. Ritchie and S. Suresh: Metall. Trans. A, 13A (1982), p. 937.

27. J. D. Embury, N. J. Petch, A. E. Wraith and E. S. Wright: Trans. Met. Soc. AIME, 239 (1967), p. 114.

28. H. L. Leichter: J. Spacecraft, 3 (1966), p. 1113.

29. K. T. Venkateswara Rao: University of California, Berkeley (work in progress)

CHAPTER V

FATIGUE CRACK GROWTH: SMALL CRACKS

5.1 INTRODUCTION

Reliability of safety-critical components and structures is of prime importance for modern aerospace applications. This is generally assessed using fracture mechanics-based methodologies, wherein, flaws are assumed to pre-exist from the initial loading cycle, and the lifetime of the structure estimated as the number of cycles to grow such a flaw to failure. By integrating, the experimental growth rate (da/dN) response of fatigue cracks plotted as a function of the stress intensity range (ΔK) in a given microstructure under representative environmental and loading conditions, from initial to final crack sizes, these lifetimes may be computed (1).

Although the approach is considered to be inherently conservative, as the crack initiation life is assumed to be zero, problems can arise from the "anomalous" behavior of small cracks ($\lesssim$ 1 mm), which approach the dimensions of the microstructure or local plasticity (2). Such small cracks are known to propagate at ΔK levels well below the fatigue threshold, ΔK_{TH}, below which fatigue cracks are presumed dormant, and in general to grow at rates far in excess of long ($\gtrsim$ 10 mm) cracks at the same (nominal) stress intensity range (2-7). As a result, there exists a strong potential for dangerously non-conservative life predictions, since damage-tolerant lifetime calculations are almost invariably based on long crack data.

Advanced aluminum-lithium alloys are of particular interest in

this regard, as despite their unquestionable superior (long) fatigue crack growth properties over traditional high-strength aluminum alloys (8-14), there are serious doubts concerning their resistance to small fatigue cracks (15,16). In view of the significance of the "small crack" effect in potential airframe and fuel tank materials, the objective of the present chapter is to examine the growth rate characteristics of naturally-occurring, microstructurally-small (2-1000 μm), surface cracks in a series of commercial aluminum-lithium alloys, and compare such behavior with that observed (17) in traditional high-strength 2124 and 7150 aluminum alloys.

5.2 EXPERIMENTAL DETAILS

Smooth rectangular bend samples of Al-Li alloys, 2091 and 8091 and traditional alloys, 2124 and 7150 were tested in various tempers (L-T orientation) using replication techniques (see Ch. II for details). Small crack growth resistance of 2090 was evaluated in the T8E41 temper for the L-T, T-L and T-S orientations. Cracked specimens and acetate replicas were subsequently examined in the scanning electron microscope.

5.3 RESULTS

5.3.1 Behavior in 2090-T8E41

The fatigue crack growth rate behavior of microstructurally-small (2 to 1000 μm) surface cracks in 2090-T8E41 (R = 0.1) is plotted in Fig. 5.1 as a function of crack length (i.e., depth of the surface flaw) for the L-T, T-L and T-S orientations. It is seen that cracks as small as 2 μm can grow at rates exceeding 10^{-10} m/cycle without any

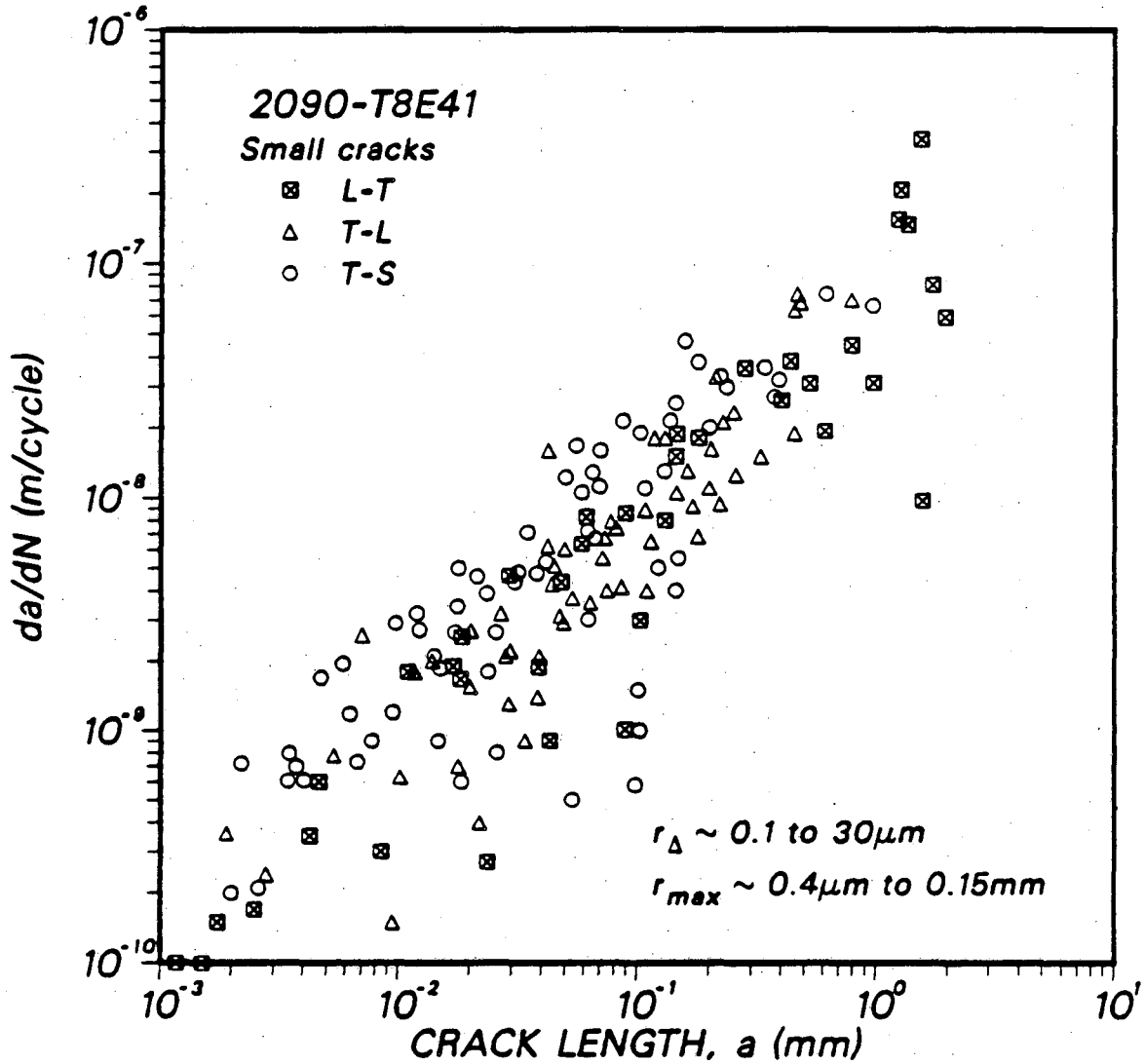

XBL 8610-3624

Fig. 5.1: Variation in the growth rates, da/dN, of small (2 to 1000 μm) surface fatigue cracks in 2090-T8E41 as a function of crack length, a, at R = 0.1. Data are plotted for the L-T, T-L and T-S orientations, based on replication measurements on SEN(B) specimens.

clear effect of plate orientation.

The above data on small cracks, now replotted as a function of ΔK, are compared with long crack results from the previous chapter, in Fig. 5.2. Clearly, there is significant scatter in the small crack results, although this is to be expected as growth rates are measured below continuum levels, and reflect local variations in the crack velocity as it encounters various microstructural features. However, at the same ΔK, growth rates for small cracks exceed those of long cracks, similar to behavior reported in other material systems (2-7,15-17). The effect becomes most pronounced with decreasing growth rates, such that at near-threshold levels, the propagation rates of small cracks can be upto 2-3 orders of magnitude faster than long cracks. Furthermore, they continue to propagate at ΔK levels less than 1 MPa$\sqrt{m}$, without any apparent sign of an intrinsic threshold.

5.3.2 Aluminum-Lithium Alloys 2091 and 8091

Corresponding growth rate properties of small cracks in 2091 and 8091 are shown in Fig. 5.3. Results for the T351 and T8X tempers of 2091 (Fig. 5.3a) and T351 temper of 8091 (Fig. 5.3b) are plotted as a function of ΔK and are compared with long crack data. Behavior appears essentially similar to 2090-T8E41, in that small cracks grow at rates far faster than long cracks at equivalent near-threshold stress intensity levels, and further continue to propagate at stress intensities as low as 0.7 MPa$\sqrt{m}$, well below the long crack threshold ΔK_{TH}.

Notably, unlike long crack behavior, small cracks in 2091 (Fig. 5.3a) tend to be far less sensitive to microstructure. For

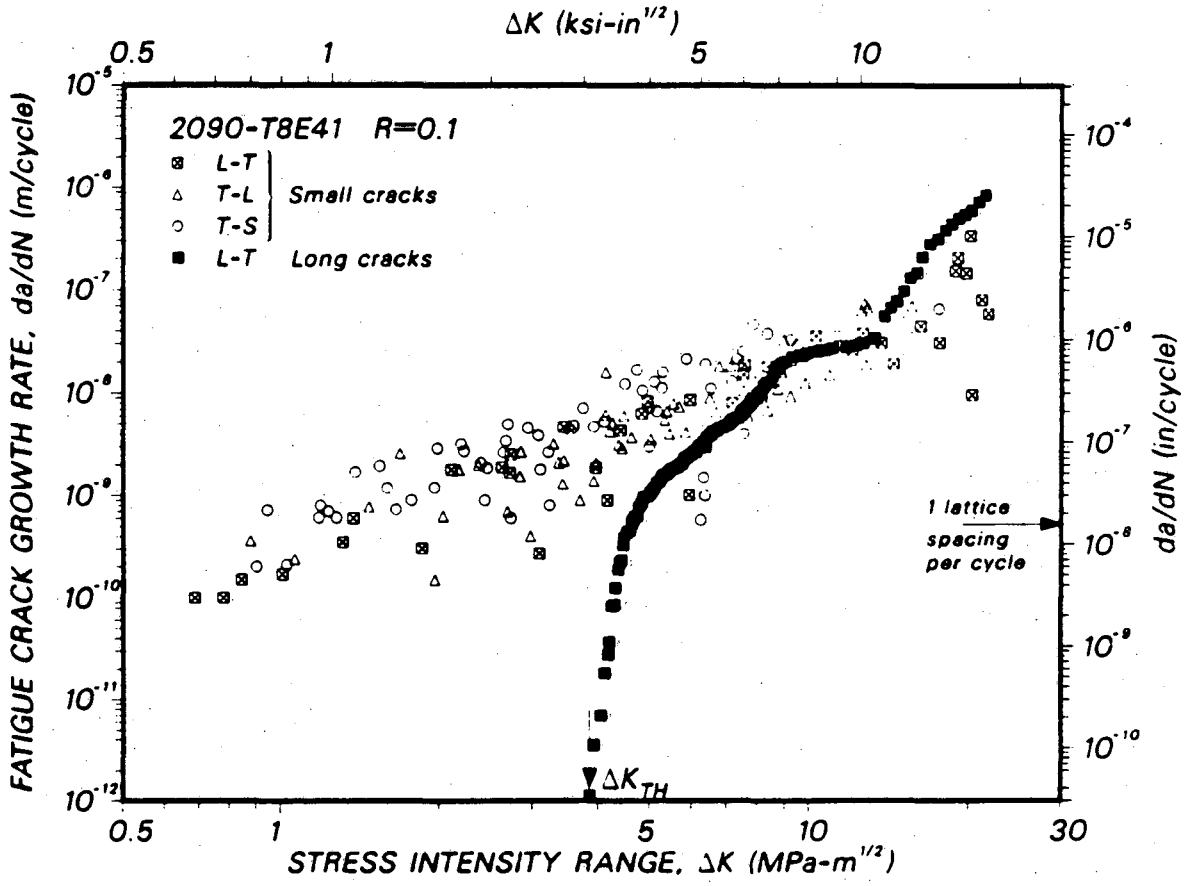

XBL 871-3199 A

Fig. 5.2: Comparison of the growth rates of long (≳ 10 mm) and small (2 to 1000 μm) fatigue cracks for the L-T, T-L and T-S orientations in 2090-T8E41 as a function of the nominal stress intensity range, ΔK (R = 0.1).

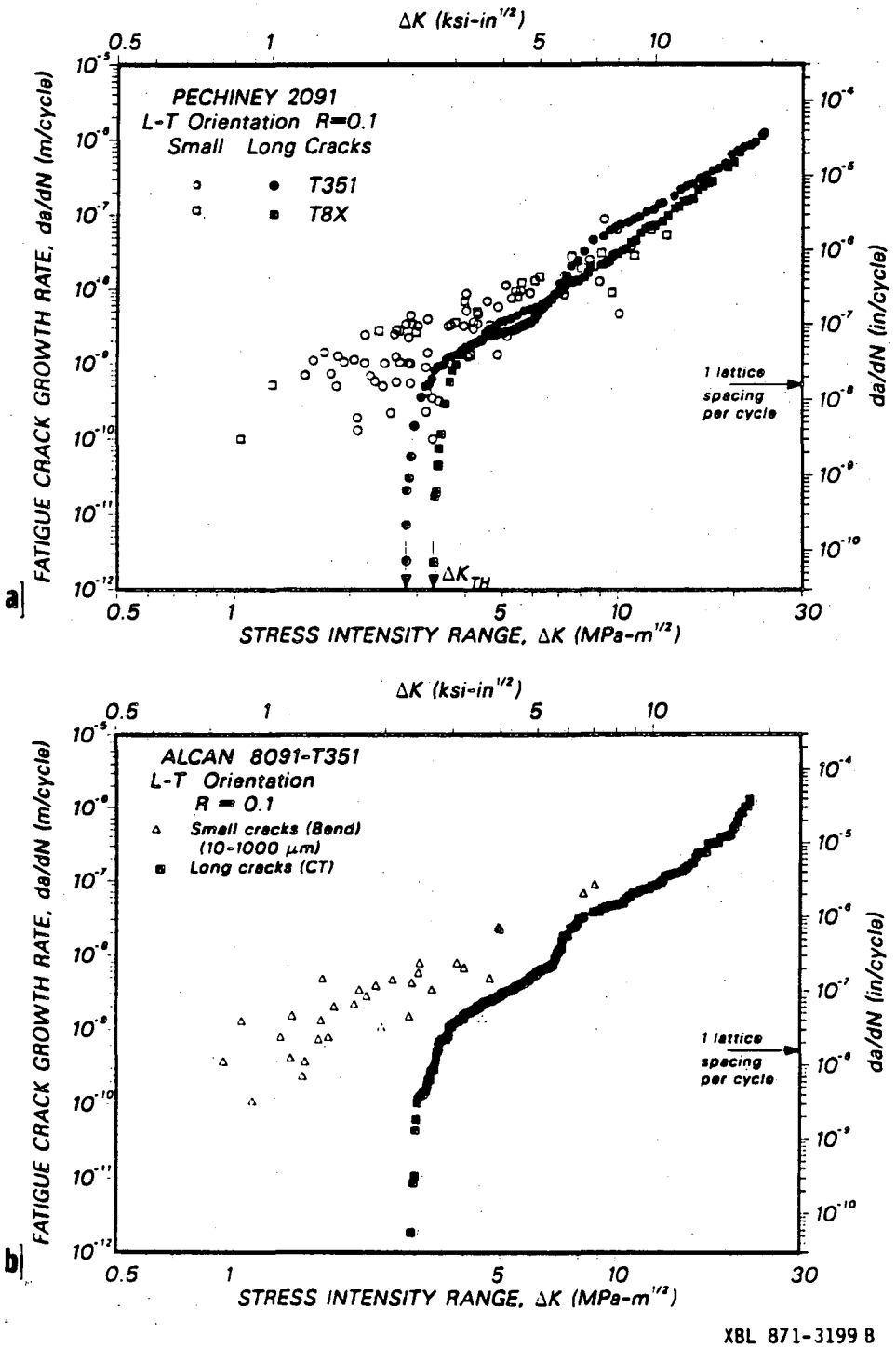

Fig. 5.3: Behavior of small (2-1000 μm) fatigue cracks in a) underaged (T351) and peak aged (T8X) microstructures of Pechiney-2091 and b) underaged Alcan-8091 (L-T orientation, R = 0.1). Corresponding long (≳ 10 mm) crack results are also plotted.

example, the distinctly superior crack growth properties of the peak aged microstructures, which are clearly observed for long cracks (see Ch. IV), are simply not evident in the small crack results.

Nucleation of these incipient, microstructurally-small fatigue cracks is seen to occur along slip bands, preferentially at the local heterogeneities in the microstructure, namely, Fe-Cu rich inclusions, constituent phases or second phase particles (Fig. 5.4). Subsequent crack growth is highly crystallographic, as the crack meanders along intersecting slip bands or deflects as it encounters grain boundaries, or other microstructural barriers. However, with increasing crack lengths, and as a result increasing ΔK levels, they presumably start developing closure, due to which the growth rate behavior ultimately approaches that of a long crack.

5.3.3 Small Cracks in 2124 and 7150

Growth rate response of small fatigue cracks in traditional alloys 2124 and 7150 in the different tempers is shown in Fig. 5.5. General observations are identical to those noted above for the lithium-containing alloys, i.e., anomalously high growth rates for small cracks without any apparent effect of microstructure. However, small cracks do tend to show a decreasing tendency for crack deflection with increased aging times, similar to observations for long cracks. In addition, in view of the generally superior long crack properties of aluminum-lithium alloys, the discrepancy between long and small crack growth rates in these materials may be lower.

5.4 DISCUSSION

It is concluded from the previous chapter, that the fatigue

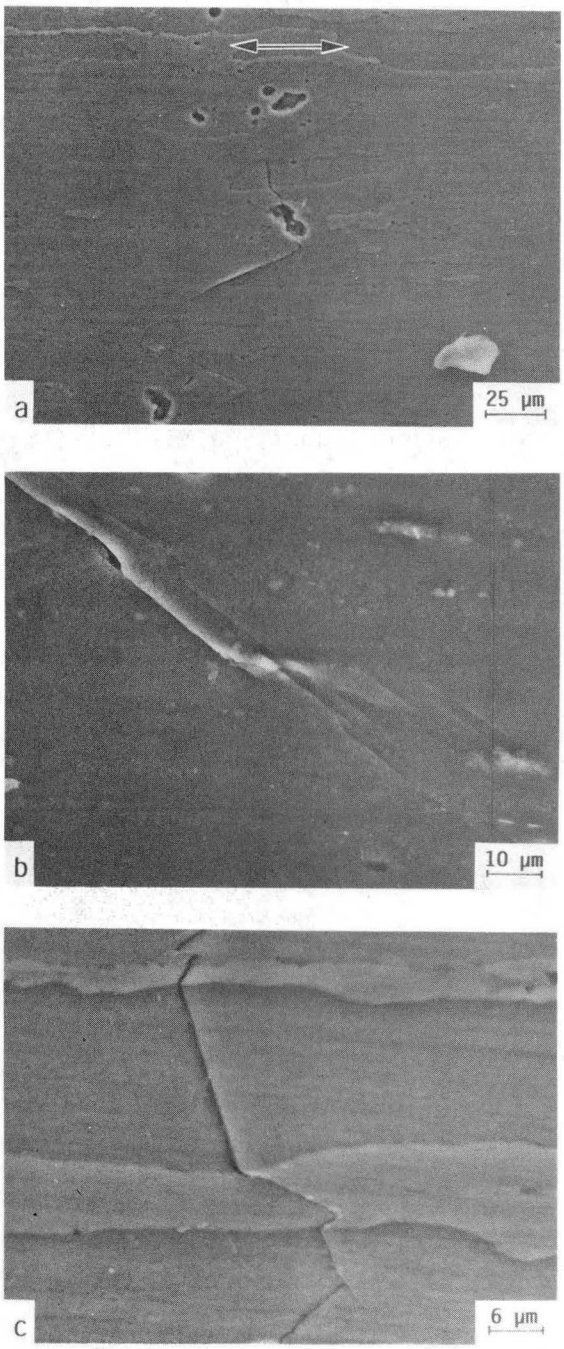

XBB 885-4510A

Fig. 5.4: Growth morphology of small surface fatigue cracks. a) Crack initiation near Fe-Cu rich inclusions, b) subsequent growth following slip band cracking and c) frequent crack deflection at the grain boundaries. Micrographs obtained by scanning electron microscopy of the gold-coated acetate replicas of specimen surfaces in 2091-T351. Arrow indicates the direction of applied stresses.

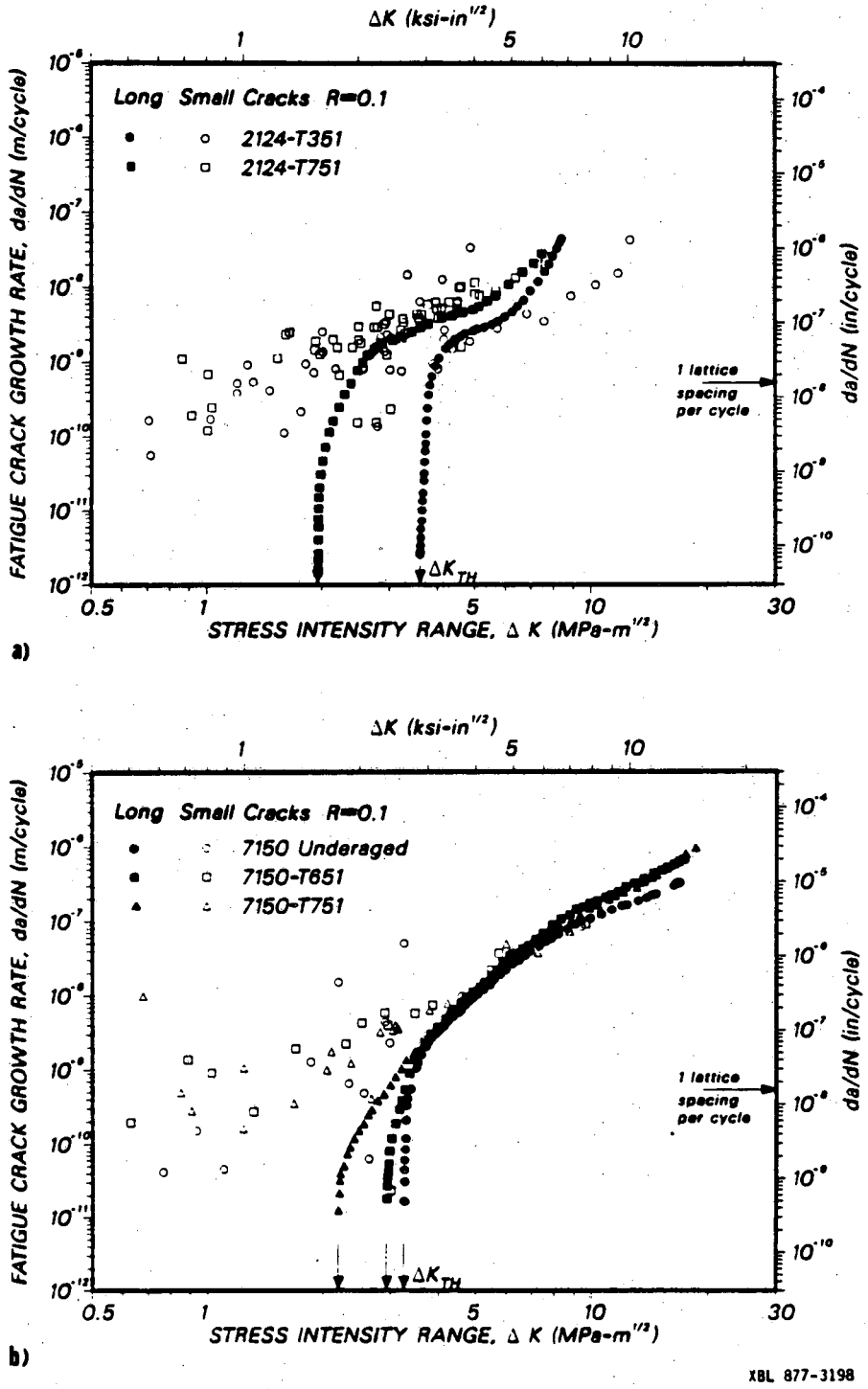

Fig. 5.5: Comparison of long (≳ 10 mm) and small (2-1000 μm) fatigue crack growth rate behavior (at R = 0.1) in a) underaged (T351) and overaged 2124 alloy, and b) underaged, peak aged (T651) and overaged (T751) 7150 alloy.

behavior of long cracks is strongly influenced by crack closure (and crack deflection) mechanisms, particularly at lower growth rates below typically 10^{-8} m/cycle. Crack closure and deflection as alluded to in earlier chapters, represent a general class of toughening mechanisms known as crack tip shielding, which act to reduce the local driving force actually experienced at the crack tip (17). In conventional high-strength aluminum alloys, the role of these closure mechanisms is restricted to near-threshold stress intensities. On the other hand, fatigue crack-paths in aluminum-lithium alloys, are especially tortuous due to the marked planarity of slip from the δ' precipitation and the strong anisotropy/texture and lack of recrystallization, which is imparted by commercial thermomechanical treatments. Consequently, as the deflected crack path morphology persists to ΔK levels as high as $\sim$ 20 MPa$\sqrt{m}$ in these materials (13), aluminum-lithium alloys tend to show generally superior (long) crack growth properties over a wide spectrum of growth rates.

Crack closure and deflection mechanisms act primarily on the wake of the crack, and thus are prone to be dependent on crack size (17). This implies that due to their limited wake, microstructurally-small cracks are unlikely to develop shielding as long cracks, and thus, at the same nominal ΔK, experience a larger effective near-tip "driving force". In fact, <u>in situ</u> closure stress measurements on small cracks have indicated negligible closure levels in 2090 and similar alloys (16). It is considered that this is primarily the reason for the marked discrepancies observed between long and small fatigue cracks; namely, anomalously faster and "sub-threshold" growth rates of small cracks

(Figs. 5.2-5.3, 5.5). However, with increasing length such cracks begin to develop closure (16,17) such that growth rates merge with long crack data once shielding levels approach that of long flaws. In the present study, this occurs at nominal ΔK levels of between 4 and 8 $MPa\sqrt{m}$, when crack lengths exceed approximately 700 to 1000 μm.

These notions can be substantiated by comparing the small crack data with that of long cracks where the role of crack closure has been minimized. This is illustrated for 2090-T8E41 in Fig. 5.6, where it can be seen that the long and small crack growth rates come into closer correspondence, when long crack data are presented in terms of ΔK_{eff}, where experimental measurements of K_{cl} are used to subtract the closure contribution. Similarly, but to a lesser extent, small crack growth rates correspond to long crack data measured at high load ratios (R = 0.75).* This implies that the behavior of small flaws largely reflects that of long cracks without the obvious benefits of closure.

Although the reduced role of crack closure at small crack sizes appears to be the prominent mechanism responsible for their accelerated growth rate behavior, it is apparent from Fig. 5.6 that small flaws still propagate below the effective threshold, indicating that the small crack effect cannot be attributed solely to the closure concept. Additional factors which have been identified as contributing to discrepancies in long and small crack behavior include enhanced crack tip opening strains (19), surface microplasticity (20), differences in

---

* Recent studies by Hertzberg and co-workers (18) have shown that by measuring long crack growth rates under constant K_{max}/increasing K_{min} loading conditions, which minimize crack closure, a conservative estimate of $\Delta a/\Delta N$ vs. ΔK behavior for small cracks can be obtained, except at very low, sub-threshold stress intensities.

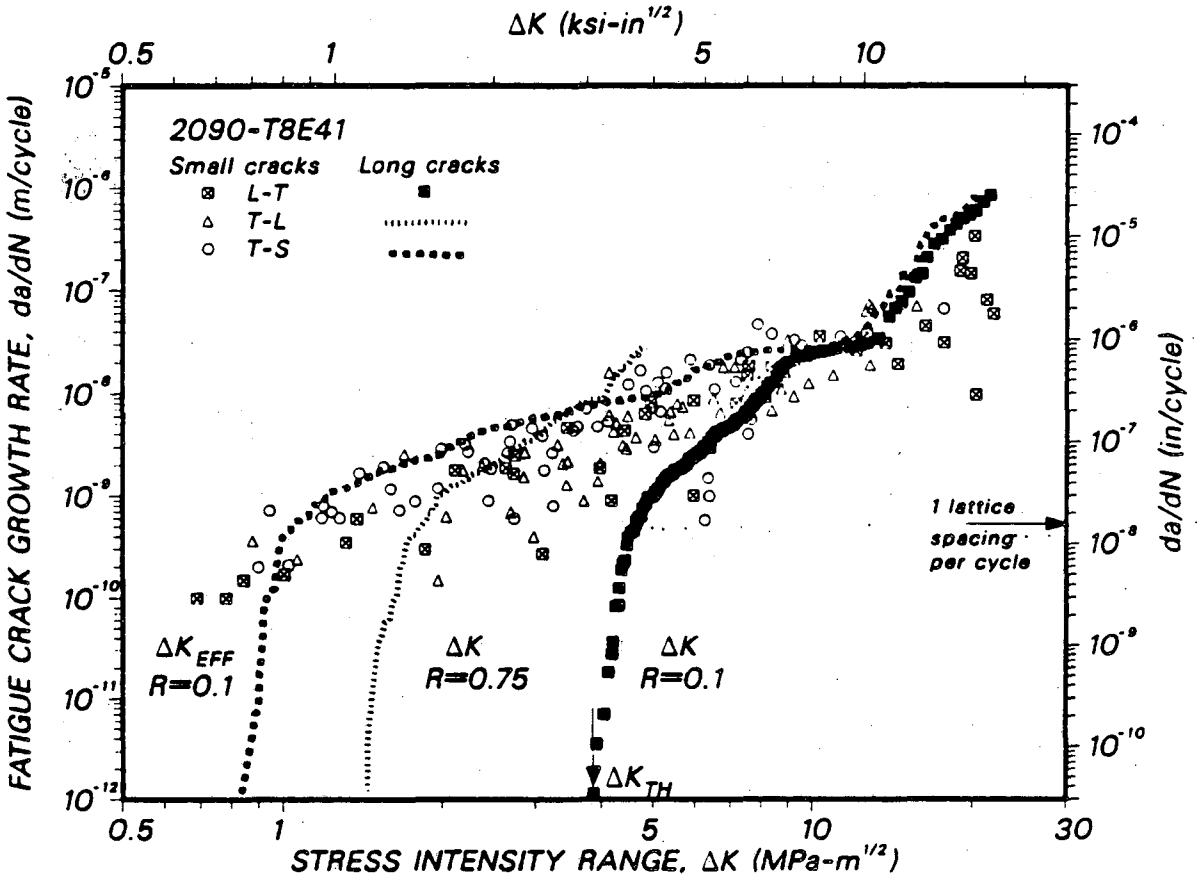

XBL 877-3201

Fig. 5.6: Long (≳ 10 mm) and small (2-1000 μm) fatigue crack growth rate behavior (at R = 0.1) in aluminum-lithium alloy 2090-T8E41 as a function of ΔK, showing comparison with i) long crack data characterized in terms of ΔK_{eff}, and ii) long crack data monitored at high load ratios (R = 0.75).

crack geometry (21,22), interactions of small flaws with the microstructural features of comparable dimensions (20,23,24), and definition of an appropriate "crack driving force" (25). Moreover, since naturally occurring, small cracks initiate at "weak links" in the microstructure, forming crack fronts which encompass only relatively few grains, unlike through-thickness long cracks their growth will not be averaged over many disadvantageously oriented grains (7).

Moreover, as long cracks in lithium-containing aluminum alloys tend to develop the most shielding due to their extremely tortuous crack paths, the difference between long and small crack growth rates appears to be maximized in these materials. As shown in Fig. 5.7, small crack growth rates in 2090-T8E41, 2091-T351 and 8091-T351 remain comparable, to behavior in 2124 and 7150 aluminum alloys. This further justifies some studies which report comparable or slightly inferior fatigue resistance of Al-Li alloys over traditional Al-alloys (26), when comparing the common S-N type behavior.

Finally, despite considerable scatter, in contrast to long crack behavior (Fig. 4.1), small crack growth rates in aluminum alloys are comparatively less sensitive to both microstructure and composition. It appears that small cracks do not perceive the continuum and their growth rate response is purely statistical in nature, determined largely by the local flaw distributions. Since long crack data at higher growth rates and at high load ratios are similarly less sensitive to microstructure (e.g., ref. 17), this suggests that the origin of microstructural effects on fatigue crack propagation behavior in aluminum alloys results primarily from shielding mechanisms. Since

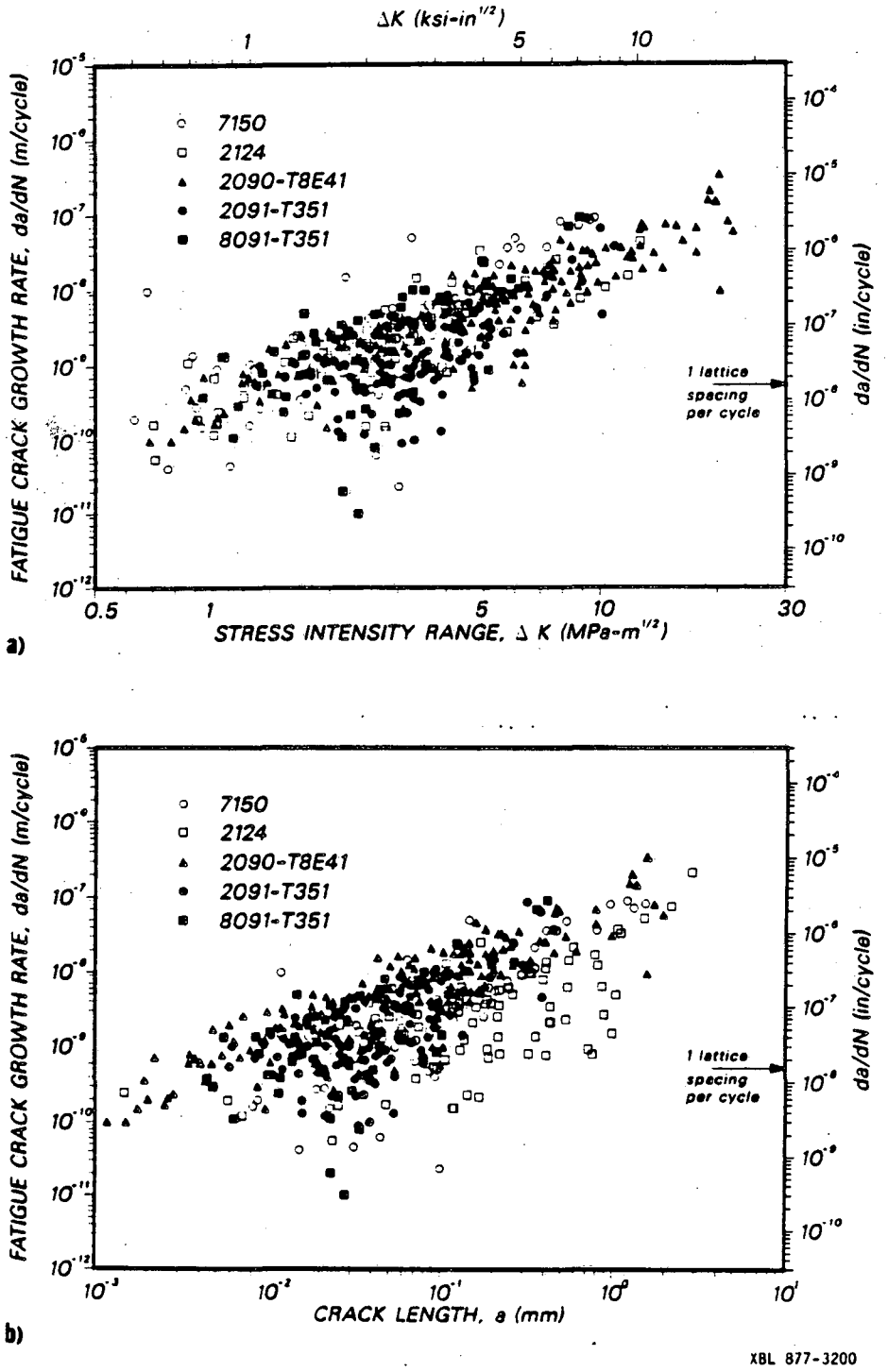

Fig. 5.7: Variation of the fatigue crack propagation rates of small (2-1000 μm) surface cracks in commercial aluminum alloys as a function of a) nominal stress intensity range (ΔK) and b) crack length (a). Data are compared for aluminum-lithium alloys 2090-T8E41, 2091-T351, 2091-T8X and 8091-T351, and traditional high-strength alloys 2124 and 7150 in various aging conditions.

slip planarity and grain size (and hence morphology of crack path) are known to be relevant, it would appear that crack deflection and resulting roughness-induced crack closure provide the major contribution.

5.5 CONCLUSIONS

From the results presented in this chapter on the fatigue crack propagation behavior of naturally-occurring, microstructurally-small (2-1000 μm) surface cracks in commercial aluminum-lithium alloys 2090-T8E41, 2091-T351, 2091-T8X and 8091-T351 and traditional high-strength aluminum alloys 2124 and 7150, the following conclusions may be made:

1. Small fatigue crack growth rates in all commercial aluminum and aluminum-lithium alloys were up to 2-4 orders of magnitude faster than corresponding growth rates for long cracks at equivalent (nominal) stress intensity ranges. In contrast to long crack results, over a wide spectrum of growth rates from 10^{-10} to 10^{-6} m/cycle, the influence of microstructure and composition on small crack behavior was relatively minor.

2. The accelerated growth rate behavior of small fatigue cracks, which predominates below typically 10^{-8} m/cycle, is attributed primarily to the restricted role of crack closure for flaws of limited wake. Principally, crack meandering and the resultant premature contact of fracture surface asperities appear to be the dominant means by which closure develops in precipitation-hardened aluminum alloy systems.

3. The discrepancy between long and small fatigue crack behavior appears to be maximized in aluminum-lithium alloys. This is in part due to their superior long crack properties which result from very high

levels of shielding promoted by tortuous crack paths (induced by intense planar slip and strong deformation texture). However, the small crack growth resistance of commercial aluminum-lithium alloys remains comparable to traditional high strength aluminum alloys.

5.6 REFERENCES

1. Anon: 'Airplane damage tolerance requirements', Military Specification MIL-A-83444, U.S. Air Force (1974).

2. S. Suresh and R. O. Ritchie: Intl. Metals Rev., 29 (1984), p. 445.

3. S. J. Hudak: J. Eng. Mat. Technol., 103 (1981), p. 26.

4. K. J. Miller: Fat. Eng. Mat. Struct., 5 (1982), p. 223.

5. J. Schijve: in 'Fatigue Thresholds', J. Backlund, A. F. Blom and C. J. Beevers (eds.), EMAS Ltd., Warley, U.K., 2 (1982), p. 881.

6. J. Lankford: Fat. Fract. Eng. Mat. Struct., 8 (1985), p. 161.

7. R. O. Ritchie and J. Lankford: Mat. Sci. Eng., 84 (1986), p. 11.

8. E. J. Coyne, T. H. Sanders, and E. A. Starke: in 'Aluminum-Lithium Alloys', T. H. Sanders and E. A. Starke (eds.), TMS-AIME, Warrendale, PA (1981), p. 293.

9. F. S. Lin and E. A. Starke: Mat. Sci. Eng., 43 (1980), p. 65.

10. A. K. Vasudévan, P. E. Bretz, A. C. Miller, and S. Suresh: Mat. Sci. Eng., 64 (1984), p. 113.

11. K. V. Jata and E. A. Starke: Metall. Trans. A, 17A (1986), p. 1011.

12. J. Petit, S. Suresh, A. K. Vasudévan, and R. C. Malcolm: in 'Aluminium-Lithium Alloys III', C. Baker, P. J. Gregson, S. J. Harris, and C. J. Peel (eds.), Institute of Metals, London, U.K. (1986), p. 257.

13. W. Yu and R. O. Ritchie: J. Eng. Mat. Technol., 109 (1987), p. 81.

14. K. T. Venkateswara Rao, W. Yu, and R. O. Ritchie: Metall. Trans. A, 19A (1988), p. 549.

15. K. T. Venkateswara Rao, W. Yu, and R. O. Ritchie: Scripta Metall., 20 (1986), p. 1459.

16. M. R. James: Scripta Metall., 21 (1987), p. 783.

17. R. O. Ritchie and W. Yu: in 'Small Fatigue Cracks', R. O. Ritchie and J. Lankford (eds.), TMS-AIME, Warrendale, PA (1986), p. 167.

18. R. W. Hertzberg, W. A. Herman, and R. O. Ritchie: Scripta Metall., 21 (1988), in press.

19. J. Lankford and D. L. Davidson: in 'Small Fatigue Cracks', R. O. Ritchie and J. Lankford (eds.), TMS-AIME, Warrendale, PA (1986), p. 51.

20. M. R. James and W. L. Morris: in 'Small Fatigue Cracks', R. O. Ritchie and J. Lankford (eds.), TMS-AIME, Warrendale, PA (1986), p. 145.

21. L. Wagner, J. K. Gregory, A. Gysler, and G. Lutjering: Small Fatigue Cracks', R. O. Ritchie and J. Lankford (eds.), TMS-AIME, Warrendale, PA (1986), p. 117.

22. A. Pineau: in 'Small Fatigue Cracks', R. O. Ritchie and J. Lankford (eds.), TMS-AIME, Warrendale, PA (1986), p. 191.

23. K. Tanaka: in 'Small Fatigue Cracks', R. O. Ritchie and J. Lankford (eds.), TMS-AIME, Warrendale, PA (1986), p. 343.

24. C. W. Brown and J. E. King: in 'Small Fatigue Cracks', R. O. Ritchie and J. Lankford (eds.), TMS-AIME, Warrendale, PA (1986), p. 73.

25. S. J. Hudak and K. S. Chan: in 'Small Fatigue Cracks', R. O. Ritchie and J. Lankford (eds.), TMS-AIME, Warrendale, PA (1986), p. 379.

26. P. Meyer and B. Dubost: in 'Aluminum-Lithium Alloys III', C. Baker, P. J. Gregson, S. J. Harris and C. J. Peel (eds.), Institute of Metals, London (1986), p. 37.

CHAPTER VI

FATIGUE CRACK GROWTH: EFFECT OF SINGLE TENSILE OVERLOADS

6.1 INTRODUCTION

Although fatigue crack growth rates characterized under constant amplitude loading are important for providing baseline crack propagation data, and defining fundamental mechanisms of crack advance, majority of components in service are subjected to variable amplitude loading, with the effect that load interaction effects are clearly of practical significance. Transient load excursions are known to affect crack growth rates, and in many cases considerably extend the fatigue life (1-22). The purpose of the present chapter is to examine the load interaction effects with respect to single peak tensile overloads in aluminum-lithium alloys, specifically 2090-T8E41.

6.2 BACKGROUND

The transient crack growth rate response for a Mode I fatigue crack following a single spike tensile overload typically involves an initial brief acceleration in crack growth immediately after the overload, followed by a prolonged period of retardation until crack arrest or growth rates return to their steady-state (baseline) levels (12) (Fig. 6.1). The magnitude of the delay following the overload is measured either in terms of crack length, i.e., the delay distance (a_d) or the crack length affected by the delay (a_{aff}), or the number of delay cycles (N_d), and for a given material, microstructure and environment is a function of the baseline stress intensity range (ΔK_B),

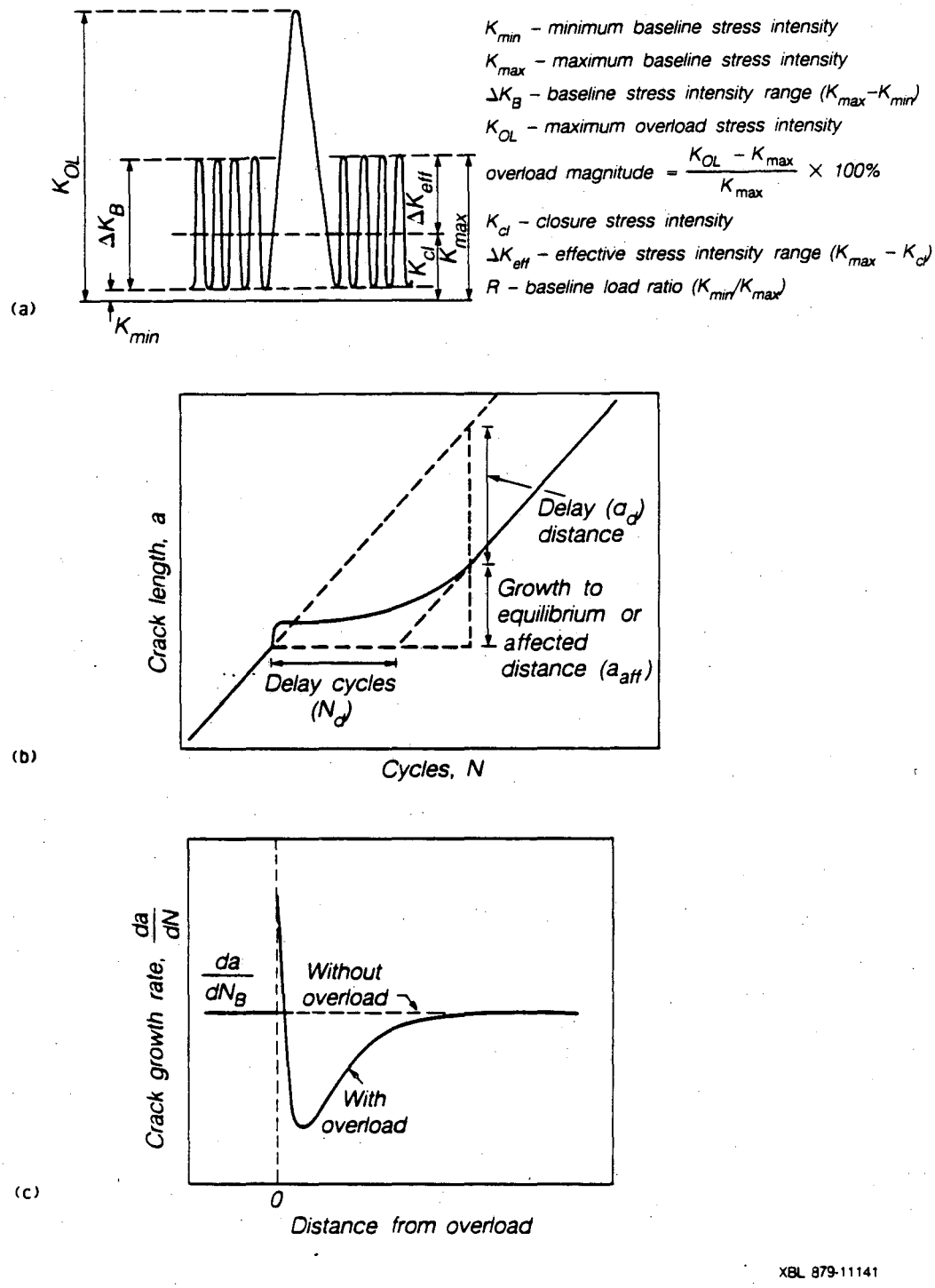

Fig. 6.1: Schematic illustration of the influence of a single (spike) tensile overload on the fatigue crack growth behavior, showing a) nomenclature, b) crack length vs. number of cycles, and c) growth rate vs. crack length behavior.

the load ratio R, the magnitude of the overload (overload ratio) and sequence, and the specimen thickness (1-28).

Despite a general accord on the macroscopic aspects of post-overload crack growth retardation phenomenon during Mode I fatigue loading (1-22), precise mechanistic origins remain unclear. Numerous mechanisms have been proposed, which rely on such concepts as a) residual stresses (1,2), where the higher strains generated in the overload plastic zone result in an increase in the residual compressive stress field ahead of the crack on unloading; b) crack closure (3-12), where the residual stresses enhance plasticity-induced closure in the wake of the advancing crack; c) plastic blunting of the crack tip at the overload (13); d) crack deflection and associated roughness-induced closure (14,15), where the local crack driving force is reduced by a deviation of the crack path and subsequent wedging of the crack surfaces by asperities; e) strain hardening (16,17), from either monotonic hardening of the material in the overload plastic zone following single overloads or cyclic hardening after block loading sequences; and f) changes in crack front profile for large overloads on thin sheets (18), where "pop-in" type crack extension at the overload precedes slower crack growth at the (plane stress) edges of the specimen.

Of these mechanisms, crack closure appears to provide the primary basis for rationalizing many of the observed effects. In fact, for Mode III fatigue crack growth in (antiplane) shear, where crack closure induced by wedge shielding mechanisms is not relevant, no transient retardations are observed and growth rates immediately accelerate on

application of the tensile overload (29). However, as most research has been performed at relatively high stress intensity ranges (2-9,13,15-24), few studies describe the micromechanisms of transient crack growth behavior at low stress intensities (12,14,26,28), where the prominent mechanisms of closure are quite different (e.g., refs. 30-33). There is also a paucity of data which show any quantitative measurement of the variation in closure during the overload sequence. Moreover, the few results which have been published, i.e., the surface observations by Davidson et al. (10) on powder aluminum alloys of an increase in closure load after the overload, and the compliance measurements of others (25-27) on both low alloy steels and aluminum alloys which show a decrease, are highly conflicting.

In view of the extremely high levels of crack closure developed in coherent particle-hardened alloys (34-39), aluminum-lithium alloy 2090-T8E41 represents an ideal material for conducting such mechanistic studies. The present study attempts to elucidate the salient mechanisms of post-overload retardation in the recently developed alloy, 2090-T8E41 and compare the behavior with traditional 2124 and 7150 alloys.

6.3 EXPERIMENTAL DETAILS

6.3.1 Single Tensile Overloads

Single peak tensile overloads of magnitudes between 50 and 150 % were applied under constant ΔK cycling conditions for a series of baseline stress intensity ranges from 4 to 14 MPa$\sqrt{m}$ at R = 0.1 with a frequency of 0.01 Hz. The transient crack growth and closure behavior were then carefully monitored immediately after the overload with the baseline loading resumed at constant ΔK. Behavior in 2090 at a

baseline ΔK of 8 $MPa\sqrt{m}$ was compared with identical experiments in 2124 and 7150. Details regarding the test set-up are given in Chapter II.

6.3.2 Surface Removal Experiments

To study the relative contributions to post-overload behavior, from deformation at the specimen surface ($\sim$ plane stress) and the interior (plane strain), experiments were additionally performed where surface layers (corresponding to 1.25 mm, i.e., 20 % of the specimen thickness) were carefully machined from each face following 100 % overloads at constant baseline ΔK values of 4 and 12 $MPa\sqrt{m}$. Results were compared with identical tests on full thickness samples.

6.3.3 Crack Closure

Macroscopic (global) measurements of crack closure were performed <u>in situ</u> using back-face strain compliance techniques and under constant amplitude cycling, closure was assessed in terms of the closure stress intensity, K_{cl} (see Ch. II). In addition, an offset elastic displacement method (12,32) was used to improve sensitivity. Following tensile overloads, two distinct indications of crack surface contact could be detected from the unloading compliance curve. These have been referred to as upper and lower closure loads (9) but are interpreted here (12) to signify changes in near-tip and far-field (global) closure during unloading. Near-tip closure, which represents wedge shielding in the immediate wake of the crack tip, was additionally evaluated using side-face strain gauges mounted 1 - 2 mm ahead of the crack tip.

6.3.4 Fractography

By periodically interrupting tests, crack tip profiles were examined metallographically at the specimen surface with both optical

and scanning electron microscopy before, during and after the overload event. In addition, on completion of the test, crack profiles on the specimen surface (∿ plane stress) were compared with those imaged at specimen mid-thickness (plane strain).

6.4 RESULTS

6.4.1 Influence of Overload Ratio

Data showing the transient growth rate response in the 2090 alloy following 50, 100 and 150 % single tensile overloads, applied at a constant baseline ΔK levels of 4 and 8 $MPa\sqrt{m}$, are plotted in Fig. 6.2 as a function of crack growth distance from the overload event. As depicted schematically in Fig. 6.1, the onset of the overload induces an initial brief acceleration followed by a period of retardation, the duration of which increases progressively with increasing overload ratio. Although 50 % overloads produce negligible effects, 100 % overloads applied at near-threshold baseline ΔK levels of 4 $MPa\sqrt{m}$ are sufficient to completely arrest the crack. Results in 7150-T651 and 2124-T351 alloys at a baseline ΔK of 8 $MPa\sqrt{m}$ are qualitatively similar, but associated retardations appear to be smaller (Fig. 6.3).

6.4.2 Influence of Baseline Stress Intensity

The extent of retardation as a function of baseline ΔK level is shown in Fig. 6.4 for 100 % overloads in the 2090 alloy. Similar to behavior reported for titanium (12) and other aluminum alloys (23,24), the magnitude of the retardation, whether measured in terms of delay distance or delay cycles, is increased either with decreasing ΔK toward the threshold or with increasing ΔK toward instability. Crack extensions over which the post-overload retardations persist (a_{aff}) are

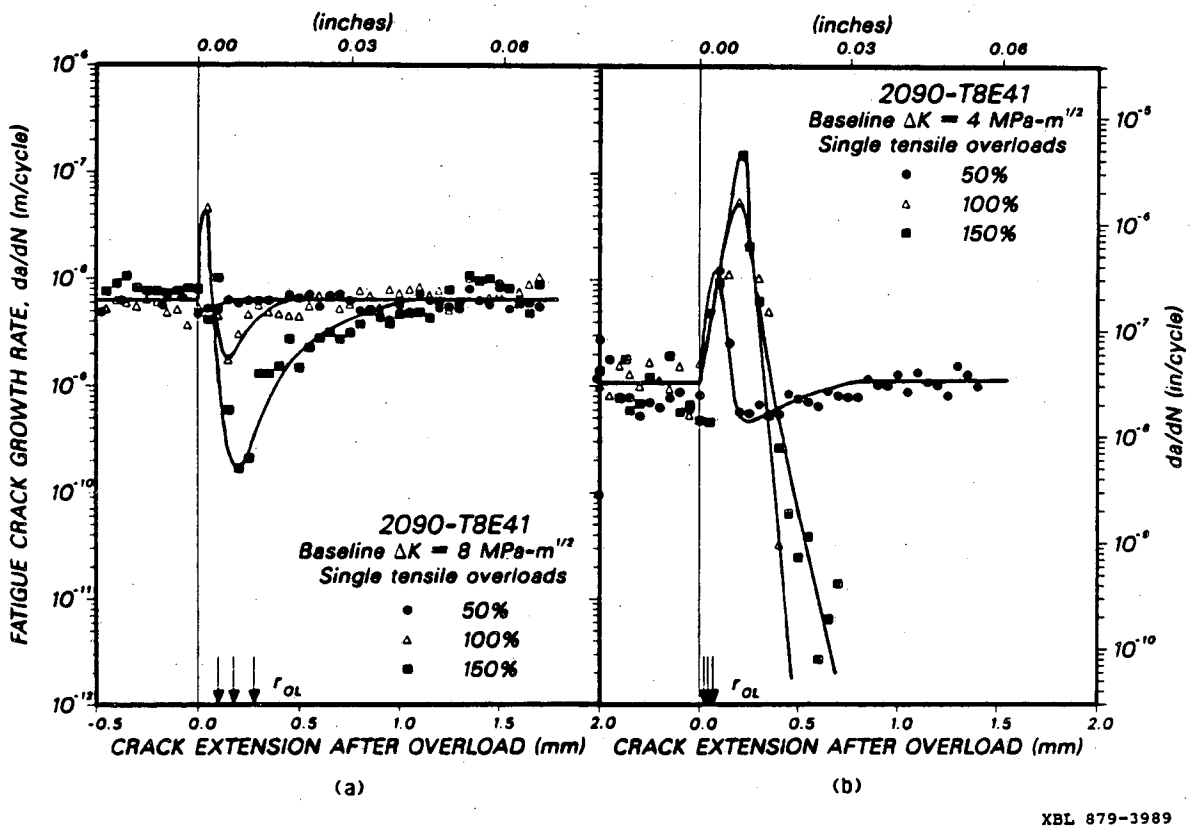

Fig. 6.2: Effect of 50, 100 and 150 % single tensile overloads on fatigue crack growth rates in Al-Cu-Li alloy 2090-T8E41 as a function of crack extension after the overload. Overloads were applied on constant baseline ΔK values of a) 8 MPa$\sqrt{m}$ and b) 4 MPa$\sqrt{m}$.

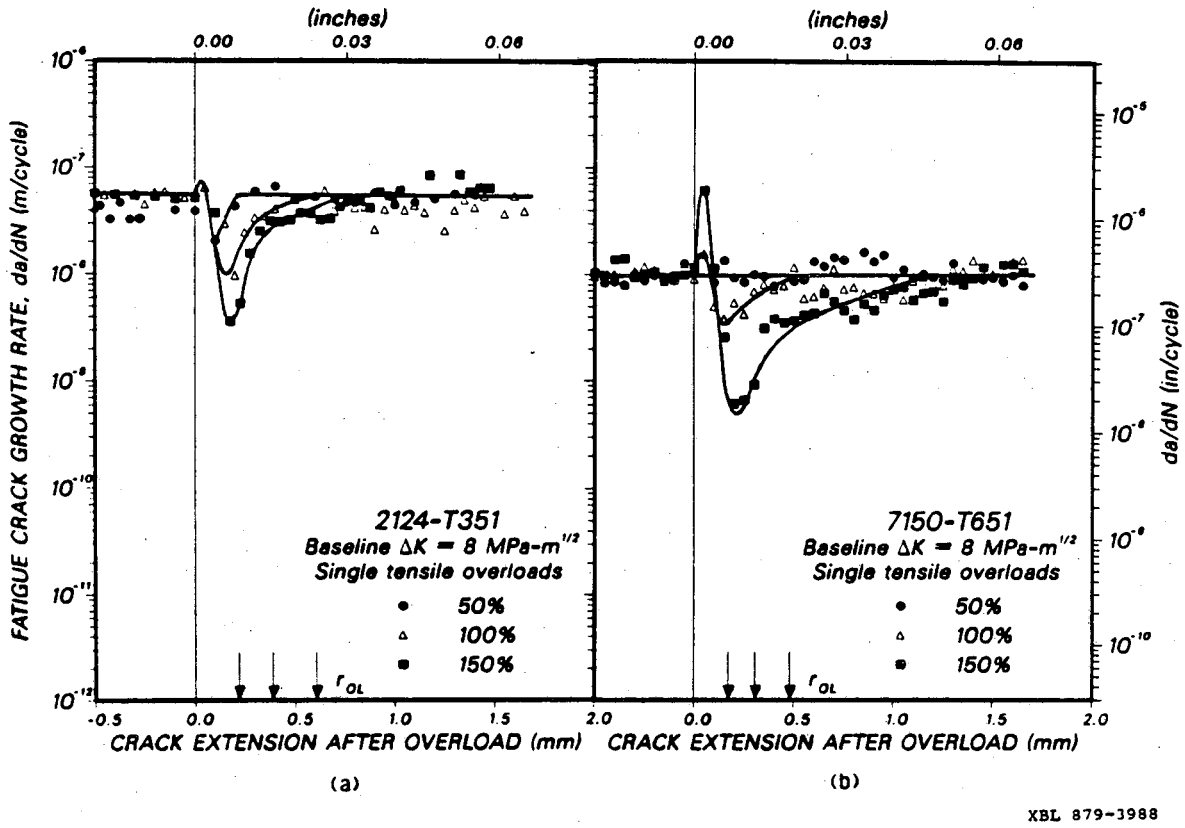

Fig. 6.3: Effect of 50, 100 and 150 % single tensile overloads on fatigue crack growth rates in a) 2124-T351 and b) 7150-T651 alloys as a function of crack extension after the overload. Overloads were applied on constant baseline cycling at $\Delta K_B = 8$ MPa$\sqrt{m}$.

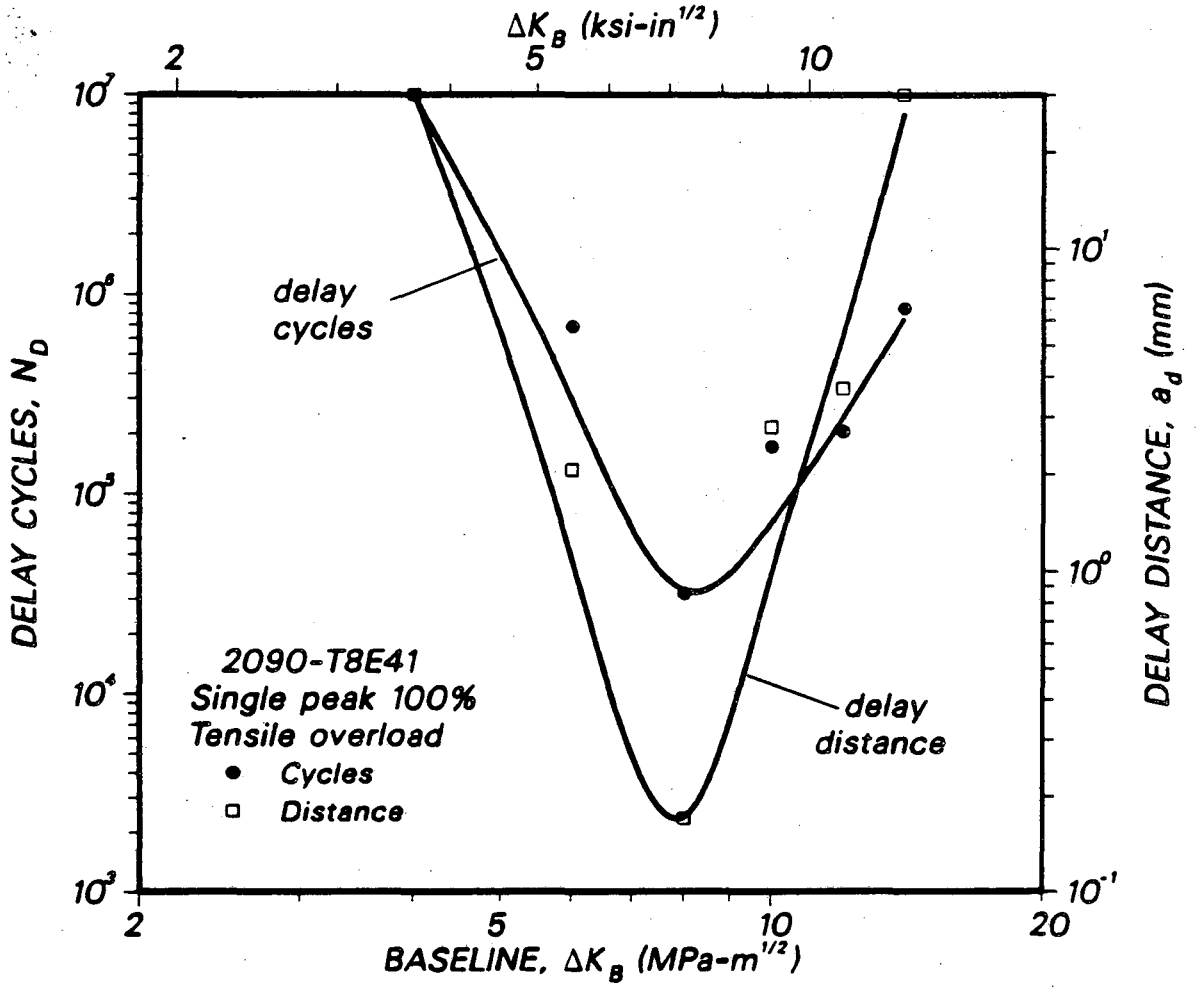

XBL 879-3987

Fig. 6.4: Influence of baseline ΔK (at R = 0.1) on the magnitude of crack growth retardation following 100 % single tensile overloads in Al-Cu-Li alloy 2090-T8E41. Post-overload retardations are characterized in terms of the delay distance and delay cycles.

compared with computed (plane stress) overload plastic zone sizes (r_{oL}) in Table 6.1. On the first order assumption that the retardation should predominate while the crack traverses the overload plastic zone (40,41), the increase in delay with higher baseline ΔK levels would appear to be reasonable as the magnitude of r_{oL} is proportional to ΔK_B^2 (for a given overload ratio). However, at near-threshold baseline ΔK levels, behavior is contrary to expectations; the magnitude of the delay increases with decreasing r_{oL} and furthermore persists over crack extensions as much as an order of magnitude larger than r_{oL}. In addition, of the three alloys tested, overload plastic zones are largest in the lowest strength 2124-T351, yet at low baseline ΔK levels, this alloy shows the least retardation behavior.

6.4.3 Fractography

Scanning electron microscopy revealed rough, highly faceted transgranular fracture surfaces in 2090-T8E41, typical of aluminum-lithium alloys (37-39), with no obvious differences in crack growth morphology or crack front profile due to the overload (Fig. 6.5). Differences were apparent, however, in crack path profiles. Shown in Fig. 6.6 are the crack tip profiles <u>at the specimen surface</u>, prior to, at and after a 100 % overload (ΔK_B = 8 MPa$\sqrt{m}$) in 2090-T8E41 (imaged at zero load). It is clearly evident that the overload causes i) pronounced crack tip blunting, which permanently props open the crack, ii) intense localized shear deformation in flow bands radiating roughly 45 deg from the crack tip, and iii) crack deflection primarily along one shear band. Subsequent crack extension within the overload plastic zone is initially deflected back toward the original crack plane (which

Table 6.1: Data Showing Transient Retardation Behavior Following Single Tensile Overloads in Aluminum Alloys.

Alloy	Baseline ΔK ($MPa\sqrt{m}$)	% Overload	Overload Plastic Zone, r_{oL}[1] (mm)	Affected Distance, a_{aff} (mm)
2090-T8E41	4	50	0.03	0.32
		100	0.04	∞
		150	0.07	∞
	6	100	0.10	1.13
	8	50	0.10	0.11
		100	0.18	0.55
		150	0.28	0.98
	10	100	0.28	1.45
	12	100	0.40	1.58
	14	100	0.54	2.50
2124-T351	8	50	0.22	0.15
		100	0.39	0.35
		150	0.61	0.61
7150-T651	8	50	0.17	0.13
		100	0.31	0.44
		150	0.48	0.98

[1] $r_{oL} \sim (1/2\pi)(K_{oL}/\sigma_y)^2$

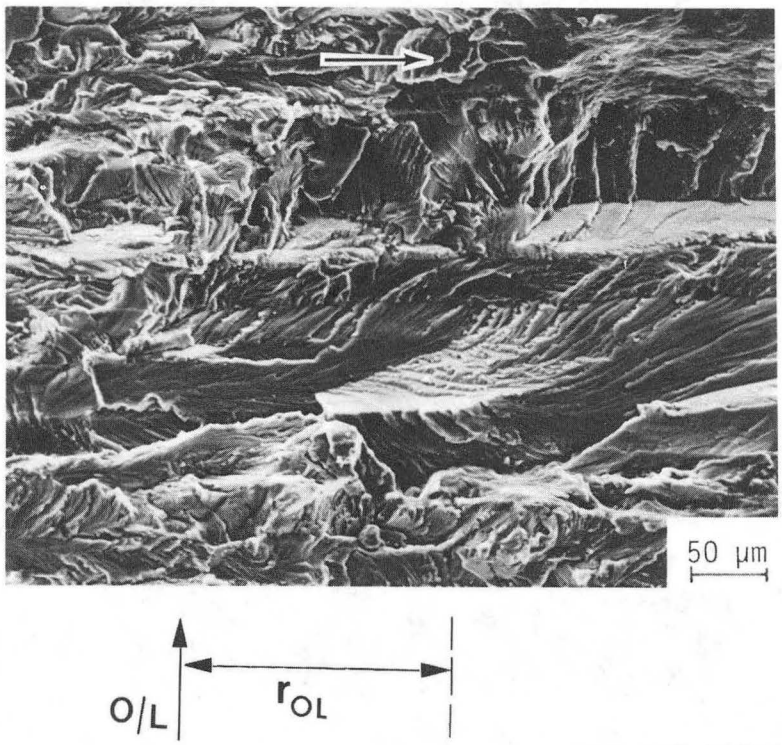

XBB 878-6967B

Fig. 6.5: Scanning electron micrography of fatigue fracture surface for a 100 % single tensile overload at ΔK_B = 8 MPa$\sqrt{m}$, showing rough, highly faceted transgranular surface with little morphological evidence of the overload. Arrow on micrograph indicates general direction of crack growth.

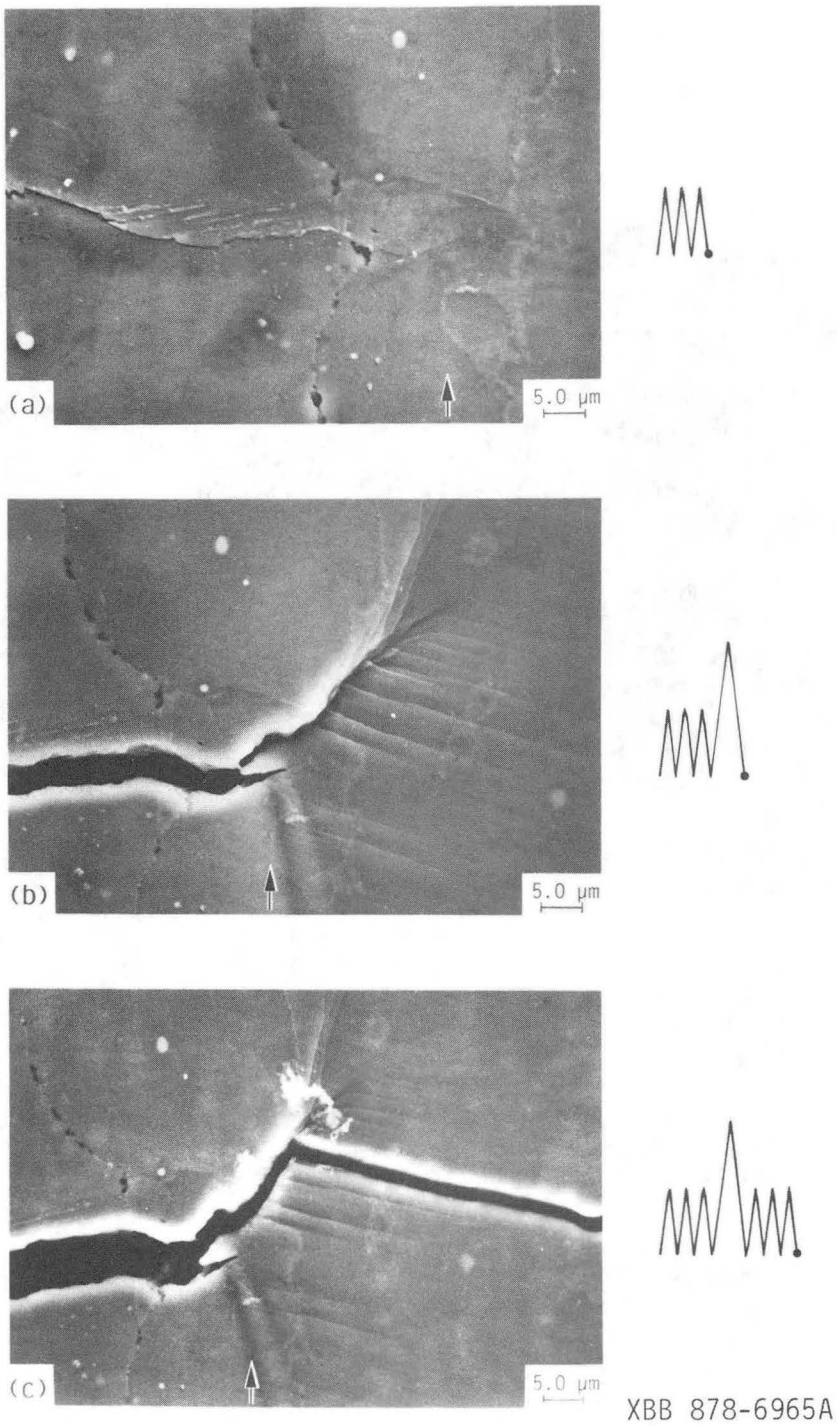

Fig. 6.6: Scanning electron micrographs of the surface fatigue crack profile, showing the original crack tip a) prior to, b) at, and c) after a 100 % single tensile overload in Al-Cu-Li alloy 2090-T8E41 at baseline ΔK of 8 $MPa\sqrt{m}$. Imaging was performed after unloading. Vertical arrows indicate position of the overload event.

enhances crack closure via asperity wedging (14)), and in general involves much reduced crack opening displacements during the delay period (Fig. 6.7a). Such crack opening displacements increase once the crack has grown out of the delay region.

Crack path profiles taken at specimen mid-thickness, however, are very different and reveal i) larger crack opening displacements, ii) no crack deflection at the point of application of the overload, and iii) a shorter delay period, as evidenced by a smaller region of crack extension with reduced crack opening displacements (Fig. 6.7b).

6.4.4 Crack Closure

The corresponding variation in crack closure during a 100 % overload (ΔK_B = 8 MPa$\sqrt{m}$) in 2090-T8E41 is shown in Fig. 6.8. Using standard back-face strain compliance techniques (32), which provide an assessment of the global, or far-field, closure along the length of the crack, no appreciable changes in closure levels could be detected, except perhaps for a slight drop in K_{cl} at the overload. However, by placing side-face strain gauges* close to the crack tip, which provide more of an assessment of the local, or near-tip, closure as the crack penetrates the overload plastic zone, the small drop in closure at the overload is followed by gradual increase in K_{cl} with crack extension toward a maximum corresponding to the minimum growth rate. Closure levels subsequently are reduced as growth rates accelerate toward pre-

---

*Note that the measurement of crack closure is sensitive to gauge location, as K_{cl} values determined globally (from back-face strains) and near the crack tip (side-face strains) are clearly different. this exemplifies the inherent difficulty in using closure corrected parameters, such as ΔK_{eff} in damage tolerant calculations. overload steady-state levels.

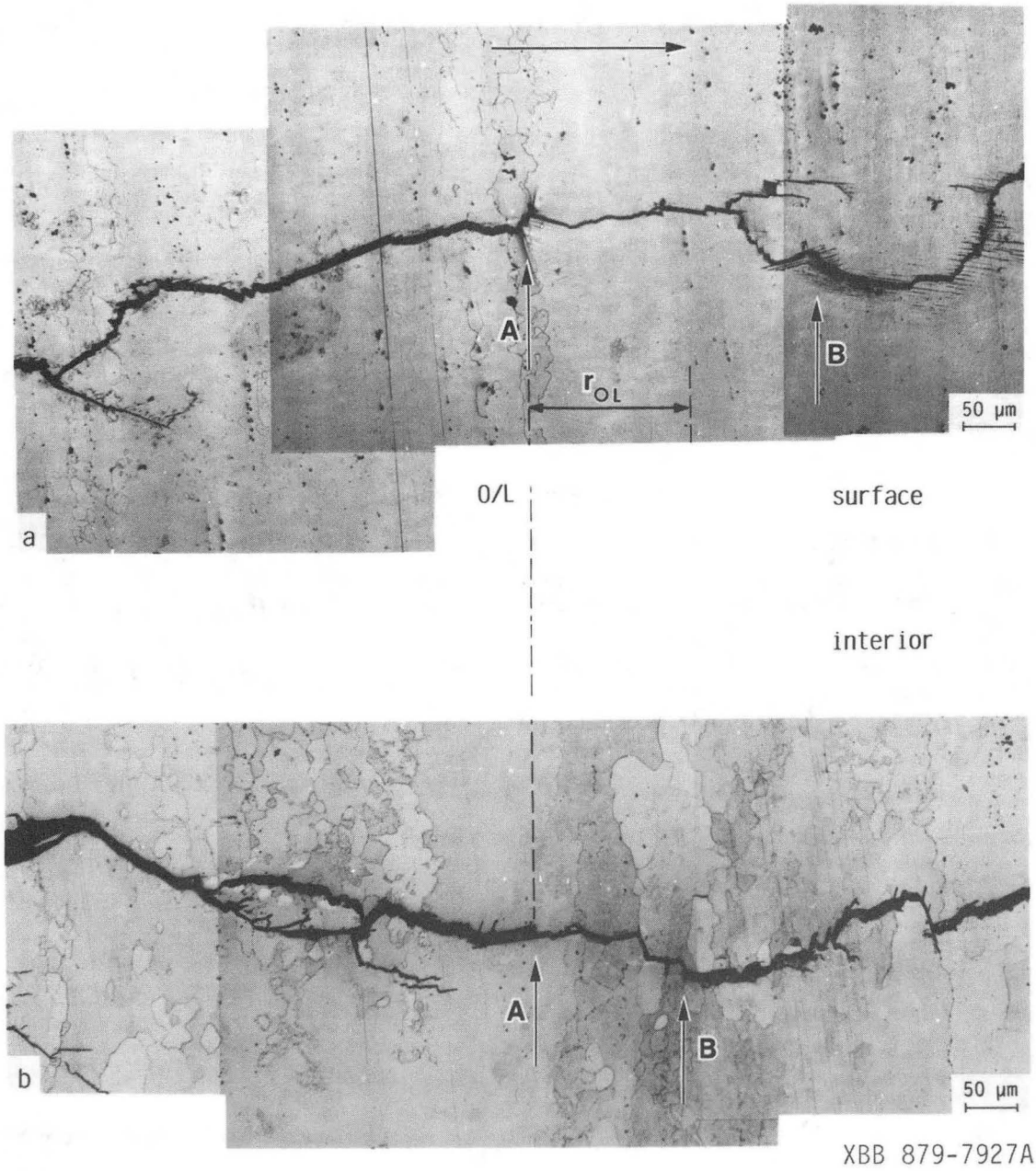

Fig. 6.7: Optical micrographs of fatigue crack profile and associated crack opening displacements for a 100 % single tensile overload at baseline $\Delta K = 8$ MPa$\sqrt{m}$ in Al-Cu-Li alloy 2090-T8E41, as imaged at a) the specimen surface, and b) the specimen mid-thickness. Note for the interior section the absence of crack deflection at the overload point (marked by the vertical arrow at A), the smaller crack length affected by the overload, and the smaller crack opening displacement in that region (A-B). Horizontal arrow indicates direction of crack growth (Keller's reagent etch).

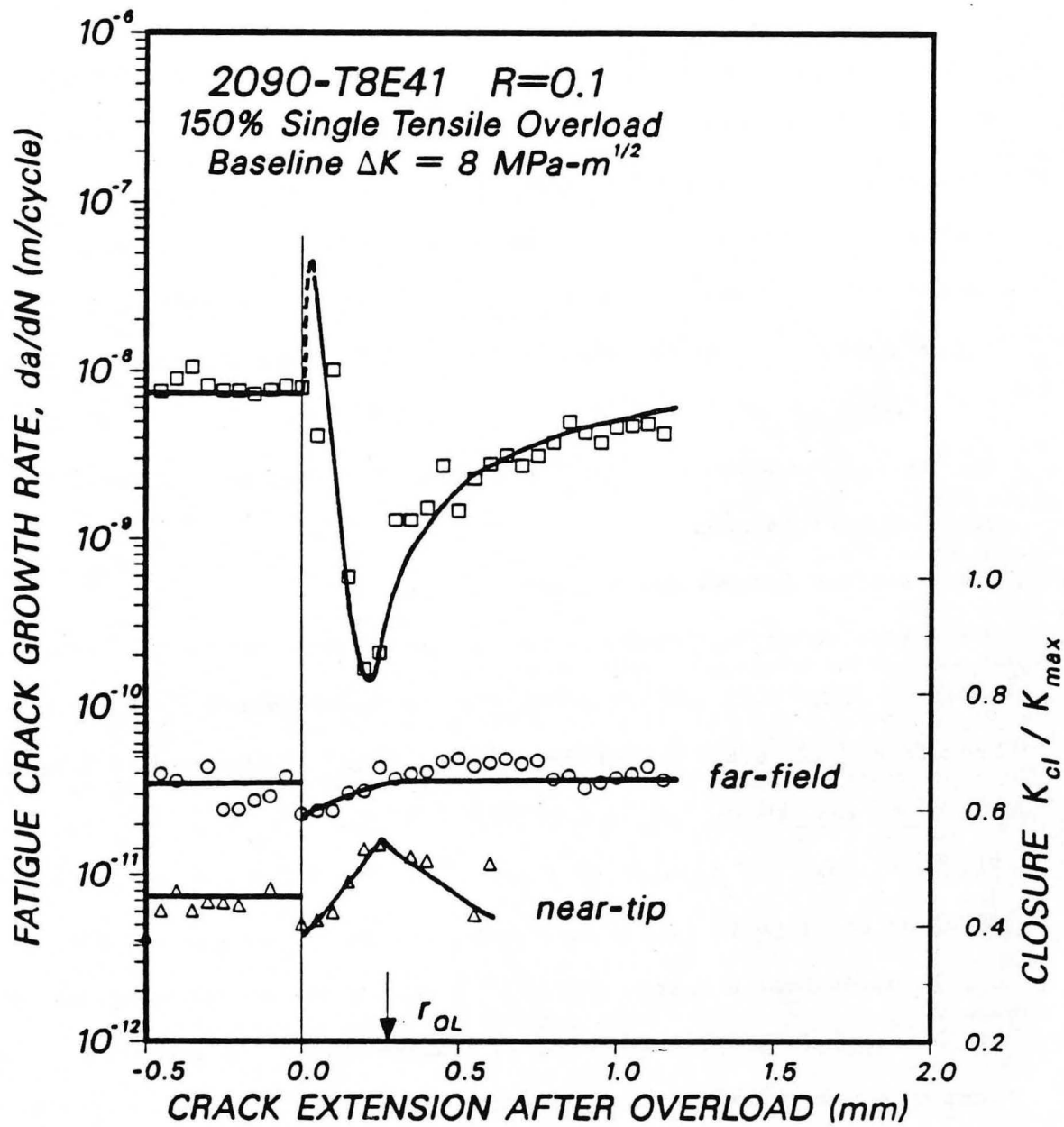

Fig. 6.8: Variation in fatigue crack growth rate and corresponding variation in far-field and near-tip crack closure levels following a 150 % single tensile overload in Al-Cu-Li alloy 2090-T8E41, as a function of crack extension after the overload. Results are for a baseline ΔK of 8 MPa$\sqrt{m}$ at R = 0.1.

As described elsewhere (12), the measured initial decrease and subsequent increase in closure are in accord with the observed transient post-overload behavior. The immediate acceleration at the overload would appear to be a result of reduced crack closure along the general wake of the crack due to blunting and associated increased crack opening displacements (Fig. 6.6b), whereas the subsequent retardation is consistent with a gradual increase in near-tip closure as the crack encounters the compressive residual stress field in the overload plastic zone.

6.4.5 Surface Removal Experiments

In view of differences in crack path profiles at the surface and interior (Fig. 6.7) and in crack closure measurements at the side and back face (Fig. 6.8), the effect of machining off the surface layers of the specimen after the application of the overload was examined. Fig. 6.9 shows the results of these tests for 100 % overloads in 2090-T8E41 at baseline ΔK levels of 4 and 8 $MPa\sqrt{m}$. It is evident that post-overload retardations are reduced by removing the surface regions, both at low and high baseline stress intensities. Clearly, as first proposed by McEvily (5), behavior at the surface contributes significantly to the retardation effect. With reference to Fig. 6.7, it is presumed that the longer delays are associated with smaller crack opening displacements and significant crack deflection which are promoted at the surface by the overload.

6.4.6 Behavior in 2124-T351 and 7150-T651

A comparison of post-overload behavior in 2090 with that in 2124-T351 and 7150-T651 is shown in Fig. 6.10 for 100 and 150% tensile

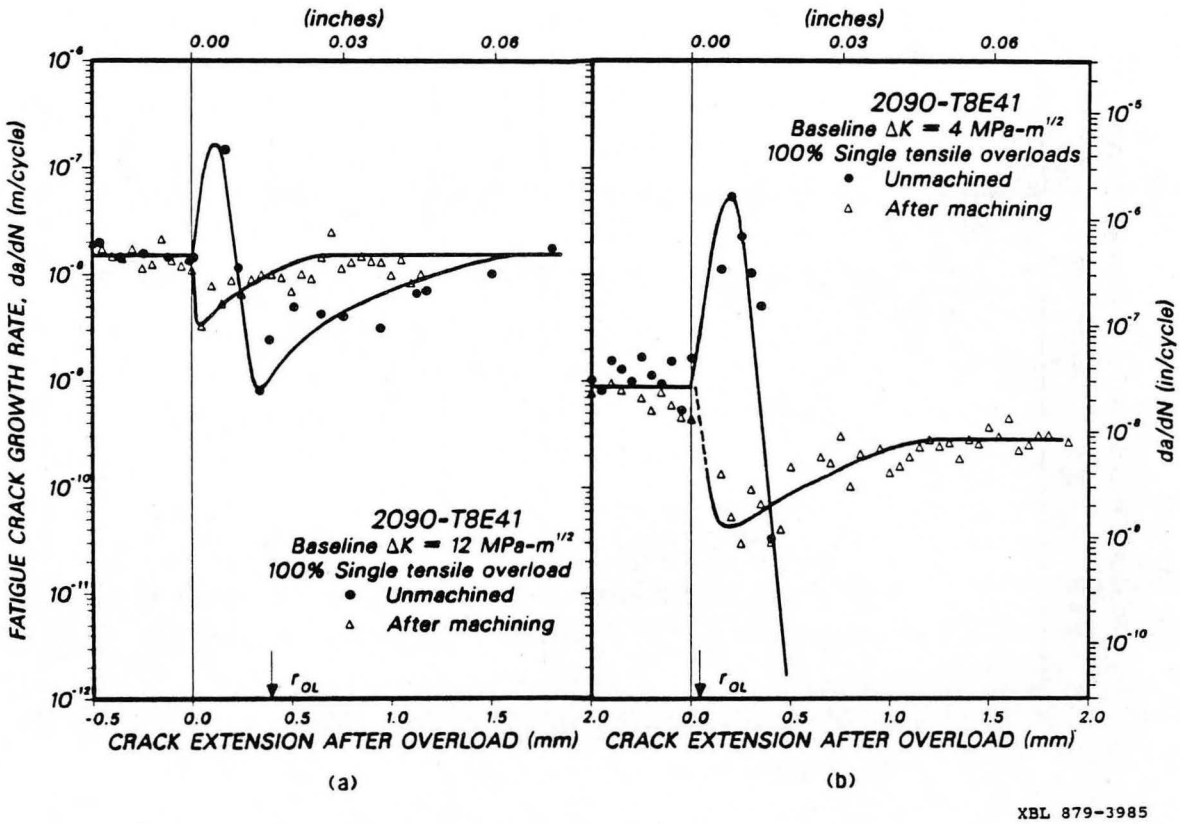

Fig. 6.9: Effect of the removal of surface layers (1.5 mm machined off each side) on crack growth retardation for Al-Cu-Li alloy 2090-T8E41 following a 100 % single tensile overload, at baseline stress intensity ranges of a) 12MPa$\sqrt{m}$ and b) 4 MPa$\sqrt{m}$.

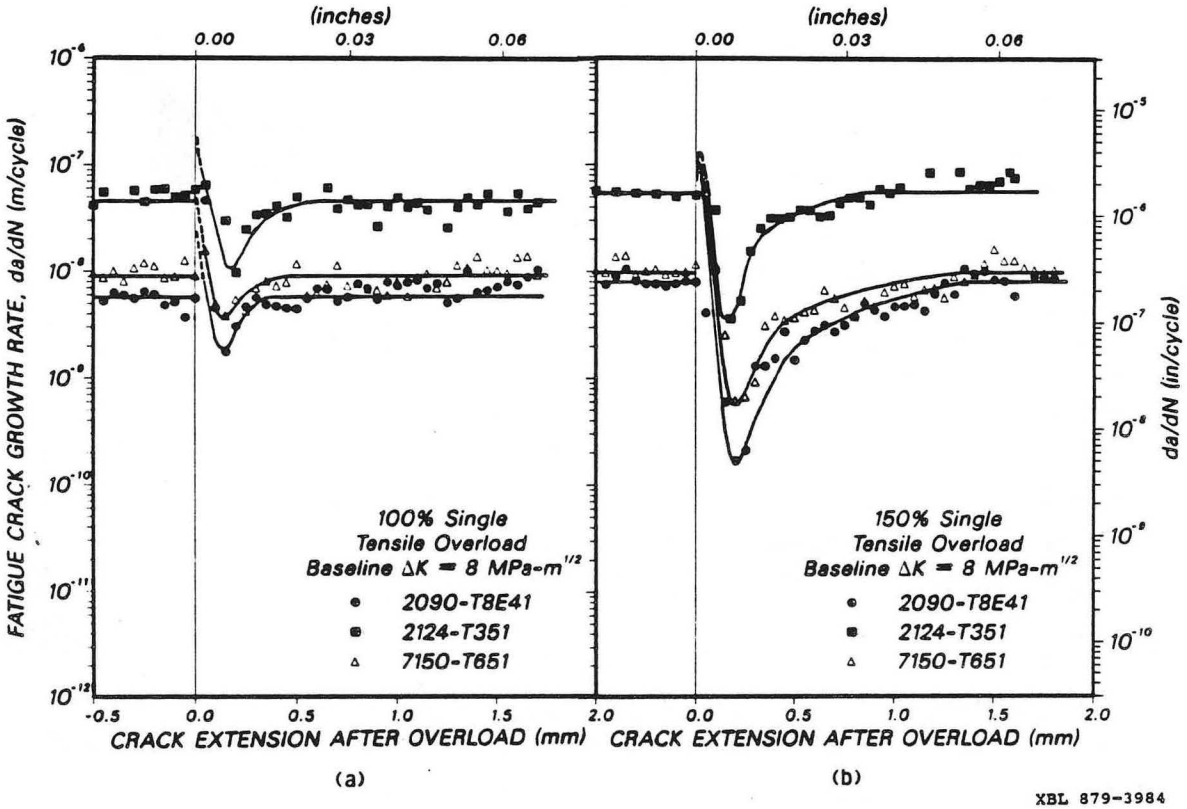

Fig. 6.10: Comparison of the effect of a) 100 and b) 150 % single tensile overloads at $\Delta K_B = 8$ MPa$\sqrt{m}$ on fatigue crack growth rates in 2090-T8E41, 2124-T351 and 7150-T651 alloys as a function of crack extension after the overload. Note the superiority of 2090, consistent with its higher levels of crack closure.

overloads at ΔK_B = 8 MPa$\sqrt{m}$. Results can be seen to be qualitatively similar, although retardations are largest in the aluminum-lithium alloy and are correspondingly associated with the highest measured levels of crack closure. Such results are consistent with reported performance of these alloys under tension-dominated variable amplitude loading spectra (42).

6.5 DISCUSSION

6.5.1 Mechanisms for Post-Overload Retardation

The experimental results and associated microscopy described above provide ample evidence of the prominent role of crack tip shielding in influencing transient crack growth behavior following tensile overloads; the principal mechanisms of shielding resulting from crack deflection and crack closure induced by cyclic plasticity and asperity wedging. Based on these results, the following mechanisms for the post-overload behavior are proposed, as illustrated schematically in Fig. 6.11.

During constant amplitude cycling at a given baseline ΔK, the crack growth rate is constant and in equilibrium with its monotonic and cyclic plastic zones and resultant closure stresses. On application of a tensile overload, severe crack tip blunting occurs via intense shear bands at the crack tip (Fig. 6.6b), resulting in wider crack opening displacements (Fig. 6.7), and consequently reduced (far-field) closure along the crack wake (Fig. 6.8), the influence of which leads to an immediate acceleration in growth rate (Fig. 6.8) Subsequent crack growth is progressively retarded as the crack extends into the overload plastic zone, as the enhanced compressive residual stresses act to

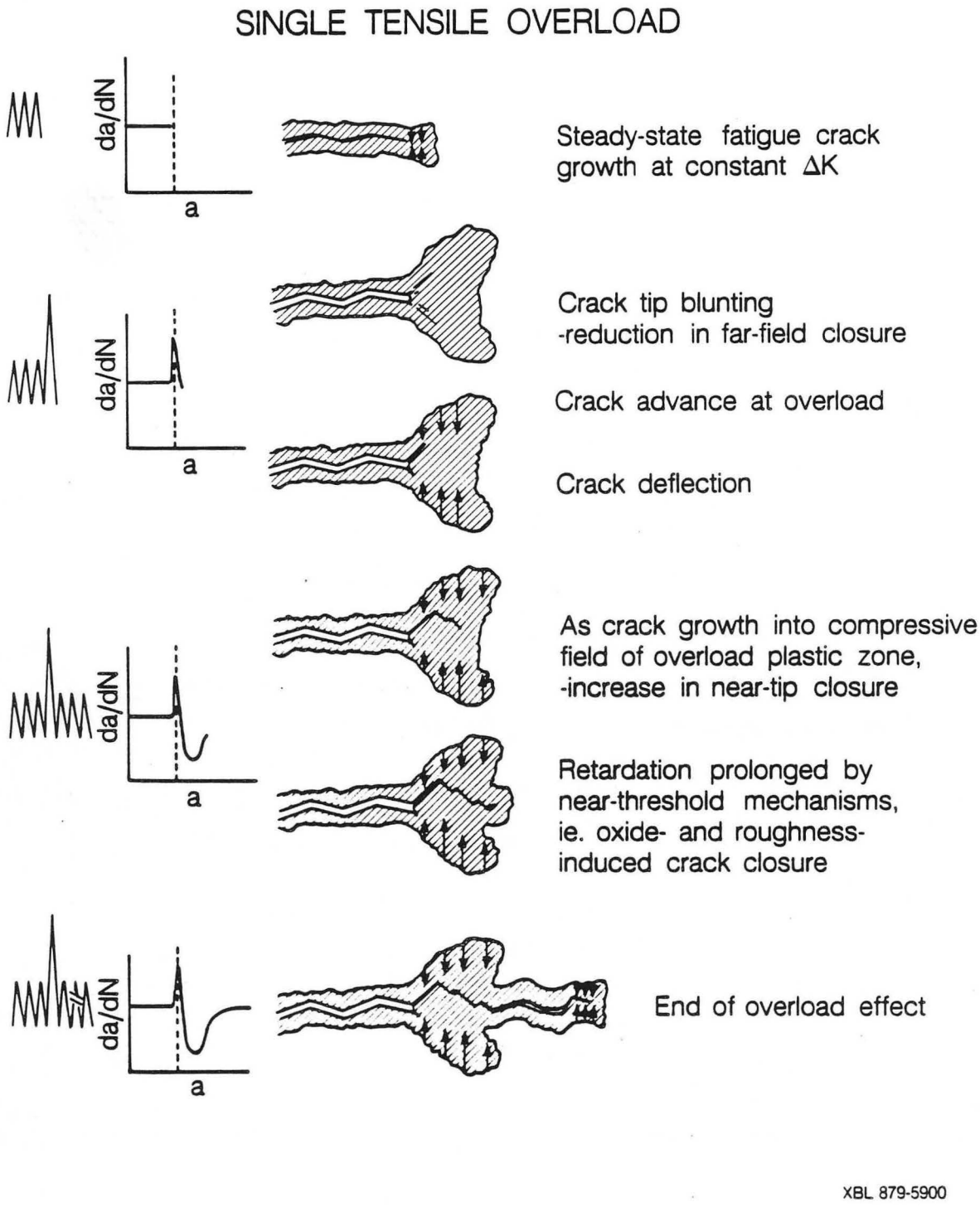

Fig. 6.11: Schematic idealization of the proposed mechanisms governing the transient fatigue crack growth behavior following a single tensile overload.

reduce crack opening displacements (Fig. 6.7) and promote increased (near-tip) closure in the immediate wake of the crack tip; the minimum growth rate corresponding to a maximum in K_{cl} (Fig. 6.8). The extent of retardation may be accentuated by crack deflection (along the shear bands) at the onset of the overload and increased crack closure from asperity wedging as the crack deviates back to its original path. However, this is predominantly a surface effect (Fig. 6.6 & 6.7), and thus the magnitude of the delay is reduced by removing the surface layers. Where the source of shielding is primarily due to plasticity-induced closure (e.g., at high ΔK_B), steady-state growth rates are largely re-established as the crack grows out of the overload plastic zone. The delay, however, may be prolonged in low baseline stress intensities and in materials such as 2090-T8E41, where enhanced crack path meandering and closure induced by asperity wedging provide additional mechanisms of retardation (Table 6.1). A similar mechanistic sequence has been proposed by Ward-Close and Ritchie to explain post-overload behavior in titanium alloys (12).

6.5.2 Crack Closure: Near-Tip vs. Far-Field

Although changes in crack closure have long been associated with post-overload retardation behavior (e.g., ref. 3), few experimental studies have provided quantitative confirmation. For example, certain authors (10) report an increase in closure loads at the overload, whereas others (25-27) report no change or a decrease. In the present work, as with a previous study in titanium alloys (12), it is shown that although the general (far-field) level of closure along the crack flank is decreased slightly by the overload due to crack tip blunting,

(near-tip) closure developed in the immediate wake of the crack tip is increased as growth extends into compressive stress field of the overload plastic zone.

The concept of dual closure levels is consistent with the observations of Nowack et al. (21), and particularly Paris and Hermann (9) who observed that elastic compliance curves displayed two distinct linear portions following a single overload cycle, corresponding to what they termed upper and lower opening loads. They reported that the upper opening load increased at the overload, whereas the lower opening load showed an immediate decrease. Here the upper opening load is interpreted as being due to the near-tip closure of the increment of crack advance <u>within the overload plastic zone</u>, and the lower opening load, due to the far-field closure of the crack length behind the overload event, as depicted schematically in Fig. 6.12.

6.5.3 Influence of Baseline Stress Intensity Range

The increase in post-overload delay with both increasing and decreasing baseline ΔK, observed in the present study (Fig. 6.4) and previously (12,23,24), is also consistent with the concept of crack closure, specifically with expected variation of the most prominent mechanisms of shielding. In aluminum alloys, these mechanisms appear to be induced by cyclic plasticity (zone shielding), crack deflection and meandering, and the consequent closure induced by wedging of enlarged fracture surface asperities (contact shielding) (32,34-39). The role of oxide-wedging appears to be relatively minor as the thickness of the excess oxide films in these alloys remains small compared to the CTODs (36,37). A schematic illustration of the

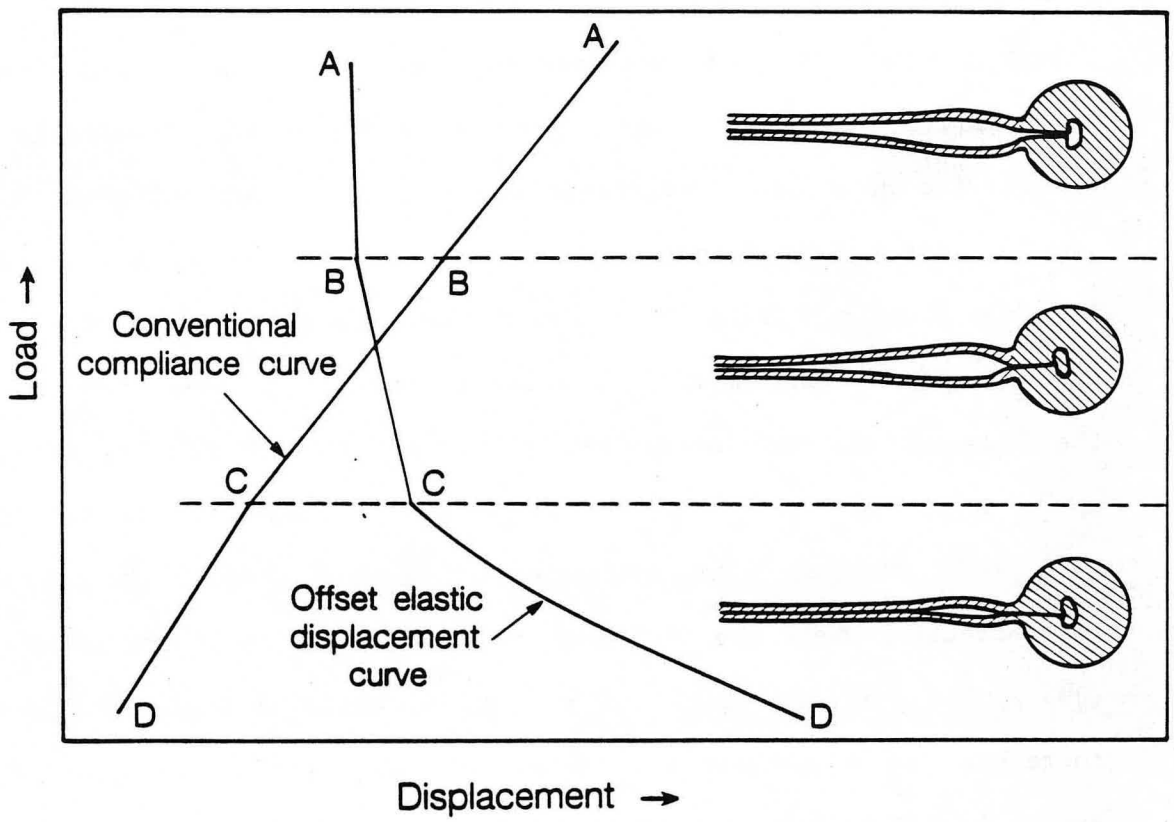

Fig. 6.12: Illustration of compliance curve, measured globally in the post-overload retardation region using a back-face strain gauge measurements, used to determine crack closure loads. Segment DC represents the crack fully closed. During segment CD the crack is open except for the post-overload extension into the overload plastic zone at the tip. In segment BA the crack is fully open.

probable variation of shielding by each of these mechanisms is shown in Fig. 6.13 as a function of baseline ΔK level (see also ref. 43). Crack deflection produces a multiplicative reduction in the local Mode I stress intensity, and therefore will have an equal effect (for a constant crack path morphology) for all values of ΔK_B. Conversely, in accord with numerical predictions (44,45), the effect of plasticity-induced closure, in common with all zone shielding mechanisms, will increase with increasing plastic zone size (and hence increasing ΔK_B), although this mechanism will diminish at very large zone sizes due to the loss of elastic constraint (i.e., as the net section stresses approach yield). The effect of wedge/contact shielding, on the other hand, will decrease with increasing ΔK_B level, as this mechanism is most effective where the CTOD and the size of the wedge are comparable (30). The combined effect of all these shielding mechanisms should therefore see a minimum at intermediate ΔK_B levels, as depicted in Fig. 6.13. Since the primary mechanisms responsible for post-overload retardation behavior clearly involve crack tip shielding, a similar variation in the magnitude of the delay with baseline ΔK level (Fig. 6.4) is to be expected.

6.6 CONCLUSIONS

Based on experimental study on the transient fatigue crack growth behavior following single (spike) tensile overloads in aluminum-lithium alloys, specifically, 2090-T8E41 and comparison to traditional 2124-T351 and 7150-T651 alloys, the following conclusions can be made:

1. The immediate, yet brief, acceleration in growth rate following the application of a single tensile overload is associated with a small

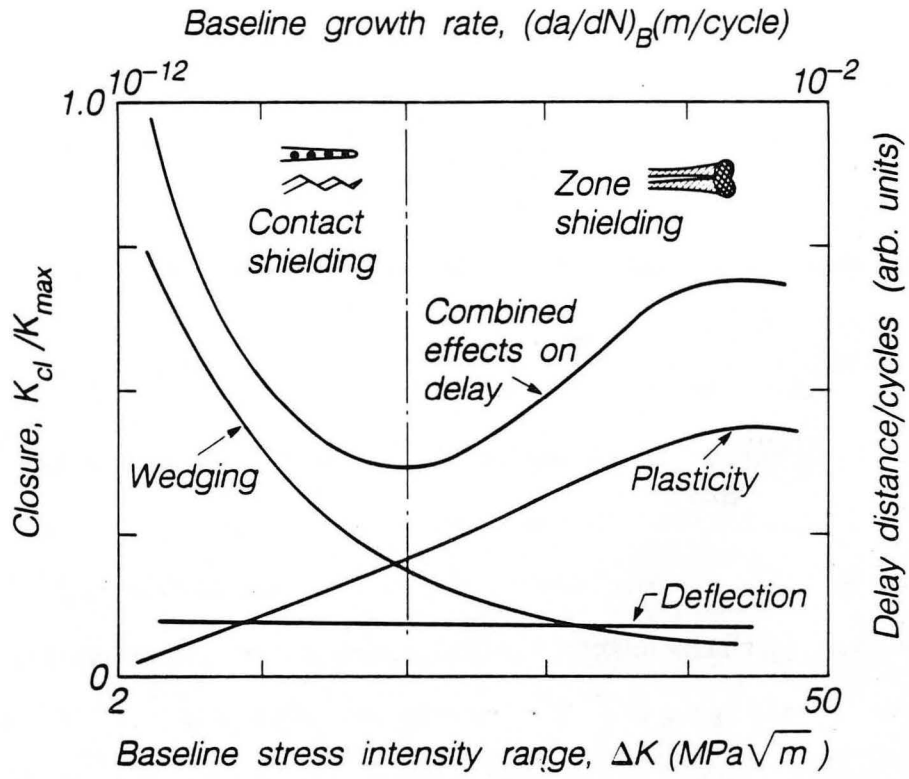

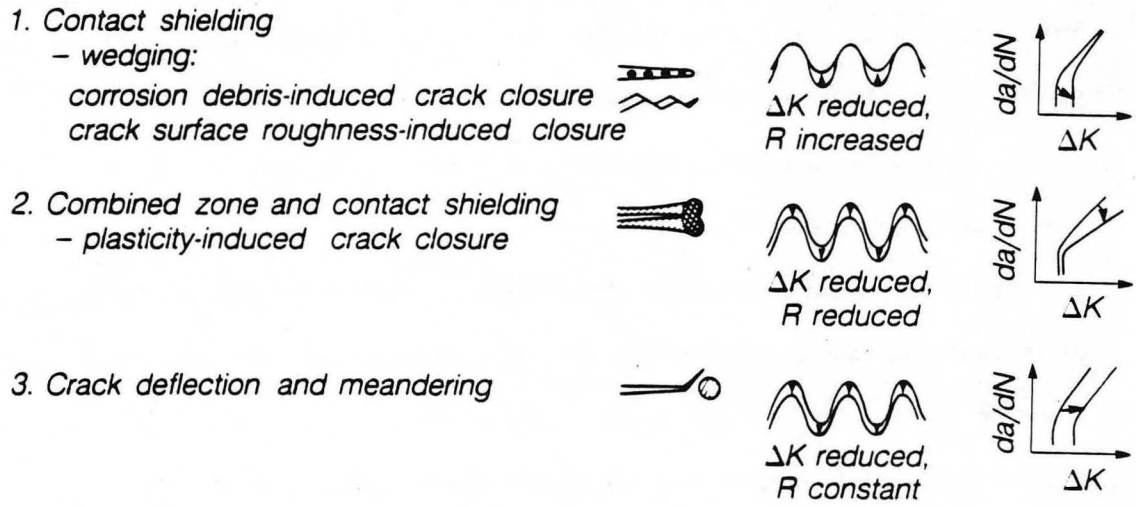

XBL 879-11154

Fig. 6.13: Schematic illustration of the variation in crack closure, defined as the ratio K_{cl}/K_{max}, with baseline stress intensity range ΔK_B, for the principal mechanisms of shielding. Contact/wedge shielding mechanisms, such as roughness-induced closure, are promoted at low ΔK whereas zone shielding mechanisms, such as plasticity-induced closure, are promoted at high ΔK.

decrease in far-field (global) crack closure (measured using back-face strain compliance techniques), due to crack tip blunting and consequent increased crack opening displacement at the overload.

2. Subsequent crack growth is progressively retarded as the crack extends into the overload plastic zone, due to the enhanced compressive residual stress field and resulting near-tip crack closure developed in the immediate wake of the crack tip (acting on the post-overload crack extension). The minimum in the retarded growth rates corresponds to a maximum in the near-tip (local) crack closure levels (measured by side-face strain gauges). The origin of such closure is associated with cyclic plasticity, crack deflection and the consequent crack wedging of enlarged fracture surface asperities. Fractographically, little evidence was seen of changes in the fracture surface morphology or the crack front profile due to the overload.

3. Based on surface observations, the application of the overload was also concurrent with marked crack deflection along shear bands at the tip and subsequent deflection back to the original crack path, both processes which contributed to the magnitude of the retardation. However, such crack deflection is specifically a surface phenomenon and was not apparent in crack path sections taken at the specimen mid-thickness.

4. The magnitude of the post-overload retardation (for a given % overload and load ratio) was found to be enhanced with both increasing and decreasing baseline stress intensity range, consistent with an increase in zone shielding (plasticity-induced closure) at high ΔK and contact shielding (roughness-induced closure) at low ΔK, respectively.

5. Aluminum-lithium alloy 2090-T8E41 was found to show greater crack growth retardation following single tensile overloads, compared to 2124-T351 and 7150-T651 alloys. This is attributed to the higher levels of crack tip shielding developed in 2090, due primarily to crack deflection and resulting roughness-induced closure arising from highly tortuous crack path morphologies.

6.7 REFERENCES

1. J. Schijve: NRL Report MP 195, National Aeronautical and Astronautical Research Institute, Amsterdam, Holland, 1960.

2. N. A. Fleck: Acta Metall., 33 (1985) p. 1339.

3. W. Elber: in 'Damage Tolerance in Aircraft Structures', ASTM STP 486, American Society for Testing and Materials, Philadelphia, PA, (1971) p. 230.

4. E. F. J. Von Euw, R. W. Hertzberg, and R. Roberts: in 'Stress Analysis and Growth of Cracks', ASTM STP 513, American Society for Testing and Materials, Philadelphia, PA, (1972) p. 230.

5. A. J. McEvily: Metal Science, 11 (1977) p. 275.

6. G. R. Chanani and B. J. Mays: Eng. Fract. Mech., 9 (1977) p. 65.

7. R. D. Brown and J. Weertman: Eng. Fract. Mech., 10 (1978) p. 867.

8. D. Gan and J. Weertman: Eng. Fract. Mech., 8 (1983) p. 155.

9. P. C. Paris and L. Hermann: in 'Fatigue Thresholds', J. Backlund, A. F. Blom and C. J. Beevers (eds.), EMAS Ltd., Warley, U.K., 1 (1982), p. 11.

10. D. L. Davidson, S. J. Hudak, and R. J. Dexter: NASA Contractor Report 172597, National Aeronautics and Space Administration, Langley Research Center (1985).

11. A. F. Blom and D. K. Holm: in 'Role of Fracture Mechanics in Modern Technology', G. C. Shih and H. Nisitani (eds.), Sijthoff and Noordhoff, (1986), p. 235.

12. C. M. Ward-Close and R. O. Ritchie: in 'Mechanics of Fatigue Crack Closure', ASTM STP 982, J. C. Newman and W. Elber (eds.), American Society for Testing and Materials, Philadelphia, PA, (1987), p. 93.

13. C. M. Hudson and H. F. Hardrath: NASA Technical Note D-960, National Aeronautics and Space Administration, Washington, DC (1961).

14. S. Suresh: Eng. Fract. Mech., 8 (1983), p. 577.

15. J. Lankford and D. L. Davidson: in 'SAdvances in Fracture Research', D. Francois et al. (eds.), Pergamon Press, Oxford, 2 (1982), p. 899.

16. R. E. Jones: Eng. Fract. Mech., 5 (1973), p. 585.

17. J. F. Knott and A. C. Pickard: Metal Science, 11 (1977), p. 399.

18. P. J. E. Forsyth: Metals Tech., 12 (1978), p. 351.

19. J. Schijve: in 'Fatigue 87', Proc. 3rd. Int. Conf. on Fatigue and Fatigue Thresholds, R. O. Ritchie and E. A. Starke (eds.), EMAS Ltd., Warley, U.K., 4 (1987).

20. D. P. Musil and R. I. Stephens: in 'Fracture 1977', Proc. 4th. Intl. Conf. on Fracture, D. M. R. Taplin (ed.), Pergamon Press, Oxford, 2 (1977), p. 1017.

21. H. Nowack, K. H. Trautmann, K. Schulte, and G. Lütjering: in 'Fracture Mechanics', ASTM STP 677, C. W. Smith (ed.), American Society for Testing and Materials, Philadelphia, PA, (1979), p. 36.

22. A. U. de Koning: in 'Fracture Mechanics', ASTM STP 743, American Society for Testing and Materials, Philadelphia, PA, (1981), p. 63.

23. R. S. Vecchio, R. W. Hertzberg, and R. Jaccard: Scripta Metall., 17 (1983), p. 343.

24. R. S. Vecchio, R. W. Hertzberg, and R. Jaccard: Fat. Eng. Mat. Struct., 7 (1984) p. 181.

25. T. C. Lindley and C. E. Richards: Mater. Sci. Eng., 14 (1974), p. 281.

26. J. T. P. de Castro and D. M. Parks: Scripta Metall., 16 (1982), p. 1443.

27. D. J. Alexander and J. F. Knott: in 'Fatigue 87', Proc. 3rd. Int. Conf. on Fatigue and Fatigue Thresholds, R. O. Ritchie and E. A. Starke (eds.), EMAS Ltd., Warley, England, 1 (1987), p. 395.

28. P. J. Bernard, T. C. Lindley, and C. E. Richards: Met. Sci., 11 (1977), p. 390.

29. H. Nayeb-Hashemi, F. A. McClintock, and R. O. Ritchie: Eng. Fract. Mech., 18 (1983), p. 736.

30. S. Suresh and R. O. Ritchie: in 'Fatigue Crack Growth Threshold Concepts', D. L. Davidson and S. Suresh (eds.), TMS-AIME, Warrendale, PA (1984), p. 227.

31. S. Suresh: Metall. Trans. A, 14A (1983), p. 2375.

32. R. O. Ritchie and W. Yu: in 'Small Fatigue Cracks', R. O. Ritchie and J. Lankford (eds.), TMS-AIME, Warrendale, PA (1986), p. 167.

33. R. O. Ritchie: in 'Mechanical Behavior of Materials-V', Proc. 5th. Int. Conf., M. G. Yan, S. H. Zhang, and Z. M. Zheng (eds.), Pergamon Press, Oxford, England (1987).

34. S. Suresh, A. K. Vasudévan, and P. E. Bretz: Metall. Trans. A, 15A (1984), p. 369.

35. R. D. Carter, E. W. Lee, E. A. Starke, and C. J. Beevers: Metall. Trans. A, 15A (1984), p. 555.

36. E. Zaiken and R. O. Ritchie: Mater. Sci. Eng., 70 (1985), p. 151.

37. K. V. Jata and E. A. Starke: Metall. Trans. A, 17A (1986), p. 1011.

38. J. Petit, S. Suresh, A. K. Vasudévan, and R. C. Malcolm: in 'Aluminium-Lithium Alloys III', C. Baker, P. J. Gregson, S. J. Harris, and C. J. Peel (eds.), Institute of Metals, London, U.K. (1986), p. 257.

39. W. Yu and R. O. Ritchie: J. Eng. Mater. Technol., Trans. ASME, 109 (1987), p. 81.

40. O. E. Wheeler: J. Basic. Eng., Trans. ASME, 94 (1972), p. 181.

41. J. Willenborg, R. M. Engle, and H. A. Wood: USAF Tech. Mem. No. AFFDL-TM-71-1-FBR, Wright-Patterson AFB, Dayton, OH (1971).

42. G. R. Chanani, G. V. Scarich, and K. M. Bresnahan: in 'Mechanical Properties and Phase Transformations in Engineering Materials', S. D. Antolovich, R. O. Ritchie and W. W. Gerberich (eds.), TMS-AIME, Warrendale, PA (1986), p. 271.

43. J. E. Allison: in 'Fracture Mechanics', ASTM STP 945, R. P. Read and D. T. Reed (eds.), American Society for Testing and Materials, Philadelphia, PA, (1987).

44. J. C. Newman: in 'Methods and Models for Predicting Fatigue Crack Growth under Random Loading', ASTM STP 748, American Society for Testing and Materials, Philadelphia, PA, (1981), p. 53.

45. M. T. Yu, T. H. Topper, D. L. DuQuesnay and M. S. Levin: Intl. J. Fatigue, 8, (1986), p. 9.

CHAPTER VII

EFFECT OF PROLONGED HIGH-TEMPERATURE EXPOSURES

7.1 INTRODUCTION

Potential structural applications for lithium-containing aluminum alloys also include advanced aerospace vehicles, such as the Advanced Tactical Fighter and the National Aerospace Plane (1-3). With certain components, such applications will involve periodic exposures to high temperatures for prolonged time periods during service, which potentially may degrade the mechanical properties of the alloys through overaging. Although the effects of such thermal conditions on the tensile properties of these materials have recently been documented (4), little information exists on the fatigue and fracture toughness properties. Hence, the objective of the present chapter is to study the influence of such high temperature exposures of upto 1000 hr at 163°C on the fatigue and fracture resistance of aluminum-lithium alloys, specifically 2090, and compare the behavior to similarly overaged alloy 2124.

7.2 EXPERIMENTAL DETAILS

Commercial plates of near-peak aged Al-Li-Cu-Zr alloy 2090-T8E41 and naturally aged Al-Cu-Mg alloy 2124-T351 were exposed to high temperatures by further aging them at 163°C (325°F) for 100 and 1000 hr to yield lightly overaged (LOA) and highly overaged (OA) microstructures, respectively. Corresponding room temperature mechanical properties are listed in Table 7.1. Fracture toughness,

Table 7.1: Room Temperature Mechanical Properties of Aluminum Alloys 2090 and 2124 as a Function of Aging Treatment

Alloy	Yield strength (MPa)	Tensile strength (MPa)	Elongation in 25 mm (%)	Fracture toughness (MPa$\sqrt{m}$)
2090-T8E41	548	579	9.3	24
2090 LOA	545	566	12.0	-
2090 OA	466	527	10.0	20
2124-T351	360	488	17.8	-
2124 LOA	474	505	10.7	42
2124 OA	432	477	8.4	45

and (long) fatigue crack propagation tests were conducted in room temperature air, using 6.35 mm thick compact C(T) specimens, machined in the T-L orientation. Constant amplitude fatigue crack growth tests were performed at R = 0.1 for all materials, as per details in Chapter II. Crack lengths and crack closure levels were continuously monitored by d-c potential and back-face strain compliance methods, respectively; fracture surfaces and crack paths were examined by scanning electron and optical microscopy.

7.3 RESULTS

7.3.1 Microstructure

As described in Chapter III, alloy 2090 in the T8E41 condition is strengthened by coherent, ordered δ' precipitates, θ'-like and T_1 plate precipitates and β' dispersoids. Precipitation is generally homogenous within the grains without any preference for grain boundaries (Fig. 7.1a). Prolonged high temperature exposures of 1000 hr at 163°C, result in the coarsening of the matrix δ', θ' and T_1 precipitates, increased density of T_1 along the subgrain boundaries, along with the formation of δ and copper-rich, plate-like precipitates at the grain and sub-grain boundaries. Consequently, a 5 μm wide, (lithium, copper) solute depleted, precipitate free zone (PFZ) develops at the high angle grain boundaries (Fig. 7.1c), similar to results reported for experimental Al-Li-Cu alloys (5,6). Recrystallization or grain growth was not observed during overaging, even for 1000 hr exposures.

7.3.2 Strength and Toughness Properties

Whereas 100 hr overaging treatments on 2090 produced only a negligible change in mechanical properties compared to the T8E41

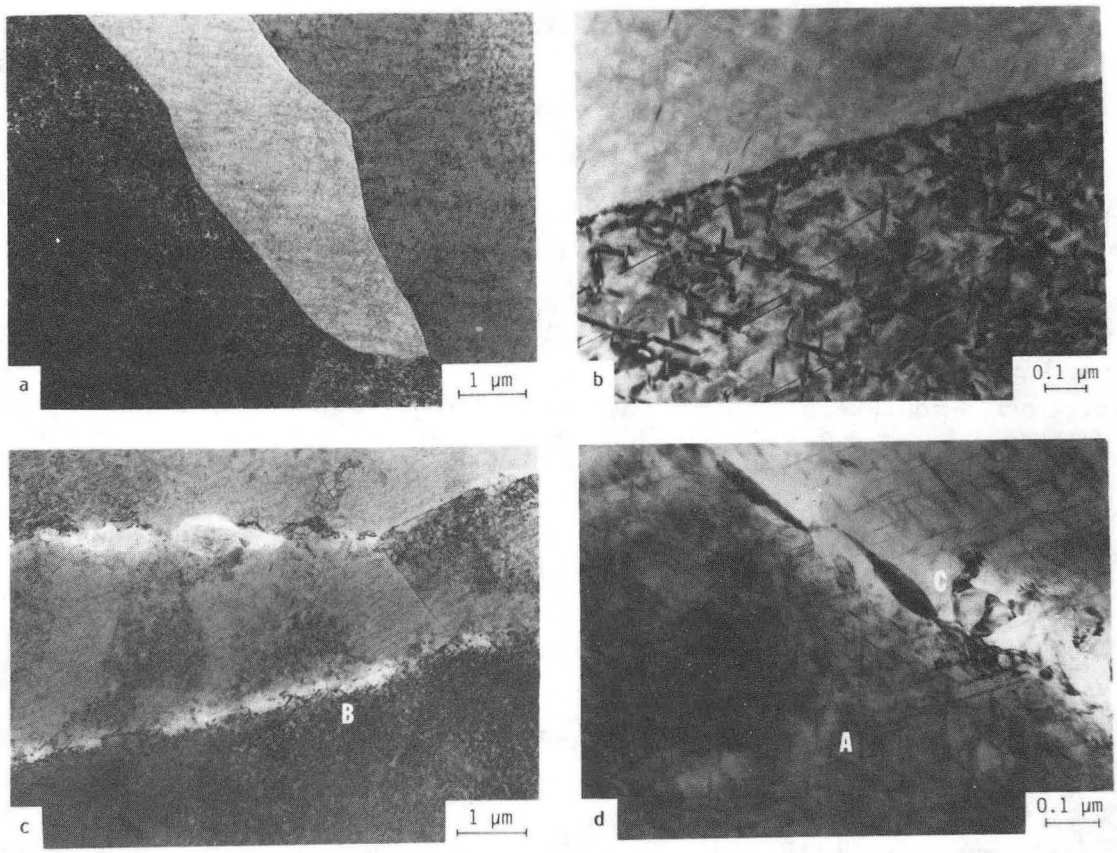

XBB 874-2890A

Fig. 7.1: Transmission electron micrographs of microstructures in the Al-Li-Cu-Zr alloy 2090 in a) b) peak-aged (T8E41) condition, and c) d) overaged (∿ 1000 hours at 163°C) condition. Prolonged aging causes coarsening of matrix precipitates δ′, T_1, θ′, subgrain boundary and grain boundary precipitation of δ or T_2 and Cu-rich precipitates (regions A and B) and resulting in precipitate-free zones.

condition, both yield strength and toughness were reduced roughly 15% following overaging for 1000 hr (Table 7.1). Corresponding results for 1000 hr overaged 2124 show a 20 % increase in strength and a marginal increase in toughness, compared to the T351 temper.

Fracture surfaces of the broken test pieces in 2090 are shown in Fig. 7.2, and indicate predominantly intergranular fracture (intergranular delamination bands run parallel to the crack growth direction), interdispersed with regions of transgranular shear and microvoid coalescence. With increased aging times, the lower toughness is associated with a more pronounced intergranular mode, consistent with the enhanced grain and subgrain boundary precipitation and related PFZs (Fig. 7.1b).

7.3.3 Fatigue Crack Growth Behavior

Constant amplitude fatigue crack propagation data and related crack closure levels are compared in Fig. 7.3 for the T8E41, LOA and OA microstructures of alloy 2090. It is observed that, although the near-threshold growth rates remain relatively unaffected, growth rates above 10^{-9} m/cycle become progressively faster with increasing aging time. Concurrently, associated levels of crack closure show a decrease (Fig. 7.3b), consistent with a change in crack path morphology (Fig. 7.4). In the T8E41 condition, fatigue crack paths show significant crack deflection and meandering, which promote premature wedging of the fracture surface asperities and lower the crack driving force experienced at the crack tip. With prolonged overaging, however, crack paths ultimately become macroscopically linear (Fig. 7.4c), accounting for the lower closure levels and faster growth rates

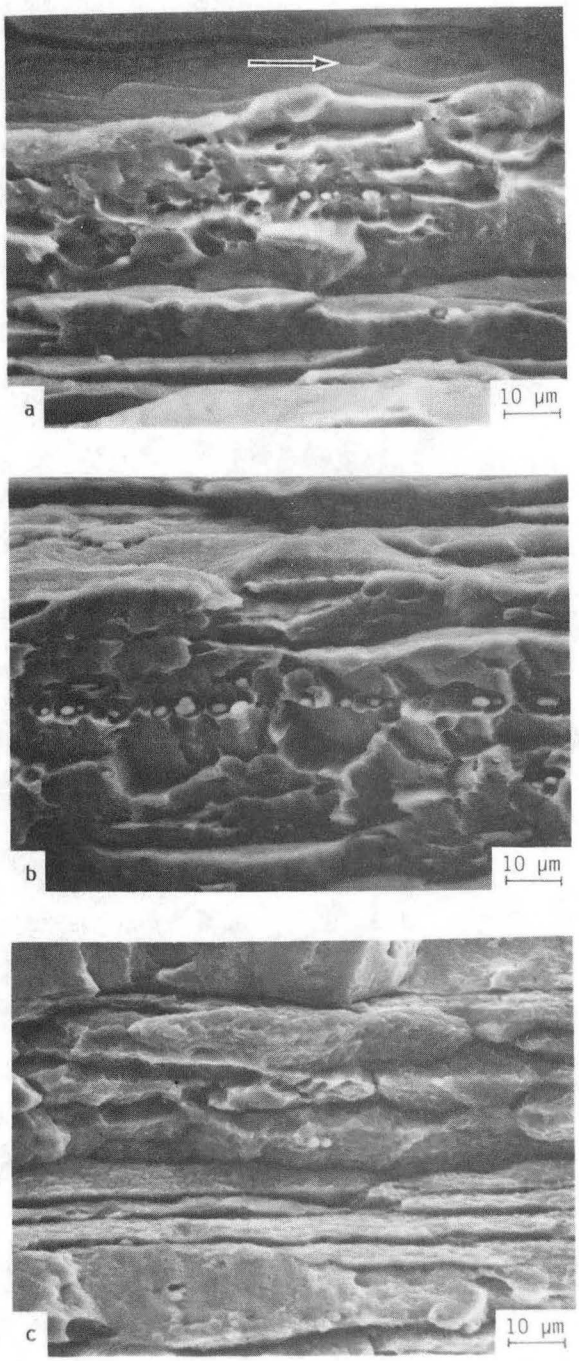

XBB 874-2891A

Fig. 7.2: Scanning electron micrographs showing predominantly intergranular fracture associated with toughness tests in alloy 2090 in a) peak-aged (T8E41), b) ∿100 hr overaged (LOA), and c) ∿1000 hr overaged (OA) conditions. Note evidence of void coalescence around 1 to 2 μm particles, which were identified as Fe/Cu-rich intermetallics. Arrow indicates general direction of crack growth.

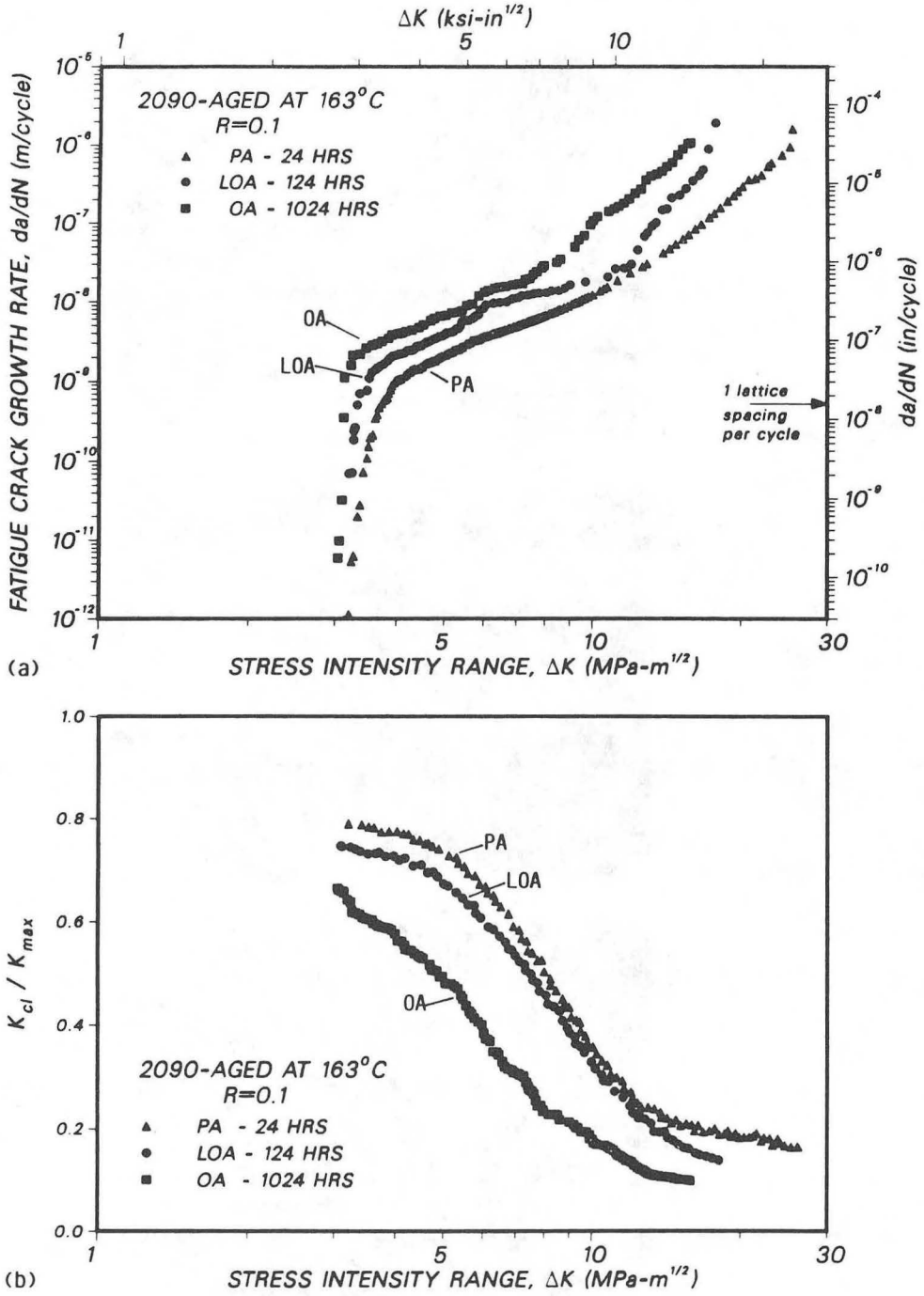

XBL 876-2523

Fig. 7.3: Variation in a) fatigue crack growth rates (da/dN) and b) crack closure (K_{cl}) levels at R = 0.1 in 2090 alloy in the peak-aged (T8E41), lightly overaged (LOA) and overaged (OA) conditions. Note the increase in crack growth rates (particularly above $\sim 10^{-9}$ m/cycle), concomitant with lower closure levels, with prolonged overaging.

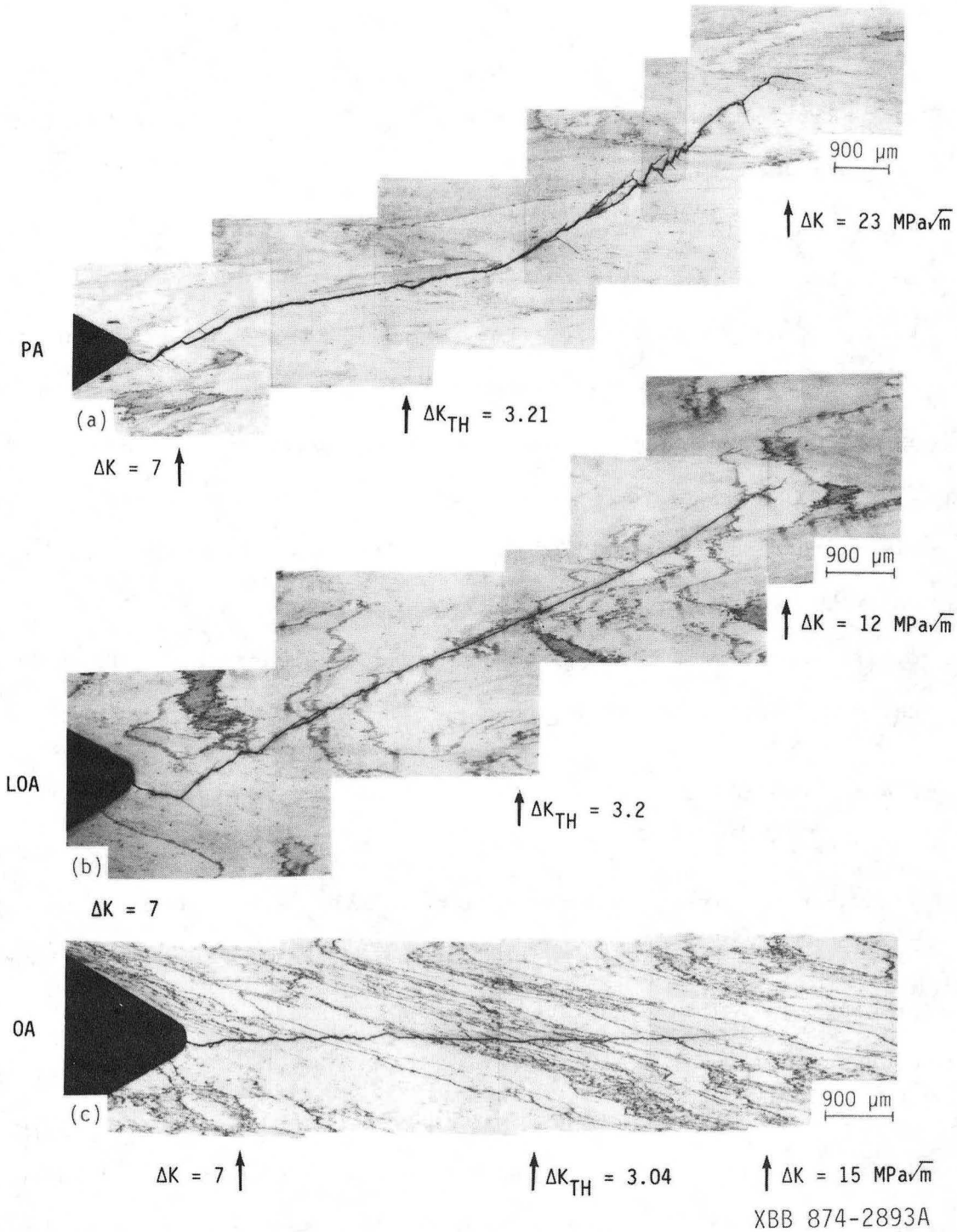

Fig. 7.4: Fatigue crack path morphologies in 2090 alloy, showing a,b) branched and meandering cracks typical of the peak-aged (T8E41) and ∿100 hr overaged (LOA) microstructures, and c) linear crack profiles typical of the ∿1000 hr overaged (OA) microstructures (Optical micrographs obtained using Keller's reagent etch).

(Fig. 7.3).

Representative scanning electron micrographs of the fatigue fracture surfaces in 2090 are shown in Fig. 7.5. It is apparent that the well-defined transgranular facets characteristic of heavily deflected crack paths in the peak-aged condition become "smoothed out" in the overaged microstructures. In addition, there is increasing evidence of crack surface oxidation in the overaged condition. Mean excess oxide thicknesses measured using Auger spectroscopy (see Ch. IV), were found to be of the order of 2 to 10 nm in these microstructures. However, these deposits were considered unlikely to contribute to crack closure (8), as their size was small compared to cyclic and maximum crack tip opening displacements (i.e., which were of the order of 50 and 150 nm, respectively, at ΔK_{TH}).

7.4 DISCUSSION

As discussed briefly in Chapter III, overaging in high-strength aluminum alloys, such as 2024, 7075, etc. generally yields microstructures strengthened by incoherent matrix and grain boundary precipitates, with associated PFZs and decreased slip planarity. Such microstructures show lower strength yet comparable, if not improved, toughness (e.g., 2124 results in Table 7.1), compared to peak tempers, due largely to a change in deformation mode from planar to dispersed slip (e.g., ref. 8). Decreasing slip planarity is often considered to improve toughness, as planar slip can lead to strain localization at grain boundaries, thereby enhancing the formation of microcracks or voids at the grain boundary precipitates (8-14).

Aluminum-lithium alloy 2090, conversely, shows a reduction

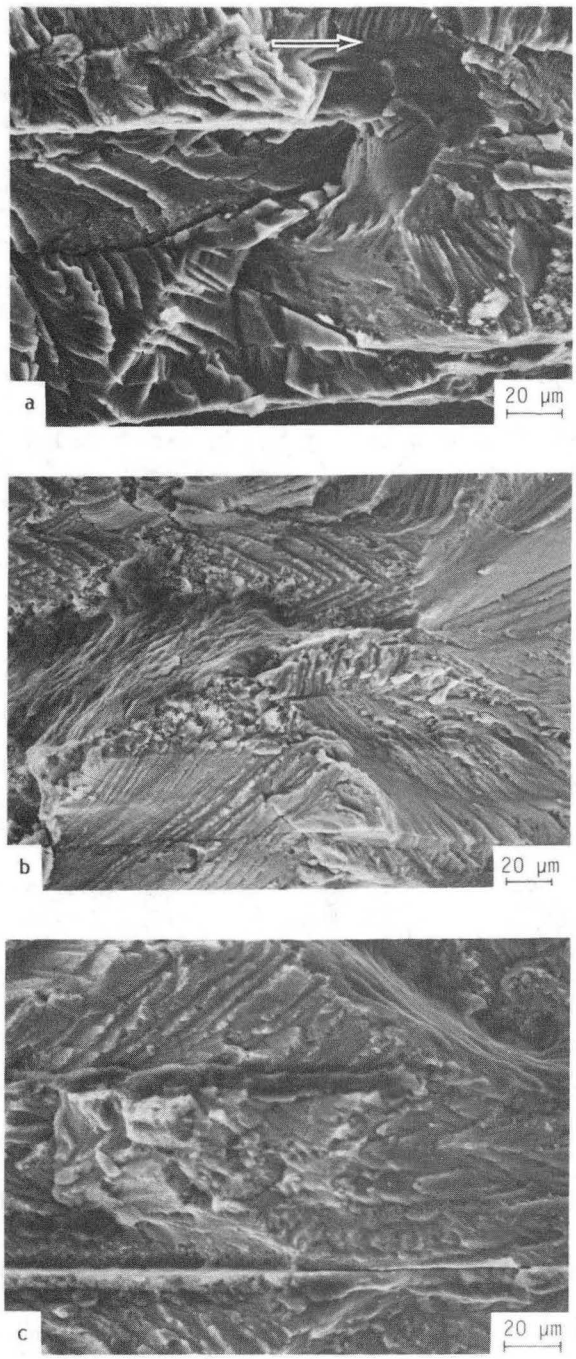

XBB 874-2892A

Fig. 7.5: Scanning electron micrographs of near-threshold fatigue fracture surfaces in 2090 alloy at $\Delta K = 3 - 8$ MPa$\sqrt{m}$ ($R = 0.1$) for a) peak-aged (T8E41), b) $\sim$ 100 hr overaged (LOA), and c) $\sim$ 1000 hr overaged (OA) microstructures. Note that fatigue fractures are transgranular compared to predominantly intergranular fracture in toughness tests (Fig. 7.2). Arrow indicates the general direction of crack growth.

(∿15 %) in strength and toughness on overaging, similar to that reported for experimental Al-Li-Cu-Zr alloys containing 2 to 3 wt% Li (7,9-13). Whereas decreased slip planarity, which results in a reduced propensity for crack bifurcation and branching, has been suggested as one mechanism for decreasing toughness with aging (9,12), no evidence was found for major geometrical changes in crack path in toughness tests of 2090, based on metallographic sectioning taken at specimen mid-thickness. Conversely, the lower toughness on overaging appears to be associated primarily with grain boundary precipitation and resulting strain localization in weak, solute-depleted precipitate-free zones and a decreased volume fraction of strengthening precipitates, similar to observations in peak aged 8091 (refer to Ch. III). It is thus apparent that the commercially peak-aged T8E41 microstructure offers optimum mechanical properties, at least with respect to strength and toughness.

With respect to fatigue crack propagation, the T8E41 microstructure similarly displays optimum properties. It is amply clear (see Ch.s IV-VI) that, this behavior can be attributed primarily to the to the highly tortuous fatigue crack paths, which result from the marked slip planarity and strong texture in this microstructure (8), which in turn promotes significant crack tip shielding or crack closure from consequent asperity wedging. With prolonged overaging, however, crack growth properties are clearly degraded, although the magnitude of the effect is not large and predominates above $\sim 10^{-9}$ m/cycle (Fig. 7.3). From Figs. 7.3 and 7.4, it is evident that the faster growth rates are directly associated with lower crack closure levels, concomitant with a decreasing tendency for crack path tortuosity, and

lower slip reversibility, from the more dispersed nature of slip in the overaged microstructures.

Despite losses in strength, toughness and fatigue resistance with prolonged exposure at 163°C, the properties of overaged 2090 remain comparable, if not superior, to similarly overaged traditional high-strength aluminum alloys in all but (ambient temperature) fracture toughness. For example, overaged 2090 displays similar strength, far superior fatigue crack growth rate behavior below $\sim 10^{-9}$ m/cycle (with a 50 % higher fatigue threshold), and identical behavior above 10^{-9} m/cycle to peak-aged and overaged 2124 alloys (Fig. 7.6a). Essentially, the linear crack paths induced by overaging in 2090 restrict the measured closure levels to that of 2124 (Fig. 7.6b). Thus, even after prolonged high temperature exposures, 2090 compares favorably with the growth-rate behavior of 2124-T351 and 7150-T651, and is superior to 7150-T751 (Fig. 7.7); a direct consequence of the high overall levels of crack closure measured in this material.

7.5 CONCLUSIONS

From the results presented in this Chapter on the fatigue and fracture toughness properties of commercial Al-Li-Cu-Zr alloy 2090-T8E41 after sustained high temperature exposures at 163°C, the following conclusions can be made:

1. Although overaging exposures for 100 hr had little effect on the mechanical properties, 1000 hr exposures were found to induce ∿15 % reductions in the yield strength and fracture toughness, compared to the peak aged condition. Such degradation in strength and toughness on overaging was attributed to the formation of subgrain boundary T_1 or

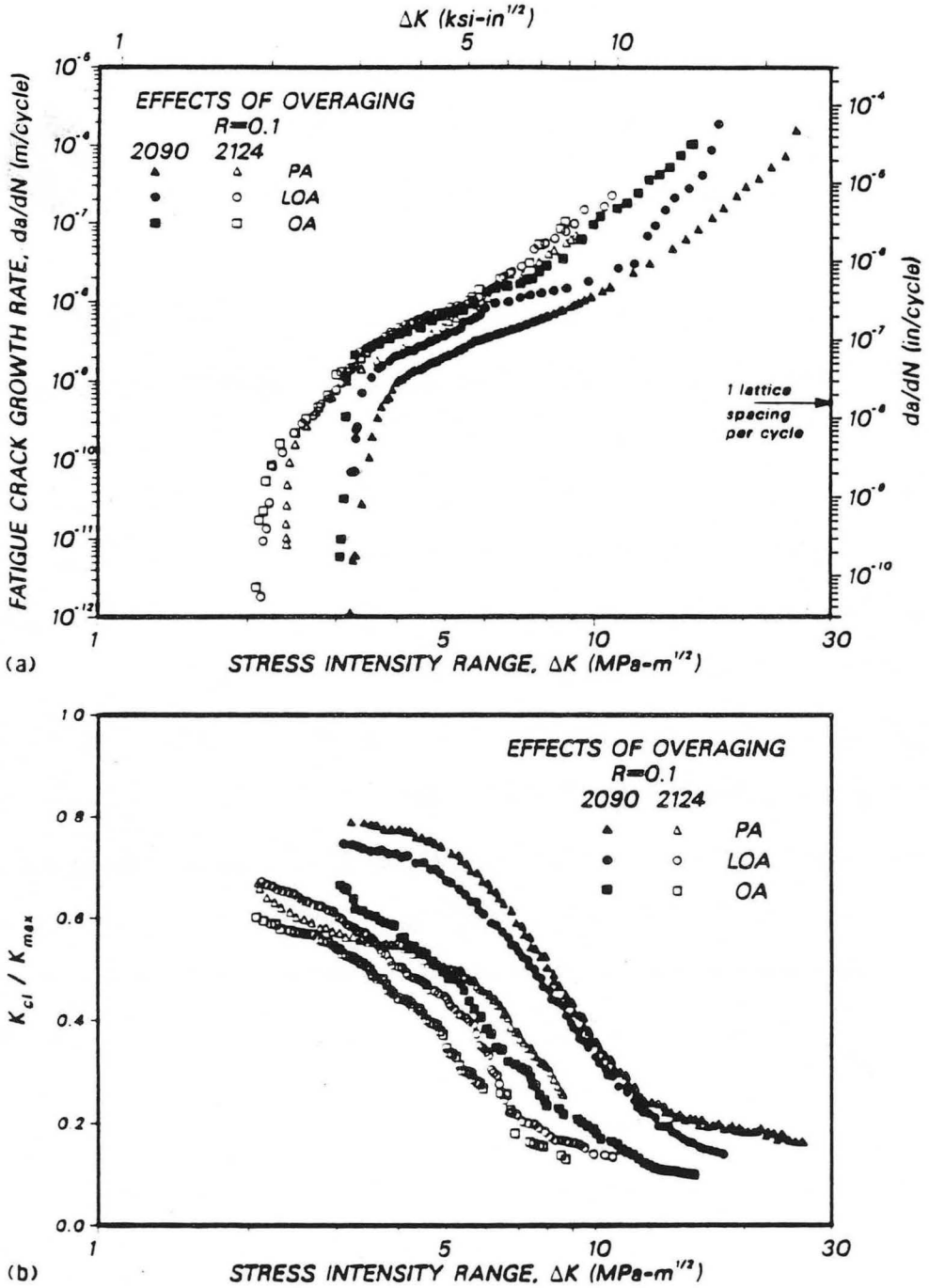

XBL 876-2524

Fig. 7.6: Comparison of a) fatigue crack propagation rates (da/dN), and b) crack closure (K_{cl}) behavior at R = 0.1 in 2090 and 2124 alloys (T-L orientation) subjected to ∿100 hr and ∿1000 hr exposures at 163°C.

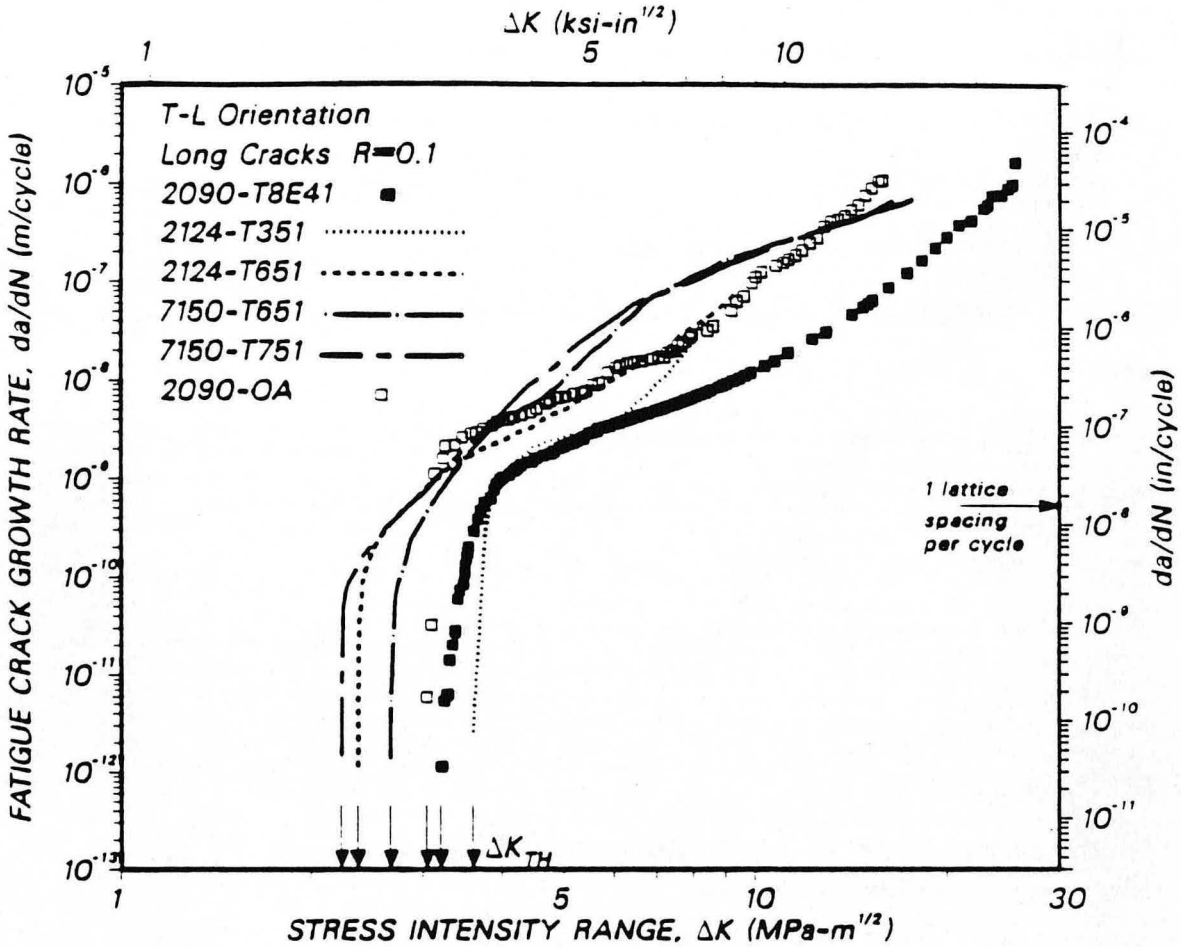

XBL 876-2525

Fig. 7.7: Comparison of the fatigue crack propagation behavior of peak-aged (T8E41) and overaged (1000 hr at 163°C) 2090 alloy with published results for 2124-T351, 7150-T651 and 7150-T751. Note how 2090, even after 1000 hr overaging exposures, remains comparable, if not superior, to traditional high strength aluminum alloys. Data for 2124 and 7150 were taken from refs. 7 and 15.

θ' precipitates and grain boundary δ or T_2 and Cu-rich precipitates, which resulted in Cu, Li-depleted and precipitate-free zones.

2. Fatigue crack growth rates above $\sim 10^{-9}$ m/cycle, progressively increased with prolonged overaging; near-threshold growth rates below $\sim 10^{-9}$ m/cycle were relatively unchanged. Such behavior was related to a measured reduction in crack closure levels, consistent with a macroscopic change from branched to linear crack paths, in overaged, compared to peak-aged microstructures.

3. Despite reductions in strength and fatigue resistance following 1000 hr exposures at 163°C, fatigue crack growth rates in overaged 2090 are still comparable, if not superior, to similarly overaged 2124 alloys, and to commercially heat-treated 2124-T351, 7150-T651 and 7150-T751 alloys.

7.6 REFERENCES

1. T. H. Sanders and E. A. Starke (eds.): Aluminum-Lithium Alloys, TMS-AIME, Warrendale, PA (1981).

2. T. H. Sanders and E. A. Starke (eds.): Aluminum-Lithium Alloys II, TMS-AIME, Warrendale, PA (1983).

3. C. Baker, P. J. Gregson, S. J. Harris, and C. J. Peel (eds.): Aluminium-Lithium Alloys III, Institute of Metals, London, U.K. (1986).

4. R. C. Malcolm, F. J. Cordier, and R. J. Bucci: Alcoa Alloy Tech. Div. Report No. 56-86-AH429, Aluminum Company of America, PA (1987).

5. C. Kumai, J. Kusinski, G. Thomas, and T. M. Devine: Corrosion, (1987), in review.

6. R. J. Rioja, P. E. Bretz, R. R. Sawtell, W. H. Hunt and and E. A. Ludwiczak: in 'Aluminum Alloys: Their Physical and Mechanical Properties', E. A. Starke and T. H. Sanders (eds.), EMAS Ltd., Warley, U. K. (1986).

7. K. V. Jata and E. A. Starke: Metall. Trans. A, 17A (1986), p. 1011.

8. G. G. Garrett and J. F. Knott: Metall. Trans. A, 9A (1978), p. 1187.

9. S. Suresh, A. K. Vasudévan, M. Tosten, and P. R. Howell: Acta Metall., 35 (1987) p. 25.

10. T. H. Sanders and E. A. Starke: Acta Metall., 30 (1982), p. 927.

11. P. J. Gregson and H. M. Flower: Acta Metall., 33 (1985), p. 527.

12. A. K. Vasudévan and R. D. Doherty: Acta Metall., 35 (1987), p. 25.

13. A. K. Vasudévan and S. Suresh: Mater. Sci. Eng., 72 (1985), p. 37.

14. B. Noble, S. J. Harris, and K. Dinsdale: Metal. Sci., 16 (1982) p. 425.

15. E. Zaiken and R. O. Ritchie: Mater. Sci. Eng., 70 (1985), p. 151.

CHAPTER VIII

FRACTURE TOUGHNESS AT CRYOGENIC TEMPERATURES

8.1 INTRODUCTION

Very recently, there has been increasing interest in the cryogenic properties of commercial aluminum-lithium alloys, following reports of a marked increase in ductility, fatigue resistance and especially fracture toughness with decrease in temperature from ambient to 4 K (1-4). As mentioned earlier in chapter I, though developed primarily as low-density high-strength airframe materials, Al-Li alloys have additionally become attractive candidate materials for liquid-hydrogen, -oxygen and -natural gas fuel tanks, in particular for existing and future transatmospheric and hypersonic aircraft applications.

Although, the behavior is not unlike other high-strength aluminum alloys (e.g., 2219) which show improved toughness at low temperatures (5), mechanistic origins of the significantly improved cryogenic properties of aluminum-lithium alloys remain unclear. Explanations based on higher strain-hardening rates, associated with more homogeneous plastic deformation (6,7), and solidification of Na, K, H-rich liquid phases at grain boundaries (2,3,8) have been proposed for Al-Li alloys, although such suggestions are seemingly inconsistent with results (4,9) which show increased low-temperature fracture toughness for the longitudinal (L-T, T-L) orientations but decreased toughness for the short-transverse (S-L, S-T) orientations. The latter

observations led to proposals (4,9) that the effect was associated more with a greater tendency for short-transverse cracking at low temperatures, similar to the early work of Carman et al. (10) on the toughness of 7075-T6. Such increased short-transverse cracking leads to enhanced crack deflection (9) and more importantly to delamination perpendicular to the crack plane (4,9) for fracture in the L-T and T-S orientations, as discussed earlier in chapter III (refer section 3.4.4), for the crack-divider and crack-arrester orientations, respectively (Fig. 3.13).

Grain structures in commercial aluminum-lithium alloys are largely anisotropic and vary in their degree of coarseness, recrystallization and texture; all factors which may markedly influence the extent of short-transverse cracking. Accordingly, it is the intent of the present chapter, to study the temperature-dependence of the toughness of commercial Al-Li alloys as a function of microstructure and plate orientation, in order to evaluate the mechanisms of extrinsic toughening resulting from delamination perpendicular to the crack plane. Moreover, since extensive low-temperature fracture-toughness data on lithium-containing alloys are not readily available in literature, the cryogenic strength-toughness relations of other aluminum-lithium alloys are concurrently verifed.

8.2 EXPERIMENTAL DETAILS

Commercial plates of commercial aluminum-lithium alloys 2091, 8090 and 8091 were studied in the naturally-aged T351 and peak-aged T8X conditions; 2090 in the experimental T8E41 temper. Fracture toughness tests were performed on fatigue precracked specimens at both ambient

(298 K) and liquid-nitrogen (77 K) temperatures in the L-T and S-L orientations (see Ch. II for details). All results represent plane-strain values, except where noted. Corresponding uniaxial tensile properties (longitudinal L direction) were assessed using 6.4 mm round tensile specimens with a 25 mm gauge length.

Fatigue-precracked compact C(T) specimens of 2090-T8E41, with varying thickness between 0.5-13 mm, were used to study the influence of thickness on fracture toughness; anti-buckling guides were employed to prevent out-of-plane shear in the thinner geometries. Since the through-thickness strength variations of commercial Al-Li alloy plate can be as large as 20 % (11), all specimens were machined from the plate mid-section.

To evaluate the influence of stress state on ductility (12), additional tests were performed at 298 and 77 K on circumferentially-notched tensile samples, with notch-root radii, ρ, varying between 0.6 and 3.2 mm. Fracture strains were determined by continuously monitoring the diameter at the notch root using a diametral extensometer, and computed from the Bridgeman analysis as (13):

$$\bar{\varepsilon}_p = 2 \ln (r_o/r_{min}) \qquad \text{.....(1)}$$

where ε_p is the equivalent plastic strain and r_o and r_{min} and the initial and minimum radii of the notched cross-section. With this geometry, the stress-state at the center of the specimen, defined in terms of the ratio of hydrostatic stress, σ, to equivalent stress, $\bar{\sigma}$, is given by:

$$\sigma/\bar{\sigma} = 1/3 + \ln \left(1 + \frac{r_{min}}{2\rho}\right) \qquad \text{.....(2)}$$

Scanning electron microscopy (SEM) was performed on all fractured samples to elucidate the failure mechanisms. Metallographic sections of the crack path morphology were taken, both parallel and perpendicular to the crack-growth direction.

8.3 RESULTS

8.3.1 Uniaxial Tensile Properties

Uniaxial tensile properties of the commercial Al-Li alloys at 77 and 298 K are compared in Table 8.1. Yield and tensile strengths show a ∿10 to 40 % increase at 77 K; surprisingly, elongation values show a larger increase by 10 to 75 % and strain-hardening coefficients by a factor of approximately two. Thus, in the longitudinal direction examined, strength, ductility and strain-hardening rates all <u>increase</u> with <u>decrease</u> in temperature. All tensile failures at 77 K were seen to occur at the maximum load, without evidence of any necking prior to fracture.

8.3.2 Fracture-Toughness Properties

Plane-strain fracture-toughness data are also listed in Table 8.1. It can be seen that, at both low and high temperatures, K_{Ic} values for the L-T (crack-divider) orientation exceed those for the S-L (crack-delamination) orientation by between 18 and 375 %; additional results in 2090-T8E41 from Ch. III show that the toughness in the T-S (crack-arrester) orientation exceeds that in the L-T orientation by 80 %. However, the low-temperature strength-toughness properties of all Al-Li alloys in the L-T orientation, except 8090-T351 and 8091-T351, are superior to that of traditional high-strength aluminum alloys (Fig. 8.1) at ambient temperatures. Not all alloys, however, show

Table 8.1: Fracture Toughness and Tensile Properties* of Commercial Aluminum-Lithium Alloys at 298 K and 77 K

Alloy	Yield Strength (MPa)		U.T.S. (MPa)		% Elongation (on 25 mm)		Fracture Toughness K_{IC} (MPa$\sqrt{m}$)		Strain-Hardening Exponent (n)	
	298 K	77 K	298 K	77 K	298 K	77 K	298 K	77 K	298 K	77 K
2090-T8E41	552	587	589	642	11	14	36	51+ (L-T)	0.06	0.15
							17	15 (S-L)		
							65	- (T-S)		
2090-OA	466	-	527	-	10	-	22	24 (T-L)		
2091-T351	369	442	451	596	10	16	33+	41+ (L-T)	0.12	0.22
							19	17 (S-L)		
2091-T8X	425	483	481	610	8	14	46+	44+ (L-T)	0.10	0.21
							25	16 (S-L)		
8090-T351	226	256	352	486	17	24	27+	20 (L-T)	0.19	0.34
							16	17 (S-L)		
8090-T8X	482	-	534	-	6	-	36	38 (L-T)	0.08	-
							13	12 (S-L)		
8091-T351	309	382	417	572	11	14	38+	28 (L-T)	0.16	0.28
							17	10 (S-L)		
8091-T8X	537	574	581	697	6	12	20	38 (L-T)	0.07	0.18
							9	8 (S-L)		

*L direction

+K_q values not meeting the ASTM plane-strain thickness criterion.

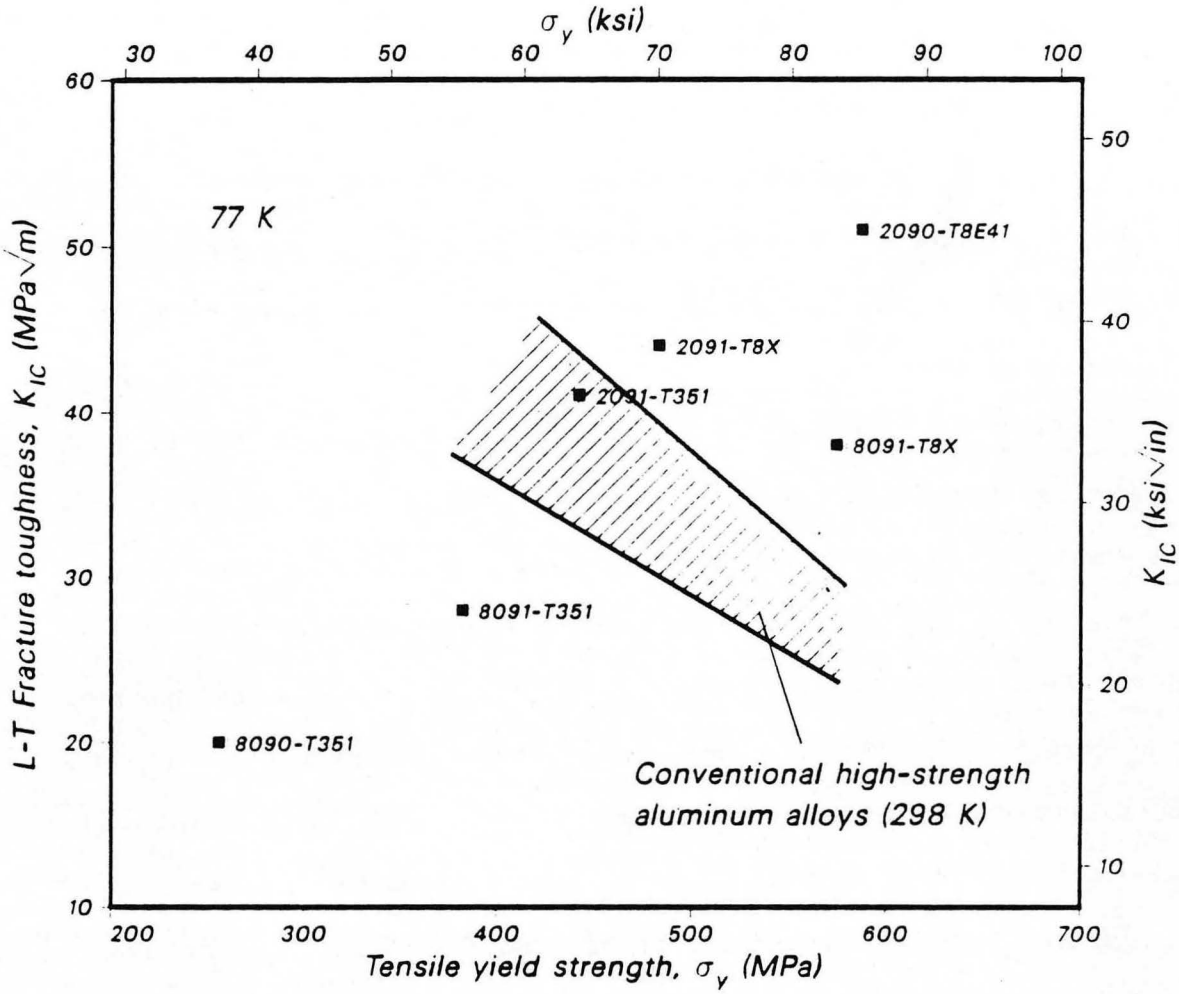

XBL 883-843

Fig. 8.1: Combination of yield-strength and fracture-toughness properties for commercial aluminum-lithium alloys at cryogenic temperatures, showing a comparison with ambient data on typical aerospace high-strength aluminum alloys (hatched region).

improved toughness at 77 K. As illustrated in Fig. 8.2, compared to ambient-temperature behavior, only 2090-T8E41, 2091-T351, 8090-T8X and 8091-T8X have higher K_{Ic} values at 77 K in the L-T orientation; 2091-T8X, 8090-T351 and 8091-T351, conversely, display the more common behavior of lower toughness at the lower temperature. More importantly, all alloys show a small decrease in toughness with decreasing temperature for the short-transverse (S-T) orientation.

8.3.3 Fractography

Distinctions between alloys which show increasing rather than decreasing toughness at lower temperatures are evident from observations of fracture-surface and crack-path morphology. Illustrated in Fig. 8.3, are the fracture surfaces for 2091-T8X at 298 and 77 K in the L-T (crack-divider) orientation. Clearly apparent is a change from fibrous, ductile fracture (microvoid coalescence around dispersoids and constituent particles, with large macroscopic shear lips) at 298 K to transgranular shear failure (with intergranular delamination bands or secondary cracks running parallel to the crack-growth direction and normal to the short-transverse direction) at 77 K, a transition which induces a marked change in crack-path morphology (Figs. 8.3c and 8.3f). The behavior is typical of microstructures which show lower toughness (L-T) at cryogenic temperatures, namely 2091-T8X, 8090-T351 and 8091-T351.

Conversely, microstructures which show higher fracture toughness (L-T) at cryogenic temperatures, namely peak aged 2090, 8090, 8091 and underaged 2091, undergo no such fracture-mode transition; a coarse transgranular shear mechanism, with regions of void coalescence (around

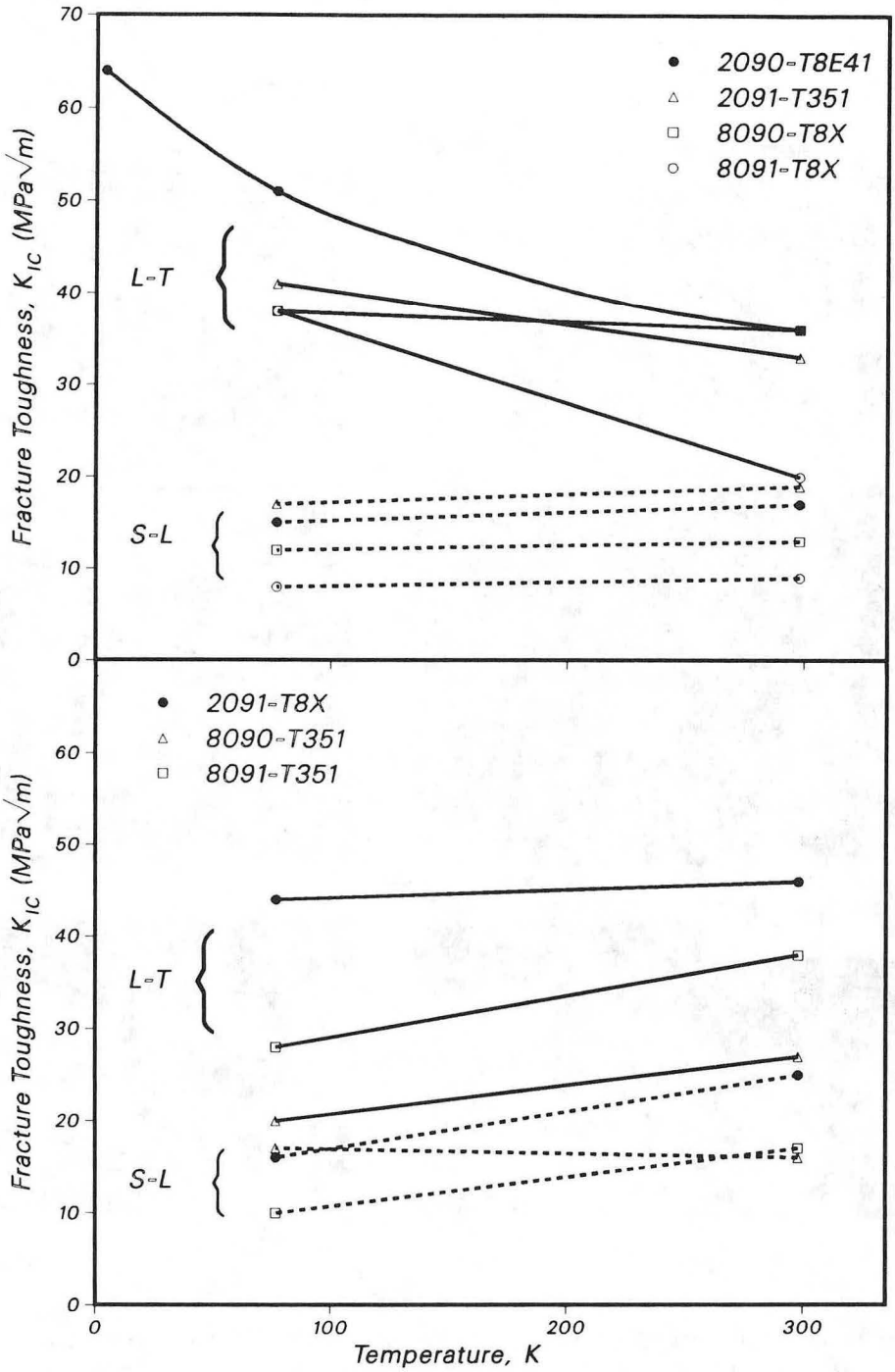

XBL 883-845

Fig. 8.2: Variation in fracture toughness K_{Ic} with temperature for commercial aluminum alloys in both L-T and S-L orientations. Note how certain alloys (2090-T8E41, 2091-T351, 8090-T8X, 8091-T8X) show an <u>increase</u> in L-T toughness with decreasing temperature, whereas the remainder (2091-T8X, 8090-T351, 8091-T351) show a <u>decrease</u>.

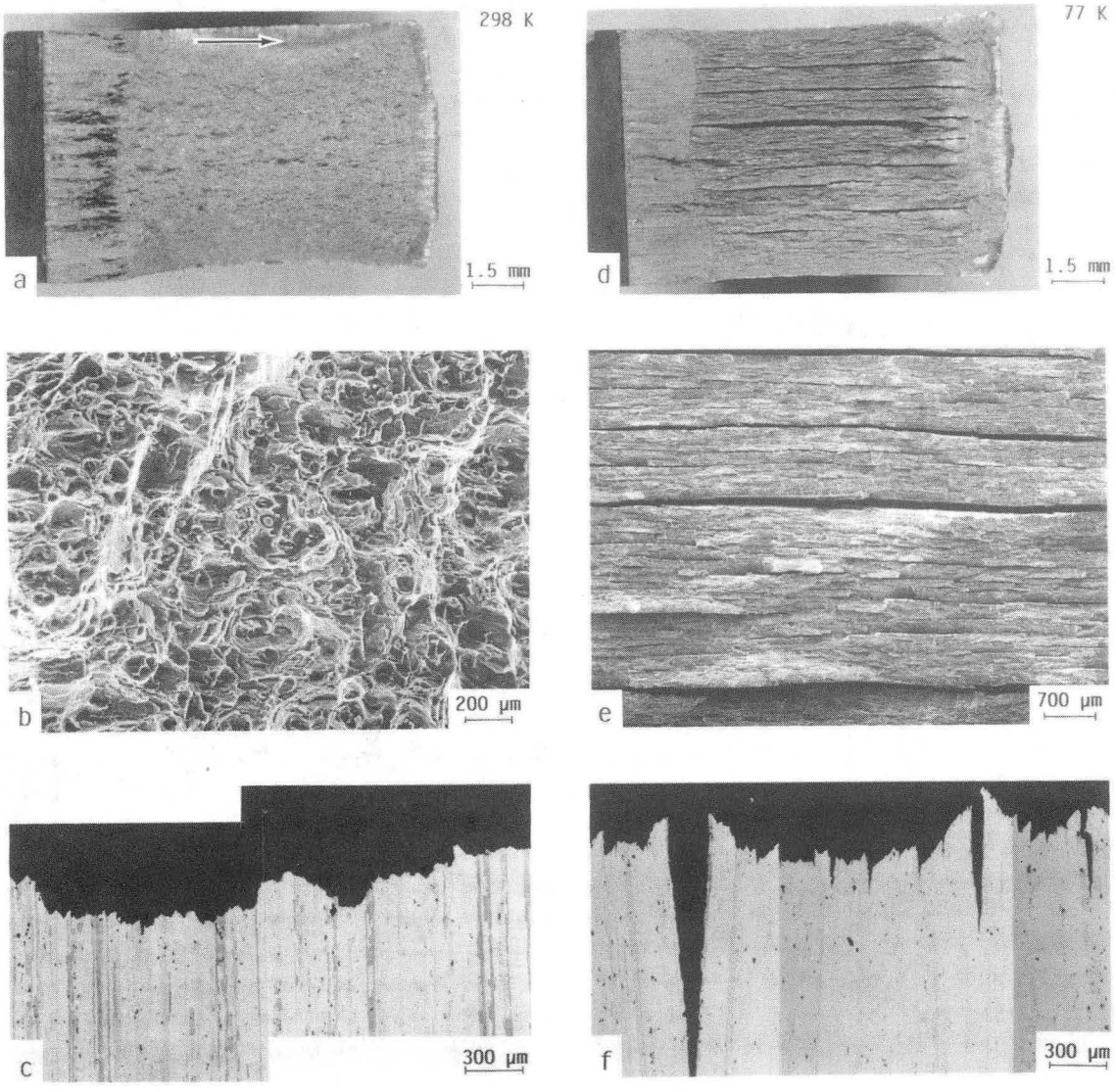

XBB 883-2352A

Fig. 8.3: Fractography and crack-path morphology for the L-T (crack-divider) orientation, typical of alloys which show a fracture-mode transition between ambient and liquid-nitrogen temperatures (2091-T8X, 8090-T351, 8091-T351), showing a,b,c) ductile microvoid coalescence at 298 K, and d,e,f) transgranular shear fracture at 77 K. Note the presence of intergranular (short-transverse) delaminations at 77 K. Fracture surfaces are for 2091-T8X. Arrow indicates general direction of crack growth.

Fe- and Cu-rich intermetallics in 2090) prevails at 77 and 298 K although the incidence and the degree of intergranular (short-transverse) delamination cracking is markedly enhanced at the liquid-nitrogen temperatures (Fig. 8.4).

Fracture surfaces for the S-L orientation, on the other hand, are totally intergranular for all alloys, and involve a delamination-type failure, decorated with interdispersed 1-5 μm diameter Fe-/Cu-rich intermetallic particles (14), both at 298 K and 77 K (Fig. 8.5).

8.4 DISCUSSION

8.4.1 Cryogenic Fracture Toughness of Al-Li alloys

The present results, despite confirming prior observations on the cryogenic properties of 2090-T8E41, clearly demonstrate that improved fracture toughness (L-T) at low temperatures is not common for all aluminum-lithium alloys. Specifically, 2090-T8E41, 2091-T351, 8090-T8X and 8091-T8X, show a marked improvement in strength, ductility and (L-T) fracture toughness with decrease in temperature. These beneficial effects however, are not seen in the short-transverse orientations, and are not at all apparent in certain alloys, namely 2091-T8X, 8090-T351 and 8091-T351, which show a fracture-mode transition from ductile fracture (microvoid coalescence) at 298 K to transgranular-shear mode at 77 K.

These observations, that the temperature dependence of K_{Ic} differs with both orientation and alloy composition/aging condition, would appear to rule out certain published explanations (2,3,6,7) for the increase in toughness with decreasing temperature in Al-Li alloys. For example, Webster (2,3,8) has claimed that the effect is due to the

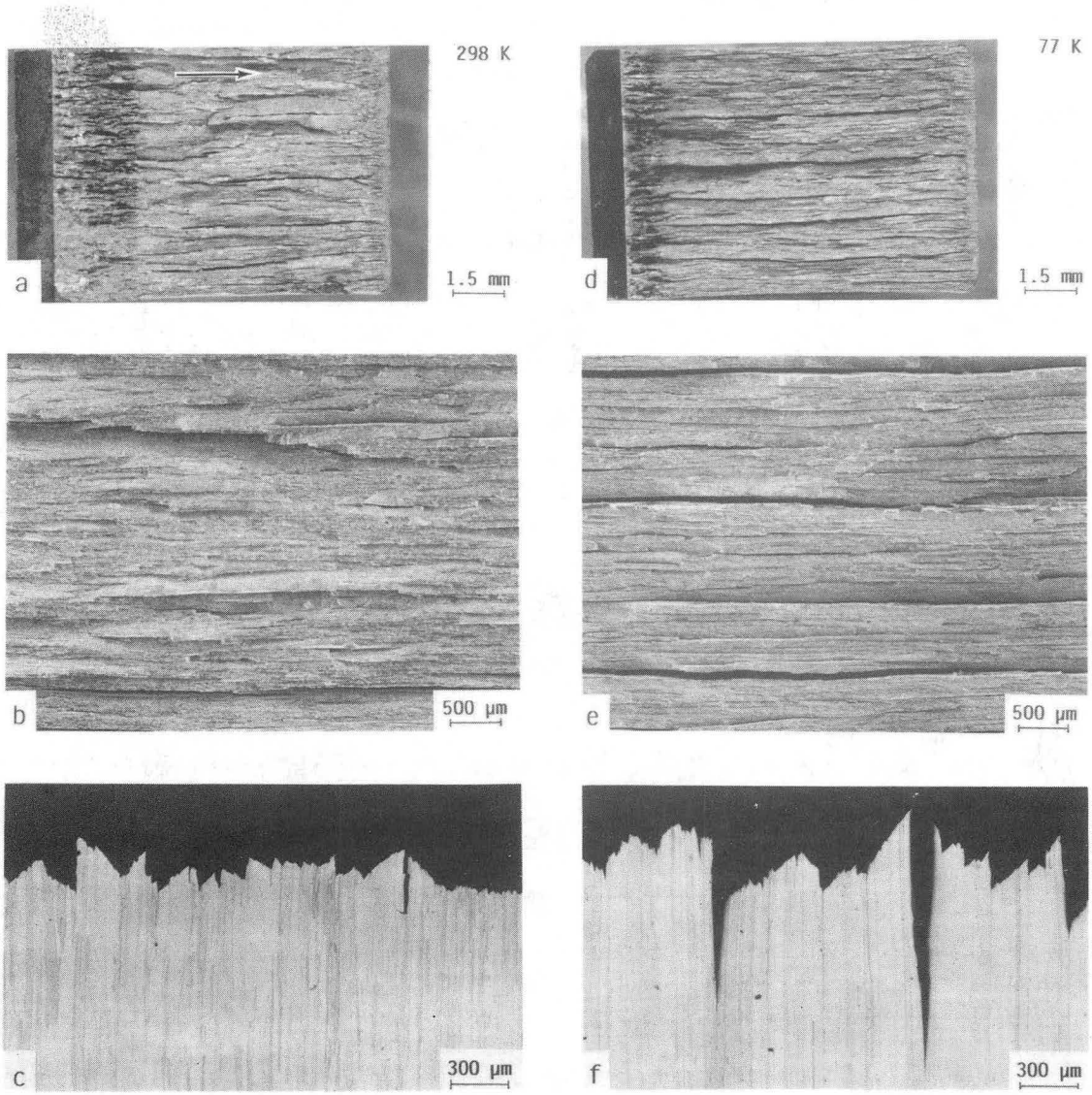

XBB 883-2353A

Fig. 8.4: Fractography and crack-path morphology for the L-T (crack-divider) orientation, typical of alloys which show no fracture-mode transition between ambient and liquid-nitrogen temperatures (2090-T8E41, 2091-T351, 8090-T8X, 8091-T8X), showing transgranular shear fracture at a,b,c) 298 K and d,e,f) 77 K. Note how the degree of intergranular (short-transverse) delamination is significantly enhanced at liquid-nitrogen temperatures. Fracture surfaces are for 2090-T8E41. Arrow indicates general direction of crack growth.

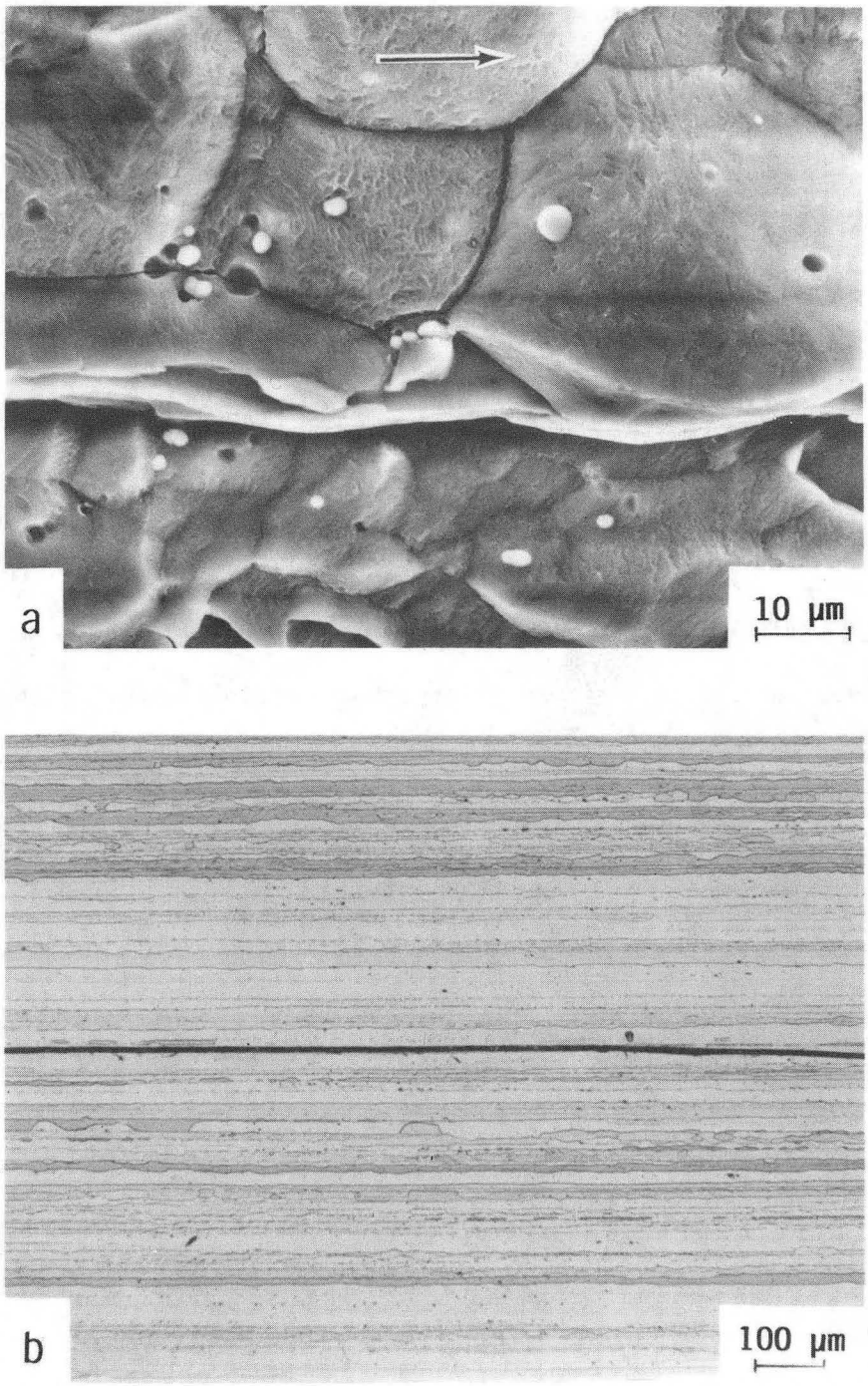

XBB 883-2354A

Fig. 8.5: a) Fractography and b) crack-path morphology for the S-L (crack-delamination) orientation, typical of all alloys at both 77 K and 298 K, showing intergranular delamination-type fracture. Fracture surfaces are for 2090-T8E41 and show evidence of 1 to 2-μm-sized iron-and copper-rich intermetallic particles. Arrow indicates general direction of crack growth.

solidification of grain-boundary Na, K and H -rich liquid phases at lower temperatures; an explanation inconsistent with the observed lower short-transverse toughness at 77 K, and with the fact that the effect can occur in either underaged or overaged microstructures, depending upon the alloy composition. Explanations based on increased homogeneity of slip (6), on the other hand, are consistent with the observed increase in strain-hardening coefficients at lower temperatures, although the higher hardening rates would only impart a beneficial influence on fracture toughness <u>if the fracture mode is strain-controlled</u> (9); however, the explanation precludes the fact that all alloys/aging conditions show improved strain-hardening coefficients at 77 K, but not all alloys show increments in K_{Ic}. Moreover, short transverse (S-L) toughness of all Al-Li alloys and microstructures indicates a drop at cryogenic temperatures.

Considering present results, explanations based on the fracture mechanism (4,9) would appear to be far more reasonable. First, Al-Li alloys, which exhibit a transition from ductile tearing (void coalescence) to transgranular shear with decreasing temperature (Fig. 8.3), would be expected to show higher (L-T) K_{Ic} values at 298 K from an increased contribution to the work of fracture from the plastic deformation involved in the tearing process; such behavior (15) has previously been reported for 7075-T6 and 7475-T6 alloys, which also show such a fracture-mode transition, which is generally the expected behavior for the fracture of metals.

Conversely, the Al-Li alloys, which have lower (L-T) K_{Ic} values at 298 K, exhibit no apparent change in macroscopic fracture mechanism;

the fracture morphology remains transgranular shear at both 77 and 298 K (Fig. 8.4a-b), similar to reported behavior (5) in 2219-T87 which also shows increasing toughness with decreasing temperature. However, there is clear evidence in these alloys of enhanced short-transverse delamination, perpendicular to the main fracture plane (Figs. 8.4c & 8.4f), at lower temperatures, consistent with the lower S-L toughness at 77 K.

8.4.2 Role of delamination toughening

It is considered that the incidence of short-transverse delamination is primarily responsible for the improvements in fracture toughness in Al-Li alloys for orientations in the rolling plane (L-T, T-L) at cryogenic temperatures. Similar to behavior in brazed, soldered or adhesively-bonded multilayer metallic laminates (16-21), granite rocks (22), as-deposited substrate-nucleated pyrolytic carbon (23), and in anisotropic materials where the toughness is low in the short-transverse (S-T, S-L) orientations (24-26), the resulting delamination perpendicular to the crack plane leads to markedly increased fracture toughness in the T-S (crack-arrester) orientations through crack deflection/bifurcation at ∿90 deg (the Cook-Gordon mechanism (27) for crack stopping at weak interfaces) as shown for 2090-T8E41 (see Fig. 3.14, Sec. 3.4.3); it <u>can</u> also lead to increased toughness in the L-T or T-L (crack-divider) orientations due to loss of through-thickness constraint (Fig. 3.13). In the latter case, toughening is only significant when the through-thickness splitting causes a plane-strain fracture process to be divided in several parallel (thin-sheet) plane-stress fractures with higher K_c values; in

high-strength/low toughness materials like pyrolytic carbon (23), even after through-thickness splitting the ligaments between the delamination cracks remain in plane strain such that the toughness of the crack-divider orientation is only marginally above that of the short-transverse (presumably due to the additional work of delamination). However, in aluminum-lithium alloys where plane-strain conditions are mostly met for thicknesses in excess of typically $\sim$5 mm*, crack-divider "delamination toughening" is clearly a reality. In addition, such delamination can increase the degree of in-plane crack deflection, which provides a further contribution to toughening (9). The estimated increase in toughness for the crack-divider (L-T) orientation in 2090-T8E41, due to enhanced short-transverse cracking is now examined in detail; analogous calculations for the crack-arrester (T-S) orientation are discussed in Ch. III.

8.4.3 Delamination Toughening in 2090-T8E41

To model simply the magnitude of "delamination toughening" for the crack-divider (L-T) orientations, it is assumed that the material behaves like a laminate, where each of n ligaments, separated by the through-thickness splitting, sees a constant tensile stress. At failure, each ligament carries a load P, given in terms of the full specimen width W and thickness B, by:

$$P = (n\, K_c^L\, W^{0.5})/\{B\, f(a/W)\} \quad , \qquad (3)$$

where f(a/W) is a function of the crack length-to-width ratio for the specific specimen geometry (28) and K_c^L is the fracture toughness of a

---

*Plane-strain conditions, as per ASTM recommendations, however, are assumed for thicknesses (B) in excess of 2.5 $(K_{Ic}/\sigma_y)^2$, where σ_y is the yield strength.

section of thickness B/n. Since the total load carried by the full thickness is nP, the fracture toughness of the laminate will be K_c^L. This constitutes a lower bound estimate as it assumes no short-transverse strength.

To evaluate this approach in the 2090-T8E41 alloy, fracture-toughness tests were performed at room temperature on 500 μm to 13 mm thick specimens to assess the influence of thickness on K_c; results are shown in Fig. 8.6. It is apparent that the plane-strain toughness value (for thicknesses greater than 5-10 mm) of 36 MPa$\sqrt{m}$ is progressively increased with decreasing test-piece thickness to a "plane-stress" value of approximately 45 MPa$\sqrt{m}$ at a 500 μm thickness, concurrent with reduction in constraint (degree of triaxiality) ahead of the crack tip.

Applying these results to crack-divider (L-T) fractures in 2090 (Fig. 8.4), it is seen that the mean spacing (thickness) of the ligaments between the major through-thickness splits at 298 K is approximately 3 mm; the K_c value at this thickness approaches that of plane strain, i.e., of the order of 36 MPa$\sqrt{m}$. In contrast, due to enhanced short-transverse delamination, the mean spacing of the split ligaments at 77 K is less than 1 mm; the appropriate K_c for each ligament is now closer to the plane-stress value, i.e, of the order of 45 MPa$\sqrt{m}$. Using these data, the fracture toughness of 2090 at 77 K would be predicted to be approximately 45 MPa$\sqrt{m}$ on the basis of the observed delamination, an estimate which is reasonably close to the measured value of 51 MPa$\sqrt{m}$.

Alternatively, an estimate of the toughness at 77 K can be made

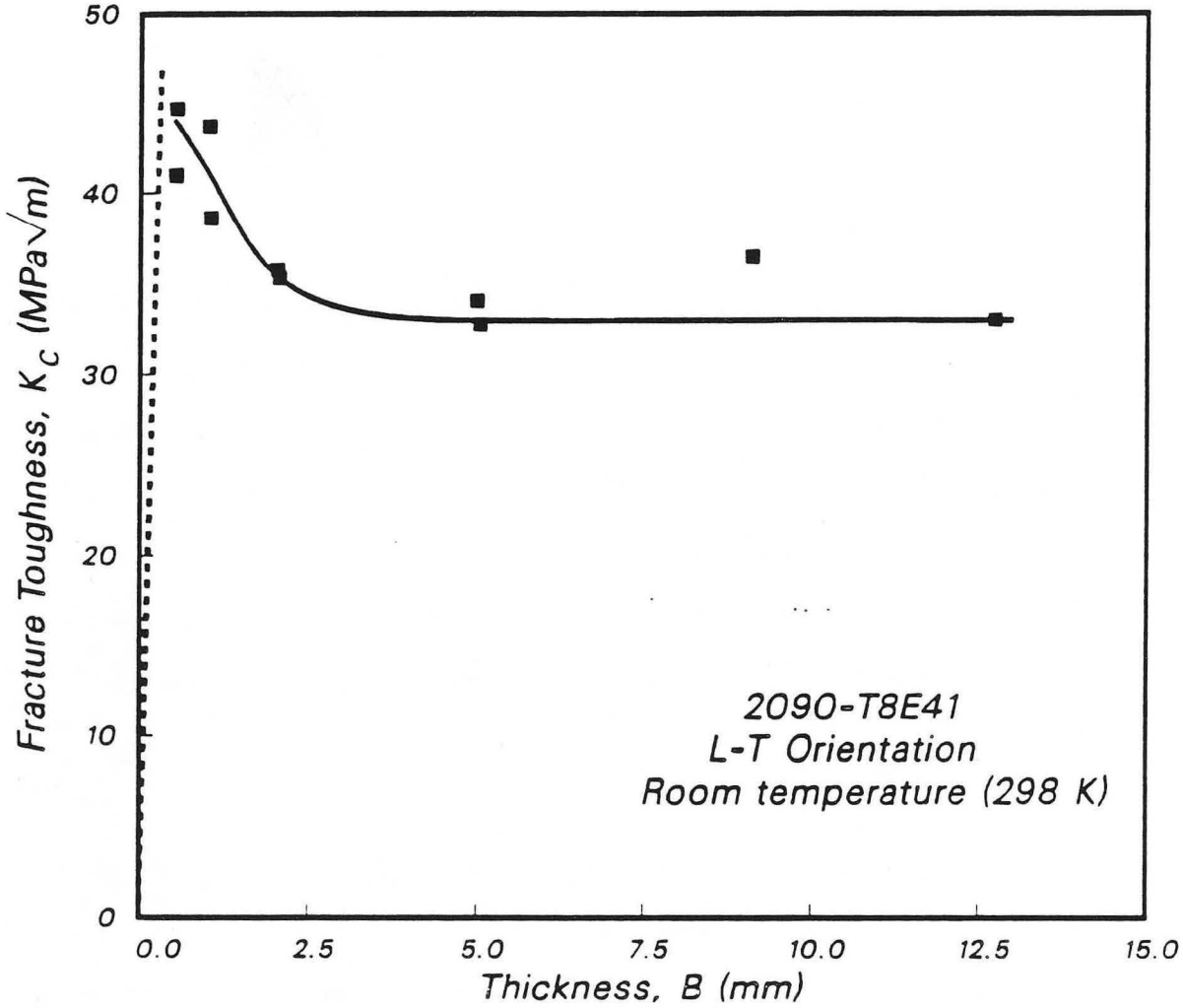

XBL 883-842

Fig. 8.6: Variation in Mode I fracture toughness K_c with test-piece thickness B for 2090-T8E41 alloy in the L-T orientation at 298 K. Tests were performed on C(T) specimens, machined from the plate mid-thickness, using anti-buckling restraints to prevent out-of-plane sliding.

from the plane-strain K_{Ic} value at 298 K through prediction of the plane-stress fracture toughness K_c^L relevant to the split-ligament size, using empirical models of Bluhm and others (29-31). Based on assumptions regarding shear-lip (plane-stress) and flat (plane-strain) fractures being predominantly volumetric and surface phenomena respectively, and on the dimensions of the plastic-zone size ahead of the crack tip, an expression for K_c^L can be derived as (32):

$$\frac{K_c^L}{K_{IC}} = \sqrt{1 + \frac{\bar{\varepsilon}_f E}{24\sigma_y} \cdot \frac{B_o}{B}} \qquad \text{.....(4)}$$

where, σ_y, $\bar{\varepsilon}_f$ and E refer to the yield strength, true fracture strain (uniaxial) and the elastic modulus, repectively. B is the thickness of the laminate and B_o is the maximum thickness in which plane-stress (shear-lip) fracture can fully develop. For the alloy 2090-T8E41, where K_{Ic} at 298 K is 36 MPa$\sqrt{m}$, σ_y = 552 MPa, $\bar{\varepsilon}_f$ = 0.086, E = 78.3 GPa and the transition from fully slant to flat fracture occurs at $\sim$2 mm (obtained by metallographically sectioning fractured test pieces of varying thickness), the model predicts values for K_c^L (B = 1 mm), and hence the fracture toughness at 77 K, to be 52 MPa$\sqrt{m}$, in excellent agreement (albeit fortuitously) with the measured value.

As K_c tends to zero as B tends to zero (Fig. 8.6), it should be noted that if the short-transverse splitting becomes too extensive, the thickness of the resulting ligaments may become so small (e.g., 100 μm) that the benefits of delamination (crack-divider) toughening may be compromised. This appears to be the case for overaged 2090, where copious grain and sub-grain boundary precipitation and the

formation of δ'-precipitate-free-zones (14) increases the tendency for delamination, such that the elevation in fracture toughness at 77 K is far smaller ($\lesssim$ 10 %) than for the T8 condition.

8.4.4 Tensile-Ductility Properties

Further evidence that delamination toughening is primarily responsible for the enhanced cryogenic toughness of certain aluminum-lithium alloys can be gained by examining the tensile-ductility properties. The observed improvement in uniaxial ductility at low temperatures also appears to be associated with loss of through-thickness constraint. Shown in Fig. 8.7 are fractographs of failed tensile specimens in the 2090-T8E41 alloy, where the increase in ductility from 298 to 77 K is over 25 %. Extensive short-transverse splitting is again evident at 77 K, but not at 298 K.

However, when the ductility in 2090 is measured under conditions approaching full triaxial (plane-strain) constraint, i.e., at $\sigma/\bar{\sigma} \rightarrow 2$ using circumferentially-notched tensile specimens, no such splitting is observed before crack initiation and the ductility (equivalent fracture strain) now <u>decreases</u> (by $\sim$40 %) with decreasing temperature from 298 to 77 K (Fig. 8.8). It is also apparent that the ductility is reduced by almost an order of magnitude by increasing the triaxial stress-state from that of uniaxial tension ($\sigma/\bar{\sigma}$ = 0.3) to that approaching plane strain; a result consistent with the observed elevation in fracture toughness in thin sections (Fig. 8.6).

8.5 CONCLUSIONS

Based on the above study of the mechanical behavior of commercial aluminum-lithium alloys, 2090, 8090, 8091 and 2091 as a function of

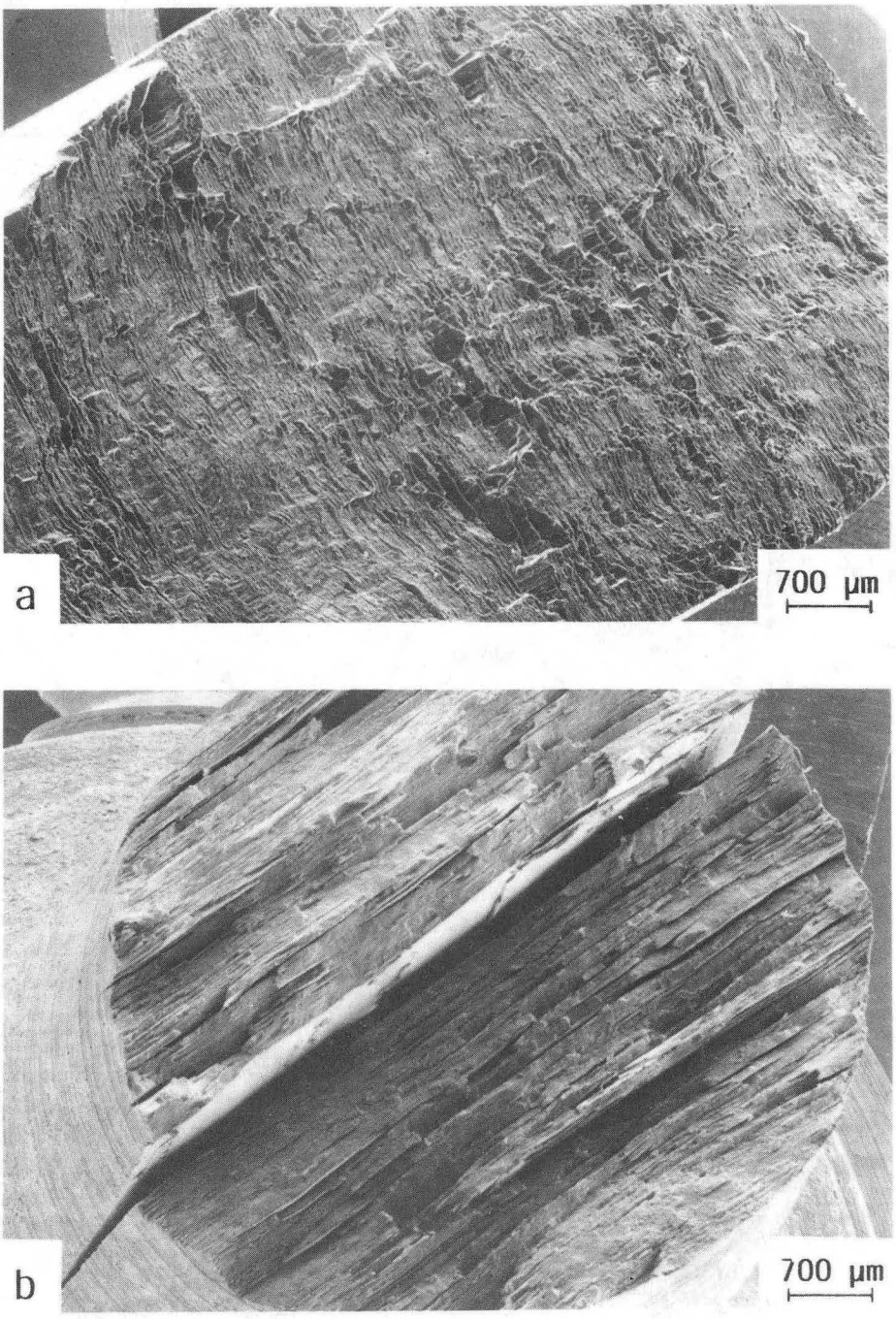

XBB 883-2356A

Fig. 8.7: Scanning electron micrographs of the fracture surfaces of unnotched round tensile specimens of 2090-T8E41 (longitudinal orientation), tested at a) 298 K, and b) 77 K, showing the presence of extensive short-transverse delamination at liquid-nitrogen temperatures.

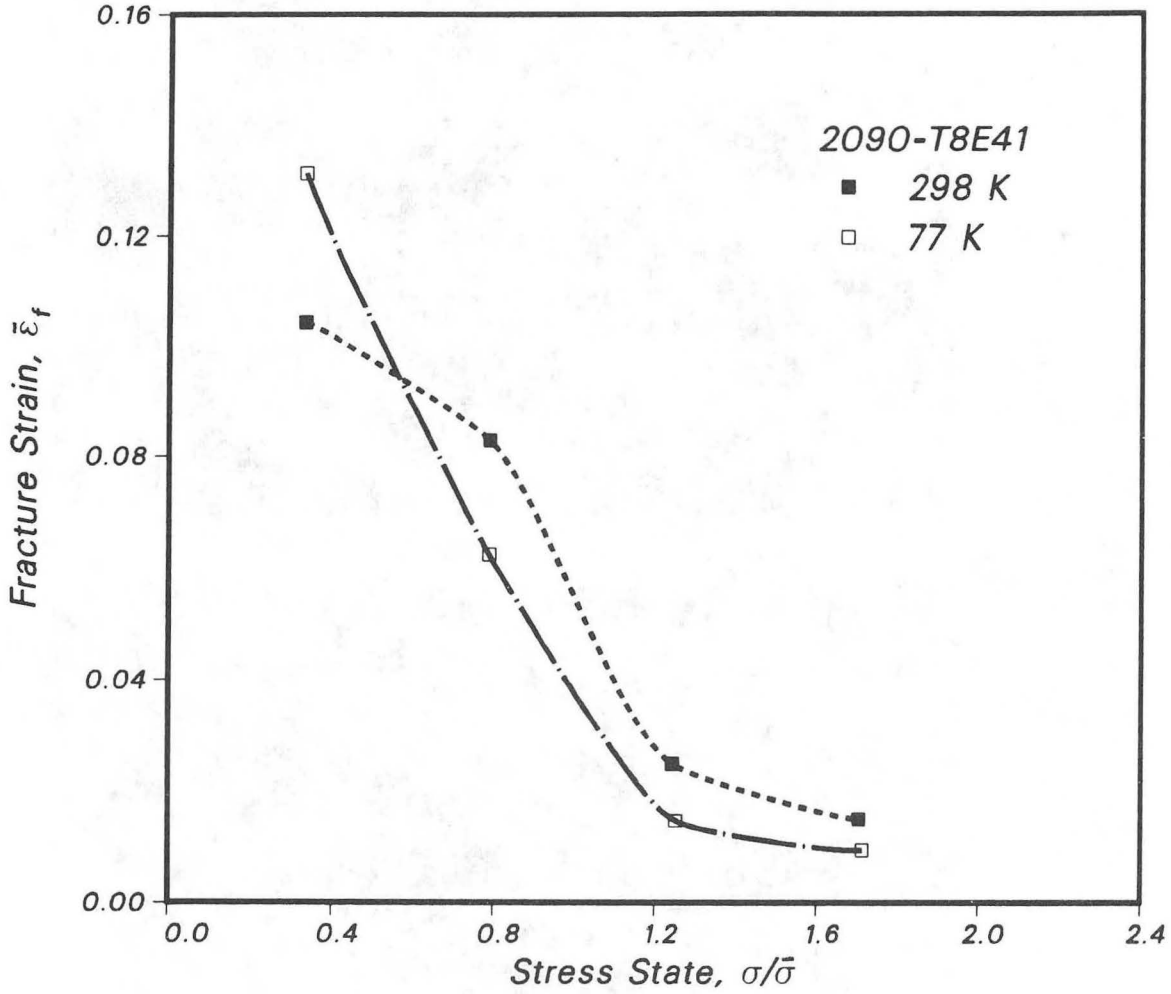

XBL 883-846

Fig. 8.8: Influence of stress-state ($\sigma/\bar{\sigma}$) on tensile ductility (equivalent fracture strain, $\bar{\varepsilon}_f$) for 2090-T8E41 (longitudinal orientation) at 298 K and 77 K. Note the <u>decrease</u> in plane-strain ductility and <u>increase</u> in uniaxial ductility with decrease in temperature.

microstructure and plate orientation at ambient (298 K) and cryogenic (77 K) temperatures, the following conclusions may be drawn:

1. All commercial alloys displayed increases in strength, uniaxial tensile-ductility and strain-hardening rates with decrease in temperature from 298 to 77 K.

2. Improvements in the plane-strain fracture toughness at cryogenic temperatures, however, are not typical of all commercial alloys. While alloys 2090-T8E41, 2090-T351, 8090-T8X and 8091-T8X showed such an <u>increase</u> in K_{Ic} for the L-T orientation between 298 and 77 K, alloys 2091-T8X, 8090-T351 and 8091-T351 conversely showed a corresponding <u>decrease</u>. Toughness in the S-L orientation however, deteriorates for all materials at low temperatures.

3. The reduction in fracture toughness (L-T orientation) with decrease in temperature, shown by alloys 2091-T8X, 8090-T351 and 8091-T351, was concurrent with a fracture-mode transition from ductile void coalescence at 298 K to a transgranular shear fracture (with some evidence of short-transverse delamination) at 77 K.

4. The increase in fracture toughness (L-T orientation) with decrease in temperature, shown by alloys 2090-T8E41, 2091-T351, 8090-T8X and 8091-T8X, conversely was associated with no (macroscopic) fracture-mode transition; however, the degree of intergranular, short-transverse delamination (splitting) on the fracture surface was significantly enhanced at 77 K, consistent with the observed decrease in S-L toughness.

5. Analogous to the behavior of laminated materials, the increase in L-T toughness, shown by alloys 2090-T8E41, 2091-T351, 8090-T8X and

8091-T8X with decrease in temperature, is ascribed primarily to a mechanism of crack-divider delamination-toughening. Essentially, the increased incidence of through-thickness (short-transverse) splitting at low temperature results in a loss of through-thickness constraint, causing the plane-strain fracture process to be divided in several parallel (thin-sheet) plane-stress fractures with higher K_c values. Thin-sheet (plane-stress) K_c values in 2090-T8E41 were found to be consistent with the observed increase in toughness.

6. The observed increase in uniaxial tensile ductility (longitudinal) with decrease in temperature also appeared to be associated with loss of constraint from enhanced short-transverse delamination at 77 K. Fracture strains measured in 2090-T8E41 under large triaxial stresses approaching plane-strain, accordingly, were found to decrease at lower temperatures.

8.6 REFERENCES

1. J. Glazer, S. L. Verzasconi, E. N. Dalder, W. Yu, R. A. Emigh, R. O. Ritchie, and J. W. Morris: Adv. Cryo. Eng., 32 (1986), p. 397.

2. D. Webster: Metals Progress, 125 (1984), p. 37.

3. D. Webster: in 'Aluminium-Lithium Alloys III', C.Baker, P. J. Gregson, S. J. Harris, and C. J. Peel (eds.), Institute of Metals, London, U.K. (1986), p. 602.

4. R. C. Dorward: Scripta Metall., 20 (1986), p. 1379.

5. F. G. Nelson and J. G. Kaufmann: in 'Fracture Toughness Testing at Cryogenic Temperatures', ASTM STP 496, American Society for Testing and Materials, Philadelphia, PA (1971), p. 27.

6. J. Glazer, S. L. Verzasconi, R. R. Sawtell, and J. W. Morris: Metall. Trans. A, 18A (1987), p. 1695.

7. F. A. Johnson and J. C. Radon: Int. J. Fracture, 8 (1972), p. 21.

8. D. Webster: Metall. Trans. A, 18A (1987), p. 2181.

9. K. T. Venkateswara Rao, H. F. Hayashigatani, W. Yu, and R. O. Ritchie: Scripta Metall., 22 (1988), p. 93.

10. C. M. Carman, D. F. Armiento and H. Markus: in 'ICF-1', Proc. of First Intl. Conf. on Fracture, T. Yokobori, T. Kawasaki and J. L. Swedlow (eds.), Sendai, Japan, 1 (1965), p. 995.

11. A. K. Vasudévan, W. G. Fricke, R. C. Malcolm, R. J. Bucci, M. A. Przystupa and F. Barlat: Metall. Trans. A, 19A (1988), p. 731.

12. R. O. Ritchie, W. L. Server, and R. A. Wullaert: Metall. Trans. A, 10A (1978), p. 1557.

13. P. W. Bridgeman: Studies in Large Flow and Fracture, McGraw Hill, New York, NY (1952.

14. K. T. Venkateswara Rao and R. O. Ritchie: Mater. Sci. Eng., 100 (1988), p. 23.

15. D. E. Pettit and J. M. Van Orden: in 'Fracture Mechanics', ASTM STP 677, American Society for Testing Materials, Philadelphia, PA (1979), p. 106.

16. H. L. Leichter: J. Spacecraft, 3 (1966), p. 1113.

17. J. D. Embury, N. J. Petch, A. E. Wraith, and E. S. Wright: Trans. Met. Soc. AIME, 239 (1967), p. 114.

18. J. G. Kaufman: J. Basic Eng., Trans. ASME, Series D, 89 (1967), p. 503.

19. N. G. Ohlson: Eng. Fract. Mech., 6 (1974), p. 459.

20. S. D. Antolovich, K. Kasi and G. R. Chanani: in 'Fracture Toughness', ASTM STP 514, American Society for Testing Materials, Philadelphia, PA (1972), p. 135.

21. S. Floreen, H. W. Hayden and J. Q. Steigelman: Trans. ASM, 62 (1969), p. 812.

22. R. A. Schmidt and T. J. Lutz: in 'Fracture Mechanics Applied to Brittle Materials', ASTM STP 678, American Society for Testing Materials, Philadelphia, PA (1979, p. 166.

23. M. Sakai, R. C. Bradt, and D. B. Fischbach: J. Mater. Sci., 21 (1986), p. 1491.

24. G. E. Pellissier: Eng. Fract. Mech., 1 (1968), p. 55.

25. R. J. Stokes and C. H. Li: Trans. TMS-AIME, 230 (1964), p. 1104.

26. K. Markstrom: Eng. Fract. Mech., 4 (1972), p. 593.

27. J. Cook and J. E. Gordon: Proc. Roy. Soc. A, A282 (1964), p. 509.

28. H. Tada, P. C. Paris and G. R. Irwin: in 'The Stress Analysis of Cracks Handbook', 2nd. edition, Paris Prod. Inc. & Del Research Corp., St. Louis, Mo (1985).

29. J. I. Bluhm: ASTM Proc., 61 (1961), p. 1324.

30. D. P. Isherwood and J. G. Williams: Eng. Fract. Mech., 2 (1970), p. 19.

31. G. C. Shih and R. J. Hartranft: Int. J. Fract., 9 (1973),p. 75.

32. D. Broek: Elementary Engineering Fracture Mechanics, 3rd. edition, Martinus Nijhoff, The Hague, The Netherlands (1984).

CHAPTER IX

CONCLUDING REMARKS

9.1 SYNOPSIS OF THE PRESENT WORK

In summarizing the observations on the mechanical properties of commercial aluminum-lithium alloys investigated, it may be concluded that the behavior is significantly influenced by extrinsic effects of crack deflection and crack closure mechanisms. In fatigue, such mechanisms are responsible for their excellent growth resistance of long cracks and enhanced retardation periods following single spike tensile overloads even after prolonged exposures at high temperatures. On the other hand, as these mechanisms are far less effective for flaws of limited wake, small crack growth rates in Al-Li alloys tend to be much faster than long cracks; the small crack resistance of Al-Li alloys remains comparable to other aluminum alloys. Moreover, fatigue properties of long cracks are strongly sensitive to plate orientation, depending upon the degree to which crack deflection is promoted in the various orientations.

Similarly, plane-strain fracture toughness properties are also highly anisotropic, with short-transverse (S-L) toughness values less than half the longitudinal (L-T) toughness. The poor short-transverse properties are a result of intergranular splitting along the weak interfaces of unrecrystallized, pan-cake shaped grain structures. Analogous to the fracture behavior of metallic laminates, the weak interfaces, in turn, benefit fracture toughness in other orientations (T-S, L-T), extrinsically through crack-arrester and crack-divider

delamination toughening. The effect is more pronounced at low temperatures, where further deterioration in short-transverse properties is primarily responsible for the remarkable strength-toughness combinations of certain aluminum-lithium alloys at cryogenic temperatures.

Overall, low-density aluminum-lithium alloys compare favorably, or in some instances exceed the strength, ductility and fracture toughness of existing aerospace aluminum alloys, particularly at cryogenic temperatures. Their long fatigue crack propagation resistance is unparalleled by monolithic or SiC-particulate-reinforced composite aluminum alloys, next only to ARALL laminates tested in the appropriate orientation (Fig. 9.1). Further improvements in these properties are projected, as research efforts continue towards obtaining a better understanding of the metallurgy of Al-Li alloys.

9.2 THE ALLOY DESIGN PERSPECTIVE

Within the framework of the present investigation, partially limited by the commercial nature of the alloys and the lack of processing facilities, some general trends in structure-property relationships for aluminum-lithium alloys may however, be noted. Peak-aged microstructures of the alloys, strengthened by homogenous distributions of T_1, S′ and θ′ plates along with δ′ spheres and β′ dispersoids, devoid of grain boundary effects, are preferred for optimal combinations of strength, ductility and fracture toughness. Although peak-aging concurrently reduces the short-transverse properties in unrecrystallized, anisotropic grain structures, it benefits properties in the other orientations through delamination

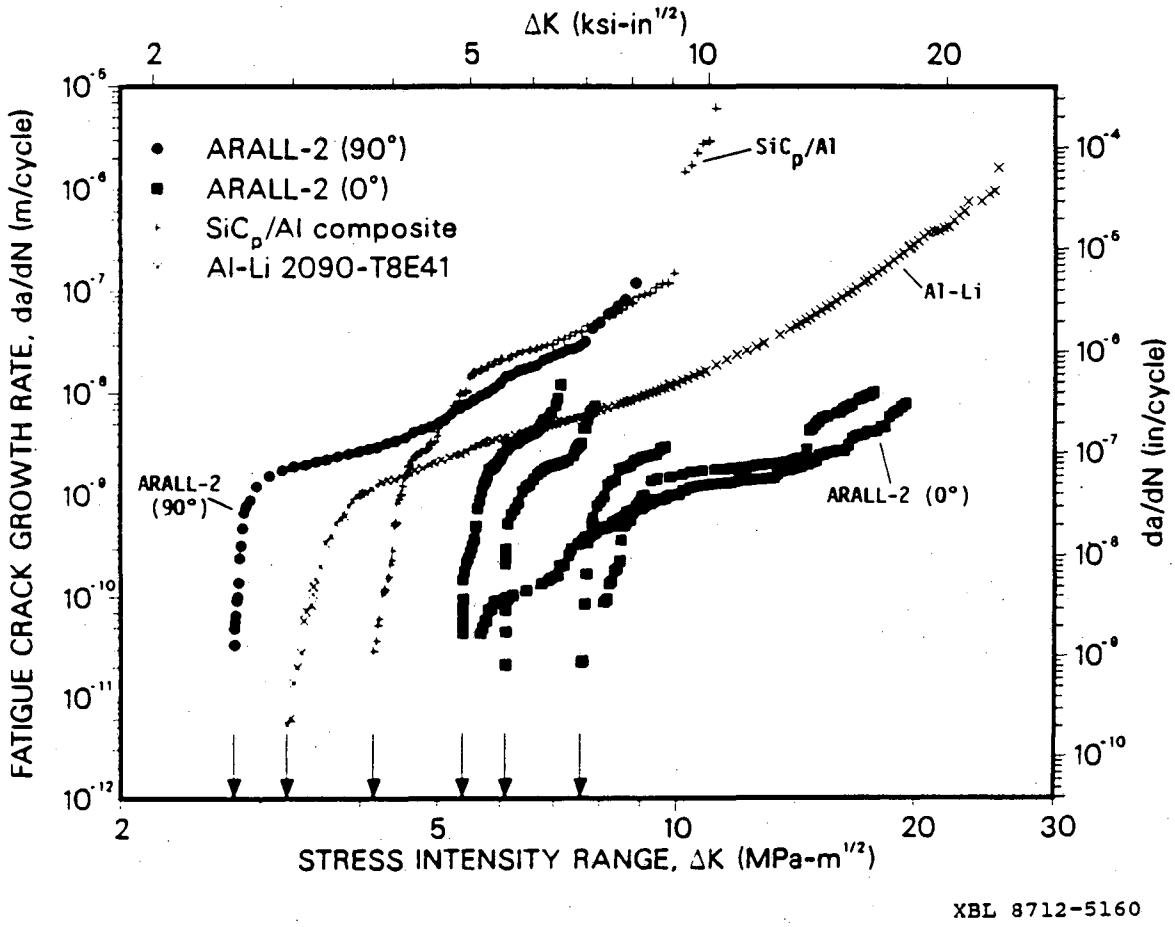

Fig. 9.1: Comparison of fatigue crack growth resistance of the competing aerospace materials, namnely, aluminum-lithium alloys (2090-T8E41), metal-matrix composites (SiC-particulate reinforced 7091 P/M aluminum alloy) and ARALL laminates. Data for ARALL and metal matrix composites taken from Refs.1 and 2, respectively.

toughening. Optimizing the amount of pre-stretch, artificial aging time and temperature are the key factors for achieving the best strength-toughness relationships in advanced aluminum-lithium alloys.

Other principal parameters of interest for further improving strength and toughness of Al-Li alloys include, modifications in alloy chemistry, grain structure and reductions in the amount of second-phase intermetallic particles. Adding transition metal elements such as Hf, Zr, and Ti to Al-Li alloys, upto 1 wt. %, alter the precipitation hardening and deformation characteristics, thereby improving the toughness of these alloys (3). Alloying rare earth elements, which form Ll_2 ordered precipitates in aluminum (4), and Al-Li based composite technologies also show exceptional promise. Concerning the preferred size and morphology of the grains, despite recent indications in Al-Li alloy sheets that recrystallized-equiaxed structures show better strength-toughness combinations (5), more work is needed to clarify the role of grain and subgrain structures on the deformation behavior.

With respect to the fatigue crack propagation resistance of long cracks in Al-Li alloys, underaged planar-slip microstructures hardened by coherent, ordered precipitates (δ' in Al-Li alloys, for example), which promote meandering and tortuous fatigue crack paths and consequent crack closure, are most beneficial. Coarse, unrecrystallized grain structures with pronounced crystallographic texture further enhance the degree of crack deflection and reduce fatigue crack growth rates.

However, for conservative fatigue-life predictions, small crack results may be more relevant to the damage-tolerant aircraft design

engineer, rather than long cracks, as the former represent the behavior of incipient, naturally-occurring flaws in structures. Present results indicate that sub-continuum growth of such defects is largely independent of alloy composition and microstructure, and improving the long-crack properties increases the discrepancy between long and small crack behavior. The small-crack problem, which is in essence created by the breakdown of linear-elastic fracture mechanics for small crack sizes, is common to near-threshold fatigue behavior of most engineering materials. Much additional research needs to be done before alloys and microstructures can be optimized for small crack fatigue resistance.

Finally, as microstructural factors which benefit one set of mechanical properties may prove detrimental to the other, it is foreseen that Al-Li alloy chemistries and microstructures will be optimized for specific applications. For example, high-strength applications demand alloys with high solute content in the peak-aged condition, whereas damage-tolerance applications prefer medium-strength underaged tempers. Other classifications and temper designations may be based on ultra-low density, cryogenic properties, superplasticity, stress corrosion and high-temperature resistance.

9.3 AREAS FOR FURTHER RESEARCH

Experimental results on the mechanical behavior of commercial aluminum-lithium alloys presented in this report indicate that the alloys can be further exploited to improve the current strength-toughness relations. This of course, will involve substantial amount of fundamental mechanical property characterization, in order to derive the structure-property relationships for Al-Li alloys. Apart from the

melting, processing and scrap related problems, other aspects of aluminum-lithium alloy development technology, that need consideration are outlined below.

It is amply clear that mechanical properties of commercial Al-Li are critically dependent on thermo-mechanical processing parameters, particularly the quench rate and the amount of stretch prior to artificial aging. Accordingly, through-thickness variations in the mechanical properties can be quite significant, due to variations in the quench rate, and hence, differences in the distribution of hardening precipitates, particularly for thick plates ($\gtrsim$ 0.5 in) and forgings. Also, cold deformation treatments are not possible for forgings and extrusions, with the effect that properties of fabricated products are below target specifications. Quench sensitivity of Al-Li alloys and properties of forgings need improvement.

The alloys presently suffer from poor short-transverse properties, the reasons for which are relatively unclear. As current melting and casting procedures guarantee low levels of Na, K and H, present results point toward grain boundary phenomena and the anisotropic nature of the grain structures as possible reasons. More work is necessary for understanding and improving the short-transverse properties.

Stress corrosion resistance of advanced aluminum-lithium alloys is comparable to traditional high-strength aluminum alloys. Despite small differences, in general, underaged and peak-aged tempers show optimal corrosion resistance for the Al-Li-Cu-Zr and Al-Li-Cu-Mg-Zr systems; overaging invariably compromises these properties (6-11).

However, the alloys are prone to "pre-exposure" cracking effects in sea water environments due to the alkaline nature of lithium (12). Also recent results indicate that hydrogen embrittlement effects can lower the ductility and short-transverse toughness (13-15). Little is known about the mechanistic aspects of such environmentally-assisted crack growth phenomena, both under static loading and corrosion fatigue conditions.

Due to the prominent role of crack closure induced by asperity wedging, observed during fatigue crack growth in Al-Li alloys at positive, low load ratios ($R = 0.1$), there are concerns about their fatigue resistance under tension-compression loading ($R = -1, -3$), where the compression portion of the cycle restricts crack closure. In addition, measured levels of crack closure, being sensitive to changes in crack path morphology, K_{cl} may depend on the specimen geometry. Accordingly, significant variations in crack growth rates between center-cracked sheet (CCS), compact tension (C(T)) and single-edge-notched bend (SEN(B)) test specimens are expected. These implications need to be examined in detail, both experimentally and analytically.

A few other aspects which need attention include, weldability of aluminum-lithium alloys, in view of their excellent cryogenic properties and potential structural applications in liquid-hydrogen, oxygen and natural gas fuel tanks, sheet metal working and superplastic forming. With an improved understanding of these factors combined by the extraordinarily rapid commercialization of technology, low density aluminum-lithium alloys are expected to be a distinct class of advanced engineering materials, for structural aerospace applications.

9.4 REFERENCES

1. R. O. Ritchie, W. Yu and R. O. Ritchie: Eng. Fract. Mech., 23 (1988), in press.

2. J. K. Shang, W. Yu and R. O. Ritchie: Mat. Sci. Eng., 102 (1988), in press.

3. F. W. Gayle, N. F. Levoy and J. B. Vandersande: J. Metals, 39:5 (1987), p. 33.

4. R. R. Sawtell: unpublished work, University of California, Berkeley.

5. W. S. Miller, J. White and D. J. Lloyd: in 'Aluminum-Lithium Alloys IV', G. Champier, B. Dubost, D. Miannay and L. Sabetay (eds.), J. de Physique Coll., 48:C3 (1987), p. 151.

6. C. Kumai, J. Kusinski, G. Thomas and T. M. Devine: Corrosion, 44 (1988), in press.

7. P. Niskanen, T. H. Sanders, J. G. Rinker and M. Marek: in Corrosion Sci., 22 (1982), p. 283.

8. E. I. Meletis: Mat. Sci. Eng., 93 (1987), p. 235.

9. T. Sheppard and N. C. Parson: Mat. Sci. Technol., 4 (1987), p. 345.

10. M. Ahmad: in 'Aluminum-Lithium Alloys IV', G. Champier, B. Dubost, D. Miannay and L. Sabetay (eds.), J. de Physique Coll., 48:C3 (1987), p. 871.

11. A. Gray: in 'Aluminum-Lithium Alloys IV', G. Champier, B. Dubost, D. Miannay and L. Sabetay (eds.), J. de Physique Coll., 48:C3 (1987), p. 891.

12. J. G. Craig, R. C. Newman, M. R. Jarrett and N. J. H. Holroyd: in 'Aluminum-Lithium Alloys IV', G. Champier, B. Dubost, D. Miannay and L. Sabetay (eds.), J. de Physique Coll., 48:C3 (1987), p. 825.

13. N. J. H. Holroyd, A. Gray, G. M. Scamans and R. Hermann: in 'Aluminum-Lithium Alloys III', C. Baker, P. J. Gregson, S. J. Harris and C. J. Peel (eds.), Institute of Metals, London, U.K. (1986), p. 310.

14. E. W. Lee and J. Waldman: in 'Aluminum-Lithium Alloys: Design Development and Application Update', R. J. Kar, S. P. Agrawal and W. E. Quist (eds.), ASM International, Metals Park, Ohio (1988).

15. K. T. Venkateswara Rao: unpublished work, University of California, Berkeley.

LAWRENCE BERKELEY LABORATORY
CENTER FOR ADVANCED MATERIALS
1 CYCLOTRON ROAD
BERKELEY, CALIFORNIA 94720